

Développement de Cellules Photovoltaiques à base de CIGS de haute performance sur substrats métalliques

Mishael Stanley

▶ **To cite this version:**

Mishael Stanley. Développement de Cellules Photovoltaiques à base de CIGS de haute performance sur substrats métalliques. Autre. Université Paris sciences et lettres, 2019. Français. NNT : 2019PSLEC023 . tel-02879968

HAL Id: tel-02879968

https://pastel.hal.science/tel-02879968

Submitted on 24 Jun 2020

HAL is a multi-disciplinary open access archive for the deposit and dissemination of scientific research documents, whether they are published or not. The documents may come from teaching and research institutions in France or abroad, or from public or private research centers.

L'archive ouverte pluridisciplinaire **HAL**, est destinée au dépôt et à la diffusion de documents scientifiques de niveau recherche, publiés ou non, émanant des établissements d'enseignement et de recherche français ou étrangers, des laboratoires publics ou privés.

PSL UNIVERSITÉ PARIS

THÈSE DE DOCTORAT
DE L'UNIVERSITÉ PSL

Préparée à École Nationale Supérieure de Chimie de Paris

Développement de cellules photovoltaïques à base de CIGS de haute performance sur substrats métalliques

Development of high performance CIGS solar photovoltaic cells on metallic substrates

Soutenue par
Mishael STANLEY
Le 22 Mai 2019

Ecole doctorale n° 397
Physique et Chimie des Matériaux

Spécialité
Chimie Physique

Composition du jury :

Christel, LABERTY-ROBERT Professeur, Sorbonne Université	*Président du Jury*
Daniel, ABOU-RAS Equivalent Professeur, HZB	*Rapporteur*
Stéphane, COLLIN Chargé de Recherche, C2N	*Rapporteur*
Louis, GRENET Chargé de Recherche, CEA	*Examinateur*
Negar, NAGHAVI Directeur de Recherche, CNRS	*Directrice de thèse*

Chimie Paris ParisTech | PSL

Doctoral Thesis

Prepared at : École Nationale Supérieure de Chimie de Paris (Chimie ParisTech)

Doctoral School: ED397 - Physics and Chemistry of Materials

Development of high performance CIGS solar photovoltaic cells on metallic substrates

Mishael Stanley

May 22, 2019

JURY MEMBERS:

Christel, LABERTY-ROBERT Sorbonne Université	Président du Jury
Daniel, ABOU-RAS HZB	Rapporteur
Stéphane, COLLIN C2N	Rapporteur
Louis, GRENET CEA	Examinateur
Nicolas, BARREAU IMN	Invité
Marie, JUBAULT EDF/IPVF	Encadrante
Negar, NAGHAVI CNRS	Directrice de thèse

Dedicated to my little brother, Uche Stanley.

RÉSUMÉ

Dans cette thèse, les méthodes de fabrication et l'optimisation des absorbeurs CIGS déposés sur des feuilles flexibles en Molybdène et en acier inoxydable sont étudiées. La feuille de Mo agit à la fois comme substrat et comme contact arrière dans les cellules, réduisant ainsi les étapes de fabrication requises pour une cellule CIGS. D'autre part, l'acier inoxydable, bien qu'il nécessite une couche barrière contre les impuretés et un dépôt par contact arrière, reste économiquement plus intéressant. Les absorbeurs CIGS ont été réalisés par un procédé de coévaporation en 3 étapes. Ce travail étudie l'impact de différentes conditions de dépôt telles que la température, l'incorporation de Na et l'optimisation du gradient de Ga sur la performance de la cellule. Différentes techniques de caractérisation telles que les mesures XRD, GD-OES, IV et EQE ont été utilisées pour étudier les propriétés des cellules. Le procédé optimisé pour le dépôt CIGS sur feuilles de Mo a donné un rendement maximum de 14,0 %, ce qui est proche du rendement record mondial de 14,6 % atteint sur les substrats de Mo. Dans le cas de l'acier inoxydable, un inconvénient majeur est la présence d'impuretés Fe nuisibles qui créent des chemins de dérivation dans l'absorbeur. Pour réduire les effets néfastes de l'impureté de Fe, nous avons introduit une couche barrière tout en limitant la température de dépôt à 480 °C afin de réduire la diffusion efficace du Fe. Une efficacité maximale de 14,2 % a été obtenue avec une épaisseur de barrière Cr de 500 nm. Enfin, le procédé de dépôt CURO appliqué aux substrats d'acier pour étudier l'effet du procédé de dépôt sur la qualité de l'absorbeur.

MOTS CLES:

Substrats métalliques ; CIGS ; Rendement ; Cellule solaires

ABSTRACT

In this thesis, the fabrication methods and optimization of CIGS absorbers deposited on flexible Mo and stainless steel foils is studied. Mo foil acts as both the substrate and back contact in the cells hence reducing the manufacturing steps required for a CIGS cell. On the other hand, stainless steel despite requiring an impurity barrier layer and back contact deposition remains economically more interesting. The CIGS absorbers herein were realized by a 3-stage coevaporation process. This work studies the impact of different deposition conditions such as temperature, Na incorporation and optimization of the Ga gradient on the cell performance. Different characterization techniques such as XRD, GD-OES, IV, and EQE measurements were used to study the cell properties. The optimized process for CIGS deposition on Mo foils yielded a maximum efficiency of 14.0 % which is close to the world record efficiency of 14.6 % achieved on Mo substrates. In the case of stainless steel, a major drawback is the presence of detrimental Fe impurities that create shunt paths in the absorber. To reduce the detrimental effects of Fe impurity, we introduced a barrier layer while limiting the deposition temperature to 480 °C in order to reduce the effective diffusion of Fe. A maximum efficiency of 14.2 % was obtained with a Cr barrier thickness of 500 nm. Finally the CURO deposition process as applied to the steel substrates to investigate the effect of the deposition process on the absorber quality.

KEYWORDS:

Metallic Substrates; Efficiency; CIGS; solar cells

ACKNOWLEDGEMENTS

A decent Ph.D thesis is incomplete without the help and support received within the research community. Hence, I would like to take a moment to acknowledge those that helped me realize this milestone in my educational career.

First off, my sincere gratitude and appreciation goes to my thesis director, Negar Naghavi and my supervisor Marie Jubault. Negar not only played the role of a scientific thesis director but also used her kind but firm words to keep me going. The impact of her steady mentorship cannot be overemphasized as they came in handy when I was at my lowest and all seemed impossible to achieve. After moving to China, she relentlessly saw to it that we held bi-weekly meetings which was an avenue to follow up on my work. I very much appreciate your candid advice and suggestions and for that, I thank you. Marie gave me the necessary trainings needed to operate the sputtering machine which I used in depositing impurity barrier layers for my stainless steel substrates. She was always gentle, soft-spoken and understanding and she was quick to boost my morale by citing her experiences as Ph.D student. Indeed, if I should go and on mentioning the impacts you both had on the successful completion of my thesis, I would probably be writing a 10-page epistle. But I'd cut it short and say thank you for everything. I sincerely thank Frédérique Donsanti who also supervised my work, curated the weekly coevap meetings and supervised the daily technical manipulation of the coevaporation machines. Fred offered numerous suggestions and constructive criticism on my presentations, papers and was always available to offer help. Your suggestions for improving my final thesis presentation are highly appreciated.

I thank Matthieu Versavel for the initial interview and accepting me to join the IRDEP team at Chatou. Your effective management of the entire team led to a great work atmosphere at Chatou and beyond. I would like to thank Daniel Lincot, the director of the now defunct IRDEP for numerous pieces of advice and brainstorming sessions we both had on new ideas and concepts on improving the CIGS thin film technology.

After the lab closure and suspension of experimental activities due to the move to a new site, a substantial part of my thesis was carried out at IMN, Nantes under the supervision of Nicolas Barreau. I would like to thank the team at IMN and especially Nicolas who made sure I was integrated into his research team. I thoroughly enjoyed working with him while in Nantes and I appreciate his insight and expertise on various matters relating to my work and other extra-curricular activities. I also will like to thank Sofia Gaiaschi and Agnès Tempez from Horiba for the GDOES, XRF and AFM measurements during the downtime at IPVF.

I thank Daniel Abou-Ras and Stéphane Collin who reviewed my final manuscript in great details and offered suggestions for improving its quality. Daniel took his time to explain concepts that were at the time vaguely understood and also sent me numerous papers which gave me a deeper understanding. I

also thank the members of my jury for taking out time from their busy lives to read my manuscript and be present during my final defense. The round table discussions, questions and constructive criticism led to the final award of my Ph.D degree. Thank you Christel Laberty-Robert, Daniel Abou-Ras, Stéphane Collin, Louis Grenet and Nicolas Barreau.

I also thank several other colleagues who were instrumental in one way or the other to the realization of my work. I thank Corentin for the training on using the GDOES machine as well as the DEKTAK profiler. Thanks to Jorge as well who took over the management of the GDOES and gave support whenever needed. I thank Enrique immensely for the IV and EQE characterizations. Thank you Samuel for the countless and never ending Mo and ZnO depositions. My gratitude also goes to Laurent Michely for the CdS depositions and after his departure, Thibaud masterfully took over the CdS depositions and was later joined by Damien. Thank you Thibaud for the work done together on understanding the influence of the modification of the CIGS absorber recipe on the CdS growth time which I presented at the end of my thesis. I thank Laurent Lombez for the Raman characterizations. Thanks to Romain and Nathaniel for the XRD characterizations. Thanks to Jessica for helping out with several SEM and EDX characterizations. Thank you Aurélien for the XRF measurements and trying to establish a model for stainless steel substrates.

I also will like to acknowledge my team members, Valentin, Matteo, Jorge, Torben and Fabien Mollica. I fondly remember all the occasions we spent troubleshooting the coevap machines under Fred's supervision. I thank my colleague and friend Harold for his thoughtfulness, kind and motivating words offered during the most trying times of my thesis, the world needs more people like you. My sincere thanks to Margot who patiently proofread my 20-page French abstract…you rock! Big thanks to the IPVF football team and to Adrien and Fabien for organizing the matches. From the depths of my heart, my gratitude also goes to Mireille, I can't thank you enough big sis. Thanks for your soothing words, your reminders, your firm and hard words which came at the right time, your endless smiles and your zest for life.

I thank my friend and brother, Arsene for his support during this journey. My gratitude goes to Sabina for her steady love and encouragement during this 3-year sojourn. Finally, I would to thank my parents Isaac and Angela Stanley, my brothers Oscar, Joel, Prince, Uche and Precious for the undying love I receive each day. In all things, I give glory to Jehovah for the gift of life.

Contents

Abstract

Acknowledgement

General Introduction 1

1. Introduction to CIGS technology 6

1.1. Overview of world energy production and consumption 6
1.2. The PV market 11
1.3. Introduction to $Cu(In,Ga)Se_2$ solar cells 15
Conclusion 29

2. Fundamentals of CIGS solar cells 34

2.1. Physics of CIGS solar cells 34
2.2. CIGS absorber fabrication 41
2.3. Buffer layer and contacts deposition 47
Conclusion 51

3. Fabricating CIGS solar cells on Mo substrates 54

3.1. Characterization of the Mo substrate 55
3.2. Deposition and characterization of CIGS absorbers grown on Mo foil 60
3.3. Optimization of CIGS absorber composition 69
3.4. Alkali doping of CIGS layers by NaF post-deposition treatment (PDT) 76
3.5. Gallium grading 82
3.6. Impact of a sputtered Mo back contact 92
Conclusion 98

4. $Cu(In,Ga)se_2$ solar cells on stainless steel substrates 104

4.1. Properties of stainless steel 104
4.2. Impurity barrier layer 105
4.3. Impact of substrate type on CIGS absorber growth at low temperature 116
4.4. CURO deposition process 129
4.5. Fabrication of CIGS absorbers via the CURO process 130
Conclusion 139

5. General conclusion and perspectives 144

Appendix 150

A. Material characterization techniques 151

A1. Scanning Electron Microscopy 151
A2. X-ray Diffraction 151
A3. Glow Discharge Optical Emission Spectroscopy 151
A4. X-ray Fluorescence 152
A5. Raman Spectroscopy 152
A6. Atomic Force microscope 152

B. Solar device characterization 153

B1. External Quantum Efficiency 153
B2. Current – Voltage characteristics 153

C. Test of the optimized process (Mo substrates) on SLG and Borosilicate glass 154

Extended Summary – French 157

General Introduction

Energy – With current statistics putting the world population at 7.7 billion, it is by no means inarguable that the demand for energy has also surged. In spite of this, the world has always relied heavily on fossil fuels which makes up 81% of the global energy usage in 2017. According to the International Energy Agency (IEA), energy production and use is responsible for two-thirds of greenhouse-gas (GHG) emissions [1]. A dire implications of this is the increase in the emission of greenhouse gases that will lead to severe consequences for the earth and its inhabitants if left unchecked. CO_2 emissions rose by 1.4% in 2017, breaking a new all-time high of 32.5 gigatonnes. To combat the debilitating climatic effects of greenhouse emissions, a climate change meeting (COP21) was held in Paris in December 2015, with the goal of setting the world on a sustainable path. Effectively curbing emissions will mean a switch to alternative and sustainable energy sources [2].

Photovoltaics (PV) is one of the numerous alternatives. It does not emit any gasses or pollutants during operation, and has a low energy pay-back time. It uses energy from the sun to produce electricity hence making it one of the cleanest forms of energy. Since energy from the sun is inexhaustible, PV modules get their "fuel" for free. Photovoltaics today are dominated by crystalline silicon technology. Among the numerous other types of PV cells, $Cu(In,Ga)Se_2$ (CIGS) thin-film solar cells are the most advanced and most efficient. They are already well developed with current record conversion efficiencies exceeding 22.6% which puts CIGS in the same level as c-Si based solar cell technologies. The cost of energy from PV modules has been decreasing and has now reached the cost range of power derived from fossil fuels plants [3]. The economic competitive edge of CIGS technologies is directly influenced by increase in cell and module efficiency along with a reduction in material usage. Conventional CIGS cells are typically fabricated on rigid sodalime glass substrates, however, this thesis aims to fabricate and optimize CIGS solar cells on flexible metallic substrates. Thus arises the question; what is the interest in making flexible CIGS solar cells?

Flexible solar cells are of great interest because they open up new applications that are otherwise impossible with rigid cells. Flexible cells can be applied on uneven surfaces and depending on the degree of flexibility of the cell, can take the form of any surface on which it is applied. Furthermore, flexible solar cells are also very lightweight compared to rigid cells made on glass. This makes them very interesting for use in space applications where weight is usually

a constraint. Finally, metallic substrates, although thin and flexible, are mechanically stable hence providing mechanical support to the solar cell or module as the case maybe. Mo substrates were used in this thesis because unlike other substrates that need a Mo back contact, the Mo substrate can play both roles as the substrate and back contact material hence eliminating the need to sputter an additional back contact. Furthermore, the best cells on metallic substrates have been achieved on stainless steel substrates hence we carried out tests on stainless steel accordingly. One of the challenges encountered in the use of metallic substrates was in the end-point detection which is difficult to observe due to the thermal properties of metals. On stainless steel, the diffusion of impurities also presents a challenge as the impurities are detrimental to the performance of the solar cell. A barrier layer was inserted between the stainless steel substrate and the Mo back contact to prevent the diffusion of Fe impurities.

PhD Thesis - The manuscript summarizes the results of the research work at the defunct IRDEP lab (now IPVF). This thesis studies the fabrication and optimization of CIGS cells on flexible metallic substrates with a goal to improving the cell performance. The flexible substrates selected for use is Mo and stainless steel foils. Part of the research work, mainly focusing on the use of stainless steel substrates, was carried out at Institut des Matériaux Jean Rouxel, Nantes (IMN) in a research collaboration. The steel substrates used in this research were tailor made and supplied by APERAM.

Chapter 1 discusses the current world energy situation with respect to demand and forecasted growth of renewables. It further highlights the state-of-art of CIGS cell technology with progresses made by different groups. Furthermore, the scope and challenges of fabricating CIGS absorbers on metallic substrates is reviewed.

Chapter 2 gives insights on the physics and operation of CIGS cells. The deposition methods used for the absorber is also described with specific attention to the parameters that directly affect CIGS film quality. Here the end-point detection, Cu-Se binaries and Ga gradients are discussed. Finally, the fabrication of the other layers that make a complete CIGS cell is presented. These include the back contact deposition (in the case of stainless steel substrates), CdS buffer layer and the transparent conducting i-ZnO/ZnO:Al window layer.

Chapter 3 presents the results obtained for the works done on the flexible Mo substrates (0.15 mm). The work followed a systematic optimization path on various aspects of the CIGS

fabrication. This included the temperature selection and process optimization, NaF post-deposition, Ga gradient and studies involving the addition of a sputtered Mo back contact.

Chapter 4 focuses on the use of stainless steel substrates (0.2 -0.3 mm). In the case of stainless steel, Fe is the basic alloying element. However it is reported that the presence of Fe in the CIGS can deteriorate the cell properties [4] [5]. Notwithstanding, It is possible to limit the diffusion of impurities either by depositing a diffusion barrier between the substrate and the back contact or to reduce the deposition temperature of the CIGS. Four different types of stainless steel were with different composition and roughness were tested using the optimized deposition process on Mo substrate at 480 °C. Depositions were made using the 3-stage and CURO deposition methods developed at IMN in Nantes. The details of these processes are presented. Finally, a comparison is made between the CIGS absorbers fabricated on stainless Steel, Mo and rigid sodalime glass (SLG) substrates.

REFERENCES

[1] International Energy Agency, “Global Energy & CO2 Status Report,” 2017.

[2] United Nations Climate Change, “Renewable energy: Catalyst for a clean energy transition,” *Organisation for Economic Co-operation and Development (OECD*. [Online]. Available: http://www.oecd.org/environment/renewable-energy-catalyst-clean-energy-transition.htm. [Accessed: 13-Aug-2018].

[3] B. Beetz and I. Clover, “2017: The PV year in review,” 05-Dec-2017.

[4] D. Amouzou, P. Guaino, L. Fourdrinier, J.-B. Richir, F. Maseri, and R. Sporken, “Dielectric and diffusion barrier multilayer for Cu(In,Ga)Se2 solar cells integration on stainless steel sheet,” *Thin Solid Films*, vol. 542, pp. 270–275, Sep. 2013.

[5] G.-L. Chiu, T. Subburaj, S. Som, C.-Y. Ou, and C.-H. Lu, “Influence of doping iron ions into Cu (In, Ga) Se2 films in the morphology and photovoltaic properties of thin-film solar cells,” *J. Ceram. Process. Res.*, vol. 18, no. 10, pp. 754–759, 2017.

CHAPTER 1

Energy produced and used in ways that support human development in all its social, economic and environmental dimensions is what is meant by sustainable energy.

-World Energy Assessment: *Energy and the Challenge of Sustainability, 2000*

INTRODUCTION TO CIGS TECHNOLOGY

The world's energy demand has surged in recent years. The year 2017 saw the global energy demand rise by 2.1% compared to 0.9% in 2016 and a 0.9% average over the past five years [1]. This rise in energy demand and production was accompanied by a corresponding increase in Carbon emissions as fossil fuels still accounted for 81% of the global energy demand in 2017. CO_2 emissions rose by 1.4% breaking a new all-time high of 32.5 gigatonnes (Gt) which is significant because global CO_2 emissions have remained relatively flat over the last three years [1]. However, it should be noted that this increase in emissions was not universal, while most major economies saw an increase in emissions, some had a decline, with the biggest reduction in carbon emissions coming from the USA. This Chapter reviews the global status of energy production and consumption and the role of solar energy. It will also discuss the growing interest in thin film solar cells with a focus on flexible CIGS cells.

1.1 OVERVIEW OF WORLD ENERGY PRODUCTION AND CONSUMPTION

1.1.1 FOSSIL FUELS

The energy demand in 2017 was led by China and India accounting for more than 40% of the total growth. Growing industrialization and population increase are major drivers in this increase in energy demand. This global trend in energy needs is expected to keep rising steadily at least for the next two decades with more than two-thirds of this growth coming from developing countries where economic and population growth is highest [2]. Figure 1.1 is a graphical representation of the growth in global energy demand by fuel types.

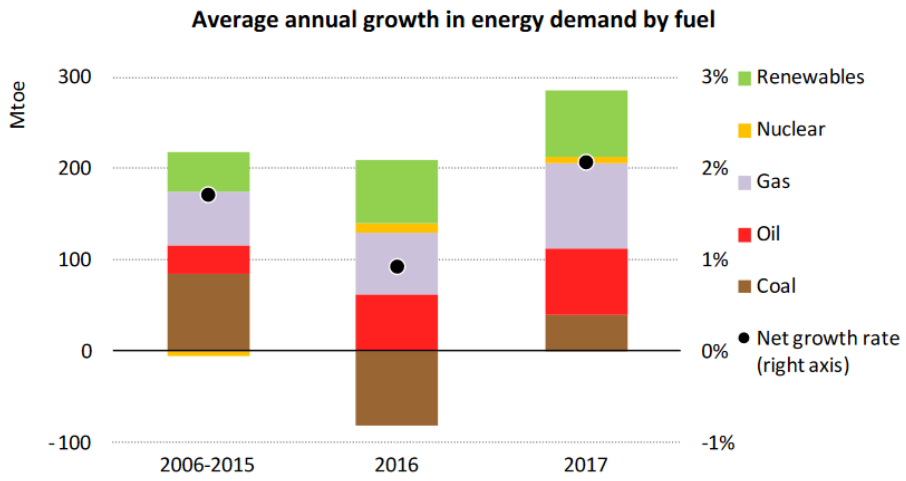


Figure 1.1 Graph representing the average annual growth in global energy demand [1]

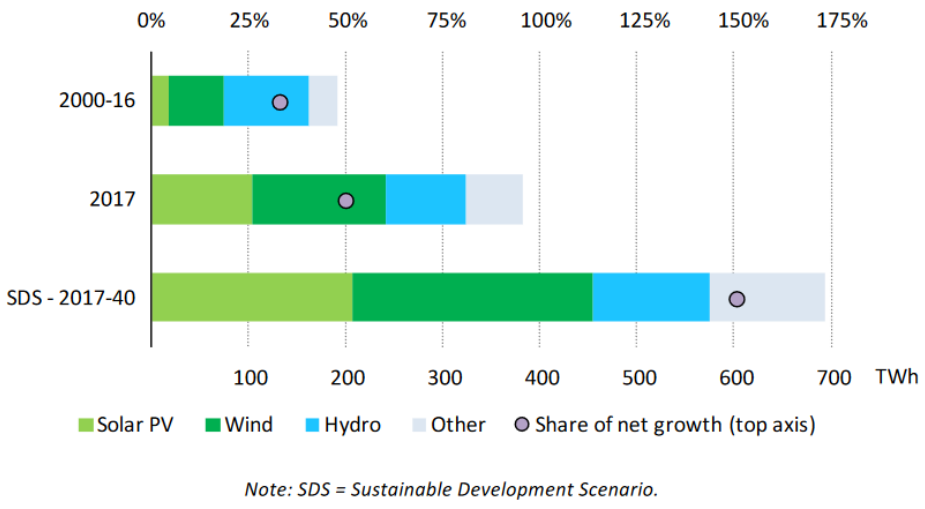
OIL - According to the 2017 Global Energy and CO_2 Status report, oil demand rose by 1.5million barrels per day (mb/d) and has been the trend since 2014. The main increase in oil demand came from the transport sector as vehicle ownerships increased in 2017. In the EU alone, oil demand saw its highest growth since 2001 peaking at 2% [1]. It is estimated that 60% of the increase in oil demand came from Asia where China although being a leading market for electric cars is also a big contributor to oil demand.

NATURAL GAS - The demand for natural gas also rose 3% in 2017 doubling its average growth of 1.5% over the past five years. China again led the sector, accounting for nearly 30% of this growth. The increase in demand for natural gas is influenced by its abundance and relatively low-cost supplies and its role in reducing emissions. It is predicted that gas demand will grow faster than oil and coal over the next five years at a relatively stable rate of 1.6% per year [3]. In Europe, after four years of decline in gas demand (2010 – 2014), demand picked up in 2015 and 2016. In France, nuclear outages, low gas prices and increasing coal prices have helped push up the demand for natural gas [3].

COAL - The global demand for coal grew by 1% following a 2.3% and 2.1% decline in the years 2015 and 2016 respectively. This increase in demand in 2017 was mainly due to an increase in coal-fired power plants which drove demand up by 3.5% compared to 2016 [1]. Again, China led this sector followed by the USA. It is reported that due to the sluggish coal demand relative to other fuels, a decline from 27% to 26% of coal's share in the global energy mix is expected by 2022 [4].

1.1.2 RENEWABLES

Interestingly, the demand for renewable energy saw the largest growth in 2017 as seen in figure 1.2 below. By the end of 2017, renewable energy based generation increased by 167 GW representing an 8.3% growth which averages out for the past seven years [5]. This data points to a rapid growth in the adoption of renewable energy and a transition to cleaner and sustainable energy sources. Renewables alone now account for 25% of global electricity generation [1]. The USA and China accounted for half of the increase in generation followed by the EU (8%), Japan and India at 6%. The IEA reported that wind power experienced the highest growth with 36% followed by solar PV at 27% [1]. An underlying factor behind this surge are substantial reductions in cost with the levelized cost of electricity (LCOE) from solar PV decreasing by 73%. The LCOE is defined as the average minimum price at which electricity must be sold in order to break-even over the lifetime of a power-generating asset. Both wind and solar PV technologies have now reached the cost range of power derived from traditional fossil fuel plants. Other sources of renewable energy also experienced some growth with hydropower at 22% and biofuels at 12% in 2017.



Note: SDS = Sustainable Development Scenario.

Figure 1.2 Average annual global growth in renewables-based generation by technology [1]

The statistics above do not include nuclear energy sources which are surrounded by doubts as to their status as a renewable energy source.

NUCLEAR ENERGY – The placement of nuclear energy under the list of renewable energy sources has been a topic of major debate. Arguments have been made for and against the inclusion of this source of energy under the renewables. Renewable energy sources are

considered as those sources that can regenerate or replenish itself indefinitely. Nuclear energy on the other hand generates energy from the fission of atoms (mainly Uranium) but cannot replenish itself indefinitely as mentioned. However, proponents of nuclear energy cite the low carbon emission aspect of nuclear energy as its major characteristic to be regarded as a renewable energy source. The most solid argument in favor of nuclear energy was given by Bernard Cohen, a former professor at the University of Pittsburg. Cohen defined the term 'indefinite' in numbers by referring to the relationship between the earth and the sun. He pointed that if current Uranium deposits can be proven to last as long as the sun (5 billion years), then nuclear energy should be considered renewable [6]. It is estimated that current reserves of Uranium can only last 1000 years if used in breeder reactors (a nuclear reactor able to generate more fissile material than it consumes) [6]. Cohen believes that the amount of Uranium far surpasses this estimate if Uranium from seawater and from eroded earth crust by rivers is considered. These Uranium sources are much more expensive to extract but Cohen argued that when extracted and used in breeder reactors, the cost/kWh is reduced by a factor of 100 as compared to light-water reactors. He concludes that all of the world's energy requirements for the next 5 billion years can be met using breeder reactors and Uranium fuel from the oceans without the cost of electricity rising more than 1% due to fuel costs [6]. The major arguments against nuclear energy's classification as renewable is the finite supply of fissile material and the amount of harmful radioactive waste spewed out during nuclear fission. Regardless of the classification of this source of energy, nuclear energy now provides about 11% of the world's electricity from 450 power reactors and is the world's second largest source of low-carbon power [7]. New investments in nuclear power will lead to a growth of 46% by 2040. While this is a significant increase, the total share of nuclear power in the global energy mix will experience a decline of 10% within the same period [8]. France relies heavily on nuclear power with around 75% of its electricity being generated from nuclear sources as at 2016 [7]. Sixteen other countries depend on nuclear power for at least one-quarter of their electricity. Figure 1.3 summarizes nuclear power production by country with data from 2016.

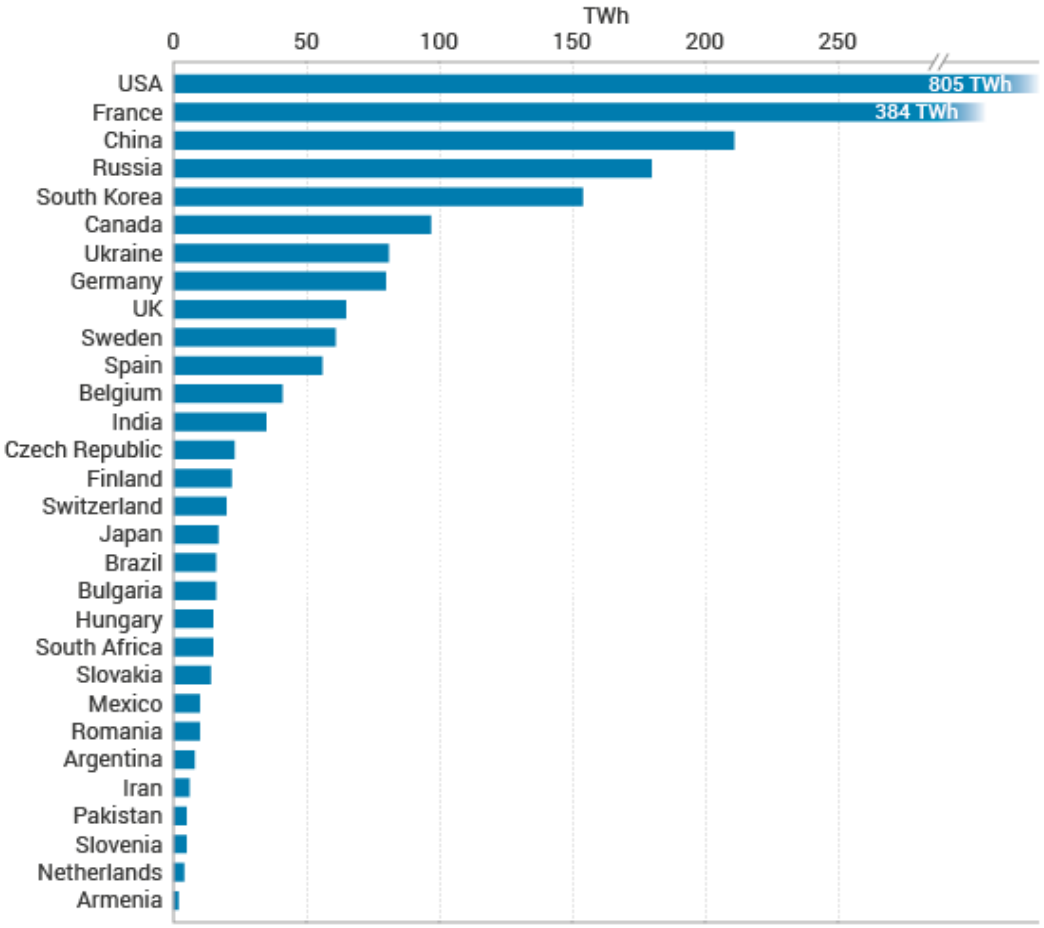


Figure 1.3. Nuclear Generation by Country for the year 2016 [7]

1.1.3 CARBON EMISSIONS

To effectively curb carbon emissions and tackle the threat of climate change, global warming has to be kept at 2°C above pre-industrial levels [9]. To achieve this, the world at large needs to develop advanced and competitive green energy technology with a long term target of reducing global warming to 1.5°C above pre-industrial levels. The strategy is to achieve short and mid-term targets of a 20% share of renewables in its energy system mix by 2020, and 27% by 2030 respectively [10]. Recent data from the European Environment Agency demonstrate that fossil fuel use has been reduced by an estimated 114 Mtoe (megaton oil-equivalent), comparable to the fossil fuel consumption of France. This was achieved by the increasing share of renewables in the energy consumption. In absolute terms, Germany, Italy and Spain achieved the largest reduction in domestic fossil fuel use and avoided greenhouse gases emissions, as a result of national renewable energy deployment since 2005. These efforts are yielding fruit as around 380Mt of carbon dioxide

emissions have been avoided, which is equivalent to the yearly emissions of Poland [10]. It is also interesting to note that prior to the year 2000, the global Gross Domestic Product (GDP) was closely linked to its CO_2 emissions and both grew at the same pace. However, from 2000 onwards, there has been a decoupling of the global GDP and carbon related emissions pointing to the development of more efficient and innovative energy solutions which is made up of a steadily increasing share of renewables (see figure 1.4).

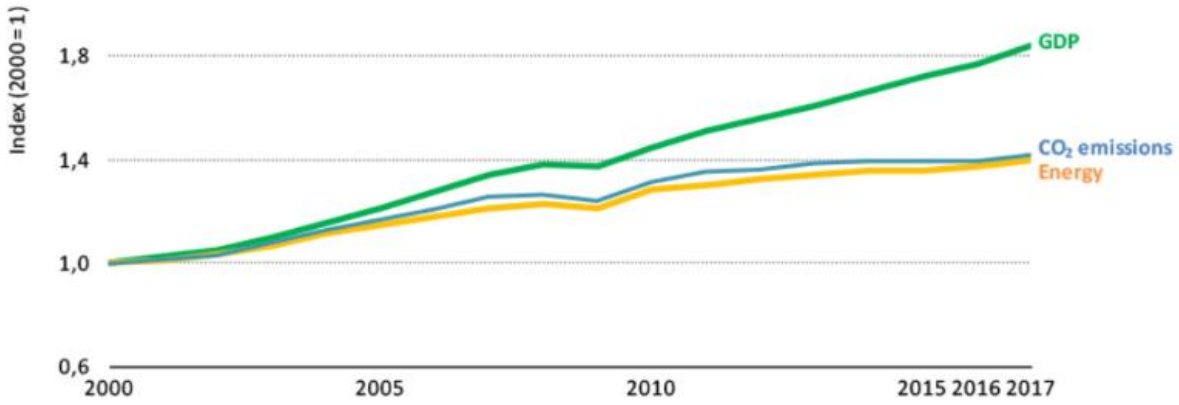


Figure 1.4. Global GDP, energy demand and energy-related carbon dioxide emissions, 2000-2017 [1]

Moving forward, it is projected that by 2030, 50% of all electricity produced and consumed in Europe will be powered by renewables, and in about 35 years it will be carbon-free. The COP21 agreement also known as the Paris agreement came into effect in 2015. According to this agreement, all parties are required to put forward their best efforts through "Nationally Determined Contributions" (NDCs). The NDC stipulates that all parties report regularly on their emissions and on their implementation strategies and efforts. Since the signing of the Paris agreement, more and more countries have given their formal consent to the agreement reaching a total of 179 parties in 2018 out of 197 parties to the convention [11].

1.2 THE PV MARKET

Till date, there has been continued growth in the PV industry with 2017 recording the most impressive developments. Rapidly falling costs of finished PV modules and improved supply chains has seen the average price of utility scale solar PV become cheaper than coal according to a report by Lazard [12]. Table 1.1 compares the LCOE of various energy sources with data extracted from the Lazard LCOE analysis done in 2017.

	Technology	Cost ($/MWh)
Renewable Energy	Solar PV –Rooftop Residential	187 – 319
	Solar PV – Utility Scale	43 – 53
	Fuel Cell	106 – 167
	Biomass	55 – 114
	Wind	30 – 60
	Geothermal	77 – 117
Conventional Energy	Nuclear	112 – 183
	Coal	60 – 143
	Gas	42 - 78

Table 1.1 Unsubsidized Levelized Cost of Energy Comparison between different technologies [12]

1.2.1 GLOBAL PV INDUSTRY AT A GLANCE

In fact, it is believed that solar energy is right on course to becoming the world's cheapest energy source by 2027 [13]. Figure 1.5 illustrates the expansion and proliferation of solar PV plants around the world. This is just one of the numerous ambitious PV projects in an effort to curb carbon related emissions and transit to renewables.



Figure 1.5. 30MW solar project using Jinko solar modules. *Source: Jinko Solar*

As of 2017, Asia continued to dominate the global solar capacity expansion with an estimated 72GW increase in production capacity. Other countries that installed more than 1GW of solar in 2017 include: USA (8.2 GW), Turkey (2.6 GW); Germany (1.7 GW); Australia (1.2 GW); South Korea (1.1 GW); and Brazil (1 GW) [5]. The installed solar

photovoltaic power capacity represents over half of all renewable energy installations in 2016. For the past 15 years, the solar PV industry has evolved into the fastest growing energy industry in the world with a compound annual growth rate (CAGR) of over 40% [5]. In prior years, PV module production was mainly dominated by Japan and Europe but with the expansion and exponential growth of the Chinese and Taiwanese PV markets, a new trend emerged in 2014 to include other countries like India, Vietnam and Malaysia contributing to the continued expansion of the production of solar PV modules both for large scale plants and distributed solar power [14]. Figure 1.6 shows the estimated module production from 2005- 2017. This is an estimated projection some companies report shipment data while others report sales data.

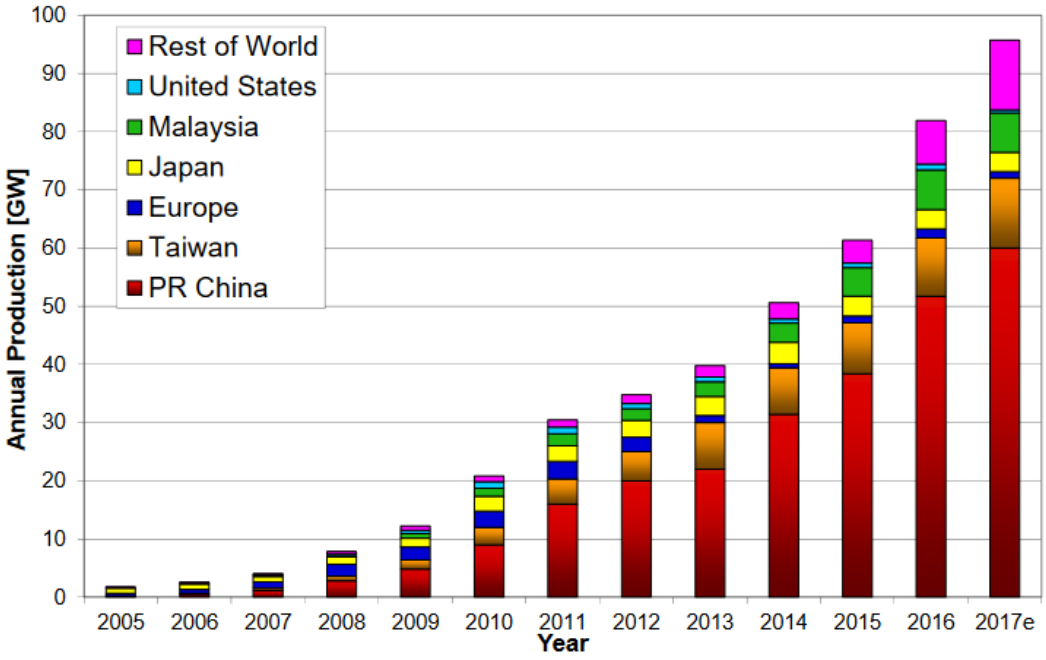


Figure 1.6. Estimated World PV cell/module production from 2005 to 2017 [14]

However, market development for solar PV systems did not follow the production at the same pace, which led to overcapacities and massive price pressure along the production value chain. This development triggered a consolidation of the manufacturing industry, which is still ongoing. The EU accounts for about 25% of the world's total installed solar capacity which provides about 4% of its electricity demand. PV module prices have seen a sharp decrease in the years 2005 – 2014, falling by more than 80%. 2015 experienced a small rise caused by increasing markets and industry consolidation, however, the downtrend in module prices resumed again in 2016 putting enormous strain on solar

module manufacturing companies existing in the value chain. Figures 1.7 represents the cumulative PV system installation statistics from 2010 – 2017 as presented by the IEA.

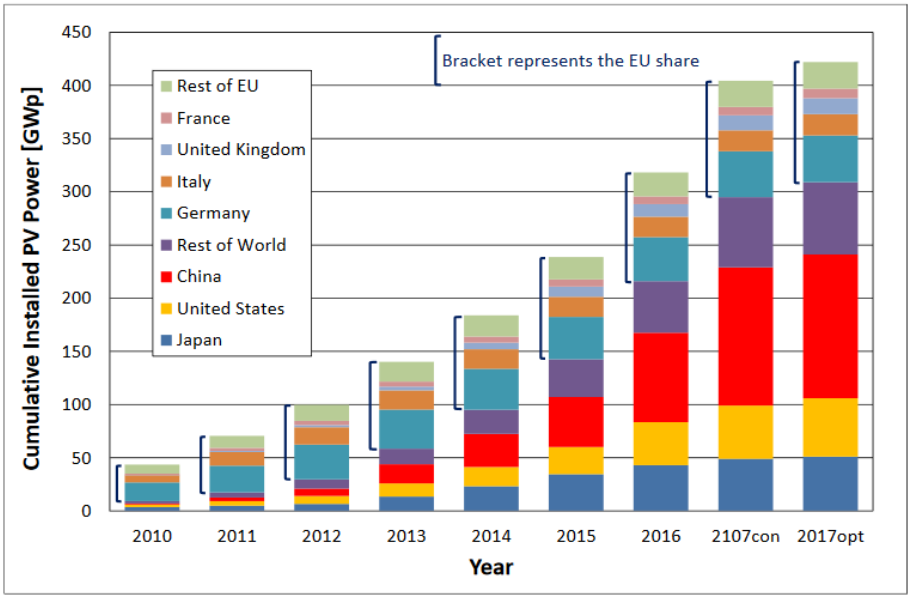


Figure 1.7 Cumulative PV installations from 2010 to 2017 [14]

1.2.2 THE FRENCH PV MARKET

The total cumulative installed capacity in France grew to over 7.1GW in 2016 which includes about 400MW in the French overseas territories. The electricity generation from PV systems reached a total of 8.3 TWh representing 1.6% of the national electricity generation during the same period. The goal of the French government is to attain 18.2 GW of installed solar PV capacity by 2023. In terms of residential scale PV installations in France, ADEME and IEA published a concise report detailing the cost of installation of these PV capacities. The system price breakdown data was collected from “Etude des retombées de la filière solaire française” study (I Care & Consult, for Enerplan / ADEME). The data here presented in table 1.2 may not be representative for small residential systems as these were not included in the survey.

Cost category	9 kW BIPV (IAB) (EUR/W)	9 kW roof-top lowest residential prices (EUR/W)	3 kW BIPV (IAB) highest residential prices (EUR/W)
Hardware			
Module	0,59	0,59	0,62
Inverter	0,16	0,16	0,18
Other (racking, wiring...)	0,54: 0,25(electricity) + 0,29(structure)	0,37: 0,25(electricity) + 0,12(structure)	0,68: 0,35(electricity) + 0,33(structure)
Soft costs			
Installation	0,65: 0,17(electricity) + 0,45(structure) + 0,03(un-tiling)	0,39: 0,17(electricity) + 0,21(structure) + 0,01(un-tiling)	0,94: 0,2(electricity) + 0,71(structure) + 0,03(un-tiling)
Customer Acquisition	0,15	0,15	0,4
Profit	(not surveyed)	(not surveyed)	(not surveyed)
Other (permitting, contracting, financing...)	0,18(grid connection) 0,14(other roof works)	0,18(grid connection) 0,00(other roof works)	0,41(grid connection) 0,16(other roof works)
Subtotal Hardware	1,29	1,12	1,48
Subtotal Soft costs	0,8(without other costs)	0,54	1,34(without other costs)
Total Installed Cost	2,09(without other costs) 2,39(with other costs)	1,66(without other costs) 1,84(with other costs)	2,82(without other costs 3,39(with other costs)

Table 1.2 Cost breakdown for a residential PV system [15]

The data shows that the total cost of setting up a residential PV system could range from EUR 1.66 – 2.82/W (excluding other costs). It however does seem that it is cheaper to install the PV systems on existing rooftops than having a Building Integrated PV system (BIPV). The next section will discuss a specific solar PV technology which has received worldwide attention and still has further potential for cost reduction and scalability.

1.3 INTRODUCTION TO $Cu(In,Ga)(Se)_2$ (CIGS) SOLAR CELLS

Today, several Solar PV cells exist commercially. The most viable and most efficient single junction cells being the crystalline Silicon cells (c-Si) which comprises both mono-crystalline and polycrystalline cell types. In thin film based cells, Cadmium Telluride (CdTe), amorphous Silicon (a-Si) and $Cu(In,Ga)Se_2$ (CIGS) cells are the most common types. This section will briefly examine the development of CIGS solar cells. It is worthy of note that thin film technologies are gradually closing up the efficiency gap with c-Si technologies. CIGS solar cells can be classified as second-generation PV technologies while crystalline Silicon cell technologies are first-generation [16]. A fundamental difference

between first and second generation PV cells is that the semiconductor material used in second generation cells have a direct band gap as opposed to the indirect band gap of silicon (first generation), but these cells still rely on a p-n junction design. The focus of this thesis will be on the CIGS thin film solar cell types.

1.3.1 CU(IN,GA)SE2 SOLAR CELLS

CIGS absorbers are made up of Cu, In, Ga and Se and is usually expressed chemically as $Cu(In_x,Ga_{1-x})Se_2$. CIGS based thin film solar cells have a long history that traces back to the 1970's. In 1975, the Bell laboratory demonstrated a conversion efficiency of 12% for a $CuInSe_2/CdS$ solar cell [17]. Since then, progressive development and improvement of the different layers of the CIGS cells have led to high cell efficiencies exceeding 22% [18] [19] [20]. In its most basic form, a CIGS cell is made up of a layered stack comprising the bottom substrate usually sodalime glass (most common substrate), a Mo (Mo) back contact, the CIGS absorber, a CdS buffer layer, a transparent conducting oxide (TCO) and finally the top contact fingers. Figure 1.8 is schematic representation of a simple CIGS solar cell and the cross-section scanning electron microscope image of a simple CIGS solar cell.

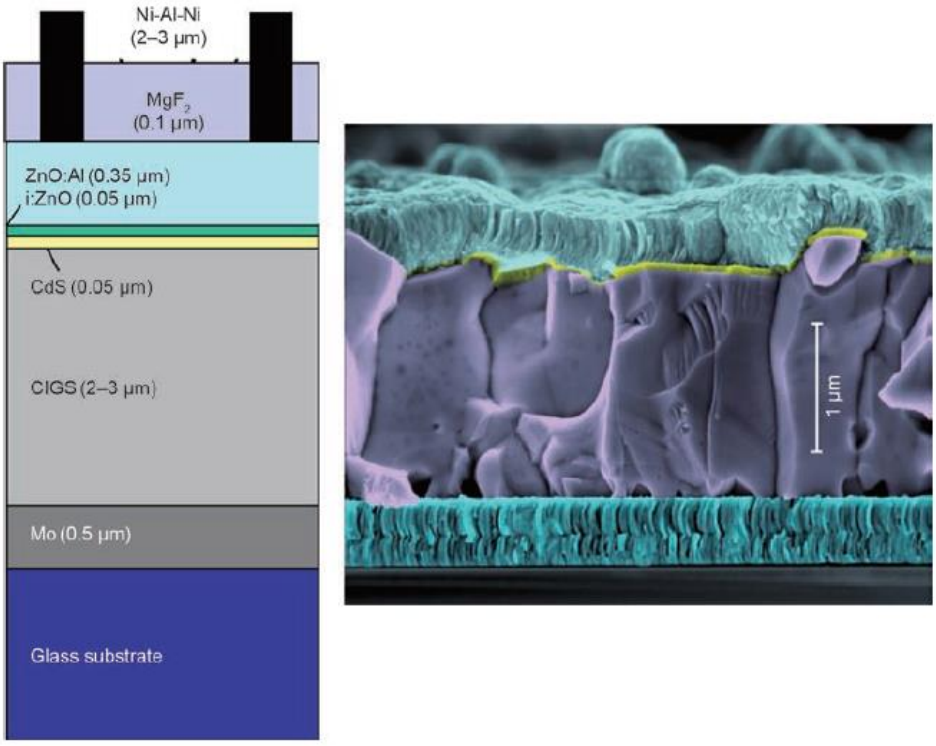


Figure 1.8 **left** - Schematic structure of the solar cell; **right** - cross-section scanning electron microscope (SEM) image of a standard CIGS solar cell.

As shown, the substrate used here is glass, however, there has been increased interest in the use of alternate substrates like thin foils of metals and polymers. One advantage of the use of these substrates is the lightweight and flexibility it introduces to the CIGS cells hence expanding its potential applications and reducing overall cost of fabrication. The function of each layer of the cell is as follows; the p-type $Cu(In,Ga)Se_2$ layer which act as the main light absorber, the n-type CdS layer which is in direct contact with the absorber layer and forms the p-n junction. At the top of the cell, a transparent electrode which is generally a ZnO/ZnO:Al bilayer, collects the electrons. At the rear part of the cell, the Mo electrode collects the holes. This is called substrate configuration, meaning that the light enters into the cell from the top. The substrate acts as a support giving some rigidity to the cell and holding all other layers in place. As the absorber layer is usually fabricated at elevated temperatures, the substrate is chosen based on its ability to withstand the deposition temperature of the absorber. In some cases where the substrate is unable to withstand such temperature, the fabrication process of the absorber and hence its deposition temperature is modified to suit the maximum tolerable temperature of the substrate.

1.3.2 CIGS ON FLEXIBLE METALLIC SUBSTRATES

Glass is arguably the most common and convenient substrate in the fabrication of CIGS solar cells. Reasons for this include but are not limited to its price, smooth surface, intrinsic alkali (Na) content, electrical insulation and its sufficient temperature stability required for CIGS depositions. A downside in the use of glass however, is its heavy weight and rigidity. Rigidity limits the number of practical applications of the CIGS cells. This constraint is overcome by the use of flexible substrates for fabricating CIGS solar cells. Table 1.3 compares the prices of a few of the well-known alternative substrates to glass.

Substrate	Price (per 100cm^2)
Sodalime Glass	$0.22
Stainless Steel Foil	$12
Aluminum Foil	$62
Polyimide Foil	$89
Titanium Foil	$138
Mo Foil	$220

Table 1.3 Price comparison of substrates used in CIGS cell fabrication

From an economical point of view, sodalime glass remains the substrate of choice as it very cheap and abundant in supply. The high-end substrates are Mo and Ti costing more $100 for a 0.2 x 100 x 100mm foil. One advantage of using flexible substrates is the potential for roll-to-roll production on a commercial scale. The most common metals that have been used for the purpose of CIGS solar cell fabrication are Stainless Steel, Aluminum, and Titanium. This thesis focuses mainly on the Stainless Steel and Mo substrates. Various works have been published detailing the use of metallic substrates in the fabrication of CIGS solar cells. Table 1.4 is a selected overview of high efficiencies already achieved in different companies and research institutes using flexible metallic substrates for CIGS solar cell fabrication.

Substrate	Deposition method	Efficiency (%)	Remarks	Ref.
Companies				
Stainless Steel	Coevaporation	17.7	Global Solar Energy (Hanergy)	[21]
Stainless Steel	Sputtering and selenization	17.3	Miasolé	[22]
Stainless Steel	Sputtering and selenization	17.0	Midsummer	[23]
Stainless Steel	Sputtering and selenization	14.0	Nuvosun (Dow)	[19]
Stainless Steel	Electrodeposition and selenization	15.4	Solopower	[24]
Al foil	Non-vacuum printing	17.1	Nanosolar	[25]
Research Institutes				
Enamelled Steel	Coevaporation	18.7	ZSW	[26]
Titanium	In-line 3-stage coevaporation	17.9	Aoyama Gakuin University, Japan	[27]
Ti-coated Stainless Steel	Coevaporation	17.7	EMPA	[28]
Mo foil	Coevaporation	14.6	AIST	[25]
Stainless Steel	Coevaporation	17.4	NREL	[29]
Cu tape		<10	IST, Germany	[25]
Ti foil		12	ZSW	[25]

Table 1.4 State-of-the-art efficiencies published by different companies and research institutes

1.3.3 APPLICATIONS

Metallic substrates have shown promising results when applied as substrates for CIGS cells. CIGS cells made on these substrates can be applied on uneven surfaces, rolled up for storage and are very lightweight. Its uses are not restricted to terrestrial applications only, it is also interesting for space applications were weight concerns are paramount. CIGS modules on flexible metal substrates have an excellent radiation tolerance and a high power to module weight ratio. The possibility of roll-to-roll production and industrial scaling of production can also significantly reduce production time and cost hence making this a viable option for commercialization. Flexible CIGS cells find its application in off-grid remote areas where access to electricity is limited or completely impossible. Figures 1.9 illustrates a number of scenarios in which these types of modules can be used.

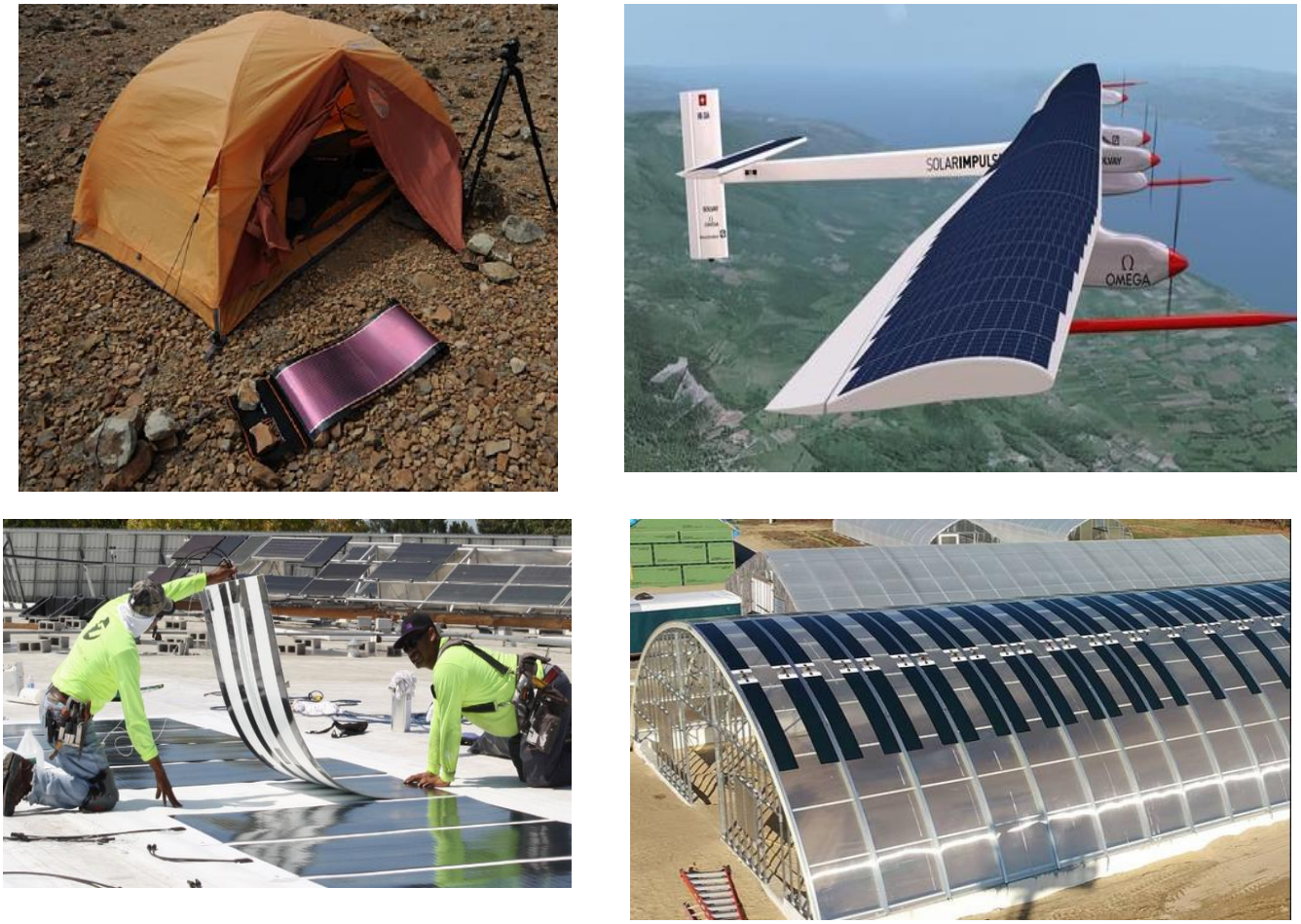


Figure 1.9 **- Top-left** - Outdoor remote use of flexible, foldable module; **top-right** - Solar Impulse 100% solar powered bi-plane; **bottom-left** – rooftop application of light, flexible CIGS modules ; **bottom-right** – Greenhouse with flexible modules on a curved roof.

1.3.4 ISSUES AND CHALLENGES

Despite these interesting new applications of flexible CIGS modules, the conversion efficiencies of the modules are considerably lower than compared to CIGS modules prepared on rigid glass substrates [30][31][32]. Efficiency limitations have been attributed to lack of Na in the metallic substrates, presence of detrimental metal impurities diffusing from the metal foil and substrate roughness amongst others. These factors will be examined.

- SUBSTRATE ROUGHNESS

Unlike glass substrates which are extremely smooth, metals have rougher surfaces due to their nature, fabrication and rolling process [33]. The roughness of these substrates can have a detrimental impact on the performances of the solar cells due to a number of reasons. However, it is unknown whether the effect occurs from differing film growth—i.e., kinetics—and hence morphology on rough substrates, or if the rough surface features provide points of high-harmful impurity diffusion into the CIGS or even device shunting [34]. Three mechanisms have been proposed in which the roughness of the substrate may impact CIGS device performance [34];

- ***Metallurgical Shunts***

Here, large surface features protruding through the back contact and/or the CIGS absorber layer can create a shunt path during cell operation.

- ***Impurities***

At high deposition temperatures, there is a higher possibility of diffusion of impurities from the metallic substrate into the CIGS absorber. On a rough substrate, this diffusion of impurities is further enhanced when there is an uneven coverage of the substrate by the back contact due to protruding substrate features. This increases the interface surface area between the substrate/back contact and the growing CIGS.

- ***Nucleation***

Surface irregularities can act as nucleation sites during the CIGS growth hence creating defects and smaller CIGS grains sizes. This is not an isolated phenomenon as the final CIGS morphology also depends on growth temperature and composition. Furthermore, the occurrence of isolated large features on the substrate surface will lead to huge dispersions in the cell parameters and hence a larger inhomogeneity in the cell parameters.

The term “roughness” does not denote a single well-defined quantity. When considering substrate roughness, it important to take into consideration the nature of the surface features (size, distribution) as well as the frequency of occurrence of these features on the substrate surface.

- IMPURITY DIFFUSION

An intrinsic property of some metallic substrates is the presence of detrimental impurities like Iron in the case of stainless steel substrates. Iron is known to be detrimental to the performance of CIGS cells [35] [36] [37]. The effect of impurity diffusion is even more pronounced at higher temperatures which favors diffusion. In stainless steel, the main alloying metal, Fe makes up around 80% of the stainless steel composition. Other constituents include Ni, Cr and Mn depending on the type of stainless steel desired. Unlike glass which is impurity free and ideal for CIGS deposition, these constituents of stainless steel can severely impact the performance of CIGS cells. The influence of Cr and Mn on CIGS devices has been previously found to be minor, whereas Fe and Ni are considered the most detrimental elements. On the other hand, the amount of Mn and Ni diffusing into the CIGS layer is usually too low in the case of stainless steel to affect the device properties [36].

The presence of Fe in the CIGS leads to the formation of deep levels in the band gap. Measures by Admittance spectroscopy identified electronic states around 300meV above the valence band. These deep levels act as recombination centers leading to a loss in the open circuit voltage (Voc) and hence the conversion efficiency of the cell [38].

It is however possible to limit the diffusion of metallic impurities into the CIGS absorber layer. The most common method to achieve this is to introduce a diffusion barrier layer which is usually deposited directly on the substrate before the back contact deposition forming a sandwich configuration; *Substrate/barrier layer/back contact*. Other methods of reducing impurity diffusion include increasing the thickness of the back contact layer and/or reducing the absorber growth temperature since the diffusion of the impurities is directly proportional to the temperature of the substrate [38].

When a barrier layer is incorporated, it can be chosen to be either conducting or non-conducting as required. Some common examples of impurity barrier layers that are most wide-spread include; Ti, Mo (and their nitrides), Cr, SiO_2 and Al_2O_3. It is worth noting

that Cr has been mentioned earlier as being an impurity that can deteriorate cell performance. However, Eisenbarth *et al* have reported on the effective barrier properties of Cr with no mention of any negative impact of the presence of Cr. In fact, by using a 100nm thick Cr barrier layer deposited directly on the stainless steel substrates, the amount of Fe in the CIGS absorber made at 525°C was reduced from 10^3 ppm to about 80 ppm [36]. The introduction of this 100nm thick Cr barrier layer to block Fe diffusion led to a gain in Voc from 436mv (cell with no barrier) to 612mV (with Cr barrier) and hence more than a 3-fold increase in conversion efficiency from 4.9% to 14.1%. Figure 1.10 shows the effective blocking properties of Cr as demonstrated by Eisenbarth *et al.* It can be seen that at a substrate temperature of 525°C, the barrier layer is able to sufficiently block the diffusion of Fe to a level lower than for the samples made at 475°C with no barrier layer.

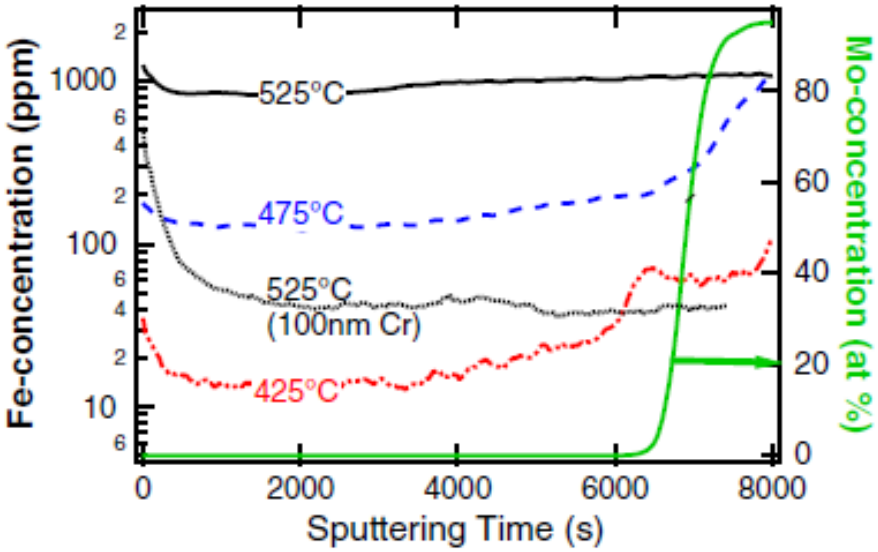


Figure 1.10 - Fe concentration in ppm by SIMS measurement. The Fe concentration is shown for 525, 475, and 425°C maximum growth temperature. The dotted curve represents an absorber evaporated at 525 °C with Cr-barrier layer [36].

Another study at EMPA by Blosch *et al.* reported on the effective use of the Mo back contact layer to block the diffusion of Fe impurities at a low substrate temperature of 475°C. By varying the sputtering conditions of the Mo back contact as well as its thickness, it was identified that the overall material density of the Mo back contact was the dominant parameter for the impurity diffusion barrier performance. A strong correlation between the Mo back contact density and its impurity blocking properties against Fe was observed using SIMS measurements. Furthermore, it was clearly observed that the CIGS solar cell efficiency showed a distinct dependence on the Fe concentration in the CIGS absorber

layer where an increasing Fe content led to lower fill factor, Jsc and Voc. A final cell efficiency or 15% was achieved using ~500nm thick Mo bilayer back contact [39].

Insulating barrier layers such as Al_2O_3 and SiO_2 have the added advantage of allowing a monolithic interconnection between cells. These oxides can be deposited either by sputtering, PE-CVD (*Plasma Enhanced Chemical Vapor Deposition*) or sol-gel method. On stainless steel, an absolute gain of about 5% have been reported using a 3 μm layer of Al_2O_3. SiO_2 deposited by sol-gel method paves way for the possibility of Na incorporation in the liquid phase [38] yielding an estimated 4% gain in efficiency as reported by Wuerz *et al.* [40]. Finally, the diffusion of impurities can also be limited by reducing the CIGS deposition temperature. However, this method will require significant optimization of the deposition parameters for the CIGS absorber in order to obtain large grain sizes which are characteristic of high performance CIGS cells.

It has been found that both grain boundary and bulk diffusion should be considered in the case of Fe atoms where as an example, the Fe atoms move via vacant sites in the growing film crystal. Hence this diffusion mechanism will result in a relatively flat Fe profile in the CIGS absorber layer [41]. Tablero *et al.* conducted some density functional calculations of chalcopyrite compounds and found that Fe can substitute on the cation sites in the CIGS absorber layer [42]. This discovery suggests that Fe might be incorporated in the CIGS absorber during its formation stage and hence follows the inter-diffusion paths of Cu, In, Ga and Se during the coevaporation process [39].

- THERMAL EXPANSION AND CIGS ADHESION

During CIGS deposition, it is important to have a good correlation between the coefficients of thermal expansion (CTE) of the CIGS absorber and the substrate. A mismatch of this physical property can lead to severe delamination of the CIGS layer from the substrate which is undesirable. In practice, CIGS absorbers are usually deposited at elevated temperatures (>450°C) and during the cool down phase of the process, there exists residual stress between the two materials (CIGS and substrate) due to their different CTEs. This stress is also proportional to the substrate temperature during the deposition. It can be expressed by the formula [38]:

$$\sigma = \frac{E_{CIGS}}{1-\upsilon_{CIGS}} (\alpha_{sub} - \alpha_{CIGS})\Delta T \qquad (1.1)$$

Where E_{CIGS} and υ_{CIGS} are the young's modulus and Poisson coefficient respectively, ΔT is the temperature difference between the deposition and ambient temperature, α_{CIGS} and α_{sub} are the CTE of CIGS and the substrate respectively. If σ is large enough, adhesion problems between the CIGS and the substrate will occur leading to delamination. Table 1.4 summarizes the CTE of two different metallic substrates, sodalime glass and polymer substrates.

Material	**CTE (10^{-6} K^{-1})**
CIGS	8.6 – 11.2
Stainless Steel	10 – 11
Mo	4.8 – 5.9
Sodalime Glass	9

Table 1.4 – Coefficient of Thermal Expansion of selected substrates used in CIGS fabrication

The CTE of sodalime glass and stainless steel both match that of CIGS hence, no delamination is expected to occur during the CIGS deposition at high temperature and subsequent cooling of the sample. On the other hand however, there is a mismatch between the CTE of CIGS and that of Mo substrate. This mismatch leads to greater stress at the interface between the growing CIGS absorber and the Mo substrate. An expected result of this is a delamination or occurrence of cracks in the CIGS.

One way of reducing adhesion problems between the CIGS and substrate is to apply an adhesion layer directly on top of the substrate before the CIGS deposition. Blosch *et al*. on the comparative study of different back contact designs for CIGS cells made on stainless steel reported a best efficiency of 17.3% using a 60nm Ti adhesion layer deposited directly on the stainless steel substrates along with a low temperature process and no additional barrier layer [43]. Another way to reduce adhesion issues is to tweak the sputtering deposition conditions of the Mo back contact by first depositing a less conductive but adhesive layer followed by a more conductive layer of Mo [38].

- SODIUM INCORPORATION

The benefit of Na impurities in CIGS cells was first reported on by Hedström *et al.* in 1993 [44]. Following this discovery, several groups have investigated the effects of Na incorporation in CIGS solar cells. The effects of Na on CIGS cells is mainly to improve the

conversion efficiencies by improving the open circuit voltage and fill factor. The short circuit current however is relatively unaffected by the presence of Na [45]. In traditional CIGS cells fabricated on sodalime glass, Na, naturally present in the sodalime glass, diffuses through the Mo back contact and into the growing CIGS absorber during the deposition step. In the case of metallic substrates however, Na is absent and hence needs to be incorporated by other means in order to realize high performance solar cells. Several methods exist for the incorporation of Na and includes but not limited to; Na post-deposition treatment (PDT), Na co-evaporation during the CIGS deposition step, Na incorporation through a Na doped back contact layer and via a Na precursor layer applied to the back contact prior to absorber deposition. Figure 1.11 is a graphic illustration of the various methods of incorporating Na in CIGS absorber layers as enumerated above.

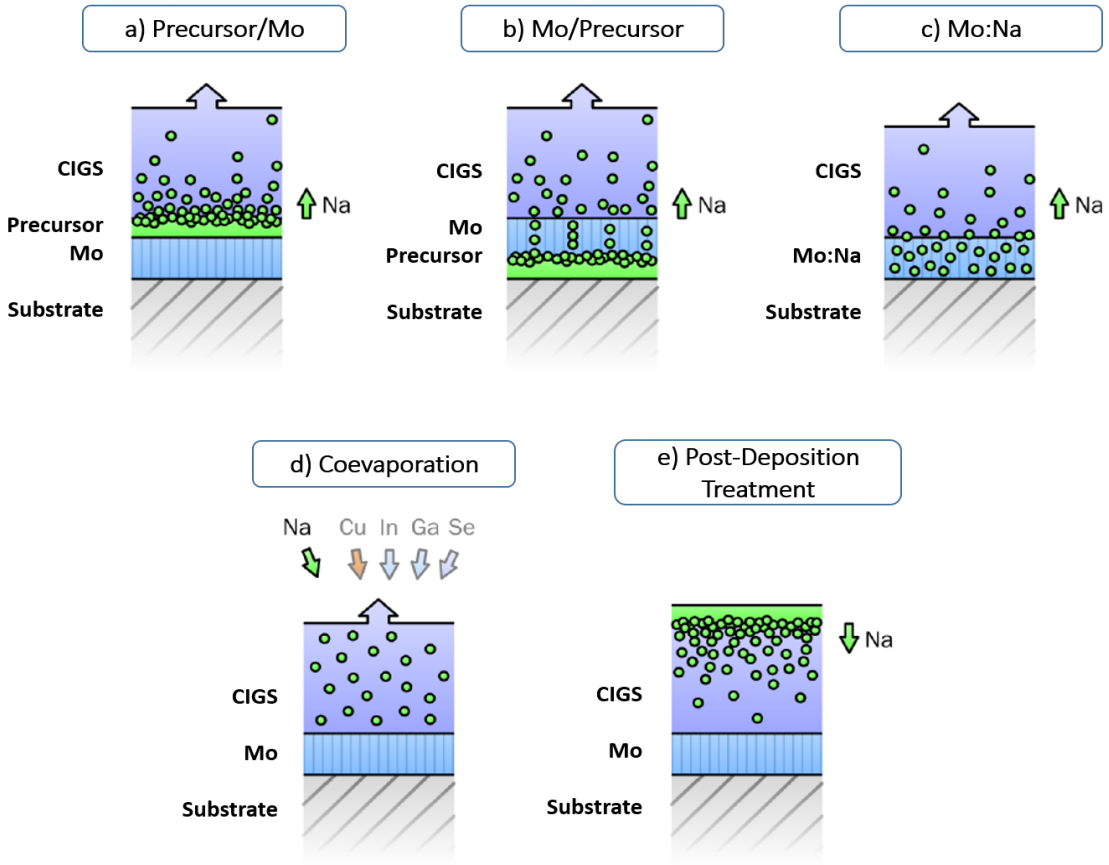


Figure 1.11 - Methods of Na incorporation in CIGS absorbers on metallic substrates. a) Diffusion during CIGS growth from a precursor layer deposited on the back contact. b) Diffusion during CIGS growth from a precursor layer deposited below the back contact. c) Diffusion from a Na doped back contact Mo:Na). d) Coevaporation CIGS constituent elements during deposition. e) Post-Deposition treatment from a Na source [38].

It should however be noted that there is a threshold for Na incorporation in the cells beyond which the presence of excess Na leads to a degradation of the solar cell performance [46] [47]. The details and mechanisms of Na incorporation will be discussed in chapter 2.

1.3.5 CELL TO MODULES

A module is simply an aggregation of cells which are interconnected to increase the power output (see figure 1.12). Although efficiencies of CIGS solar cells have exceeded 22% [20], it is very important to pay attention to module efficiency as it is an important parameter to be considered when scaling CIGS cells for commercial purposes. One reason for this is that a number of factors in the cost per watt are driven downward by increasing efficiency. These factors include material costs, throughput for a given capital investment and installation costs. A number of technological pathways exist that can help improve module efficiency. These include larger bandgap absorbers, non-absorbing heterojunctions that maintain Voc, improved TCOs and the use of optics [48].

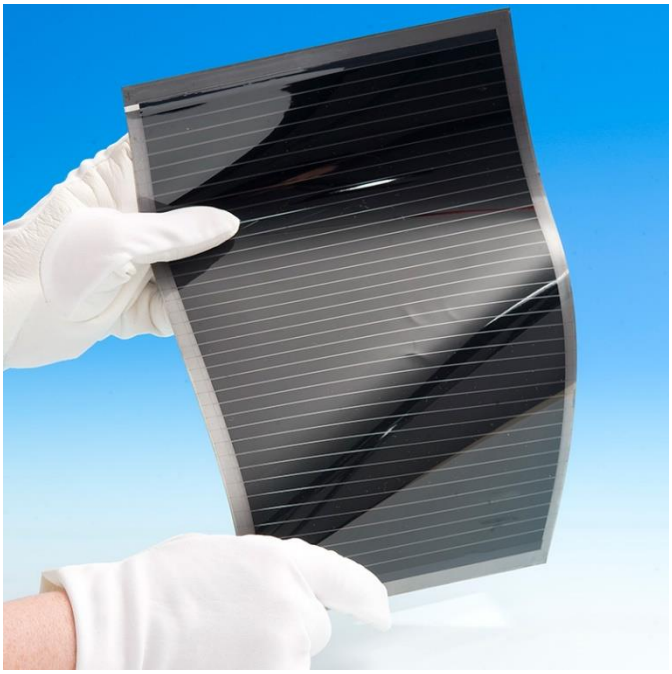


Figure 1.12 - A flexible CIGS solar module on Titanium foil. *Source – ZSW, Germany*

In order to produce meaningful amounts of electrical energy, larger areas are needed as the current depends on the cell area and illumination. Also, the cells must be connected electrically to generate higher voltages. The thin-film technology enables monolithic interconnection of the cells since patterning steps can be performed between coating steps so that the production line directly generates PV modules. The standard method of

monolithic integration involves three patterning steps: first, separation of the cells at the back contact by opening the Mo layer; second, an interconnection by opening the CIGS layer, so that an electrical contact between the front and back contacts is created during the subsequent processing steps; and third, a final patterning step for the front side cell separation [18]. This process works well on rigid glass substrates and non-conducting substrates. However, monolithic integration on metallic substrates is more challenging due to the fact that the substrates are conductive. To resolve this problem, an additional insulating layer needs to be deposited between the metallic substrate and the Mo back contact [25]. Another method of cell interconnection that has been used by SoloPower is based on a process applied to Si-wafer technology which involves connecting the cells by wiring. This method of cell interconnection was applied on stainless steel substrates and is called the stringing and tabbing method [49]. Shingling is a third method of cell interconnection suitable for application on metallic substrates. In this method, the cells are assembled in strings by connecting the front of the leading edge of each cell to the back of the tail edge of next one [25]. This method has been employed by Miasolé for cells fabricated on stainless steel substrates. Figure 1.13 is a graphical illustration of the methods described above.



Figure 1.13 – Illustration showing different methods of cell integration in a module [38]. **Left** – Monolithic integration. **Center** – Stringing and Tabbing method. **Right** - Shingling method.

Stringing and tabbing method as well as the shingling method of cell interconnection during module fabrication allows the cells to be grouped according to their respective efficiencies before being connected to make up the module. This improves the overall yield of the production unit [25]. The module voltage of the module is hence determined by the sum of the voltages of the total number of cells in series connection [18] (see figure 1.14).

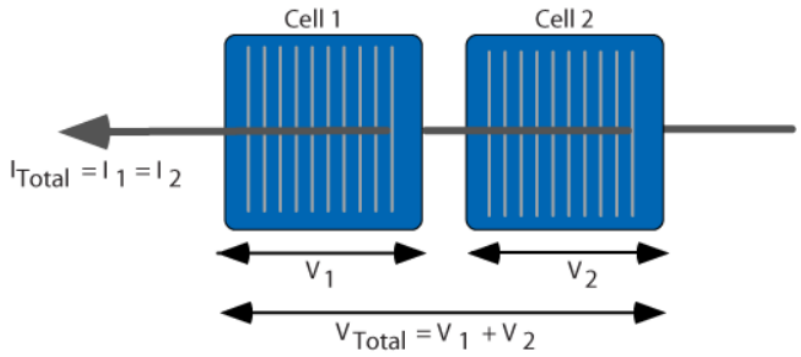


Figure 1.14 – Series interconnection of photovoltaic cell. The total output voltage is the sum of cells connected in series. *(source – PVEducation.org)*

In large devices (modules) however, power losses are inevitable due to lateral current collection. These can be minimized by adjusting grid spacing, cell dimensions and the TCO conductivity and absorption [48].

CONCLUSION

In this chapter, the global production and consumption of energy (fossil and renewable sources) have been put in perspective. It has been shown that the growth of renewables is steadily in an uptrend and should maintain this trend in order to meet the targets set for the reduction of carbon emissions and limit global warming to 1.5°C. Among the renewable energy resources, solar and wind technology are leading the trail in worldwide adoption. CIGS thin film solar cells have experienced substantial development exceeding 22% efficiency which is gradually closing the gap with single crystal Si solar cells. Extensive research into flexible substrates is ongoing especially on polyimide and metal substrates. The benefits of flexible metal substrates have been discussed as well as the challenges in fabricating high efficiency solar cells on metal substrates. The major issues are: substrate roughness, presence of detrimental impurities and Na incorporation. The next chapter will review the physics and operation of CIGS solar cells, take in-depth look at the architecture of CIGS cells and finally elaborate the specifics of CIGS fabrication on metals and alkali incorporation.

REFERENCES

[1] International Energy Agency, “Global Energy & CO2 Status Report,” 2017.

[2] F. Birol, “World Energy Prospects and Challenges,” 2005.

[3] International Energy Agency, “Gas Market Report,” 2017.

[4] International Energy Agency, “Coal 2017,” *International Energy Agency*. [Online]. Available: https://www.iea.org/coal2017/. [Accessed: 08-Aug-2018].

[5] IRENA, “Global Renewable Generation Continues its Strong Growth, New IRENA Capacity Data Shows,” 04-May-2018. [Online]. Available: http://www.irena.org/newsroom/pressreleases/2018/Apr/Global-Renewable-Generation-Continues-its-Strong-Growth-New-IRENA-Capacity-Data-Shows. [Accessed: 08-Jun-2018].

[6] B. L. Cohen, “Breeder reactors: A renewable energy source,” *Am J Phys*, vol. 51, no. 1, p. 78, 1983.

[7] World Nuclear Association, “Nuclear Power in the World Today,” Apr-2018. [Online]. Available: http://www.world-nuclear.org/information-library/current-and-future-generation/nuclear-power-in-the-world-today.aspx. [Accessed: 17-Sep-2018].

[8] International Energy Agency, “Nuclear Power,” 17-Sep-2018. [Online]. Available: https://www.iea.org/topics/nuclear/. [Accessed: 17-Sep-2018].

[9] United Nations Climate Change, “The Paris Agreement,” *United Nations Climate Change*. [Online]. Available: https://unfccc.int/process-and-meetings/the-paris-agreement/the-paris-agreement. [Accessed: 13-Aug-2018].

[10] United Nations Climate Change, “Renewable energy: Catalyst for a clean energy transition,” *Organisation for Economic Co-operation and Development (OECD*. [Online]. Available: http://www.oecd.org/environment/renewable-energy-catalyst-clean-energy-transition.htm. [Accessed: 13-Aug-2018].

[11] United Nations Climate Change, “Paris Agreement - Status of Ratification,” *United Nations Climate Change*. [Online]. Available: https://unfccc.int/process/the-paris-agreement/status-of-ratification. [Accessed: 13-Aug-2018].

[12] Lazard, “Lazard’s Levelized Cost of Energy Analysis - Version 11.0.” Nov-2017.

[13] B. Beetz and I. Clover, “2017: The PV year in review,” 05-Dec-2017.

[14] A. JAEGER-WALDAU and EU Commison Joint Research Centre, *PV status report 2017 study.* 2017.

[15] ADEME and IEA, “National Survey Report of PV Power Applications in FRANCE,” 2016.

[16] K. Ranabhat, L. Patrikeev, A. Antal’evna-Revina, K. Andrianov, V. Lapshinsky, and E. Sofronova, “An introduction to solar cell technology,” *Istraz. Proj. Za Privredu*, vol. 14, no. 4, pp. 481–491, 2016.

[17] J. L. Shay, S. Wagner, and H. M. Kasper, "Efficient CuInSe2/CdS solar cells," *Appl. Phys. Lett.*, vol. 27, no. 2, pp. 89–90, Jul. 1975.

[18] M. Powalla *et al.*, "Advances in Cost-Efficient Thin-Film Photovoltaics Based on Cu(In,Ga)Se 2," *Engineering*, vol. 3, no. 4, pp. 445–451, Aug. 2017.

[19] T. Feurer *et al.*, "Progress in thin film CIGS photovoltaics - Research and development, manufacturing, and applications: Progress in thin film CIGS photovoltaics," *Prog. Photovolt. Res. Appl.*, 2016.

[20] Solar Frontier, "Solar Frontier Achieves World Record Thin-Film Solar Cell Efficiency of 22.9%." [Online]. Available: http://www.solar-frontier.com/eng/news/2017/1220_press.html. [Accessed: 18-Sep-2018].

[21] S. Wiedeman *et al.*, "Manufacturing ramp-up of flexible CIGS PV," in *2010 35th IEEE Photovoltaic Specialists Conference*, Honolulu, HI, USA, 2010, pp. 003485–003490.

[22] Miasolé, "Miasolé." [Online]. Available: http://miasole.com/miasole_news/.

[23] Midsummer, "Technology." [Online]. Available: http://midsummer.se/technology.

[24] S. Aksu, S. Pethe, A. Kleiman-Shwarsctein, S. Kundu, and M. Pinarbasi, "Recent advances in electroplating based CIGS solar cell fabrication," in *2012 38th IEEE Photovoltaic Specialists Conference*, Austin, TX, USA, 2012, pp. 003092–003097.

[25] P. Reinhard *et al.*, "Review of Progress Toward 20% Efficiency Flexible CIGS Solar Cells and Manufacturing Issues of Solar Modules," *IEEE J. Photovolt.*, vol. 3, no. 1, pp. 572–580, Jan. 2013.

[26] M. Powalla *et al.*, "CIGS Cells and Modules With High Efficiency on Glass and Flexible Substrates," *IEEE J. Photovolt.*, vol. 4, no. 1, pp. 440–446, Jan. 2014.

[27] Nakada, T, Yagioka, T, Kuraishi, T, and Mise, T, "CIGS thin film solar cells on flexible foils," presented at the 24th EPVSEC, 2009, p. 2425–2428.

[28] F. Pianezzi *et al.*, "Electronic properties of Cu(In,Ga)Se $_2$ solar cells on stainless steel foils without diffusion barrier: Electronic properties of CIGS solar cells," *Prog. Photovolt. Res. Appl.*, vol. 20, no. 3, pp. 253–259, May 2012.

[29] Miguel A. Contreras *et al.*, "Progress Toward 20% Efficiency in Cu(In,Ga)Se2 Polycrystalline Thin-film Solar Cells," *Prog. Photovolt. Res. Appl.*, vol. 7, pp. 311–316, 1999.

[30] W. Thongkham, A. Pankiew, K. Yoodee, and S. Chatraphorn, "Enhancing efficiency of Cu(In,Ga)Se2 solar cells on flexible stainless steel foils using NaF co-evaporation," *Sol. Energy*, vol. 92, pp. 189–195, Jun. 2013.

[31] M. Lee *et al.*, "Highly efficient flexible CuIn0.7Ga0.3Se2 solar cells with a thick Na/Mo layer deposited directly on stainless steel," *Appl. Surf. Sci.*, vol. 346, pp. 562–566, Aug. 2015.

[32] A. Chirilă *et al.*, "Potassium-induced surface modification of Cu(In,Ga)Se2 thin films for high-efficiency solar cells," *Nat. Mater.*, vol. 12, no. 12, pp. 1107–1111, Nov. 2013.

[33] K. Herz, A. Eicke, F. Kessler, R. Wächter, and M. Powalla, "Diffusion barriers for CIGS solar cells on metallic substrates," *Thin Solid Films*, vol. 431–432, pp. 392–397, May 2003.

[34] W. K. Batchelor, I. L. Repins, J. Schaefer, and M. E. Beck, "Impact of substrate roughness on CuInxGa1−xSe2 device properties," *Sol. Energy Mater. Sol. Cells*, vol. 83, no. 1, pp. 67–80, Jun. 2004.

[35] K.-B. Kim, "Effect of Metal Barrier Layer for Flexible Solar Cell Devices on Stainless Steel Substrates," *Appl. Sci. Converg. Technol.*, vol. 26, no. 1, pp. 16–19, 2017.

[36] T. Eisenbarth, R. Caballero, C. A. Kaufmann, A. Eicke, and T. Unold, "Influence of iron on defect concentrations and device performance for Cu(In,Ga)Se2 solar cells on stainless steel substrates: Influence of iron on Cu(In,Ga)Se2 solar cells," *Prog. Photovolt. Res. Appl.*, vol. 20, no. 5, pp. 568–574, Aug. 2012.

[37] F. Pianezzi *et al.*, "Influence of Ni and Cr impurities on the electronic properties of Cu(In,Ga)Se $_2$ thin film solar cells: Influence of Ni and Cr impurities in CIGS," *Prog. Photovolt. Res. Appl.*, vol. 23, no. 7, pp. 892–900, Jul. 2015.

[38] C. Roger, "Developpement de cellules photovoltaïques à base de CIGS sur substrats métalliques.," PhD Thesis, Université de Grenoble, 2013.

[39] P. Blösch *et al.*, "Diffusion barrier properties of Mo back contacts for Cu(In,Ga)Se2 solar cells on stainless steel foils," *J. Appl. Phys.*, vol. 113, no. 5, p. 054506, 2013.

[40] R. Wuerz *et al.*, "CIGS thin-film solar cells on steel substrates," *Thin Solid Films*, vol. 517, no. 7, pp. 2415–2418, Feb. 2009.

[41] R. Schlesiger *et al.*, "Design of a laser-assisted tomographic atom probe at Münster University," *Rev. Sci. Instrum.*, vol. 81, no. 4, p. 043703, Apr. 2010.

[42] C. Tablero, "Ionization Levels of Doped Copper Indium Sulfide Chalcopyrites," *J. Phys. Chem. A*, vol. 116, no. 5, pp. 1390–1395, Feb. 2012.

[43] P. Blösch *et al.*, "Comparative Study of Different Back-Contact Designs for High-Efficiency CIGS Solar Cells on Stainless Steel Foils," *IEEE J. Photovolt.*, vol. 1, no. 2, pp. 194–199, Oct. 2011.

[44] J. Hedstrom *et al.*, "ZnO/CdS/Cu (In, Ga) Se/sub 2/thin film solar cells with improved performance," in *Photovoltaic Specialists Conference, 1993., Conference Record of the Twenty Third IEEE*, 1993, pp. 364–371.

[45] D. Rudmann, "Effects of sodium on growth and properties of Cu(In,Ga)Se_2 thin films and solar cells," ETH Zurich, Switzerland, 2004.

[46] Y. Sun *et al.*, "Review on Alkali Element Doping in Cu(In,Ga)Se 2 Thin Films and Solar Cells," *Engineering*, vol. 3, no. 4, pp. 452–459, Aug. 2017.

[47] V. Fjallstrom *et al.*, "Potential-Induced Degradation of CuIn$_{1-x} \hbox{Ga}_{x}$Se$_{2}$ Thin Film Solar Cells," *IEEE J. Photovolt.*, vol. 3, no. 3, pp. 1090–1094, Jul. 2013.

[48] I. Repins, S. Glynn, J. Duenow, T. J. Coutts, W. K. Metzger, and M. A. Contreras, “Required material properties for high-efficiency CIGS modules,” in *Thin Film Solar Technology*, 2009, vol. 7409, p. 74090M.

[49] M. Pinarbasi *et al.*, “Flexible cells and modules produced using roll-to-roll electroplating approach,” presented at the 35th IEEE Photovoltaic Specialists Conference, 2010, pp. 000169–000174.

CHAPTER 2

The use of alternative energy is inevitable as fossil fuels are finite.

- GAWDAT BAHGAT, *Alternative Energy in the Middle East, 2017.*

FUNDAMENTALS OF CIGS SOLAR CELLS

Photovoltaic (PV) modules are devices with the ability to convert incident sunlight to usable electrical energy. A recurring issue however, has been the price of such PV modules. While there has been a drastic decrease in the average cost of PV and an increasing module performance, the most efficient crystalline silicon cells are very likely to hit a lower price limit owing to the relatively expensive cost of processing. A potentially successful range of PV modules which can be scaled and mass produced at a cheaper cost are the thin film solar cells. This chapter examines the building blocks of CIGS thin film solar cells and discusses the several parts that make up a working CIGS cell albeit on metallic substrates.

2.1 PHYSICS OF CIGS SOLAR CELLS

In solar cells, incident photons from sunlight excite electrons from the valence band of the semiconductor into the conduction band. This creates an electron-hole pair which is separated by a p-n junction. The generated photoelectrons are transported through an external circuit and can be used to power an electrical load. In the case of CIGS solar cells, the CIGS absorber layer is where most of the photon absorption and generation occurs. An intrinsic property of CIGS is its high light absorption, where 90 % of incident light is absorbed in the first micrometer of the CIGS material [1].

The slightly Cu-deficient CIGS absorber layer is made up of $Cu(In_x,Ga_{1-x})Se_2$ where x can vary from 1 (pure Cu, In, Se) to 0 (pure Cu, Ga, Se). The structure of the CIGS compound is tetrahedral in nature having the chalcopyrite crystal structure as depicted in Fig. 2.1.

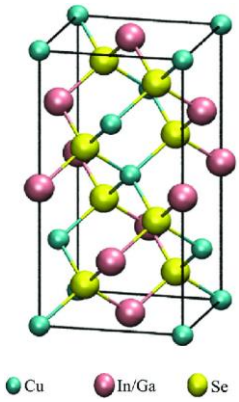


Figure 2.1 - Crystal structure of a tetrahedral chalcopyrite CIGS unit cell.

Each Se atom is bonded to two In/Ga atoms and two Cu atoms leading to a total of four bonds on the Se atom. In and Ga atoms occupy the same atomic sites and the bandgap of the CIGS material is tunable from 1.04 eV (pure CIS) to 1.68 eV (pure CGS). This introduces the concept of the GGI (Ga content) of the absorber layer which is expressed as [Ga] / ([Ga] + [In]). The bandgap can be derived as a function of the GGI using the expression;

$$E_g(GGI) = 1.01 + 0.626 \cdot GGI - 0.167 \cdot GGI\ (1 - GGI) \qquad 2.1$$

2.1.1 BAND STRUCTURE OF CIGS CELL

A typical CIGS cell is a heterojunctions device made up of a junction between semiconductors with different bandgaps. Figure 2.2 is an illustration of the band diagram of a CIGS solar cell under zero-bias voltage. The CIGS material which is a slightly Cu-deficient p-type semiconductor creates a junction with an n-type buffer layer deposited on top of it hence causing a bending of the valence and conduction bands. The CIGS layer is split into a majority carrier depleted space charge region (SCR) and a quasi-neutral region (QNR). The p-n junction establishes an electric field at the SCR. Electrons generated within the SCR or close to it are immediately swept across due to the electric field. When the electrons are generated in the QNR of the absorber, they need to diffuse towards the SCR and again are swept across the junction. However, due to recombination, not all generated photoelectrons arrive at the junction.

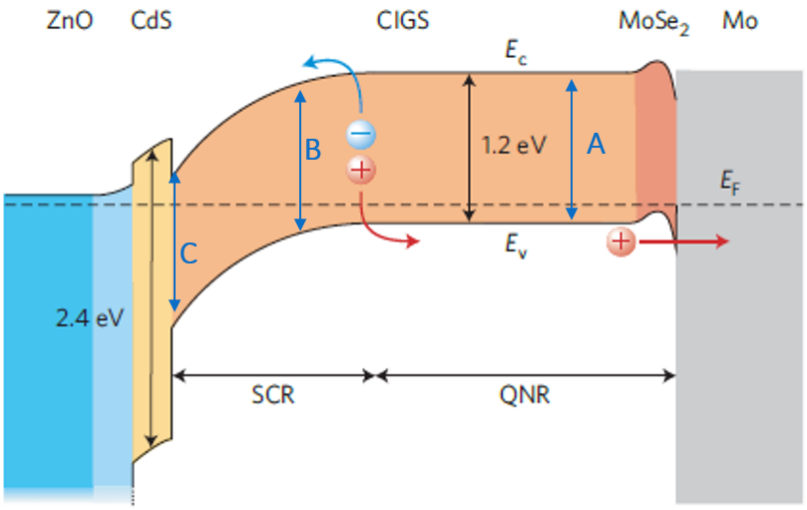


Figure 2.2 – Schematic band diagram of a CIGS solar cell under zero-bias voltage condition. The CIGS absorber layer optimally has an average bandgap energy of about 1.2 eV. The p–n junction is formed with an n-type CdS buffer layer that has a bandgap energy of around 2.4 eV. The front contact consists of a bilayer of intrinsic and aluminum-doped ZnO layers that have a wide bandgap over 3 eV. The back contact is Mo. Also shown are the conduction band energy E_C, valence band energy E_V, Fermi level E_F, space charge region (SCR), and quasi-neutral region (QNR) [2]

The n-type buffer layer is ideally selected to have a large bandgap such that most of the incident radiation is transmitted to the CIGS absorber layer. To improve the transport of generated carriers, an ohmic front and back contact layers are required. The preferred back contact used is Mo because, during the growth of the CIGS absorber, a thin interface layer of $MoSe_2$ is formed, resulting in a quasi-ohmic contact [2].

2.1.2 MODE OF OPERATION OF CIGS SOLAR CELLS

CIGS solar cells absorb photons from the solar spectrum in order to produce energy. The solar spectrum can be approximated by a blackbody radiation described by the Planck's Law at a temperature of 5800 K. There also exists a difference in spectra measured at the top of the atmosphere and the surface of the earth due to atmospheric scattering and absorption. The spectrum arriving on earth takes into account the absorption by various entities in the earth's atmosphere for an incident angle of 48°. This gives rise to the global AM1.5 incident spectral irradiance density shown in figure 2.3.

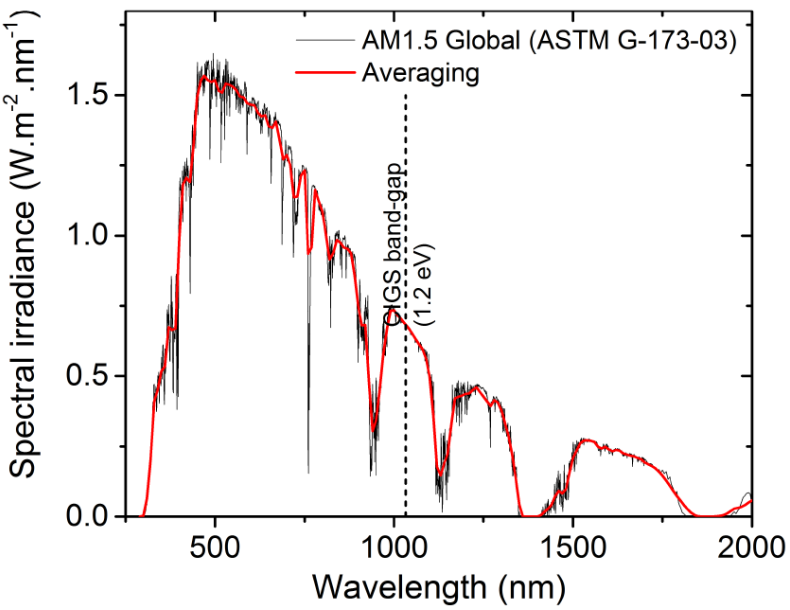


Figure 2.3 - AM1.5 solar spectrum. In red: averaging used for photocurrent calculations [3]

CURRENT-VOLTAGE PROPERTIES OF CIGS CELLS

When a CIGS cell is irradiated with photons, electron-hole pairs are created. Typically, the built-in voltage induced by the pn junction is responsible for separating and collecting the charges. The conversion efficiency of the cell is determined by the output power divided by the solar irradiation as expressed in equation 2.2. Figure 2.4 illustrates the diode curve of a typical working solar cell.

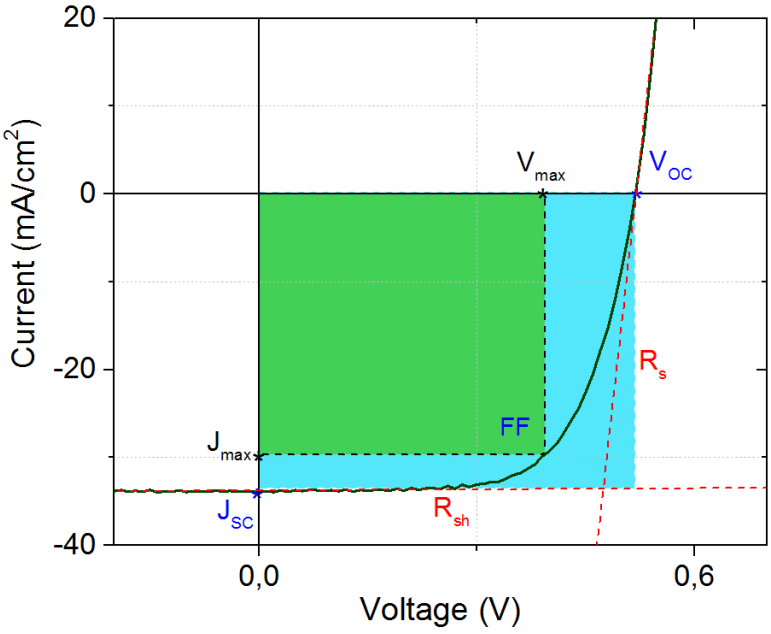


Figure 2.4 – Current-Voltage (I-V) curve of a CIGS solar cell fabricated in-house on a stainless steel substrate

The efficiency can be determined using three photovoltaic output parameters namely; the open circuit voltage (V_{oc}), the short circuit current (J_{sc}) and the fill factor (FF). The efficiency (η) can be defined as the ratio of the maximum power obtainable from the cell to the power of the incident radiation and is given by;

$$\eta = \frac{J_{max} \cdot V_{max}}{P_{irrad}} \qquad 2.2$$

If the FF is described by the ratio of the green to the blue highlighted areas in figure 2.4, it can be written as;

$$FF = \frac{J_{max} \cdot V_{max}}{J_{sc} \cdot V_{oc}} \qquad 2.3$$

Substituting for the value of FF in equation 2.2 gives the expression for the efficiency as;

$$\eta = \frac{J_{sc} \cdot V_{oc} \cdot FF}{P_{irrad}} \qquad 2.4$$

The V_{oc} is the voltage at the open circuit condition where the total current flowing through the circuit is zero (J = 0). The J_{sc} on the other hand is the current density at zero (V_{oc} = 0). In an ideal solar cell, the J_{sc} is equal to the photogenerated current J_L. The FF is the measure of the "squareness" of the J-V curve (equation 2.3).

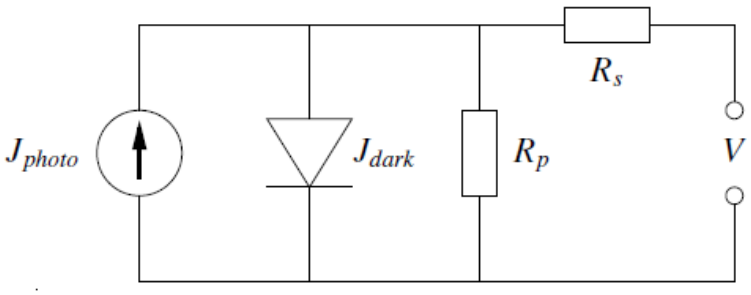


Figure 2.5 – Circuit equivalent of a solar cell with a single diode.

The equivalent circuit of a solar cell is shown in figure 2.5. R_s denotes the series resistance in the device while R_p is the parallel resistance or shunt in the cell. J_{photo} is the photocurrent. If the R_s *and* R_p are both assumed to be zero and infinity respectively, the diode will be ideal and the shape of the I-V curve will be almost rectangular in shape with FF ≈ 1. The J(V) characteristics of the cell is also defined as

$$J(V) = J_{dark} + J_{photo} = J_0 \cdot \left(exp^{\frac{qV}{BkT}} - 1\right) + J_{photo} \qquad 2.5$$

Where B is the diode ideality factor (B = 1 for an ideal diode) and J_0 is the reverse saturation current density of the diode. When the current is equal to zero, the V_{oc} can be expressed as;

$$V_{oc} = \frac{BkT}{q} \ln\left(\frac{J_{photo}}{J_0} + 1\right) \quad 2.6$$

At short circuit conditions, $J = J_{sc}$ hence;

$$J_{sc} = J_0 \left(exp\frac{qV_{oc}}{BkT} - 1\right) \quad 2.7$$

GENERATION

The CIGS material has a strong absorption coefficient mainly due to the fact that it has a direct bandgap. As such, most incident photons in the visible and near-infrared spectrum (250 – 1300 nm) are absorbed in the first few hundred nanometers of the material. Figure 2.6 shows a simulated External Quantum Efficiency (EQE) extracted from [4]. The blue shaded region under the curve represents the proportion of photogenerated carriers that contribute to the output current, J_L which can be calculated from the relation;

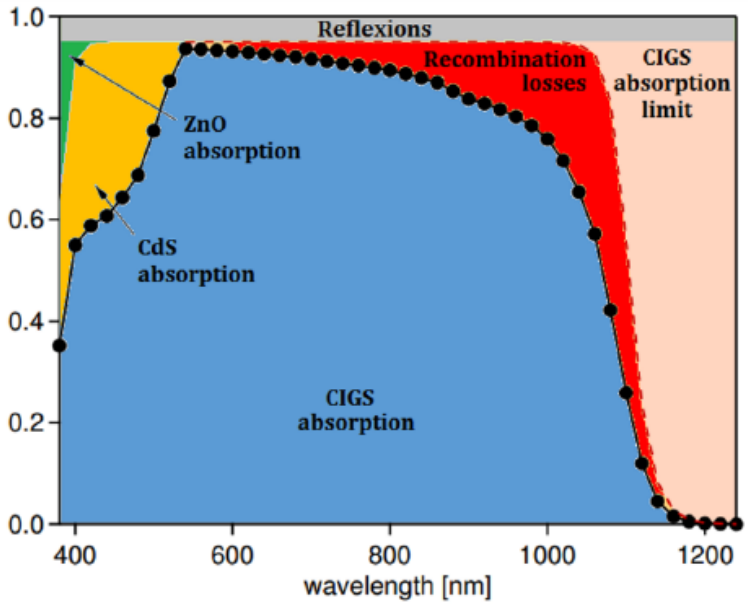


Figure 2.6 – EQE showing photon absorption regions in a CIGS cell [5]

$$J_L = q \int_{\lambda} \phi(\lambda) \cdot EQE(\lambda) d\lambda \quad 2.8$$

Where $\phi(\lambda)$ is the AM1.5 flux density per unit wavelength [$cm^{-2}nm^{-1}S^{-1}$] and q is the elementary charge. The grey region represents reflections off the surface of the cell and is purely optical while the losses in the other regions are purely electronic. These losses arise mainly from electron-hole pairs that are generated outside the CIGS absorber. These do not contribute to the output current since they are not collected due to the absence of an electric field and/or due to defects in the CIGS material which results in recombination. The active recombination mechanisms in a CIGS cell will be discussed.

RECOMBINATION MECHANISMS IN CIGS CELLS

There are three main recombination mechanisms in CIGS cells identified in the labelled regions in figure 2.2:

- ***Recombination in the Quasi-Neutral Region (QNR) of the absorber (Region A)***

The recombination in this region can be attributed to defects in the CIGS bulk and at the back contact interface. The current recombination depends on the collection function that governs the minority carrier concentration. Only the quasi-Fermi level for electron varies with the applied bias for low and medium voltages. A direct consequence of this is that the ideality factor for this type of recombination is 1.

- ***Recombination in the Space-Charge region (SCR) of the absorber (Region B)***

This region is where the electric field created by charge separation occurs and is close to the CIGS/CdS interface. The width of the SCR also varies with the applied bias. For a mid-gap defect, the activation energy is *Eg/*2 and leads to an ideality factor of 2. The ideality factor of 2 can also be seen as a symmetric variation of the quasi-Fermi level with respect to the defect level for the applied bias. Bulk recombination, especially in the SCR, dominate in high efficiency CIGS-based solar cells.

- ***Recombination at the CIGS absorber – CdS buffer layer interface (Region C)***

Recombination in this region depends on the conduction band offset (ΔE_c) between the CIGS and the CdS at the interface. For $\Delta E_c < 0$ (i.e. spike between the CIGS and the CdS), the activation energy is equal to the CIGS band-gap at the interface leading to an ideality factor of 1. For $\Delta E_c > 0$ (i.e. cliff between the CIGS and the CdS), the activation energy is reduced by ΔE_c leading to an ideality factor between 1 and 2 [3]. For further readings on recombination mechanisms, it is recommended to consult various textbooks such as [6].

2.2 CIGS ABSORBER FABRICATION

The preparation of a CIGS based solar cell starts with the growth of the CIGS absorber layer on a Mo-coated substrate. The processes for the fabrication of the absorber material can be classified broadly into two types: (i) deposition of a precursor layer followed by an annealing step where the metal precursors react with the chalcogenide (in our case, Se) to form $CuIn_{1-x}Ga_xSe_2$ and (ii) coevaporation of all the constituent elements hence forming the final material during the deposition. Regardless of what type of process is used, it important that certain conditions are respected in order to obtain a functional grade material. These conditions include: (i) an overpressure supply of the chalcogen, (ii) a substrate temperature around 500°C to ensure proper recrystallization of the film (low temperature process have been devised for use on substrates with low thermal stability) [7] [8] [9], (iii) an overall Cu-poor composition in the film, (iv) a [Ga]/([Ga] + [In]) composition between 0.2 – 0.3 and (v) adequate supply of Sodium. In this work, the 3-stage coevaporation process is adopted for the deposition of the CIGS films. However, other modified coevaporation processes (CUPRO and CURO) were utilized on stainless steel substrates (see sec. 4.2).

2.2.1 CO-EVAPORATION

Thermal coevaporation of the constituent elements have long been used in the CIGS fabrication and has resulted in the highest recorded efficiencies for CIGS solar cells [10] [11] [12] [13]. This method requires the simultaneous evaporation of Cu, In, Ga and Se in a high vacuum chamber as shown in figure 2.6. The source temperature of the elements are set such that it is high enough to melt the relevant species and facilitate evaporation. As mentioned earlier an excess of the chalcogen (Se) is required because Se has a small sticking coefficient and a high vapor pressure [14]. On the other hand, the sticking coefficients of Copper, Indium and Gallium are close to unity hence the fluxes are tuned adequately to achieve the final desired stoichiometric ratio.

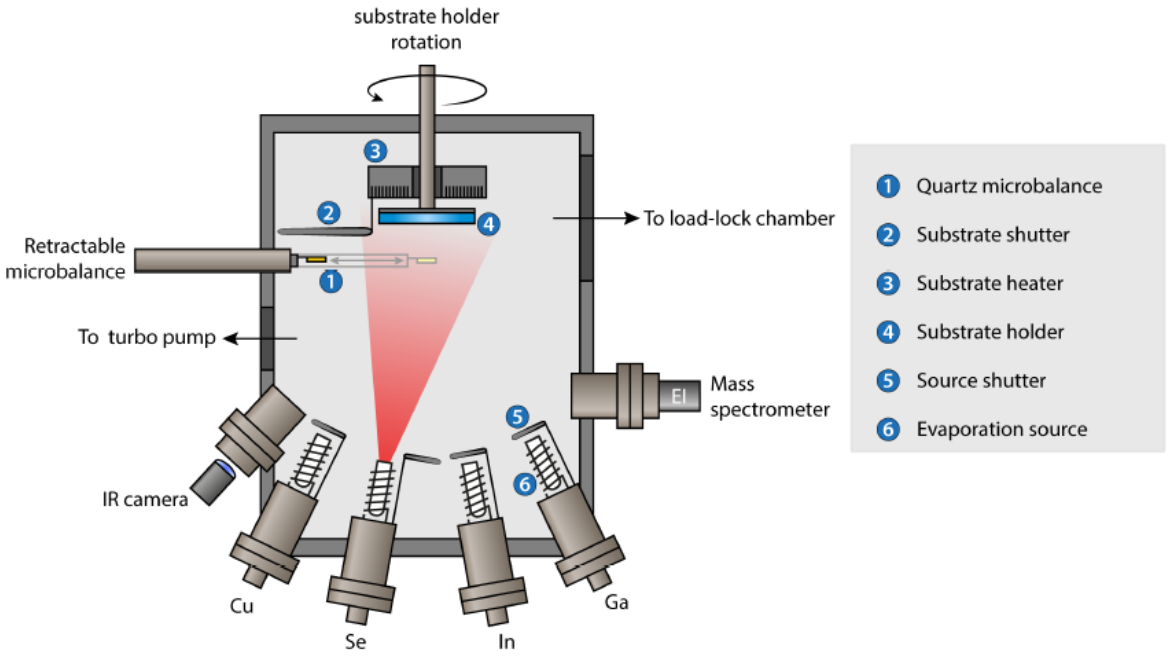


Figure 2.7. Coevaporation reactor used for CIGS deposition [3]

- One-Stage process

This is the simplest method of fabricating CIGS absorbers by coevaporation. In this process, all the constituent elements are evaporated simultaneously from the start to the finish of the deposition process at a constant substrate temperature. The final composition of the film can be controlled by simply adjusting the fluxes (and hence temperature) of the individual elements. It is also sometimes referred to as *constant rate deposition.*

- Boeing process

This is a 2-stage process and was developed in the 1980s. It consists of two phases in the fabrication if the CIGS film. In the first stage, the elements are evaporated simultaneously with the elemental fluxes fixed, such that a Cu-rich film is formed at the end of the 1st stage. The film formed in the first stage is a mix of stoichiometric CIGS and the Cu-Se binary phase. The presence of Cu2-xSe which is in the semi-liquid phase improves the inter-diffusion of the elements which leads to better crystallization. In the 2nd stage, the Cu flux is shut off while the Cu-rich film is exposed to In and Ga flux which results in a final slightly Cu-poor absorber layer at the end of the deposition process. The grain growth of the CIGS films is improved due to the incorporation of a Cu-rich phase during the deposition [15].

- Three-Stage process

As the name implies, there are 3 stages in the deposition of the absorber material. Figure 2.8 illustrates this. The Se flux is constant throughout the duration of the process. In the first stage, In, Ga and Se are evaporated at a substrate temperature of 350 – 400 °C. The duration of this stage is predetermined by the temperature (hence fluxes) of the In and Ga sources and at the end of this step, an $(In,Ga)_2Se_3$ precursor is formed.

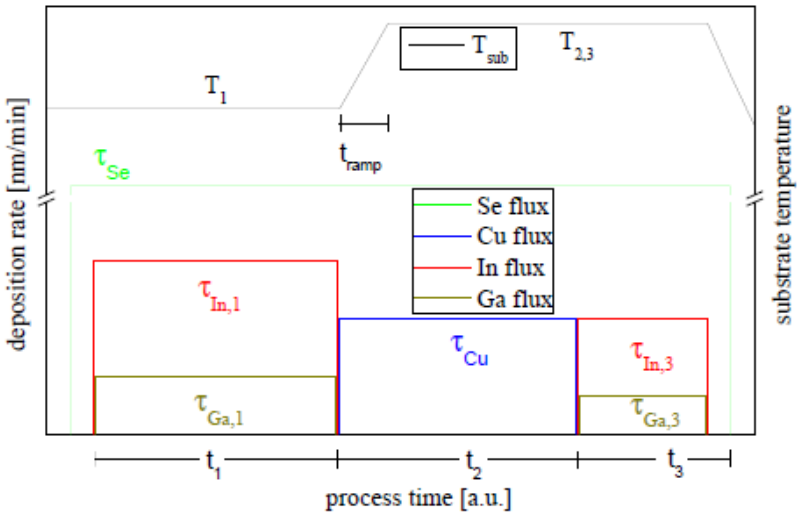


Figure 2.8 - Coevaporation and temperature profile for a 3-stage process. Substrate temperatures are 350-450 °C during the first and 500 – 550 °C during the second and third stages [16]

The substrate temperature is then ramped up to $T_{2,3}$ (>450 °C) at the start of the second stage and Cu is evaporated while the In and Ga fluxes are turned off. The second stage is a crucial part of the entire process as recrystallization occurs in this stage hence forming large grain sizes. Once stoichiometry is attained, further evaporation of Cu will result in the formation of Cu_xSe (Cu-rich phase) that starts growing on the surface. The end of the second stage is marked by the formation of this phase (CGI > 1) and is aptly called the "end-point detection". With the completion of the second stage, the Cu is then turned off at the start of the third stage, while the substrate temperature is kept the same as the second stage. In and Ga are again evaporated with Se in order to reach a final Cu-poor film with CGI < 1.

2.2.2 END-POINT DETECTION AND Cu_xSe BINARY FORMATION

The end point detection method is very useful in determining the end of the second stage during the 3-stage process. If we focus solely on the stoichiometric transitions between the stages, it is easy to see that at the start of the second stage (see figure 2.7), the CGI = 0. However, as the second stage advances during the evaporation of Cu and Se, the film grows to stoichiometry (CGI = 1) and continues till CGI > 1. At this point, the Cu rich film already shows the segregation of the Cu_xSe binary phase at the surface. Although, the metallic nature of these phases does not allow the formation of efficient solar cells its importance is given by its role during film growth as shown in figure 2.9.

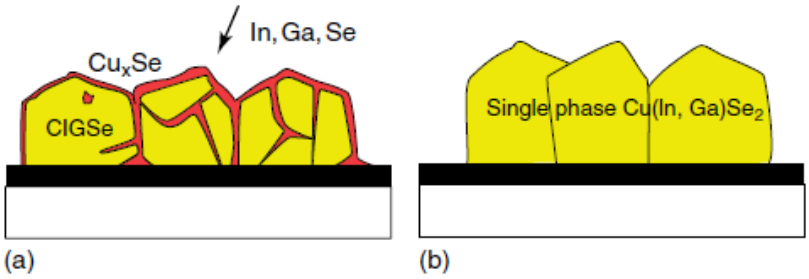


Figure 2.9 - Model of Cu(In,Ga)Se_2 growth in the presence of Cu_xSe. (a) Liquid–solid growth takes place due the presence of Cu_xSe. (b) Fully crystallized slightly Cu-poor Cu(In,Ga)Se_2 film.

According to the model in figure 2.9a, the Cu binary phase exists in a quasi-liquid state on the surface of the film. Since this semi-liquid phase has a higher emissivity than the CIGS, the substrate temperature drops (See sec. 2.2.2). Due to a control loop feedback system between the substrate power supply and the thermocouple measuring substrate temperature, the operating power increases to maintain the initial imposed temperature. The drop in temperature continues till it starts to stabilize pointing to a near saturation of the entire surface by the Cu_xSe phase. This signals the end point of the second stage, so the Cu flux is turned off. In fig. 2.9a, the binary compound covers the surface of the film and the grain sizes are quite small, however, as In and Ga are evaporated in the third stage of the coevaporation process, the Cu_xSe binary is gradually consumed and nucleation occurs leading to a final Cu poor film with large grain sizes (fig. 2.9b)[6]. If excesses of the binaries remain at the end of the entire process, these can be removed by etching the film in a cyanide solution [6].

2.2.3 GALLIUM GRADIENTS

Gallium gradients in CIGS solar cells play an important role in the performance of CIGS thin film solar cells. In this section, the formation and effects of the Ga gradient is discussed. In very simple terms, the Ga gradient can be approximated as a V-shaped Ga concentration across the bulk of the absorber *i.e* an increased Ga concentration towards the front and back surfaces of the absorber material and a minimum point in the middle. The minimum point forms a notch structure and can be approximated as a low bandgap semiconductor sandwiched between two higher bandgap semiconductors (front and back sides of the absorber material with higher Ga content).

- **Effects of gallium gradient**

Generally, having a Ga gradient is advantageous in a CIGS cell as an increased Ga concentration towards the back surface of the CIGS absorber material increases the back surface field in the conduction band [17] [16]. This phenomenon causes electrons to be repelled from the back contact hence reducing detrimental recombination at the contact. This back surface field induced by the Ga grading can improve the V_{OC} and can increase the J_{SC} due to a more efficient carrier collection. At the front surface of the CIGS material, having an increased Ga content reduces the bandgap mismatch between the CIGS and the CdS buffer layer. It is also shown that the V_{OC} increases while the J_{SC} decreases with an enhanced average Ga/III in the SCR [18]. The notch of the gradient profile is beneficial because the low Ga content (low bandgap) in this region allows the absorption of low energy photons hence increasing the J_{SC}. However, the distance of the notch to the SCR must be tuned appropriately. Typically, the notch should be very close to the SCR so that the generated carriers can be swept across under the influence of the electric field at the junction [19] [16] [20] [18].

- **Gallium gradient formation**

Due to the nature and design of the 3-stage coevaporation process, a Ga gradient is intrinsically obtained in most CIGS absorber materials fabricated using this process [18] [2]. This means we can obtain a Ga gradient without the need to adjust the In/Ga fluxes in the first and third stages of the coevaporation process. However, the Ga gradient might not be optimal hence an active Ga gradient control is required for full optimization to improve cell performance.

In his thesis, T.Klinkert studied the variation of the Ga gradient by a variation of the substrate temperature in the third stage between 480 °C - 540 °C [16] . Figure 2.10 shows the evolution of the Ga gradients in the CIGS absorber materials with respect to the third stage substrate temperature. It is observed that as the substrates temperature is gradually increased by 20 °C steps, the notch of the Ga gradient becomes flatter reaching a maximum for a substrate temperature of 540 °C.

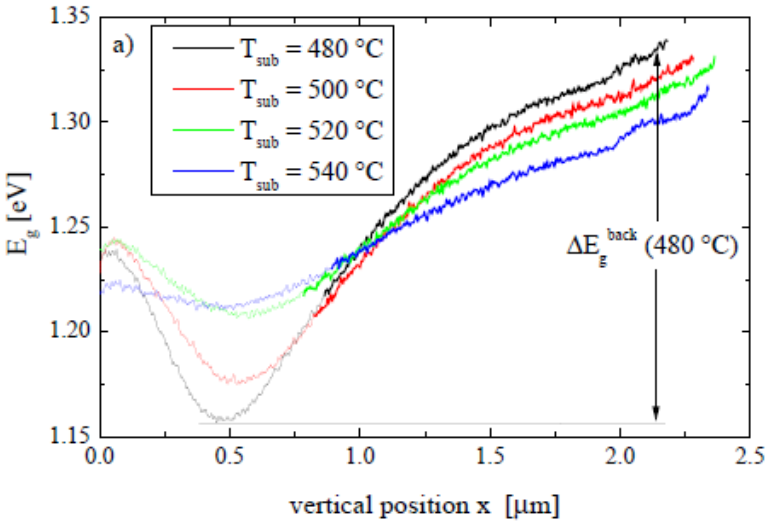


Figure 2.10 – Ga gradient profile of CIGS absorber materials with respect to varying substrate temperatures

This can be attributed to increased diffusion of Ga at higher temperatures. The effect of the change in notch steepness when the temperature is increased is reflected in the electrical properties of the cell. Firstly, the absorption in the near infrared region of the spectrum decreases with increasing substrate temperature as seen in figure 2.11. This lines up well with the prior explanation above that a lower notch favors the absorption of low energy (long wavelength) photons. In addition, there was a decrease in the V_{OC} and J_{SC} as the notch became flatter (increasing substrate temperature).

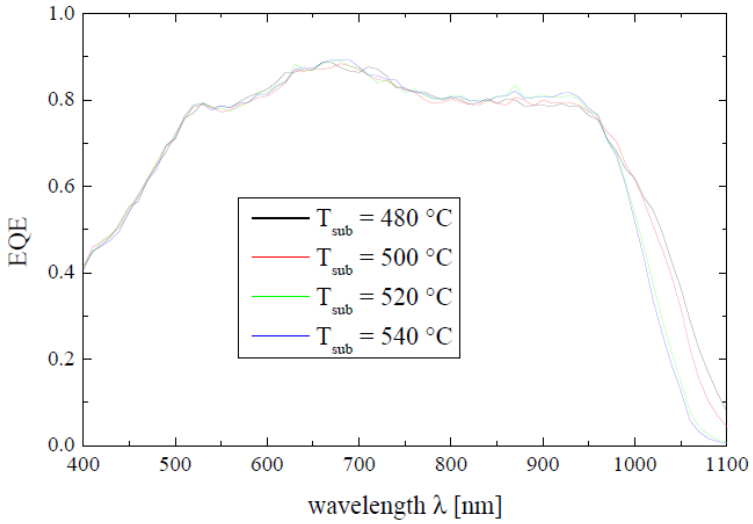


Figure 2.11 – External quantum efficiency of the solar cells with varied Ga gradient notch depth

Other factors that influence the formation of Ga gradients include alkali metal supply, Se rate and In/Ga fluxes during the absorber deposition.

2.3 BUFFER LAYER AND CONTACTS DEPOSITION

The deposition of the CIGS absorber material is just one step in the fabrication of a working CIGS solar cell. As seen in sec. 1.3.1, the CIGS solar cell is made up of a stack of unique functional layers which are deposited in separate deposition processes (vacuum and non-vacuum). In sequential order, the Mo back is deposited first. In the case of stainless steel substrates where an impurity barrier layer is required, the barrier layer is deposited first before the back contact is added. Following the Mo back contact deposition, the CIGS absorber is grown as described in sec. 2.2.1 or other suitable methods [21] [22] [23] [24]. The next step in the fabrication process is the deposition of the CdS buffer layer via a non-vacuum process or other alternative buffer layers (Cd-free CIGS cells) employed in the CIGS industry [16] [25] [26]. The transparent i-ZnO/ZnO:Al window layer is then sputtered on top of the stack. Figure 2.12(a) is the cell architecture when a Mo foil substrate is used while figure 2.12(b) is the configuration for a stainless steel substrate which is also applicable to glass or polyimide substrates.

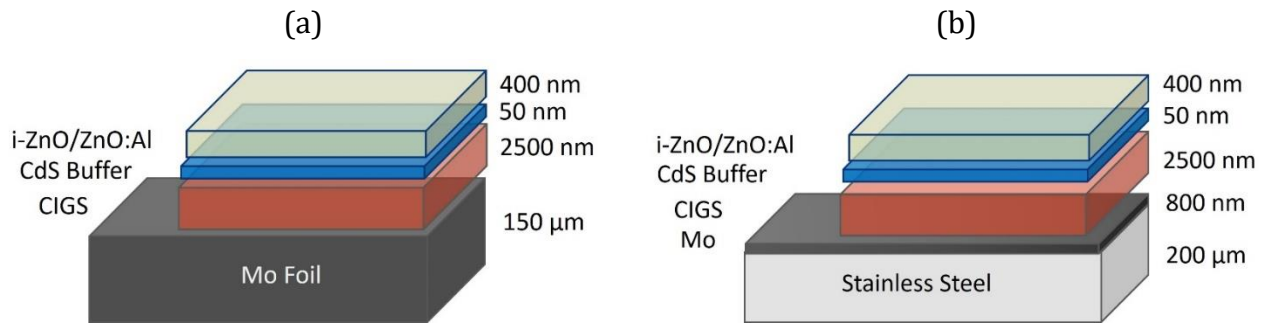


Figure. 2.12 CIGS cell architecture using (a) Mo substrate and (b) Stainless steel substrate. The configuration in (b) is also applicable to process using glass or polyimide substrates

2.3.1 MO BACK CONTACT

Mo is the preferred metal back contact used in CIGS solar cells. Mo is suitable for this role because of the formation of an $MoSe_2$ which is a thin film that favors the formation of an ohmic contact [27]. The Mo back contact is most commonly deposited either by radio-frequency sputtering (RF) or magnetron sputtering (DC magnetron) in an Argon atmosphere. The necessary conductivity and thus Mo thickness depends on the cell or module configuration. The sputtered Mo back contact creates a good adhesion surface for the CIGS absorber and has a sheet resistance of ~0.2 Ω/sq. In cells made on sodalime glass, the Mo back contact layer can regulate the diffusion of intrinsic Na from the SLG substrate into the growing CIGS material. The RF (13.56 MHz) sputtering deposition eliminates the accumulation of charges on the surface while using magnetron sputtering reduces the working gas pressure and leads to a better quality of the Mo layer. The Mo target has a purity of 99.95 % and the substrate is positioned parallel to the target surface with a fixed scan rate and a distance of 55 mm from the target. A pre-etch is done on the surface of the substrate with an Argon plasma treatment to remove any impurities on the surface and to activate the surface. The working pressure can be adjusted and is fixed between 2 mTorr and 20 mTorr by varying the mass flow of the Argon gas and keeping the DC current at 1.0 A or RF power at 600 W [28]. When RF mode is used for the deposition, the changes in the resistivity of the film is minimal and fluctuates between $1 - 1.5 \times 10^{-5}$ Ωcm as the working pressure increases. On the other hand, while working in the DC mode, the resistivity of the Mo film increases, reaching 4×10^{-5} Ωcm as the working pressure increases. With this information, the quality of the Mo thin films can be optimized as required. In this thesis, the standard back contact is an 800 nm thick Mo layer deposited by DC magnetron sputtering on the relevant substrate. The Mo target is rectangular with a purity of 99.95 % purity is used.

2.3.2 $MoSe_2$ LAYER

$MoSe_2$ is a very thin layer of material formed during the pre-selenization step prior to CIGS absorber deposition. Its crystal structure is shown in figure 2.13, where it usually occurs in a hexagonal phase with weak Van Der Waals bonds among the *c*-axis. The hexagonal structure consists of Se-Mo-Se sheaths which are separated from each other by a gap and have a perpendicular orientation to the *c*-axis.

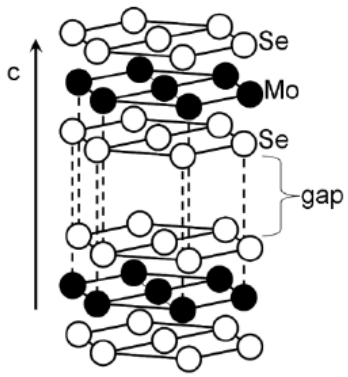


Figure 2.13 - Anisotropic crystal structure of hexagonal $MoSe_2$ [29]

$MoSe_2$ is a layered p-type semiconductor with bandgap of 1.41 eV [30] and creates an ohmic contact at the Mo/CIGS interface [29] [27] [30]. This is important for the CIGS solar cell as it has been reported that the absence of an ohmic contact could lead to a formation of a Schottky barrier which inevitably leads to substantial resistive losses [31]. The presence of an $MoSe_2$ improves the efficiency of the CIGS solar cell and should be noted that optimization of the thickness and orientation of this film is crucial to the performance of a CIGS cell [32]. As reported by different groups, the thickness and growth of the $MoSe_2$ layer formed is influenced by the sputtering pressure and/or power of the Mo back contact layer [30] [33] as well as the Se flux during just before the start of the CIGS absorber deposition (pre-selenization) [27].

2.3.3 BUFFER LAYER DEPOSITION

CdS, deposited in a chemical bath, is used as a so called buffer layer on top of the CIGS absorber. The CdS buffer layer is deposited in a chemical bath via a process known as the chemical bath deposition (CBD) method at bath temperature between 60 °C-70 °C. CBD CdS involves the precipitation of CdS from the solution onto the absorber. With this method, a thin and conformal buffer layer (30–60 nm) is usually obtained after 5–10 min deposition The solution used is a mix of Thiourea ($SC(NH_2)_2$) as sulfur precursor,

Ammonium (NH_4OH) as complexing agent and Cadmium Acetate as Cd donor. The final layer thickness is usually around 50 ± 5 nm. In our samples, it was observed that a modification of the CIGS absorber growth process led to a modification of the CIGS surface which in turn resulted in varying growth speeds of the CdS buffer layer. The CdS material is an n-type semiconductor with a bandgap of 2.4 eV and forms a heterojunction with the CIGS absorber layer which creates an electric field and aids in the collection of generated charge carriers. It also passivates the surface of the CIGS absorber and protects the CIGS material during the sputtering of the TCO window layer [3]. The disadvantages with CdS is the relatively low band gap of 2.4eV. This results in a loss of efficiency since few of the charge-carriers generated in the buffer layer are collected at the contacts. Furthermore, cadmium is toxic to humans and hence, other alternative buffer layers such as Zn(O,S) are being investigated as a suitable replacement.

2.3.4 i-ZnO/ZnO:Al FRONT CONTACT

The front contact of a CIGS solar cell consists of a highly conductive ZnO:Al layer (300-500 nm) on top of a highly resistive layer of i-ZnO (50-100 nm). At the front of a CIGS solar cell, the window layer acts as an electrical contact and as a window to allow light through to the absorber layer. A connection between the back contact and the front contact in the solar cell will create a short circuit in the cell by forming a highly conductive ohmic shunt path. This type of shunts can be introduced in a solar cell by scratches or pinholes through the CdS and CIGS layers. Since the intrinsic zinc oxide layer is highly resistive it can be expected to protect solar cells from this kind of shunts. Without the i-ZnO layer, a scratch or a hole would form a shunt path between the Mo back contact and the Aluminum doped zinc oxide front contact. The transparent conducting window layer must be highly transparent to allow maximum photon absorption in the cell, and must have a low sheet resistance to laterally transport the current over macroscopic distances to the nearest metal contact finger or interconnect. The i-ZnO/ZnO:Al window layer is degenerately doped semiconductor as a transparent conducting oxide layer (TCO). ZnO has a wide bandgap of 3.3 eV. Successful optimization of Al-doped ZnO comes from a trade-off between its high electrical conductivity and high optical transmittance. The window layers used in this work were 450 ± 50 nm thick.

CONCLUSION

In this chapter, we have reviewed the basic fundamentals detailing how makeup and functioning of a typical CIGS solar cell. The formation of the junction and the relevance of the SCR and QNR regions have been outlined. The various electrical properties of the cell were also discussed and derived, giving an understanding of the mode of operation of CIGS cells and solar cells in general. Furthermore, it was shown that the bandgap of the CIGS solar cell can be tuned as required giving rise to the concept of Ga gradients in the solar cell. Well optimized Ga gradients are beneficial and increase cell performance especially with respect to the open circuit voltage and short circuit current. The formation and effect of Ga gradients at the front, close to the SCR and at the rear of the absorber material were discussed. The Ga gradient can be adjusted either by simply tuning the substrate temperature in the 3rd stage of the deposition process or an active control of the In/Ga fluxes during the absorber deposition. The formation of Cu-rich binaries during CIGS deposition was also discussed in relation to the end point detection which is very helpful in determining phase change and hence control of the 3-stage deposition process. Finally, the deposition methods for the other layers that make up a fully functional CIGS cell was presented. Equipped with this knowledge, chapter 3 will focus on the fabrication of CIGS cells on Mo foil substrates.

REFERENCES

[1] M.-D. Gerngro\s s and J. Reverey, "CIS/CIGS based Thin-film solar cells," *Fac. Eng. Univ. Kiel*, 2008.

[2] A. Chirilă *et al.*, "Highly efficient Cu(In,Ga)Se2 solar cells grown on flexible polymer films," *Nat. Mater.*, vol. 10, no. 11, pp. 857–861, Sep. 2011.

[3] F. Mollica, "Optimization of ultra-thin Cu(In,Ga)Se2 based solar cells with alternative back-contacts," UPMC, 2017.

[4] M. Gloeckler, "Device physics of Cu (In, Ga) Se2 thin-film solar cells," PhD Thesis, Colorado State University, 2005.

[5] T. Le Petit, "Influence of KF post deposition treatment on the polycrystalline Cu (In, Ga) Se2/CdS heterojunction formation for photovoltaic application," l'Université de Nantes, 2015.

[6] H. W. Schock and R. Scheer, Eds., *Chalcogenide Photovoltaics : Physics, Technologies and Thin Film Devices.* Weinheim: Wiley-VCH-Verl, 2012.

[7] R. Caballero, C. A. Kaufmann, T. Eisenbarth, T. Unold, R. Klenk, and H.-W. Schock, "High efficiency low temperature grown Cu(In,Ga)Se2 thin film solar cells on flexible substrates using NaF precursor layers," *Prog. Photovolt. Res. Appl.*, vol. 19, no. 5, pp. 547–551, Aug. 2011.

[8] X. He *et al.*, "The role of Na incorporation in the low-temperature processed CIGS thin film solar cells using post deposition treatment," *J. Alloys Compd.*, vol. 658, pp. 12–18, Feb. 2016.

[9] K. Zhang *et al.*, "Fabricating highly efficient Cu(In,Ga)Se2 solar cells at low glass-substrate temperature by active gallium grading control," *Sol. Energy Mater. Sol. Cells*, vol. 120, pp. 253–258, Jan. 2014.

[10] I. Repins *et al.*, "19·9%-efficient ZnO/CdS/CuInGaSe $_2$ solar cell with 81·2% fill factor," *Prog. Photovolt. Res. Appl.*, vol. 16, no. 3, pp. 235–239, May 2008.

[11] P. Jackson, R. Wuerz, D. Hariskos, E. Lotter, W. Witte, and M. Powalla, "Effects of heavy alkali elements in Cu(In,Ga)Se $_2$ solar cells with efficiencies up to 22.6%," *Phys. Status Solidi RRL - Rapid Res. Lett.*, vol. 10, no. 8, pp. 583–586, Aug. 2016.

[12] T. Feurer *et al.*, "Progress in thin film CIGS photovoltaics - Research and development, manufacturing, and applications: Progress in thin film CIGS photovoltaics," *Prog. Photovolt. Res. Appl.*, 2016.

[13] P. Jackson *et al.*, "Properties of Cu(In,Ga)Se $_2$ solar cells with new record efficiencies up to 21.7%: Properties of Cu(In,Ga)Se $_2$ solar cells with new record efficiencies up to 21.7%," *Phys. Status Solidi RRL - Rapid Res. Lett.*, no. 1, pp. 28–31, Jan. 2015.

[14] J. Scholdstrom, "Thermal Radiation from co-evaporated Cu(In,Ga)Se2 - End-point detection and control," Uppsala University, Uppsala, Sweden, 2012.

[15] C.-H. Huang, W.-J. Chuang, C.-P. Lin, Y.-L. Jan, and Y.-C. Shih, "Deposition Technologies of High-Efficiency CIGS Solar Cells: Development of Two-Step and Co-Evaporation Processes," *Crystals*, vol. 8, no. 7, p. 296, Jul. 2018.

[16] T. Klinkert, "Comprehension and optimisation of the co-evaporation deposition of Cu (In, Ga) Se2 absorber layers for very high efficiency thin film solar cells," PhD Thesis, Université Pierre et Marie Curie-Paris VI, 2015.

[17] S. Schleussner, U. Zimmermann, T. Wätjen, K. Leifer, and M. Edoff, "Effect of gallium grading in Cu(In,Ga)Se2 solar-cell absorbers produced by multi-stage coevaporation," *Sol. Energy Mater. Sol. Cells*, vol. 95, no. 2, pp. 721–726, Feb. 2011.

[18] T. M. Friedlmeier *et al.*, "High-efficiency Cu(In,Ga)Se2 solar cells," *Thin Solid Films*, Aug. 2016.

[19] M. Saadat, M. Moradi, and M. Zahedifar, "CIGS absorber layer with double grading Ga profile for highly efficient solar cells," *Superlattices Microstruct.*, vol. 92, pp. 303–307, Apr. 2016.

[20] J. Chantana *et al.*, "Determination of open-circuit voltage in Cu(In,Ga)Se2 solar cell by averaged Ga/(In + Ga) near its absorber surface," *J. Appl. Phys.*, vol. 114, no. 8, p. 084501, Aug. 2013.

[21] U. P. Singh and S. P. Patra, "Progress in Polycrystalline Thin-Film Cu(In,Ga) Se 2 Solar Cells," *Int. J. Photoenergy*, vol. 2010, pp. 1–19, 2010.

[22] S. Niki *et al.*, "CIGS absorbers and processes," *Prog. Photovolt. Res. Appl.*, vol. 18, no. 6, pp. 453–466, Sep. 2010.

[23] V. K. Kapur, A. Bansal, P. Le, and O. I. Asensio, "Non-vacuum processing of CuIn1−xGaxSe2 solar cells on rigid and flexible substrates using nanoparticle precursor inks," *Thin Solid Films*, vol. 431–432, pp. 53–57, May 2003.

[24] M. Stanley, M. Jubault, F. Donsanti, and N. Naghavi, "Flexible Cu (In, Ga) Se2 Based Solar Cells Using Mo Foils as Substrate," *Phys. Status Solidi C*, vol. 14, no. 10, 2017.

[25] W. Hsu *et al.*, "Electron-Selective TiO2 Contact for Cu(In,Ga)Se2 Solar Cells," *Sci. Rep.*, vol. 5, p. 16028, Nov. 2015.

[26] Miguel A. Contreras *et al.*, "Progress Toward 20% Efficiency in Cu(In,Ga)Se2 Polycrystalline Thin-film Solar Cells," *Prog. Photovolt. Res. Appl.*, vol. 7, pp. 311–316, 1999.

[27] T. Klinkert *et al.*, "New insights into the Mo/Cu(In,Ga)Se $_2$ interface in thin film solar cells: Formation and properties of the MoSe $_2$ interfacial layer," *J. Chem. Phys.*, vol. 145, no. 15, p. 154702, Oct. 2016.

[28] M. Jubault, L. Ribeaucourt, E. Chassaing, G. Renou, D. Lincot, and F. Donsanti, "Optimization of Mo thin films for electrodeposited CIGS solar cells," *Sol. Energy Mater. Sol. Cells*, vol. 95, pp. S26–S31, May 2011.

[29] D. Abou-Ras, "Structural and chemical analyses of buffer layers in Cu(In,Ga)Se$_2$ thin-film solar cells," Ph.D thesis, ETH Zurich, 2005.

[30] Y.-C. Lin, M.-T. Shen, Y.-L. Chen, H.-R. Hsu, and C.-H. Wu, "A study on MoSe2 layer of Mo contact in Cu(In,Ga)Se2 thin film solar cells," *Thin Solid Films*, vol. 570, pp. 166–171, Nov. 2014.

[31] G. Gordillo, F. Mesa, and C. Calderón, "Electrical and morphological properties of low resistivity Mo thin films prepared by magnetron sputtering," *Braz. J. Phys.*, vol. 36, no. 3B, pp. 982–985, 2006.

[32] M. Kim, J. Lee, Y. Lee, J. Jeong, and K.-B. Lee, "Structural and compositional analyses of Cu(In,Ga)Se $_2$ thin film solar cells with different cell performances," *J. Vac. Sci. Technol. B Nanotechnol. Microelectron. Mater. Process. Meas. Phenom.*, vol. 34, no. 3, p. 03H121, May 2016.

[33] X. Zhu, Z. Zhou, Y. Wang, L. Zhang, A. Li, and F. Huang, "Determining factor of MoSe2 formation in Cu(In,Ga)Se2 solar Cells," *Sol. Energy Mater. Sol. Cells*, vol. 101, pp. 57–61, Jun. 2012.

CHAPTER 3

The sun bathes Earth in ample energy to fulfill all the world's power needs many times over. It doesn't give off carbon emissions. It won't run out. And it's free.

- SUSANNAH LOCKE, *Scientific American*, *2008*

FABRICATING CIGS SOLAR CELLS ON MO SUBSTRATES

INTRODUCTION

In the previous chapter, we have described the typical CIGS cell architecture, absorber fabrication and its properties. This chapter will focus on the development of CIGS absorbers on Mo substrates. An interesting feature in the use of Mo foil is the fact that it can act both as the substrate and back contact hence eliminating the need to sputter any additional Mo back contact. For the records, there has been very few (if any) publications detailing the fabrication of CIGS solar devices on Mo substrates especially using the 3-stage co-evaporation process. The chapter starts with a review of the properties of Mo foil substrate and its suitability for CIGS cell fabrication and then compared with sodalime glass substrate which is the industry standard. Subsequently, the substrate temperature measurement method in the coevaporation reactor is discussed to make a distinction between the imposed and measured temperature. The ideal deposition temperature for CIGS depositions on the Mo substrate is then selected by comparing results obtained at various deposition temperatures using the standard process parameters of the 3-stage deposition process. The deposition of CIGS on Mo presents some challenges peculiar to Mo foil. These challenges are (i) observing the end point detection at the end of the second stage of the deposition and (ii) there termination step in the 3rd stage which impacts the CGI of the CIGS absorbers. These led to an optimization of the deposition process to suit the deposition on Mo. Alkali metal incorporation was implemented on the samples followed by an optimization of the Ga gradient which both led to an increase in cell efficiency. It was observed during the studies that a modification of the deposition process also modified the CIGS morphology. This led to a variation in the CdS buffer layer growth kinetics. The results are discussed. Finally, the impact of sputtering an extra layer of Mo on the Mo foil substrate was investigated using different Mo back contact layer thickness at a CIGS deposition temperature of 480 °C and 550 °C.

3.1 CHARACTERIZATION OF THE MO SUBSTRATE

3.1.1 Properties of Mo

Mo is widely adopted as a suitable back contact material due to its properties. These include its stability at the processing temperature for the CIGS absorbers, and its resistance to alloying with Cu and In as well as a low contact resistance at the Mo/CIGS interface. In a typical CIGS architecture on SLG where a Mo back contact is usually sputtered on the glass substrate using either a RF or DC magnetron sputtering, it is important to tune the sputtering parameters of the Mo layer in order to achieve an adhesive layer as well as a low-resistive layer. Mo has a particularly good resistance to corrosion by mineral acids, provided oxidizing agents are not present. It is also resistant to many liquid metals and to most molten glasses. In inert atmospheres, it is unaffected up to 1760°C by refractory oxides [1]. The resistivity of 99.97% pure Mo foil is around 5.5 × 10^{-6}Ωcm [1]. In terms of its coefficient of thermal expansion (CTE), Mo is quite suitable for use in CIGS cells because its CTE of 4.9 × 10^{-6} K^{-1} is close in the range of that of CIGS films (8 – 11 × 0^{-6} K^{-1}). This results in a smaller stress between the Mo/CIGS layers. Table 3.1 below summarizes the some of the properties of Mo just described.

Coefficient of thermal expansion CTE (10^{-6} K^{-1})	4.8 – 5.9
Fusion Temperature (°C)	2,623
Thermal conductivity at 20 °C ($Wm^{-1}K^{-1}$)	142
Electrical conductivity at 20 °C ($\Omega^{-1}m^{-1}$)	$17{,}9 \cdot 10^{6}$
Resistivity (Ωm)	$5.5 \cdot 10^{-8}$
Crystal structure	body-centered cubic

Table 3.1 Properties of Mo

- Surface Morphology

In this thesis, all work on Mo substrates was carried out on 99.97 % pure Mo substrates with a thickness of 150µm. The substrates were supplied by GoodFellow. Figure 3.1 is a surface SEM image of the Mo foil at a 5000x magnification. At this magnification, it is quite easy to see some surface features that disrupts the smoothness of the substrate. These are random surface irregularities perhaps resulting from the rolling process during the substrate fabrication. Our interest lies in the micro structure of the surface of the

substrate when analyzed by AFM. With AFM, we are able to measure the average surface roughness of the substrate.

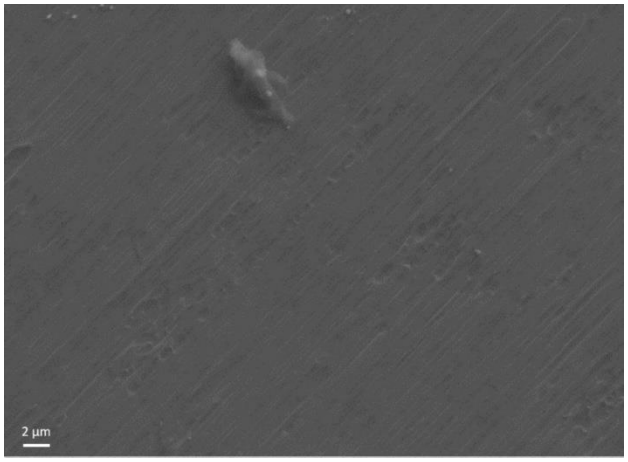


Figure 3.1 SEM surface morphology of a 150µm thick Mo foil

In figure 3.2, AFM scans on the Mo foil and a sputtered Mo/SLG layer [2] is shown in 3D scan highlighting the surface features. The average roughness (Ra), is given in table 3.2. It is observed that Mo sputtered on sodalime glass has a much smoother surface than the Mo substrate. This derives from the fact that sodalime glass has a very smooth surface (R_a = 2.5 nm) hence resulting in smoother surfaces during Mo sputtering as opposed to a rolled Mo foil. The roughness of a substrate can impact the performance of the resulting CIGS cell fabricated on such a substrate. The possible negative effects of a substrate's roughness have been discussed in section 1.3.4.

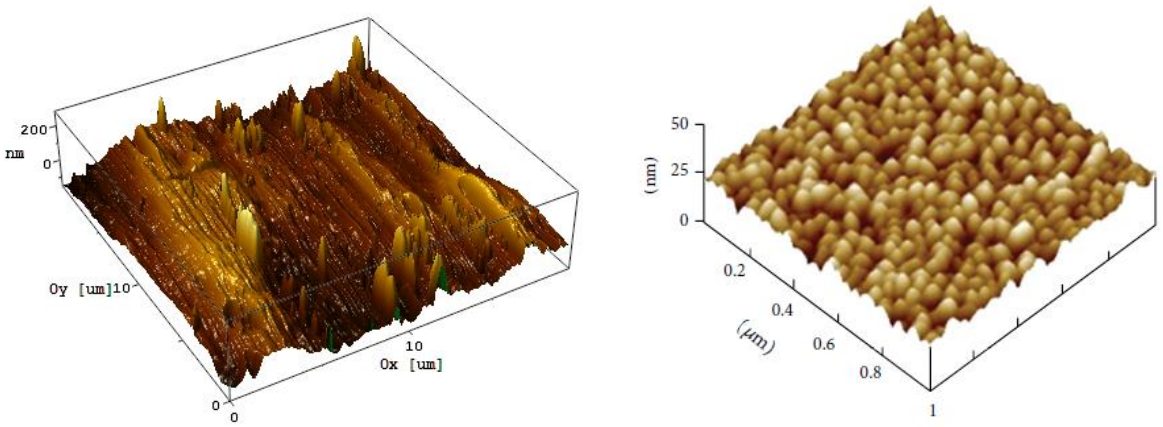


Figure. 3.2 3D AFM surface scan of (a) 150µm thick Mo foil [in-house] (b) Mo/SLG (sputtered) [2]

From figure 3.2, it can also be seen that the morphology of both surfaces are distinctive. While Mo foil has randomly distributed features (peaks and troughs), the sputtered Mo models the flat surface of the SLG glass. The grains of the sputtered Mo are rounded on the top and are quite evenly distributed across the surface with no prominent peaks/troughs.

	Ra (nm)	**RMS (nm)**
Mo foil (150µm)	83.0	103.0
Mo/SLG (Sputtered)	3.0	-

Table 3.2 Surface roughness of Mo foil vs sputtered Mo/SLG as measured by AFM. The Ra is the arithmetic average of surface heights measured across a surface or simply average the height across the microscopic peaks and valleys while the RMS is the Root Mean Square of a surface's measured microscopic peaks and valleys.

- Mo foil and sputtered Mo crystal orientation

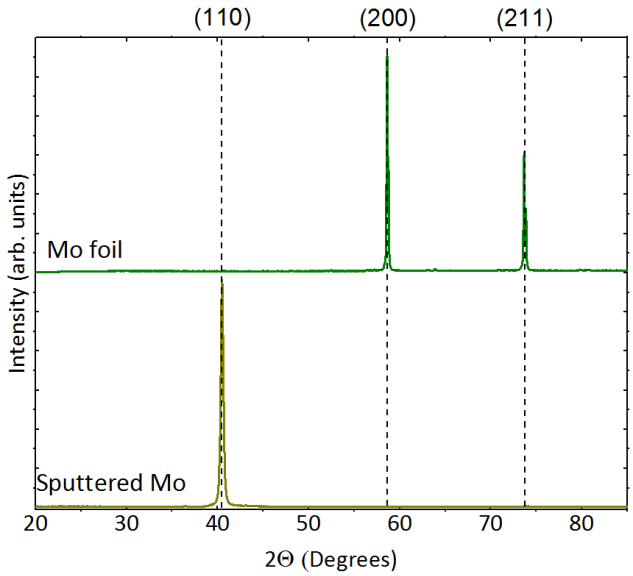


Figure. 3.3 XRD diffractogram of a Mo foil and Mo layer sputtered on sodalime glass

Another difference between Mo foil and sputtered Mo (on metal, glass, polyimide etc.) is their orientation (figure 3.3). A plain Mo foil which is used in this work exhibits an orientation perpendicular to the (200), (211) lattice plane while Mo sputtered on top of a Mo foil and/or other substrates has an orientation perpendicular to the (110) lattice plane as seen in figure 3.3. This difference in orientation can impact the growth and orientation of the CIGS absorber as will be discussed subsequently in section 3.5.

- Reflectivity of Mo

The reflectivity of the Mo foil was measured in a wavelength range of 250nm to 2000nm. This was compared alongside a plain SLG substrate coated with a layer of sputtered Mo back contact. Figure 3.4 shows that the reflectivity of the plain Mo foil closely matches that of the Mo/SLG substrate. A high reflectivity of the back contact is favorable in CIGS solar cells as this reflectance reduces the amount of light absorbed at the CIGS/Mo interface, hence increasing the pathway of light and inevitably the absorption within the CIGS bulk [3] [4]. The effect of having a highly reflective back contact is negligible for thick CIGS absorbers but becomes more important when dealing with ultrathin CIGS absorber layers. Lundberg *et al.* measured the total reflectance and transmittance on two different CIGS structures [5]. In the first case, the CIGS was deposited directly on glass while the second case involved a CIGS layer deposited on a glass/Mo configuration.

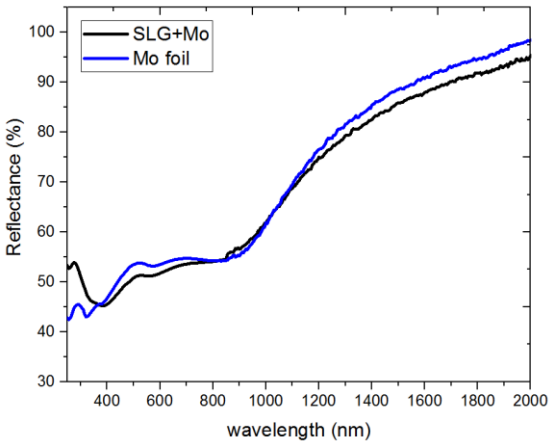


Figure. 3.4 Reflectivity of a plain Mo foil vs Mo/SLG

Here an assumption was made that the optical properties of the CIGS were the same, this justification was made by the comparison of the total reflectance measurements of the two configurations. In order to eliminate the influence of a difference in surface morphology of the CIGS layers, they were both polished before the measurement (figure 3.6).

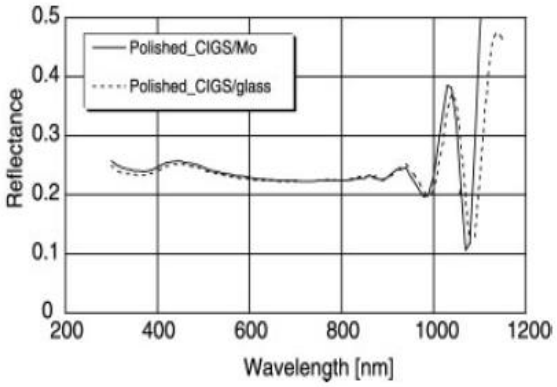


Figure. 3.5 Total reflectance curves from CIGS grown on glass (dotted) and CIGS grown on Mo (solid) [5]

The result indicates that when the CIGS layer is thick enough, the influence of the reflection in the CIGS/Mo and CIGS/glass interface is negligible [5]. Further studies on the influence of the back contact reflectivity on the photocurrent of CIGS cells as the thickness of the absorber layer is varied has been carried out by F.Mollica [6].

- Mo substrate vs SLG

The properties of Mo that makes it a viable candidate for the back contact include its inertness, stability at high temperature and low contact resistance to CIGS [2] [7]. Usually, the back contact layer is deposited on the substrate by sputtering. SLG is the most common type of substrate used for CIGS cells. However, in our case, we have chosen a Mo foil which will play the role of the substrate and back contact simultaneously. This material has similar properties as a sputtered Mo contact except for its surface morphology and orientation.

	Mo Foil	**Sodalime Glass**
CTE (10^{-6} K^{-1})	4.8 – 5.9	9
Fusion Temperature (°C)	2,623	562
Intrinsic Na impurity	✗	✓
Thickness (mm)	0.15	3.0
Flexibility	✓	✗
Roughness, Ra (nm)	82.9	2.5

Table 3.3 A comparison of the properties of Mo foil and plain sodalime glass.

A major difference between the classic Mo/SLG architecture and the Mo foil is flexibility, surface roughness and Na content from the SLG as enumerated in table 3.3. SLG is rigid which limits the range of applications it can be used for. The implementation of a Mo foil increases the use cases as the Mo foil (150 μm) is flexible and can be bent without deformation. Since Mo foil is Na free, there is no beneficial intrinsic diffusion of Na during CIGS deposition as in the case of SLG. Hence, an external source of Na has to be taken into account while depositing CIGS absorbers on a pure Mo foil. The Mo/SLG configuration has a very smooth surface (R_a ~3 nm) which is an advantage over Mo foil (R_a ~83 nm) as this eliminates problems resulting from uneven surfaces that can create pinholes or shunts.

3.2 DEPOSITION AND CHARACTERIZATION OF CIGS ABSORBERS GROWN ON MO FOIL

This section discusses the details of the 3-stage process used in depositing the CIGS absorbers on Mo foil. The temperature measurement scheme will also be discussed and a distinction will be made between imposed and measured temperatures. Preliminary temperature studies were carried out by varying the second and third stage temperature. This was done to select a baseline temperature that yields satisfactory CIGS absorber quality in terms of the Cu and Ga gradient and grain size and will be discussed. The CIGS deposition in this section was done with no NaF post deposition. The aim was to select a baseline deposition temperature for subsequent experiments.

3.2.1 Substrate temperature measurement

In our system, the measurement of the substrate temperature is carried out by a thermocouple which is placed between the heating filament and the backside of the substrate. The thermocouple has no physical contact with the substrate due to the substrate rotation. Hence we expect a discrepancy between the imposed temperature (set point temperature) and the measured temperature by the thermocouple. Due to the thickness of some substrates (e.g. SLG – 3mm), there will be some difference between the temperature measured at the back side of the substrate and the real surface temperature which is most important to us. One way to measure the surface temperature of a substrate is by using an infrared (IR) camera. The principle contained herein is that of a black body emitter. According to Stefan-Boltzmann law which describes the power radiated from a black body in terms of its temperature, the total radiant heat energy emitted from a

surface is proportional to the fourth power of its absolute temperature. This law applies only to black bodies that are capable of absorbing all incident heat radiation. In the case of non-black bodies, which applies to our substrates, the emissivity ϵ of the material in question needs to be taken into account.

$$J = \epsilon \sigma T^4 \qquad 3.1$$

Where J is the total energy emitted by a body, ϵ is the emissivity of the body (ϵ = 1 in the case of an ideal black body), σ is a constant and T is the temperature of the body.

T.Klinkert by means of an infrared (IR) camera, measured the real temperature of (a) SLG/Mo (b) SLG/Mo/CIGS and (c) Mo bulk which were pre-heated in a furnace to a set point temperature of 400°C and left to stabilize for 20 min [8]. Figure 3.6 is an infrared image of the materials in the furnace taken with an infrared camera immediately after the furnace was open.

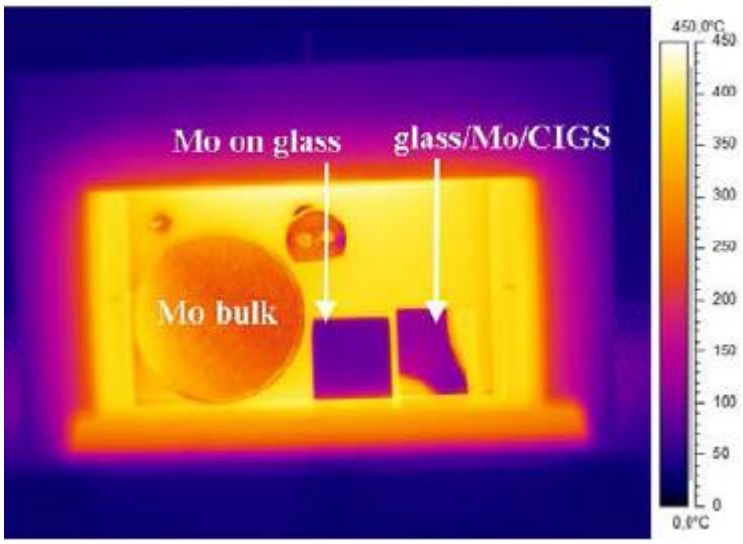


Figure. 3.6. Infrared images of (a) SLG/Mo (b) SLG/Mo/CIGS and (c) Mo bulk. The emissivity of the materials were assumed to be unity in this image [8]

One deduction that can be made already by visual inspection of the color-temperature scale in figure 3.6 is that the Mo bulk has a lower emissivity than SLG/Mo and SLG/Mo/CIGS. The Mo bulk also has a much higher temperature than the Mo/SLG sample. This observation is further supported by material emissivity calculations using the *ThermaCAM Researcher Professional 2.10* by FLIR Systems [8]. The difference ($T_{IR} - T_1$) between the temperature measured by the IR camera, T_{IR} and the imposed temperature T_1 and the difference ($T_{IR} - T_2$) between the temperatures measured by the IR camera, T_{IR} and the measured thermocouple temperature T_2 were calculated and plotted to give an

evolution of the material temperature across different temperature ranges as seen in figure. 3.7.

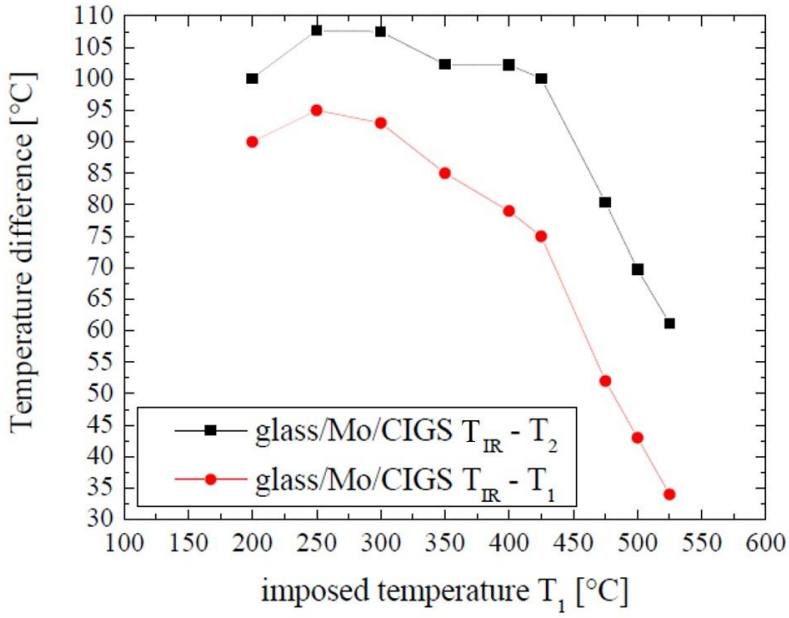


Figure. 3.7 Plotted temperature difference between the thermocouple (T_1 and T_2) and the temperature measured by the infrared camera (T_{IR}) [8]

In a T_1 range between 200 °C and 425 °C, the temperature difference $T_{IR} - T_2$ is quite stable at 100 – 107 °C while $T_{IR} - T_1$ varies between 75 and 95 °C. As the temperature increases however, the differences ($T_{IR} - T_1$) and ($T_{IR} - T_2$) both decreases. While it is beneficial to know the real substrate temperature, we only need the imposed 'set point' temperature and measured output temperature of the thermocouple for our research and optimization steps. Hence in this work, any quoted temperature will be that measured by the thermocouple unless otherwise stated. It should also be noted that for the same imposed temperature (T_1), the temperature measured by the thermocouple (T_2) is always higher on the Mo foil than on Mo/SLG.

3.2.2 Deposition temperature selection for CIGS growth on Mo foil

In the 3-stage process employed in this thesis, the first stage is set a relatively lower substrate temperature while the second and third stage are pinned at a higher temperature. In order to select a baseline temperature for our experiments, we did three experimental runs. In the first stages, we fixed the substrate temperature at 400 °C while the second and third stages for the three runs were done at 450, 465 and 480 °C respectively. The deposition chamber pressure was around 1.6 x 10^{-7} mbar and the substrate rotation speed was set to

5.0 rev/min. The fluxes used for this experimental run have not been optimized for Mo substrates but are the same as the standard fluxes used for Mo/SLG depositions. Table 3.4 details the fluxes for the individual elements in each stage of the coevaporation process.

(1st stage)

Substrate Temperature, T_1	400 °C
In Flux	6.3 nm/min
Ga Flux	5.3 nm/min
Duration	45 min

(2nd stage)

Substrate Temperature, T_2	400 ↗ 450 °C, 465 °C, 480 °C
Cu Flux	8.0 nm/min
Duration	41 – 46 min

(3rd stage)

Substrate Temperature, T_3	450 °C, 465 °C, 480 °C
In Flux	8.2 nm/min
Ga Flux	3.0 nm/min
Duration	23 – 29 min

Table 3.4. CIGS deposition parameters for three different absorber layers with varied 2nd and 3rd stage temperature using the 3-stage process. The first stages of each run have been kept constant.

The duration of the 1st stage is pre-set to 45min. the duration of the 2nd stage is determined by the time it takes to form a Cu-rich compound and then Cu_xSe phase which is semi-liquid and has a higher emissivity than the growing CIGS layer. This leads to a drop in the substrate temperature and is a good indicator of the end point of the 2nd stage as already described in Section 2.2.1. The duration of the 3rd stage is determined by the amount of time it takes to consume all of the Cu_xSe formed. The consumption of the Cu_xSe is accompanied by a rise in the substrate temperature since the growing layer goes from Cu-rich to stoichiometry and then finally to a Cu-poor CIGS layer. The end of the deposition is hence determined when the temperature stabilizes after the Cu_xSe binary

has been neutralized. This is the standard experimental 3-stage process used throughout this work unless otherwise stated.

- Absorber composition

The final composition of the CIGS absorbers in the three experimental runs were measured by XRF and are given in table 3.5.

$T_{2,3}$	450 °C	465 °C	480 °C
[Cu] (at. %)	19.8	21.8	20.5
[In] (at. %)	16.7	18.7	18.2
[Ga] (at. %)	10.2	10.9	9.1
[Se] (at. %)	53.3	51.3	50.7
[Cu]/([Ga]+[In])	0.74	0.74	0.75
[Ga]/([Ga]+[In])	0.38	0.37	0.33
2nd stage	41 min	46 min	44 min
3rd stage	23 min	25 min	29 min

Table 3.5. Summary of the deposition parameters and elemental compositions of the CIGS absorber deposited at 3 different substrate temperatures $T_{2,3}$ of the 2nd and 3rd stages.

The values recorded in table 3.5 show little variation in the Cu and Ga contents of the absorbers. The final slightly Cu-poor film was fairly constant in terms of the CGI ($0.74 \leq CGI \leq 0.75$) while the GGI was within the limits we expected ($0.33 \leq GGI \leq 0.38$). We deduce that regardless of the variation of $T_{2,3}$, the elemental compositions of the absorbers were fairly constant since the fluxes were the same. We might attribute the small variations between the three processes to uncontrollable variations in the deposition system associated with the ramping of substrate temperature, elemental source radiation and charge level in the crucibles.

- Absorber crystal orientation

The XRD measurements of each of the CIGS absorbers reveals 3 distinct peaks as seen in figure 3.8:

- Two peaks belonging to the Mo foil substrate. It is interesting to note here that the Mo peaks have a clearly defined and preferred orientation perpendicular to the (200) and (211) lattice plane while Mo sputtered on SLG (Mo/SLG) exhibits a preferred orientation perpendicular to the (110) lattice plane.
- A preferred CIGS orientation perpendicular to the (112) lattice plane. The (220)/(204) peak is not visible.

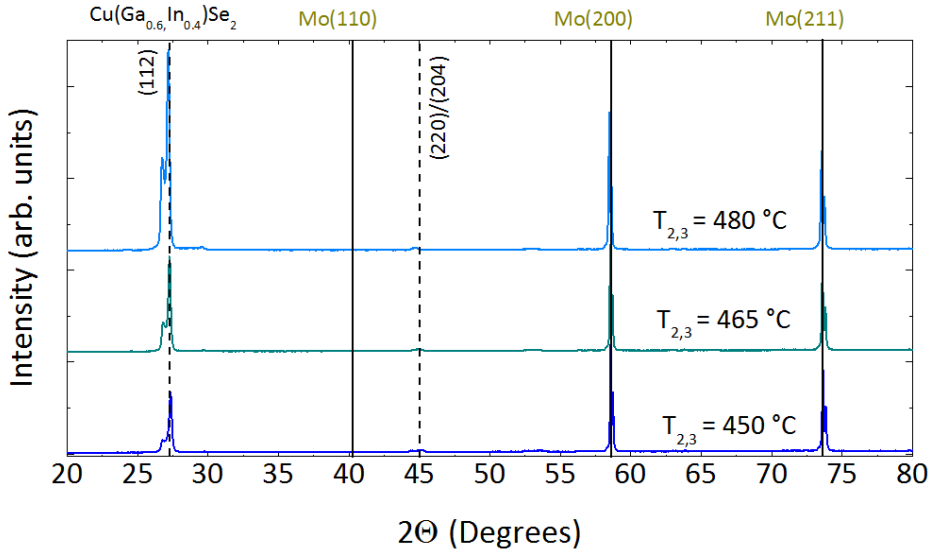


Figure. 3.8. XRD diffractogram of the CIGS absorbers with varying 2nd and 3rd stage temperature. The Mo orientation perpendicular to the (110) plane does not occur on the Mo foil substrate.

The strongly preferred orientation perpendicular to the (112) lattice plane of the CIGS film might suggest that the $(In,Ga)_2Se_3$ precursor formed during the first stage of the process was oriented perpendicular to the (006) lattice plane as this usually results in final CIGS absorbers growing perpendicular to the (112) plane. (220)/(204) perpendicular plane oriented CIGS films on the other hand are favored by (300)-oriented $(In,Ga)_2Se_3$ precursors [9].

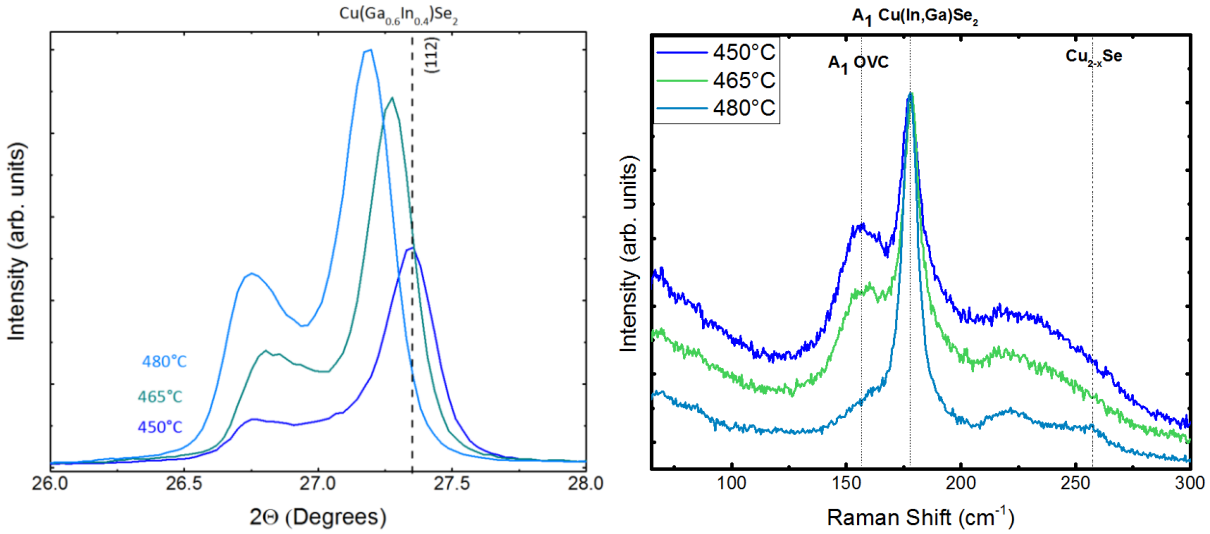


Figure. 3.9 (a) The (112) peak position for the samples with varying 2nd and 3rd stage temperatures. The dotted line is a guide for the eye and (b) the Raman spectra of the CIGS absorbers.

Figure 3.9(a) shows the position of the (112) Bragg reflection of the samples at 450 °C, 465 °C, and 480 °C. There is a main peak and a smaller shoulder between 2θ angle 26.7° and 27.2°. The main (112) peak corresponds to the $Cu(Ga_{0.6}In_{0.4})Se_2$ phase while the smaller shoulder is the Ga-poor $Cu(Ga_{0.3}In_{0.7})Se_2$ phase. As the 2nd and 3rd temperatures were increased from 450 °C to 480 °C, the Ga-poor CIGS peak intensity increases. Although we observe this trend, we cannot conclude that this is solely a function of the temperature as we do not have enough statistical evidence to support this. Furthermore, if we consider the GGI values of the films, the sample at 480 °C has the lowest GGI of 0.33. As seen in literature, the (112) XRD diffraction peak shifts to lower values for correspondingly lower GGI values [10] [11]. For the sample at 480 °C (GGI = 0.33), the (112) peak occurs at 27.1° compared to 27.4° for the sample made at 450°C (GGI = 0.38). Figure 3.9(b) presents the Raman spectra of the absorbers. Raman scattering allows us to observe the presence of Ordered Vacancy Compounds (OVCs) such as $Cu(In,Ga)_3Se_5$ or $Cu_2(In,Ga)_4Se_7$. The main A_1 OVC peak appears in the spectral region 150-160 cm^{-1} [12]. In figure 3.9(b), the appearance of OVCs is pronounced when the fabrication temperature is 450 °C. The main OVC Raman peaks reduces as the temperature increased. At 480 °C, there is no OVC peak occurring around 150 cm^{-1}. According to Witte *et al.* the OVCs are present in CIGS absorbers that are Cu-poor with a CGI less than 0.70 [13] however, we observe the OVC peaks for the sample fabricated at 450 °C and 465 °C. On the other hand, we do not observe the occurrence of a Raman peak at ~260 cm^{-1} which corresponds to the A1 mode of Cu–Se compounds like CuSe or Cu_2Se.

- Absorber elemental composition profile

In order to understand the profiling of the constituent elements across the bulk of the absorbers, we did some GDOES measurements on the samples which is shown in figure. 3.10. It is seen here that the substrate temperature in the 2nd and 3rd stages had an impact on the Ga content of the samples.

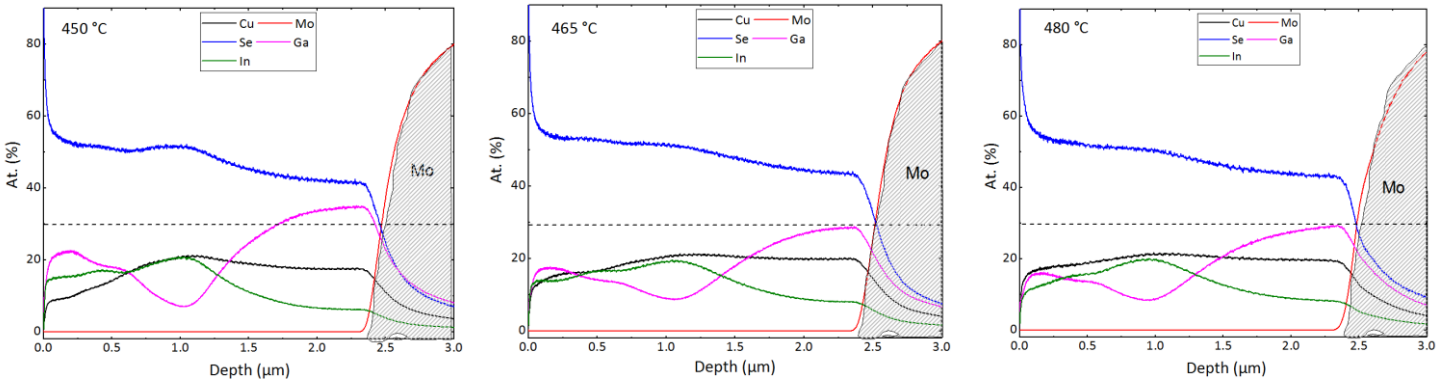


Figure. 3.10. Elemental composition profiling of the samples by GDOES. The dotted line is a guide and marks the 35% atomic concentration level

With reference to the dotted line which marks the 30% atomic concentration, the GDOES profile of the sample at 450 °C shows a large Ga concentration (34.6%) towards the back surface of the absorber (CIGS/Mo interface). On the other hand, the samples at 465 °C and 480 °C both have Ga concentrations of 28.5 % and 29.2 % respectively at the backside. The slope of the Ga profile is also steeper for the sample at 450 °C. An explanation for this might be the increased diffusion of Ga across the bulk at higher deposition temperatures. The Cu profile also appears smoother at higher temperatures than at a lower substrate temperature which is also the case for Se. A small ridge is seen in the Se profile at a depth of about 1 µm for the sample at 450 °C. This ridge is smoothened out when the temperature is elevated. Figure 3.11 is the GGI profile of the absorbers. The Ga content near the back contact is higher for the absorber made at 450 °C and almost identical for the samples at 465 °C and 480 °C respectively. The lower Ga-content of these samples can be ascribed to an improved Ga diffusion due to the higher processing temperature [14] [15]. Furthermore, the slope of the Ga content is much steeper at 450 °C and progressively reduces as the temperature increases up to 480 °C. Irrespective of the deposition temperature, the notch position of the samples was found at ~1.0 µm from the surface.

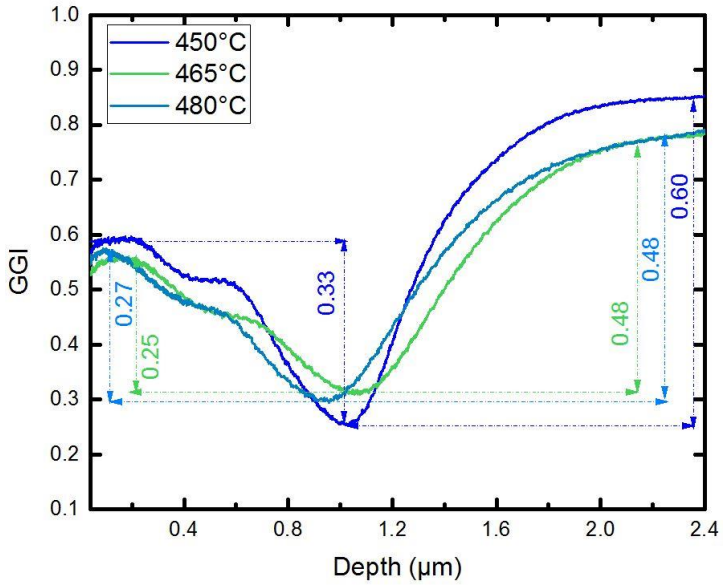


Figure. 3.11. Ga profile of the CIGS absorber fabricated at different temperatures.

- Impact of deposition temperature on the solar cell parameters

The samples were processed into solar cells by the deposition of a CdS buffer and then the window layer following the procedure and process parameters already described in section 2.3. Their current-voltage characteristics were measured under an illumination of 1 sun (1000 Wm^{-2}, AM1.5G). The values presented in table 3.6 are the maximum values obtained. As the substrate temperature increased, the Voc of the solar cells increased while the fill factor decreased. The low Voc observed on the samples is due to an absence of Na incorporation in the absorbers. The cell processed at a 480 °C achieved a maximum efficiency of 9.0 % regardless of the absence of Na treatment.

	Voc (mV)	***Eff (%)***	***Jsc (mA/cm^{-2})***	***FF (%)***
450 °C	512	8.9	29.2	59.3
465 °C	519	8.1	27.3	57.7
480 °C	530	9.0	30.5	55.5

Table 3.6 I-V parameters of the processed cells.

This was mainly due to a better Voc and Jsc compared to the other samples. Figure 3.11 is a plot of the efficiency of the cells with their respective error. The superior Voc observed might be due to the higher temperature which likely improved the recrystallization in the 2nd stage of the deposition resulting in less grain boundaries. Further evidence is required

to confirm this. Higher temperatures however are known to be beneficial for CIGS growth [16] [17]. Following these results, 480 °C was selected as the default deposition temperature in this work.

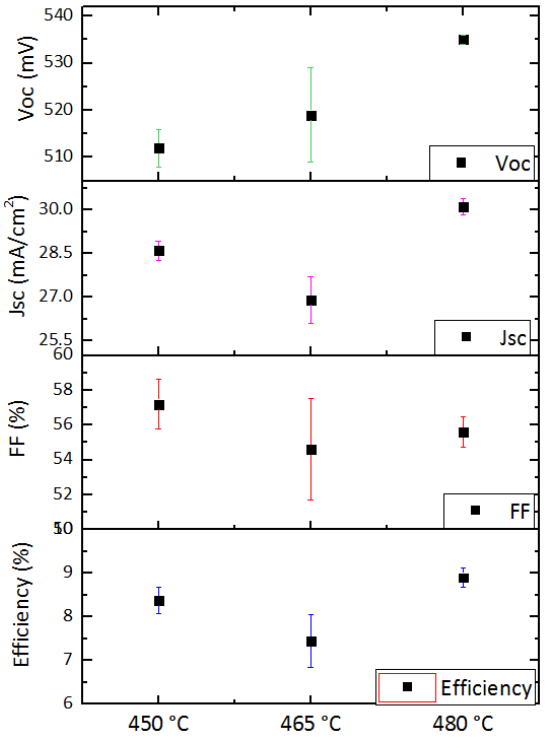


Figure. 3.11. Solar cell parameters of the samples processed at varying 2nd/3rd stage temperatures.

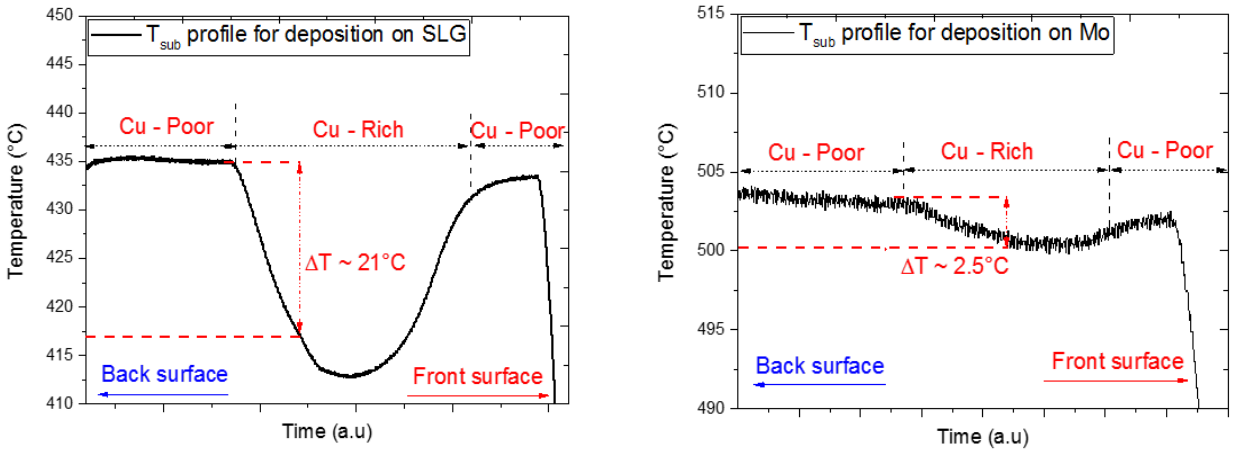
3.3 OPTIMIZATION OF CIGS ABSORBER COMPOSITION

Here we discuss the challenges and optimization of the deposition of CIGS on Mo using the standard process parameters enumerated above (optimized for SLG based depositions) in our lab. This process has not been optimized for depositions on Mo substrates. It is important to highlight the challenges encountered during the deposition process on Mo; challenges that so far seems peculiar to Mo substrate based CIGS absorbers. The challenges observed appear to be peculiar to the Mo substrate as other processes on SLG substrates do not exhibit the same trend. An approach to resolving these challenges is presented and the results discussed.

3.3.1 Challenges in determining the end-point on Mo substrates

The first challenge encountered while making $Cu(In,Ga)Se_2$ depositions on Mo foils is the difficulty in determining the exact end-point of the 2nd stage which should mark the

transition to the 3rd stage. For CIGS materials deposited on glass substrates, the temperature change in the 2nd stage is very distinct and easily seen on the process graph. However, it was observed that on Mo substrates, the temperature change after the formation of Cu_xSe was very small which led to difficulties in precisely determining the end-point of the 2nd stage. To put this in perspective, Figure 3.12 is a comparison of the process temperatures for depositions on glass and Mo foil.



(a) (b)

Figure. 3.12 CIGS growth temperature profile for $Cu(In,Ga)Se_2$ on (a)Glass and (b) Mo foil

For a deposition on glass, the transition from Cu-poor to the Cu-rich phase (formation of Cu_xSe) is accompanied by change in temperature (ΔT) of 21°C due to the formation of the Cu binary with higher emissivity than CIGS. On the contrary, in the case of Mo, a very small change (ΔT) is observed (~2.5°C). This small change is almost at par with the noise levels of the thermocouple hence making it difficult to determine the end of the second stage. In typical setup, a glass plate is placed on top of the flexible Mo foil to make it flat during CIGS coevaporation as shown in the schematic in figure 3.13.

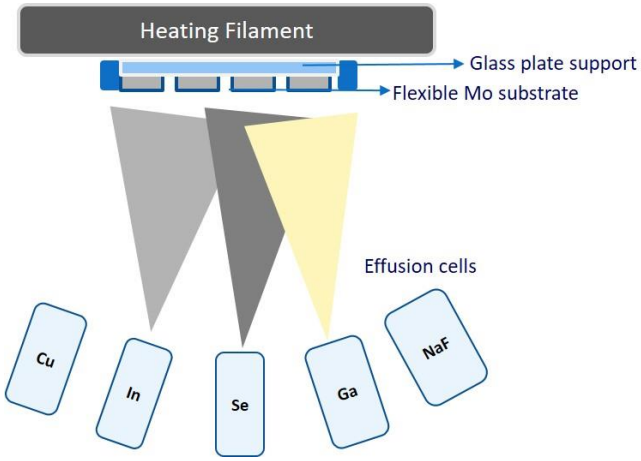


Figure. 3.13 Deposition schematic showing substrate back support using glass plates.

It was suspected that end-point detection issue might be due to the configuration of the setup, we tried different back plate setups using a 10 x 10cm Quartz plate and 10 x 10cm Mo plate with a thickness of 3mm, however, the results remained the same. An explanation can be given by considering the thermal conductivity Mo and its R-value which is roughly defined as its resistance to heat flow. Mo has a thermal conductivity, **λ**, of 142 W/mK while that of SLG is 0.92 – 1.05 W/mK. The R-value is then defined as;

$$R = {}^{l}/_{\lambda} \tag{3.1}$$

Where l is the thickness of the material being considered. In standard depositions, the thickness of the SLG substrate is 3 mm while the Mo is 0.15 mm thick. Hence, from equation 3.1, it can be easily deduced that the SLG substrate has an R-value that is 3 orders of magnitude greater than that of Mo. An implication of this is that Mo will heat up very fast to compensate for temperature changes during CIGS deposition. This makes it hard to observe small temperature fluctuations due to the formation of Cu_xSe binaries used in the end point detection. This challenge in accurately determining the end-point of the CIGS affects the reproducibility of CIGS experimental runs.

3.3.2 Optimization of CGI in the absorbers: Impact of the third stage termination step

It has been reported that the ideal compositional parameters recommended for high efficiency cells is 0.88 < CGI < 0.95 and GGI ≈ 0.3 [18]. There is however no consensus regarding the ideal CGI ratio required for high efficiency cells. This springs from the fact that new high efficiency results are widely spread over the CGI parameter field. Jackson *et al.* have reported cell efficiencies exceeding 19% with a CGI ≈ 0.70 and at the same time,

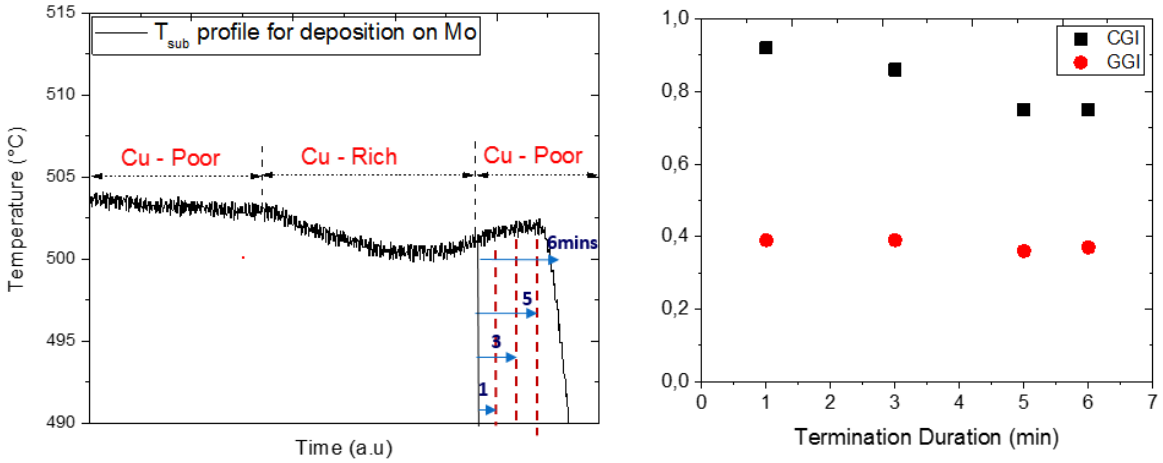
there have been cells with Cu composition approaching stoichiometry (CGI = 0.98) that still yielded efficiencies of 18.6% [18].

- ### Experimental setup

In section 3.2, the initial temperature experiments on Mo substrates using the standard process resulted in final CIGS absorber layers that were relatively Cu-poor (CGI ≈ 0.75). This cells were made without any alkali post-deposition and the efficiency was low reaching an average efficiency of 8.9% (max. 9.0 %) at 480 °C. Since it is possible to get better performing cells over a wide range of Cu compositions, we adjusted this process to yield higher CGI values on the Mo substrates. In general, for depositions on sodalime glass, the process is usually terminated approximately 6 min after reaching stoichiometry in the third stage of coevaporation. This 6-minute window is required to achieve a slightly Cu-poor film at the end of the third stage. In our case, we repeated the experimental procedure but shortened the termination step to 5, 3 and 1min respectively and then observed the evolution of the CGI (figure 3.14). The deposition temperature mentioned refers to the 2nd and 3rd stage substrate temperatures.

- ### Final absorber composition

Figure 3.14a is the deposition process graph which illustrates how the termination time at the end of the 3-stage is varied. The imposed deposition temperature is 480 °C but as can be observed in the process graph, the Mo substrate temperature measured by the thermocouple is higher (~504 °C). The graph is divided into 3 regions representing growth condition in each stage of the process. As explained in sec. 2.2.1, the process starts with a Cu-poor film which turns Cu-rich at the end of the 2nd stage and finally turns slightly Cu-poor in the 3rd stage. Figure 3.14b is the evolution of the CGI and GGI. The CGI and GGI values obtained by XRF measurements done on the final absorber layers.



(a) (b)

Figure 3.14 (a) Deposition temperature profile showing reduction of termination time steps after plateau formation (b) Evolution of CGI and GGI for each termination time step

The results presented show that the CGI can be adjusted by reducing the termination time of the 3rd stage after stoichiometry is achieved. The CGI increased from 0.75 for a time step of 6 minutes to 0.92 for a time step of 1 minute. The modification of this part of the CIGS deposition process has no effect on the Ga composition (GGI). It remained fairly constant (GGI ≈ 0.39). Table 3.7 summarizes the Cu and Ga compositions of the samples.

	T_{sub} (°C)	Termination (min)	CGI	GGI
mcigs06	480	6	0.75	0.37
mcigs07	480	5	0.75	0.36
mcigs08	480	3	0.86	0.39
mcigs09	480	1	0.92	0.39

Table 3.7 Elemental composition of samples with different 3rd stage termination times

- Final absorber morphology

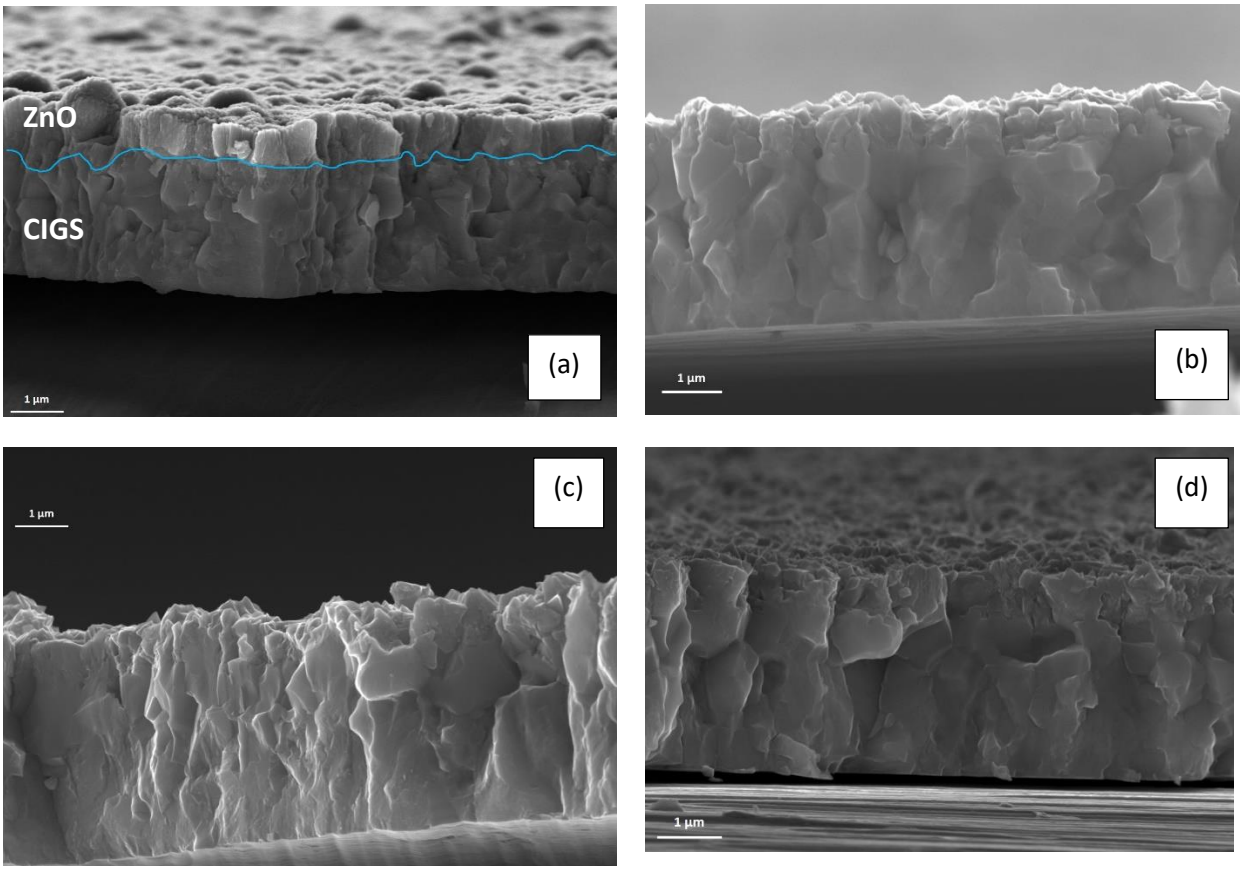


Figure. 3.15 SEM cross-section of the samples with varying CGI values corresponding to the different termination time after 3rd stage plateau formation (a) 6mins (b) 5mins (c) 3mins (d) 1min. Note that (a) has the CdS buffer and window layer deposited already, the boundary is marked by the blue line. However, at this zoom level, it difficult to see the CdS layer.

The cross-sectional morphology of the samples were analyzed by SEM and shown in figure 3.15. The samples terminated at 3 and 6min (figure. 3.15a and 3.15c) reveal small grain sizes especially towards the back side of the absorber. The grains are fused with no distinctive grain boundaries. However, the samples terminated after 1 min and 5 min (fig. 3.15b and 3.15d) have slightly larger grain sizes. The differences in the Cu composition does not seem to have an effect on the surface morphology as there is no observable trend in the morphologies of the samples. Noticeably, the sample with a 3min termination has poorly formed CIGS grain sizes among the others. It is mostly dominated by tiny grains that are lumped together.

In order to have a better idea of the evolution of the structure of the samples, Raman measurements were performed (figure 3.16). Raman spectroscopy give supplementary information on the CIGS such as the presence of Ordered Vacancy Compounds (OVC). In

figure 3.16, the A_1 CIGS mode for the samples occurs at a Raman shift of 177 – 178 cm^{-1} which is typical for films with GGI ≈ 0.3. [13].

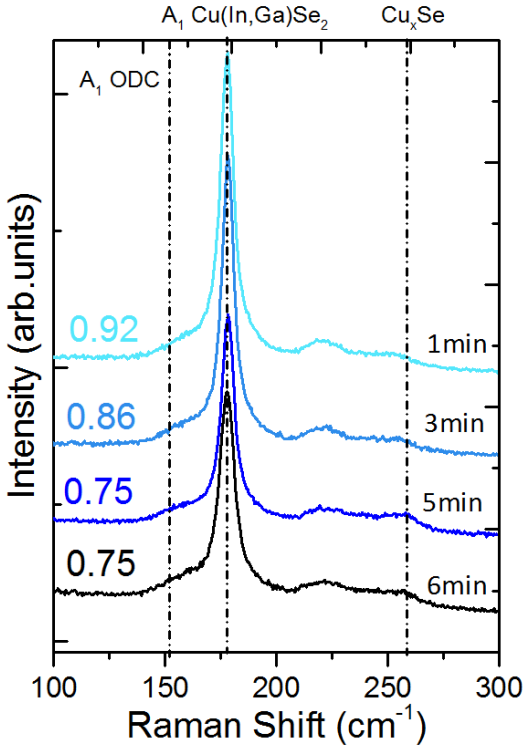


Figure. 3.16 Raman measurements of samples with varying 3rd stage termination time with their respective CGI

For samples with CGI > 1, the Raman shift of 260 cm^{-1} is assigned to the A_1 mode of Cu–Se compounds like CuSe or Cu_2Se and is labeled with Cu_xSe in fig 3.17 [19]. However, we observe no Cu_xSe binaries on all of the samples. This is expected as the Cu_xSe phase exists when the final absorber is above stoichiometry (CGI≥1) [13]. Since our samples have CGI in the range 0.75 – 0.92, we also do not observe the shoulder broadening at 150cm^{-1} due to OVCs [20] [21]. The broadening due to OVCs becomes visible when the CGI drops below 0.74 [13]. The result thus indicates that adjusting the termination step at the end of the 3-stage of the deposition does not give rise to OVCs nor Cu-Se binaries.

- ## Electrical properties of the finished solar cells

The individual samples were completed into cells and the IV characteristics were measured under an illumination of AM1.5G. The electrical properties showing the best performing cells are summarized in table 3.8 below.

	Termination (min)	CGI	Eff (%)	Voc (V)	Jsc (mA/cm²)	FF (%)
mcigs06	6	0.75	8.7	0.53	29.2	55.5
mcigs07	5	0.75	8.8	0.52	27.9	61.0
mcigs08	3	0.86	8.9	0.50	28.8	62.4
mcigs09	1	0.92	9.5	0.51	28.6	65.0

Table 3.8 Electrical properties of samples with different 3rd stage termination times

The efficiencies of the cells progressively increases with an increase in the CGI and a decrease in the termination time of the 3rd stage. A maximum efficiency of 9.5% was achieved for the cell terminated after 1min (CGI = 0.92). The increase in the Efficiency is mainly due to an increase in FF from 55.0 % (CGI = 0.75) to 65.1 % (CGI = 0.92) while the Jsc and Voc remained constant. The results reveal that we are able to optimize the CGI of our films by adjusting the duration of the 3-stage. We improved the CGI from 0.75 to 0.92 with no addition of Na. Hence, for subsequent CIGS absorber depositions, once stoichiometry is reached in the 3rd stage, we limit the termination time to 1min to correspond with the results above.

3.4 ALKALI DOPING OF CIGS LAYERS BY NAF POST DEPOSITION TREATMENT (PDT)

Hedstrom et al. [22] reported that the crystalline structure and device performance of CIGS absorber developed on soda lime glass (SLG) substrate is significantly better than that developed on borosilicate glass and other substrates. The reason for this phenomenon is the intrinsic incorporation of sodium (Na), which increases the open-circuit voltage (V_{OC}) and the fill factor (FF), and therefore increases device efficiency [23]. Na occurs naturally in sodalime glass and during CIGS fabrication, the Na in the SLG diffuses through the Mo back contact and into the growing CIGS film. In our case however, the Mo substrate is Na-free. Hence to compensate for this deficit, we have to incorporate Na externally. This is done by the post-deposition of NaF. This deposition step is done at the end of the 3-stage process after the final absorber has been obtained.

It is generally agreed that the effect of alkali doping is to passivate defects at the CIGS grain boundaries and donors without affecting the absorber crystallinity [23] [24]. Indeed, several models have been developed to explain the passivation effect of Na. These include the passivation of defects at grain boundaries due to the enhancement of the oxidation of Se vacancies [25] , elimination of In_{Cu} defects [26] and the introduction of a shallow acceptor defect [27]. Another study reported that when Na is present in small quantities, it forms defects on Cu (Na_{Cu}) and In (Na_{In}) sites. The Na_{In} creates acceptor levels that are shallower than Cu_{In} defects with the dominant effect of a direct substitution of Na_{InCu}. Thus in small concentrations, Na eliminates In_{Cu} defects hence effectively increasing the hole density [28]. This typically lowers the Fermi level energy and remove carrier traps which leads to an increase in the Voc.

It has also been reported that alkaline elements mainly segregate at grain boundaries and only a small portion is incorporated into the CIGS grains [26]. It has further been demonstrated that Na increases the hole concentration in the CIGS absorber. In Na-free substrates (no PDT), the typical hole concentration in CIGS is about 10^{14} cm^{-3}, however, by incorporating Na via a post deposition process, the hole concentration can be increased by 2 orders of magnitude [26]. It is possible to estimate the increase in the Voc due to an increase in hole concentration using the expression:

$$\Delta Voc = \frac{k_B}{q} \mathrm{T} \ln\left(\frac{N_{NaF\ PDT}}{N_{No\ PDT}}\right) \tag{3.2}$$

Where k_B is the Boltzmann constant, T is the temperature, q the charge. The values of $N_{NaF\ PDT}$ and N_{noPDT} are obtained from measurements and are given as $N_{NaF\ PDT} = 8 \times 10^{15}$ cm^{-3} and $N_{noPDT} = 1 \times 10^{14}$ cm^{-3}. These are the hole concentrations in the device with NaF PDT and without PDT [26]. The expression in equation 3.2 leads to an expected increase in Voc of 110mV.

While it is agreed that the dominating effect of Na is the same regardless of the incorporation technic, it should be noted however, that the presence of Na during the CIGS growth influences a change in the microstructure and optoelectronic properties of the absorber. This was confirmed in [23] where the presence of Na during growth impedes the inter-diffusion of In and Ga. Rudmann *et al.* further reported the difference between PDT and Na diffusion through SLG substrate [29] [30]. It was reported that when Na diffuses into the CIGS layer from the SLG at a low substrate temperature of 400 °C, the cell properties deteriorate but these low temperature condition favored Na incorporation via

PDT and resulted in the best efficiency. However, as the substrate temperature is increased, the diffusion of Na from SLG yielded superior cell performances than Na PDT. It is however, hard to compare the absorbers made at high temperature due to the fact that Na influences the inter-diffusion of In and Ga and hence will result in a bandgap grading that is different for the PDT and SLG samples.

3.4.1 NaF post-deposition treatment (PDT) process

The CIGS absorbers used were deposited using the standard 3-stage process. The absorber films were grown on Mo substrates at our standard imposed substrate temperature of 480°C while adopting the 1mn termination step descried above and using the standard process parameters. For the NaF post-deposition, the substrate temperature is ramped down to 350°C. The flux of the NaF is set to 2.0 nm/min. Se is always present during the post-treatment. For each sample treated with NaF, the duration of exposure to the NaF flux is done for 10, 20 and 30minutes respectively. At the end of the evaporation of NaF, the samples are further annealed under a constant flux of Se at 350°C for 10 minutes before the temperature is ramped down to 250°C and then allowed to cool down to 150°C in the absence of Se. The cells are hence labeled Na10/Se10, Na20/Se10 and Na30/Se10 for the 10, 20 and 30 minutes of NaF evaporation respectively. The reference cell deposited in the same run as is labeled “no Na” (see table 3.9)

Substrate Temperature, T	350 °C
NaF Flux	2nm/min
Se Flux	57 - 61 nm/min
Duration	0, 10, 20, and 30 min
Annealing in Se atmosphere	10 min

Table 3.9 NaF Post-Deposition treatment parameters

3.4.2 Material and electrical characterization of the samples

The composition of the absorbers, [Cu]/[In]+[Ga] and [Ga]/[Ga]+[In] were estimated by X-ray fluorescence (XRF) while the Ga gradient across the entire bulk and the depth composition profile of the absorber was measured using Glow Discharge Optical Emission Spectroscopy (GD-OES) on a Horiba Jobin-Yvon instrument. The structure of the films were determined by X-ray diffraction analysis (XRD) on a PANalytical *Empyrean*

instrument. The opto-electronic cell properties of cells (Jsc, Voc, Eff and FF) were characterized by current-voltage (I-V) measurements under AM 1.5G illumination at 25°C. The external quantum efficiencies (EQE) were measured using an IQE200 Newport instrument. The performances of these cells are compared with that of the reference cell (no NaF post treatment).

- Effect of NaF PDT on the absorber composition

Whatever conditions used for NaF deposition and Se-post treatments, no real change in the global GGI of the absorbers is observed. However the CGI for all the samples with Na incorporation is slightly lower than the reference cell without Na. Na10/Se10 and Na20/Se10 both had a CGI of 0.83 while the CGI of Na30/Se10 decreased further to 0.80.

	CGI	**GGI**
No Na	0.92	0.39
Na10/Se10	0.83	0.37
Na20/Se10	0.83	0.34
Na30/Se10	0.8	0.4

Table 3.10 Elemental composition of samples with NaF PDT measured by x-ray fluorescence (XRF)

Table 3.10 shows the variation of the composition of the samples as measured by XRF. It has been reported that the addition of alkali (NaF/KF) leads to Cu depletion of the surface composition [31] [32]. This can explain why the samples with NaF treatment had a lower CGI than the reference cell with no post treatment of NaF.

- Effect of NaF PDT on the absorber structure

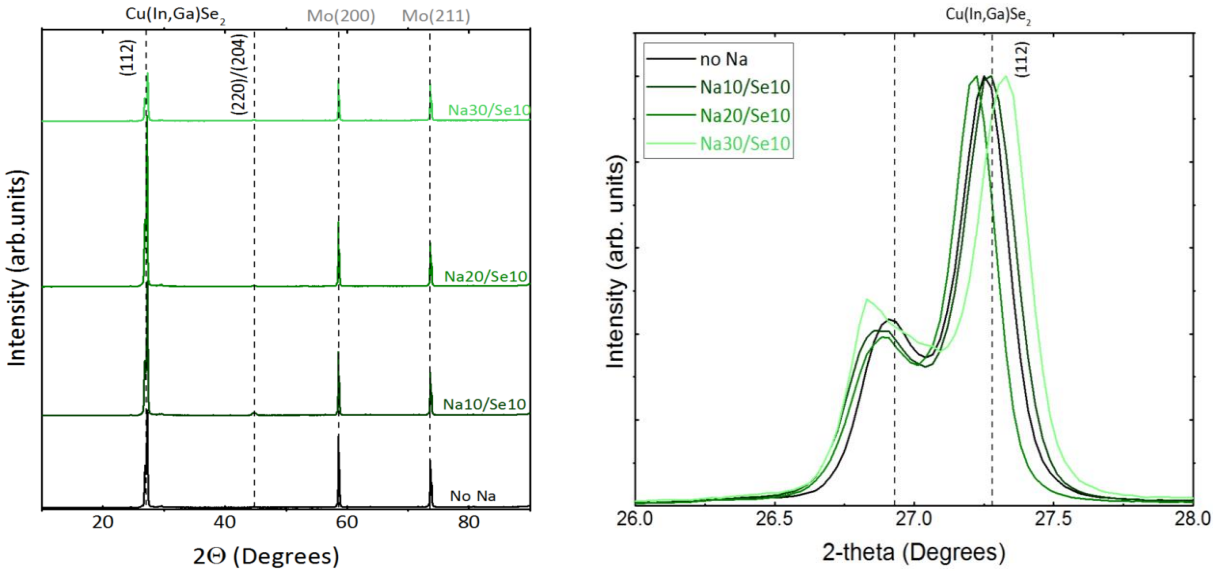


Fig. 3.18 XRD patterns of samples with different Na post-deposition treatment times: (a) Diffractogram (b) CIGS orientation perpendicular to (112) plane lattice

The XRD patterns of the samples revealed the slight variation of the GGI in figure 3.18. The double-peak reflection can be attributed to varying [In]/[Ga] ratios which translates to a separation of CIGS phases [30]. The two CIGS phases, identified here by comparing with the CIGS definition file 00-035-1102, are $CuGa_{0.3}In_{0.7}Se_2$ occurring at 2θ=26.9° and $CuGa_{0.6}In_{0.4}Se_2$ at 2θ=27.3°. The appearance of these double peaks is due to the inhomogeneous Ga grading in the sample arising from the 3-stage process [30]. Results from the x-ray diffraction patterns also showed that the preferred orientation is perpendicular to the (112) lattice plane regardless of NaF post treatment. The (220)/(204) peak is barely visible. The result shows that Na does not modify the absorber grain size and/or orientation thereby confirming what has been previously reported about the post-deposition of Na by Rudmann et al [29].

- Effect of NaF PDT on the absorbers' electrical properties

Table 3.11, figure 3.19 and 3.20 summarizes the electrical parameters and performances of each of the samples as a function of Na post-treatment conditions. The I-V measurements of the various samples showed the beneficial effect introduced by the incorporation of Na via the post deposition treatment of finished absorbers with NaF. The most significant improvement in the cell performance of the samples with NaF PDT was

observed in an increase in the Voc and FF leading to higher efficiencies. Table 3.6 summarizes the electrical parameters of each of the samples. The values presented are the maximum obtained values for each sample.

	Eff (%)	Voc (V)	Jsc (mA/cm²)	FF (%)
No Na (Ref)	10.3	0.51	31.1	65.2
Na10/Se10	13.1	0.59	31.5	70.5
Na20/Se10	13.5	0.6	31.8	70.4
Na30/Se10	12.9	0.6	28.1	68.8

Table 3.11. Summary of electrical properties of samples with NaF post-deposition treatment

The Voc increases by ~90 mV for the samples with NaF post-deposition [26]. However the cell with higher NaF exposure has a slightly lower FF. For a longer NaF deposition time, the FF and Jsc both decrease [33]. The improvement in the Voc and FF can be attributed to an increase in the net carrier concentration and a decrease in resistivity of the CIGS by 1 – 2 orders of magnitude [34].

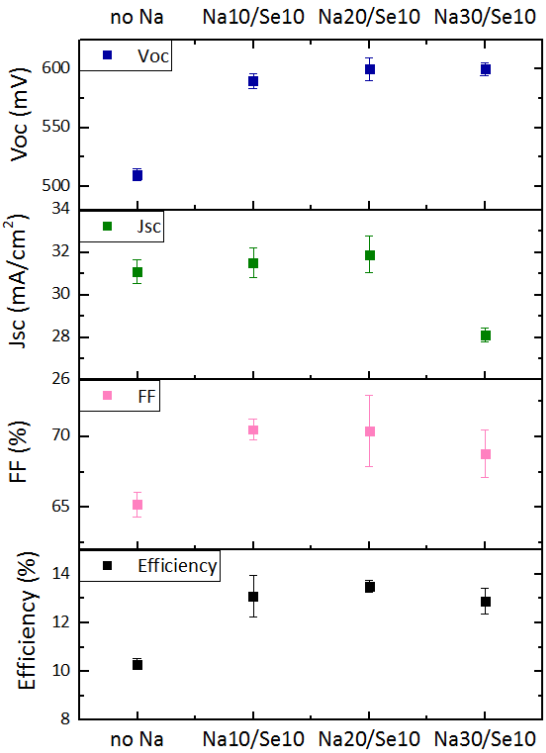


Figure. 3.19 Summary of electrical properties of the cells with different NaF PDT scheme

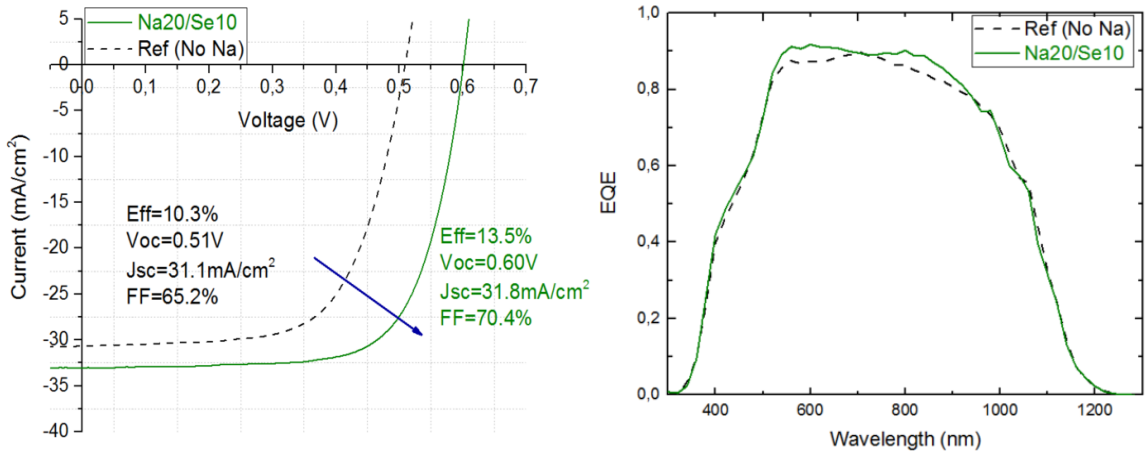


Fig. 3.20 (a) I-V curve comparison of best cell with Na incorporation vs Ref (no Na) (b) EQE curve for both samples

The results show that Na incorporation has no impact on the short circuit current however, it greatly influences the open circuit voltage and fill factor of the cells leading to better performances. An explanation for the observed increase in the Voc has been given above as various studies have reported on this effect. The new developed sample with adequate Na incorporation (Na20/Se10) is adopted as a standard reference for subsequent depositions on Mo.

3.5 GALLIUM GRADING

A major factor that significantly influences the quality and performance of CIGS solar devices is the Ga gradient across the cell. Typically, using a 3-stage process introduces a Ga gradient across the CIGS absorber due to the varying fluxes of Ga/In in each stage of coevaporation and also due to the slow diffusion rate of Ga. Ideally, the Ga gradient can be tuned in such a way that it brings beneficial effects. A CIGS absorber fabricated by a 3-stage process usually has 3 distinct zones of varying Ga content which extends from the back to front of the absorber. In the first stage, In, Ga and Se are coevaporated and taking into consideration the slow diffusion rate of Ga, we obtain a high Ga content near the back contact of the absorber. In the second stage, Cu is coevaporated alongside Se while the fluxes of In and Ga are turned off. This leads to a region of low Ga content and is usually situated in the bulk of the absorber close to the surface. In the final stage, Cu is shut off while In and Ga are further coevaporated to obtain a final slightly Cu-poor film. The Ga gradient in this region is higher than that in the middle section but usually lower than the

Ga content close to the back contact. Figure 3.21 is a typical Ga profile in a CIGS cell and it illustrates the three most important zones of varying Ga content.

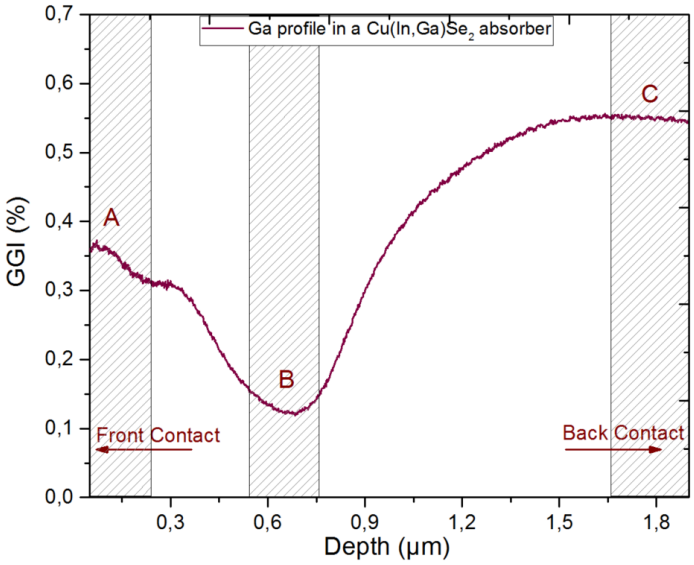


Fig. 3.21 Ga gradient profile of a CIGS absorber fabricated by a 3-stage process on Mo foil

Region A is also referred to the front grading of the CIGS absorber. This region of relatively higher Ga content has some benefits to the performance of the CIGS material. It has been reported that the higher Ga content close to the front surface results in an increased Voc due to the widening of the bandgap in the space charge region (SCR) [35] and since the dominant part of recombination occurs in the space charge region, locally increasing the bandgap in this region can reduce the recombination [36]. The higher bandgap close to the surface might also play a role in improving the quality of the CIGS/CdS interface by introducing a better bandgap matching between the two materials although this remains unclear as high efficiencies have been obtained with flatter and with steeper Ga profiles near the CdS buffer interface [37]. **Region B** otherwise called the "notch" typically occurs inside or close to the space charge region. A low Ga content in this region invariably leads to a lower bandgap which has the beneficial effect of increasing the photocurrent density due to better absorption of low energy photons [38] [37]. **Region C** occurs at the back contact interface and is called the back grading. The higher Ga content at the back of the absorber occurring at the CIGS/Mo back contact interface plays a passivating role by creating back-surface field which repels minority carriers thus reducing recombination at the back contact [39].

3.5.1 SAMPLE PREPARATION

In the context of our study, the effect of the GGI on cell performance is considered. In order to study only the effect of the Ga gradient close to the surface of the cell, the first and second stages of the 3-stage deposition process were kept constant and only the Ga flux in the third stage was varied in order to modify the front surface as well as the position of the notch. For comparison, we use the standard reference cell recipe obtained from the NaF PDT optimization (table 3.12).

(1st stage)

Substrate Temperature, T_1	400 °C
In Flux	6.3 nm/min
Ga Flux	2.7 nm/min

(2nd stage)

Substrate Temperature, T_2	400 ↗ 480 °C
Cu Flux	8.0 nm/min

(3rd stage)

Substrate Temperature, T_3	480 °C
In Flux	7.5 nm/min
Ga Flux	2.0, 2.5 nm/min

Table 3.12. Process parameters for the absorbers with Ga grading.

3.5.2 ABSORBER MATERIAL CHARACTERIZATION

- Absorber composition

X-ray fluorescence (XRF) measurements of the composition of the CIGS absorbers revealed a systematic decrease in the GGI as a function of the Ga flux during deposition (table 3.13). The reference cell has a GGI of 0.34 while mcigs030 ($C_{0.28}$) and cell mcigs039 ($C_{0.24}$) with modified Ga gradients have GGI ratios of 0.28 and 0.24 respectively. The CGI of the absorbers however remained constant. The evolution of the Ga composition is visualized in figure 3.22.

	3rd stage Ga flux (nm/min)	CGI	GGI
Ref	3.0	0.83	0.34
mcigs030 ($C_{0.28}$)	2.5	0.84	0.28
mcigs039 ($C_{0.24}$)	2.0	0.83	0.24

Table 3.13. [Ga]/([Ga]+[In]) of the absorbers with varying 3rd stage Ga flux.

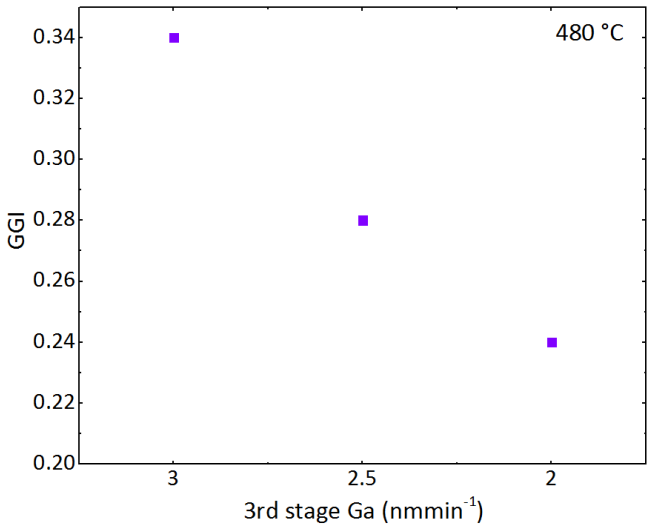


Fig. 3.22. Evolution of the GGI with respect to a variation of the Ga flux in the 3rd stage of the deposition process

- Absorber morphology

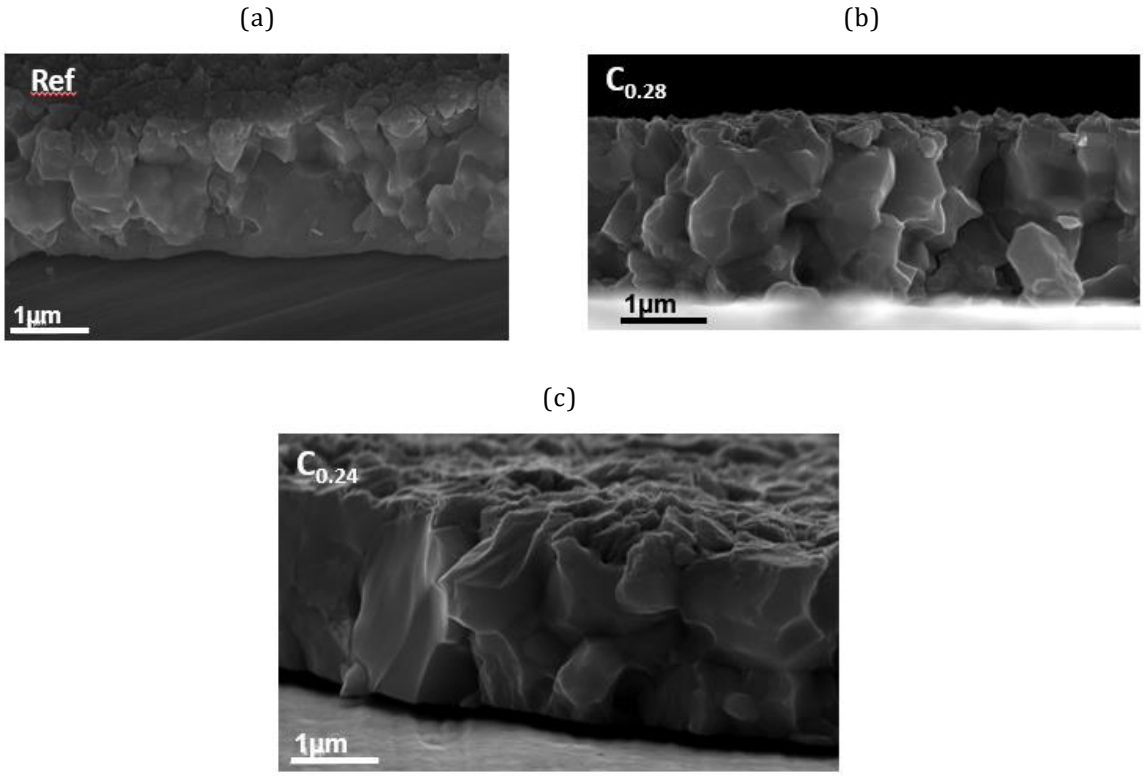


Fig. 3.23 SEM cross-section of the absorber layers: (a) Reference cell (Ga – 3.0 nmmin^{-1}); (b) $C_{0.28}$ (Ga – 2.5nmmin^{-1}) and (c) $C_{0.24}$ (Ga – 2.0 nmmin^{-1}).

Figure 3.23 is a cross section SEM image of the samples showing their individual morphology. $C_{0.28}$ ([Ga]/([Ga]+[In]) = 0.28) has larger grains compared to the reference cell although the grains are smaller than that observed in $C_{0.24}$ ([Ga]/([Ga]+[In]) = 0.24). $C_{0.24}$ presents sufficiently large grain sizes extending from the back side to the surface of the absorber. Comparing this with the respective GGI of the absorber and the Ga gradient (figure 3.24a), the trend show that smaller grains towards the back surface of an absorber is favored when there is a high Ga concentration in this region of the absorber layer. In fact, it has been reported that small grain sizes in absorber layers are usually observed when the [Ga]/([Ga]+[In]) content towards the Mo back contact is enhanced [14] [40] [5].

- Ga grading in the absorber layers

A special quality of CIGS material is its variable bandgap, which can be changed by varying the Ga/(In+Ga) ratio. This quality can be used not only to optimize the general bandgap level, but to obtain different band gap at different depths in the CIGS absorbers. The most efficient Ga gradient configuration is the V-shape configuration that consists of a front and

back contact grading. The bandgap gradient at the back contact fixed such that it assists carrier collection in the absorber by repelling electrons from the recombining back contact, and thus improve fill factor. The front contact grading is set to have a high open-circuit voltage, combined with a good short-circuit current density. The high open circuit voltage is due to a decrease in interface (or space-charge region) recombination due to a higher bandgap at the Cu(In,Ga)Se_2/CdS interface. A good short-circuit current density is maintained due to a smaller bandgap region in the absorber. Front grading is thus highly desirable. However, the bandgap grading has to be controlled in order to avoid the formation of a notch (difference between minimum and maximum bandgap) that is too deep or pronounced. Figure 3.24 (left) shows the evolution of the Ga gradients across the absorber bulk measured by GD-OES. The modification of the front surface GGI profile results in a shift of the notch closer to the surface and the Space Charge Region (SCR). The notch position of $C_{0.24}$ sample is 0.66µm from the surface while $C_{0.28}$ is 0.58 µm from the surface. By comparison, the notch of the reference cell lies deeper in the CIGS bulk at a distance of 0.77 µm from the surface. The notch positions of the modified samples can permit the generation of charges closer to the SCR which in turn enhances charge collection due to the electric field. This corresponds to literature reports that the position of the notch has an effect on the collection and can reduce SCR recombination [40].

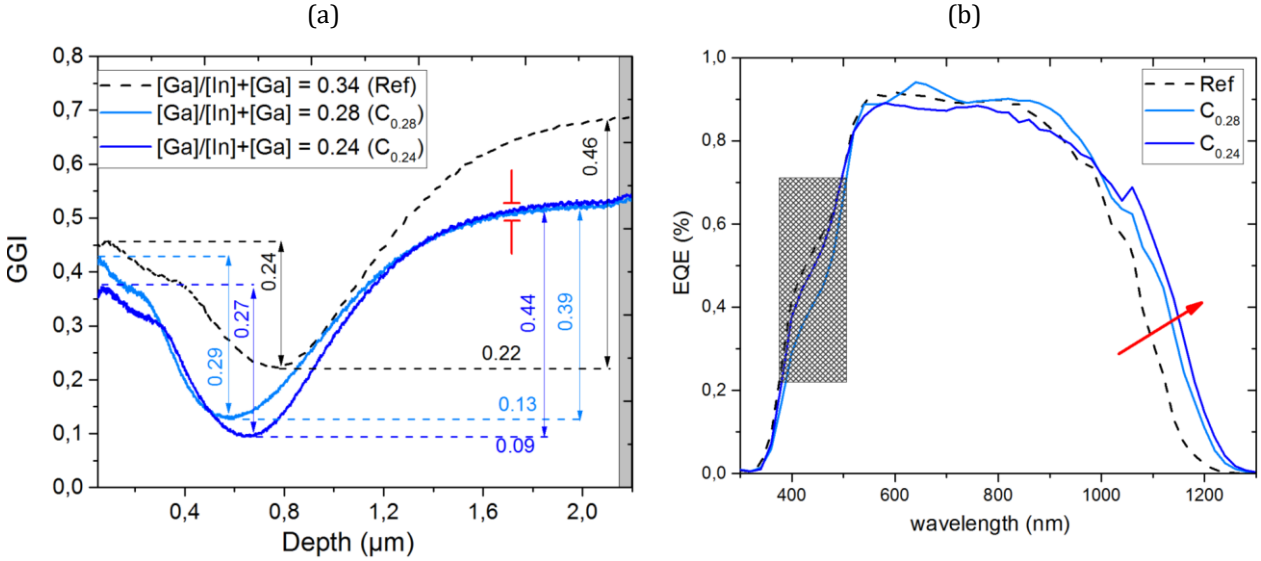


Fig. 3.24. (a) GGI profile across the bulk of the absorbers measured by GDOES and (b) EQE response of the completed cells

Cells up to 22 % have been achieved by keeping the notch position a few microns from the CdS/CIGS interface [37]. The Ga profile towards the back contact of the modified

samples are identical since the fluxes were identical in the first stage of the process. The reference sample has a much higher Ga content in this region. The modified samples also have a deeper notch than the reference pointing to a lower bandgap in this region. In many $Cu(In,Ga)Se_2$ films, composition gradients leading to a band gap gradient, also affect the steepness of the long-wavelength part of the EQE curve. This observation is also evident in the EQE measurements of the samples (figure 3.24a) as the absorption increases in the higher wavelength region of the incident photons. This difference in bandgap is believed to enhance the absorption of low energy photons [41]. The EQE of $C_{0.24}$ slightly surpasses that of $C_{0.28}$ and the difference can be seen in the measured *J*sc of the samples (table 3.14).

	GGI	Eff (%)	*V*oc (V)	*J*sc (mA/cm^{-2})	FF (%)
Ref	0.34	13.5	0.60	31.8	70.4
$C_{0.28}$	0.28	12.9	0.59	32.2	67.7
$C_{0.24}$	0.24	14.0	0.58	34.2	70.4

Table 3.14 Electrical properties of samples with modified Ga gradient

We obtained a current gain of +2.3 mAcm^{-2} when comparing the best cell ($C_{0.24}$) with the reference. It is also observed that there was a slight drop in the Voc as the GGI reduced, however, we were able to reach a maximum recorded efficiency of 14.0 % on Mo substrates with a modification of the Ga gradient. The double-grading in the absorber has the advantage of reduced recombination at the back contact due to the higher band gap and the gradient also directs minority charge carriers (electrons) towards the space-charge region for collection [37].

The grayed out area in figure 3.24(b) is a region impacted by light absorption of the CdS buffer layer. The differences in absorption seen in this area is due to slight variations in thickness of the CdS layer. Although, care is taken to deposit the same thickness of CdS, uncontrollable run-to-run experimental variations might result in varying thickness of the buffer layer. The variation is low and the growth of the CdS also depends on the absorber surface. As the GGI at the surface of the CIGS is modified, the CdS growth speed and thickness is also affected. Since a new all-time efficiency of 14 % was obtained after this experiment, we adopted this new process as the standard optimized process for depositions on Mo substrate.

- ## Effect of the modified Cu(In,Ga)Se_2 on the CdS buffer layer deposition time

As discussed above, the CdS deposited on the absorber layers did not have the same thickness as observed by the variation of EQE of samples at low wavelength. (Figure 3.15b). A CdS buffer that is too thick will result in short circuit current losses in the cell as the absorption taking place in the CdS layer is not converted. However, the CdS layer also creates and improves the junction properties at the CdS/CIGS interface if properly optimized leading to the improvement in Voc and FF. The thickness of the CdS is usually optimized to compensate for the optical and electrical effects imposed by the buffer layer [42]. In our case, the modified CIGS process used to obtain the Ga grading in the absorber (sec. 3.3.1) also led to a modification of the growth kinetics of the CdS layer. In order to confirm this hypothesis, CdS buffers layer were deposited at the same time on a CIGS absorber layer (standard process) and on a second absorber layer (with a modified process) where both absorbers have been deposited on Mo substrates. For each absorber, 4 deposition times were tested and their effect on the EQE response were compared. Four samples each of both absorbers were placed into a CdS deposition bath where the deposition time was varied between 1m30s – 5m20s at a bath temperature of about 60 °C. Figure 3.25 is a picture of the surfaces of the absorbers for each CdS duration. The figure is just a visual guide showing the growth of the CdS on both substrates and the differences therein.

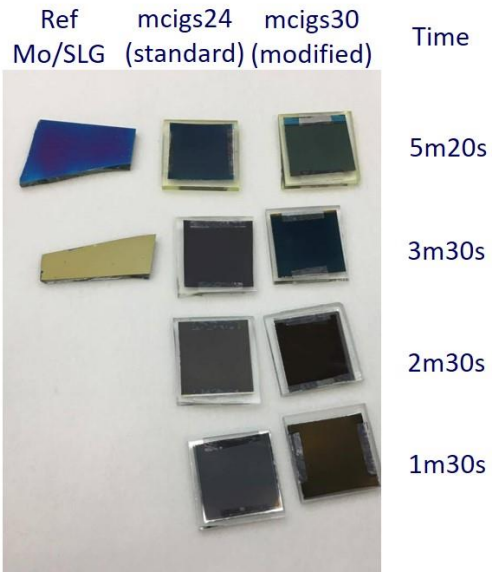


Fig. 3.25. Picture showing the different color shades on the absorbers corresponding to the deposition time of CdS. The reference is a Mo/SLG substrate which is used as a control.

The reference glass/Mo samples (control substrate) give an indication of the end of the deposition process through a color change to blue. Typically, the standard duration for CdS deposition (for a thickness of around 50 nm on the standard absorbers is around 5 min. For CIGS solar cells, the change of the color of the absorber after CdS deposition can give an indication of the evolution of the thickness of the buffer layer. As observed in figure 3.25, for the absorbers with a modified process, a color change is observed already after a CdS deposition time of 1m30s which indicates that the CdS growth has started. For the standard CIGS absorber however, at 1m30s no visible change in the color of the absorber is noticed. The standard samples starts to undergo a color change for a CdS deposition time around 3m30s. At 5m20s, the sample with the modified process starts to turn yellowish while the standard sample has a bluish shade as expected.

The EQE response of the samples were also measured as a function of the CdS deposition time. Figure 3.26 shows how the CdS deposition time impacts the EQE of the cells. In figure 3.26a and b, two regions are to be considered;

- The short wavelength region (~300 – 500 nm) – for both samples, it is observed that the longer the deposition time (thicker CdS), the greater the loss in absorption in this region. This is due the parasitic absorption of light in the CdS buffer layer at wavelengths below ~520 nm to corresponding to the CdS band gap 2.42 eV. The loss in EQE for $\lambda < 500$ nm is proportional to the CdS thickness since it is commonly assumed that electron–hole pairs generated in the CdS are not collected. However, at least a 50nm thick CdS layer is required for optimal performance of the cells. When the CdS layer is too thin, substantial losses in Voc and FF occur [43].
- The long wavelength region (~600 – 1200nm) – In this region, there is a big loss in the spectral responses of the cells for a CdS deposition time of 1m30s for the standard cells. For the modified cells, the loss in spectral response is lower, however the response at 1m30s and 2m30s are still poor. This change of EQE for wavelength > 500 nm can be explained by a too thin CdS buffer layer leading to the decreased collection at the CIGS/CdS interfaces. As reported in [42], devices with a very thin CdS layer experience a deterioration of the spectral response over the entire wavelength spectrum.

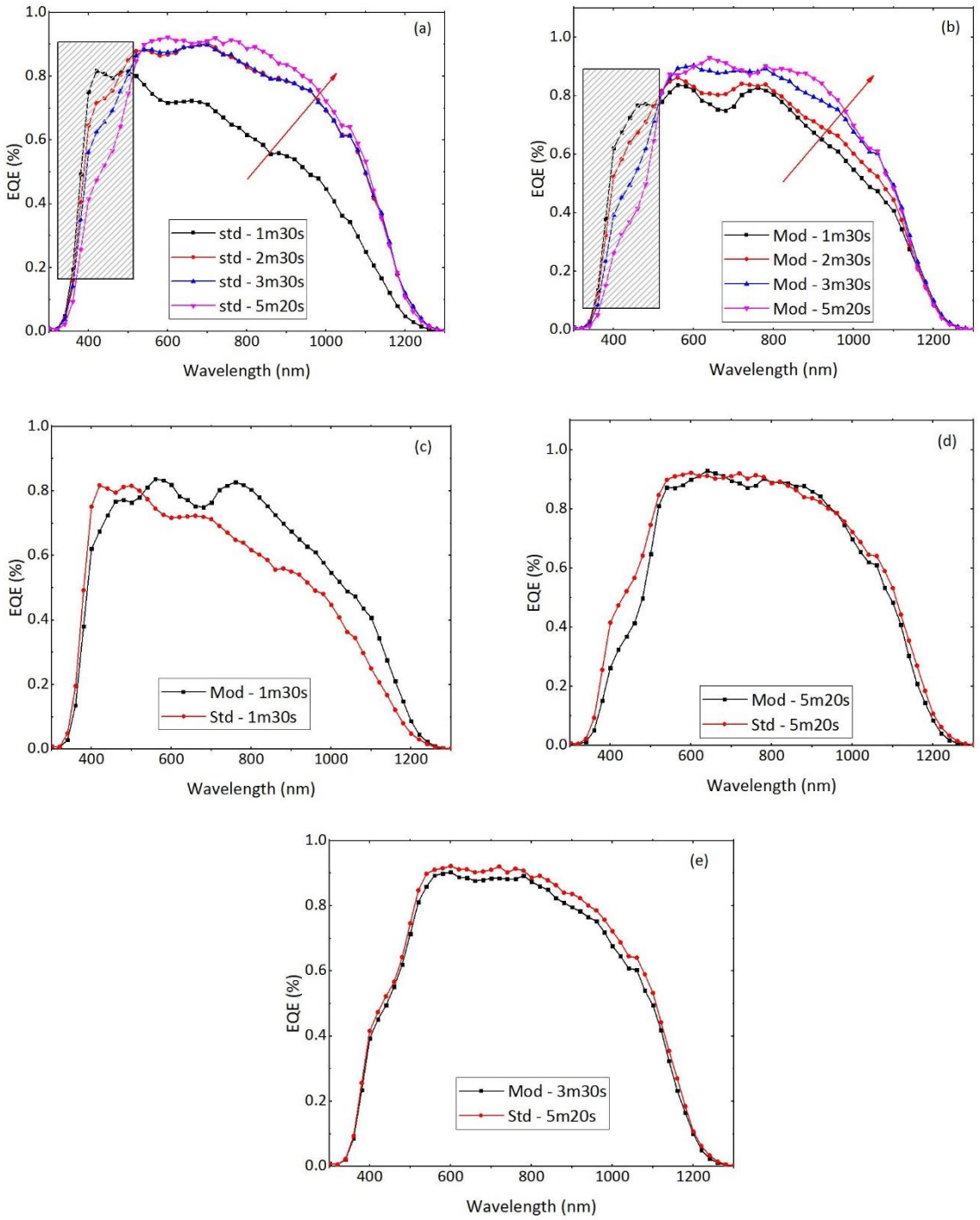


Fig. 3.26. Variation of the EQE responses of the standard and modified cells with respect to the CdS deposition duration: (a) and (b) shows the evolution of the EQE response to deposition time for the standard and modified samples. (c) and (d) compares the sample responses after the shortest and longest deposition time while (e) shows the optimum CdS deposition time for each sample (Std and Mod) that yields approximately the same CdS thickness.

We can correlate the results to literature since we know that after a duration of 1m30s – 2m30s, the deposited CdS thickness is still very small. The losses can be further attributed to recombination in the SCR as was reported in [43] where a decrease in SCR

recombination was accompanied by an increase in the CdS thickness. In figure 3.26(c), the EQE of the standard and modified samples after 1m30s CdS deposition time are compared. The losses in the long wavelength region are still present for both samples, however, the loss is smaller for the modified sample. This could point to a faster growth of the CdS on the modified sample hence leading to a thicker CdS film after such a short deposition time. To confirm this theory, figure 3.26(d) reveals that after 5m20s of CdS deposition, the spectral response in the near-infrared region is restored. Both samples have an almost identical EQE response in this region. Nevertheless, in the near-UV region (short wavelength), the standard cell has a better EQE response than the modified cell. The greater absorption recorded by modified cell after 5m30s in the wavelength region, $\lambda < 500$ nm further proves that the deposition rate of CdS is faster on the modified cells, hence leading to a thicker CdS film. Finally, we try to find the optimum deposition time for both sample types that will result in approximately the same CdS thickness. In Figure 3.26(e) two cells with similar EQE are compared. While for the standard sample, the CdS duration is 5m20s, on the modified cell, a very similar EQE curve is obtained for a CdS deposition time of only 3m30s. This confirm that the surface composition of CIGS absorbers has a direct impact on the growth kinetics of the CdS buffer layer.

3.6 IMPACT OF A SPUTTERED MO BACK CONTACT

As observed in the work done so far, cells on pure Mo foil still exhibit lower Voc and FF than standard CIGS cells made on SLG regardless of the deposition conditions. In the following section, the impact of an extra layer of Mo sputtered on the Mo foils will be discussed in terms of its effect on the growth of CIGS absorbers as well as the performance of solar cells. In section 3.1.2.1, we showed that, based on XRD measurements (Figure 3.4), Mo sputtered on sodalime glass has a different orientation than Mo metal foil. Mo foils have an orientation perpendicular to the (200), (211) lattice plane while sputtered Mo has an orientation perpendicular to the (110) lattice plane. In order to study the impact of sputtered Mo on the preferred orientation of the CIGS and cell performance, two thicknesses of Mo (a thin 100 nm and a thick 800 nm) were sputtered on the Mo foils and compared to a reference Mo foil (Ref) with no sputtered Mo layer. CIGS absorbers were then deposited at two different temperatures of 480 °C and 550 °C by coevaporation.

3.6.1 Physical and structural properties of the CIGS absorbers

At the end of the CIGS deposition cycle, XRD measurements were carried out on the samples to study the effect of the sputtered Mo back contact layer thickness on the orientation of the CIGS film. The diffractogram of the samples as seen in figure 3.27 reveals an interesting trend on the influence of a sputtered layer of Mo. Figure 3.27(a) and (d) are stacked graphs showing different peaks of the samples deposited at 480 °C and 550 °C respectively. Firstly, it is observed (Figure 3.27 c and f) that the intensity of Mo (110) increases with the increase of the thickness of sputtered Mo. Although we can spot the emergence of the (110) peak of the sputtered layer, the (200) and (211) peaks of the Mo foil remain dominant. For samples deposited directly on Mo foil (See 3.1.3.2, figure 3.9), the preferred orientation of the CIGS film is usually (112) and this is also replicated in the samples having an extra layer of sputtered Mo. Figure 3.27(b) and (c), highlight the (112) and (220)/(204) peaks of the CIGS absorbers. For a deposition temperature of 480 °C (Figure 3.27 b), a comparison drawn between the CIGS (112) and (220)/(204) peaks shows little influence of the sputtered Mo layer on CIGS growth orientation, while the (112) remains the preferred orientation.

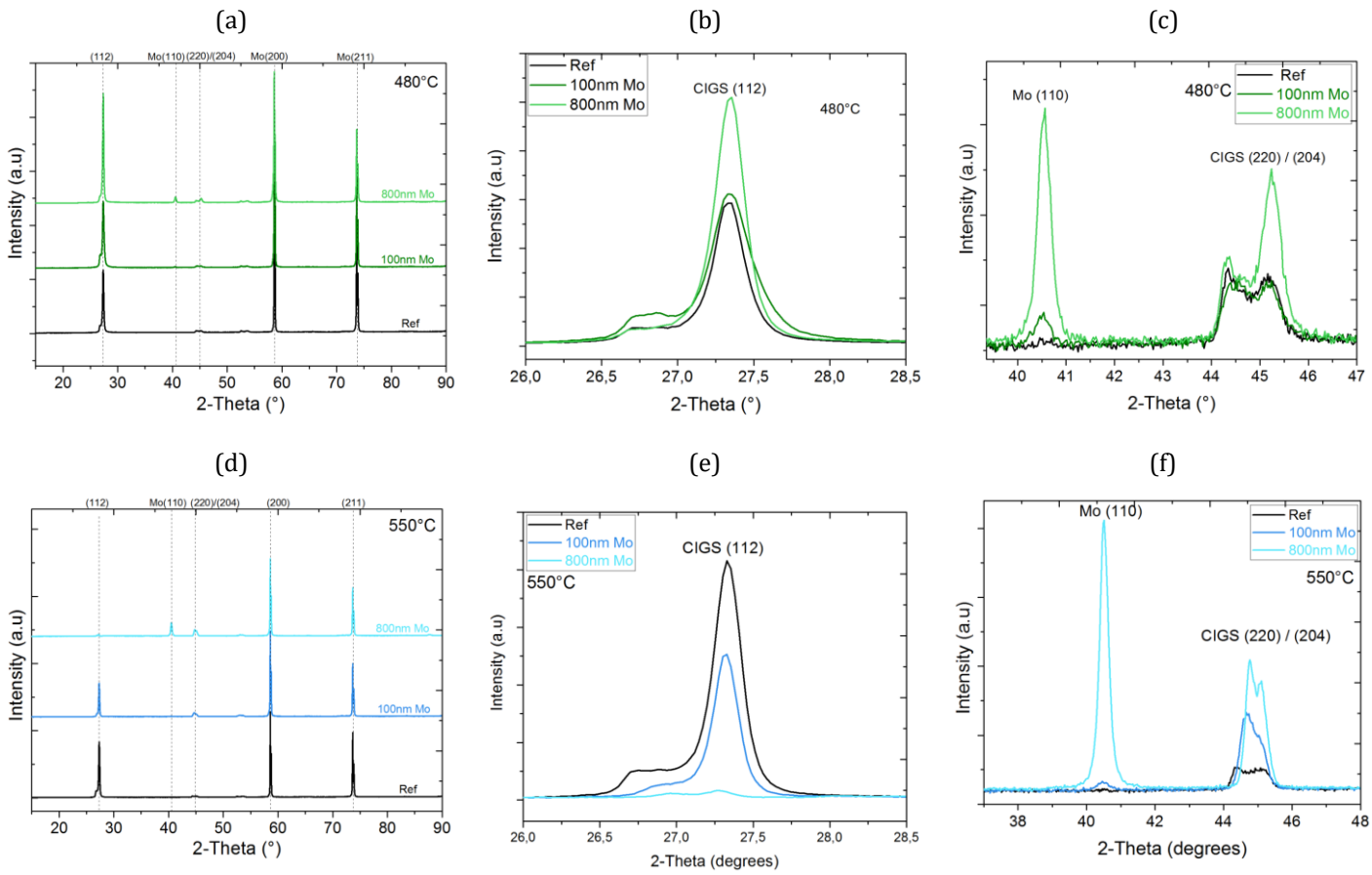


Fig. 3.27 XRD diffractogram of (a) intensity stack comparing the peaks of the ref, 100nm Mo and 800nm Mo deposited at 480°C (b) superimposition of the (112) orientations of the samples (c) superimposition of the (220)/(204) peak of the three samples at 480 °C (d) intensity stack comparing peaks of the ref, 100nm Mo and 800nm Mo deposited at 550°C (e) superimposition of (112) XRD peak of the samples and (f) superimposition of the (220)/(204) peak of the samples at 550 °C.

When the CIGS deposition temperature is increased to 550 °C, a trend starts to emerge and the influence of the sputtered Mo becomes more obvious on the orientation growth of the CIGS absorbers. In figure 3.27 (e) and (d), it is observed that the preferred orientation of CIGS switches from being perpendicular to the (112) lattice plane to the (220)/(204) lattice plane as the thickness of the sputtered layer of Mo increases from 0 to 800 nm. In fact there is an incremental increase of the intensity of the (220)/(204) peaks and a decrease of (112) peak of the CIGS absorber as the thickness of the sputtered Mo is increased. To conclude, at 480 °C the CIGS preferred orientation is (112) regardless of the sputtered Mo layer thickness, however, at 550 °C, as the thickness of that sputtered Mo layer increases, the preferred orientation of CIGS is perpendicular to the (220)/(204) lattice plane.

X-ray fluorescence (XRF) measurements were conducted on the samples in order to observe the influence of sputtering a Mo back contact on the Mo foil substrates on the composition of the Table 3.15 lists the measured CGI and GGI values of the samples.

	T (°C)	CGI	GGI
Ref	480	0.74	0.36
100nm Mo	480	0.76	0.37
800nm Mo	480	0.76	0.36
Ref	550	0.80	0.37
100nm Mo	550	0.80	0.38
800nm Mo	550	0.84	0.39

Table 3.15 CGI and GGI of samples with a sputtered Mo back contact

For the samples processed in the same batches (same deposition temperature), there is no trend in the evolution of the CGI and GGI whatever the Mo orientation and thickness. However, when the separate batches are compared (deposition temperature of 480°C vs 550°C), we observe that the CGI of the samples at 550°C (0.80 – 0.84) are significantly higher than those at processed at 480°C (0.74 – 0.76) while the GGI of all the samples ranged between 0.36 – 0.39. We can from these results that the relative compositions of the samples and their variability are due to the processing temperatures of the samples and not due to the presence of a sputtered layer of Mo.

3.6.2 ELECTRICAL PERFORMANCE

In table 3.16, the electrical performance of the best cells as a function of the sputtered Mo thickness and absorber's deposition temperature are compared. For a deposition temperature of 480 °C, the presence of the sputtered layer of Mo is detrimental to the cells as the conversion efficiency decreases from 13.9 % for the reference cell to 6.0 % for the cell having an 800 nm thick layer of sputtered Mo. This huge drop in efficiency is attributed to a sharp drop in the Voc, Jsc and fill factor. It is seen that even with a thin layer of sputtered Mo (100 nm), the properties of the cell is critically affected. The most profound effect is observed on the Jsc and efficiency which both dropped to about 48 % of the values of the reference cell. On the other hand, at a higher CIGS deposition

temperature of 550 °C, the presence of the sputtered Mo back contact has a reverse impact on the cell performance as compared to the samples at 480 °C. In fact, a slightly better performance in terms of the efficiency and fill factor is observed for the cell with 800 nm of sputtered Mo. This represents ≈10 % improvement over the reference cell. The fill factor and efficiency of the cell with 800nm of Mo reaches a peak of 65.0 % and 11.8 % respectively as compared to 62.2 % and 11.3 % for the reference cell. The changes in the Voc and Jsc are very small. The fill factor however, increases slightly with the thickness of the sputtered Mo layer.

	T (°C)	Eff (%)	Voc (V)	Jsc (mA/cm²)	FF (%)
Ref	480	13.9	0.62	31.9	70.5
100 nm Mo	480	6.4	0.49	22.3	59.4
800 nm Mo	480	6.0	0.55	17.6	62.1
Ref	550	11.3	0.59	30.6	62.2
100 nm Mo	550	11.0	0.58	29.6	63.8
800 nm Mo	550	11.8	0.60	30.1	65.0

Table 3.16 Electrical properties of samples having an extra layer of sputtered Mo back contact

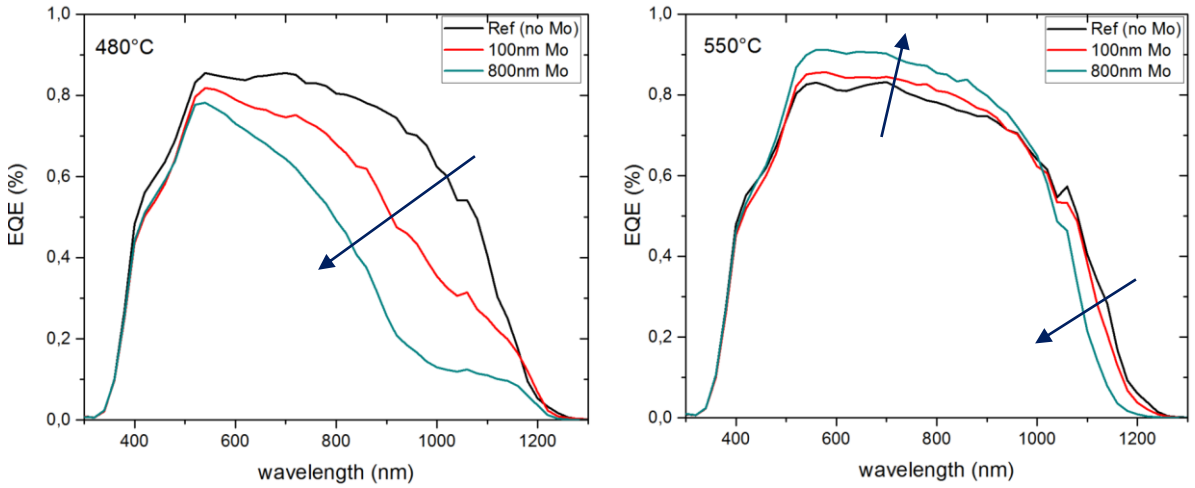


Fig. 3.28 Spectral response of the samples with varying thickness of sputtered Mo at a CIGS deposition temperature of (a) 480 °C and (b) 550 °C

The evolution of EQE response of the best cells are presented in figure 3.28. As observed for cells deposited at 480 °C, an important loss in absorption in the range 550 nm – 1200 nm is observed. This drop in the EQE response is usually due to poor charge collection. Two main reasons can cause a decrease in Jsc: a lower charge carrier generation (less

photons are absorbed into the CIGS layer) or a lower charge carrier collection (charge-carriers recombination) [6]. Since the CIGS absorber have the same thickness and are made in the same experimental run, it is assumed that the CIGS quality is the same hence a difference in the EQE is attributed to the presence of the sputtered Mo back contact. For the cells at 550 °C however, we observed two distinct regions where the absorption is affected. The first is the region between 550 nm and 950 nm where an increase in the EQE is observed as the thickness of the sputtered Mo back contact is increased from 0 nm to 800 nm. The increase in this region could be due to an improved passivation by the Mo back contact at higher temperatures leading to a gain in the EQE as the thickness of the Mo back contact increased. The EQE however, decreased in the near-infrared region 1000 – 1200 nm. The loss of spectral response is this region is correlated to absorption in the CIGS absorber of low energy electrons due to a lower CIGS bandgap as well as an improved carrier collection at long wavelengths due to the additional effective electric field obtained from the increased GGI ratio towards the back contact [44] [45].

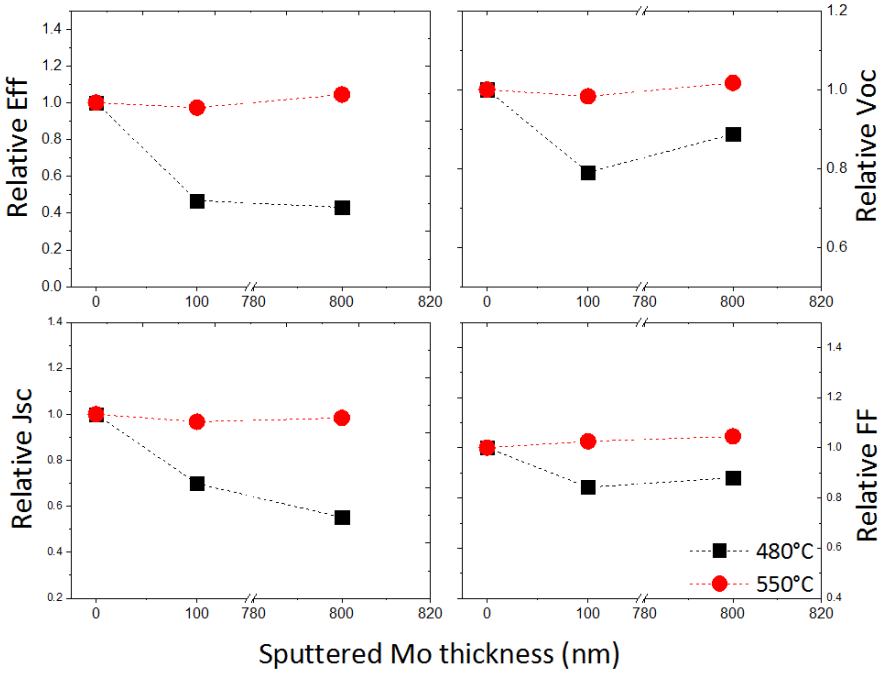


Fig. 3.29 Relative performances of the cells with different thicknes of sputtered Mo back contact.

We can conclude that the sputtered back contact is only beneficial for cell properties at elevated temperatures, in our case, 550 °C. These results shows clearly that for each substrate, the deposition conditions much be adapted individually to achieve an optimized deposition. Figure 3.29 compares the relative change in electrical properties of the cells at the two deposition temperatures and as function of the thickness of sputtered

Mo back contact. At 480 °C, the presence of a sputtered Mo layer is bad for the cell performances with the most profound effect on the Jsc and efficiency which both drop to about 48 % of the values of the reference cell. On the other hand, when the deposition temperature is increased to 550 °C, the efficiency, Voc and FF improves by ~10 % for the 800 nm thick sputtered Mo back contact.

CONCLUSION

The properties of Mo and the optimization of the initial standard CIGS deposition process have been presented. Using AFM studies, the Mo foil used was found to have an average roughness of 83 nm. This is much higher than the surface roughness of a Mo/SLG stack which is the standard architecture for rigid SLG substrates. A comparison between Mo and SLG substrate was also presented with the advantages of using a flexible metal substrates. While SLG contains Na impurity which is released and incorporated in the absorber during CIGS growth, Na has to be incorporated externally by post-deposition on the Na-free Mo substrate. A review of the real substrate temperature carried out using an infrared camera was also discussed [8]. The comparison between 3 deposition temperatures yielded a maximum efficiency of 9.0 % at 480 °C. Choosing this as the standard deposition temperature, the CGI of the absorbers were optimized by varying the duration of the final termination step in the 3rd stage after the plateau (CGI = 1) was attained. This led to an improvement in the CGI from 0.75 to 0.92 when the time was limited to 1 min after plateau formation on the process curve. The efficiency recorded was 9.5 %. Although the Voc and Jsc remained relatively unchanged by this modification, the FF improved as the time was reduced.

Na incorporation by PDT was done using the newly developed process. As already extensively detailed in literature, Na incorporation was beneficial for the cells as they experienced an increase mainly in the Voc and FF. the best cell (13.5 %) was obtained when the duration of the Na flux was 20 min with a post Se annealing of 10 min. It was also seen that the CGI of the final absorber decreased as the amount of Na added increased. This is supported by reports that alkali incorporation leads to a Copper depletion on the surface [32]. Using this process, the Ga gradient was tuned by playing on the Ga flux in the 3rd stage of deposition while keeping the 1st and 2nd stages constant. As a result, the initial GGI of the reference cell (0.34) was tuned till an absorber with a GGI =

0.24 was obtained. GDOES measurements of the samples revealed some small grains near the CIGS/Mo interface for the reference cells while the cell with GGI = 0.24 had large fully formed grains that extended from the back to the surface of the absorber. The best efficiency (max.) of 14.0 % was obtained with the GGI of 0.24 and EQE measurements showed a better spectral response in the near-infrared region of light. This points to increased absorption due to the lower GGI (lower bandgap) which makes it possible to absorb low energy photons. It was observed however that the CdS growth kinetics was modified for the optimized absorber as the surface and elemental composition had been modified. Studies on the CdS growth speed showed a faster growth on the modified absorbers in comparison with the original default recipe, hence we tuned the CdS deposition time to match the new absorbers. We studied further the effect of pre-depositing a Mo back contact layer on the Mo substrate. Two temperatures were studied and it was observed that the cell performances were degraded more at 480 °C than at 550 °C. The underlying reason still needs further investigation. The maximum efficiency hence attained in this work on Mo substrate was 14.0 %. The next chapter will address the fabrication of CIGS solar cells stainless steel.

REFERENCES

[1] "Mo Technical Data." [Online]. Available: http://www.espimetals.com/index.php/online-catalog/97-technical-data/Mo/108-Mo. [Accessed: 22-Feb-2018].

[2] P. Huang, C. Huang, M. Lin, C. Chou, C. Hsu, and C. Kuo, "The Effect of Sputtering Parameters on the Film Properties of Mo Back Contact for CIGS Solar Cells," *Int. J. Photoenergy*, vol. 2013, pp. 1–8, 2013.

[3] M. Jubault, L. Ribeaucourt, E. Chassaing, G. Renou, D. Lincot, and F. Donsanti, "Optimization of Mo thin films for electrodeposited CIGS solar cells," *Sol. Energy Mater. Sol. Cells*, vol. 95, pp. S26–S31, May 2011.

[4] K. Orgassa, H. W. Schock, and J. H. Werner, "Alternative back contact materials for thin film Cu(In,Ga)Se2 solar cells," *Thin Solid Films*, vol. 431–432, pp. 387–391, May 2003.

[5] O. Lundberg, M. Bodeg\a ard, J. Malmström, and L. Stolt, "Influence of the Cu (In, Ga) Se2 thickness and Ga grading on solar cell performance," *Prog. Photovolt. Res. Appl.*, vol. 11, no. 2, pp. 77–88, 2003.

[6] F. Mollica, "Optimization of ultra-thin Cu(In,Ga)Se2 based solar cells with alternative back-contacts," UPMC, 2017.

[7] G. Gordillo, F. Mesa, and C. Calderón, "Electrical and morphological properties of low resistivity Mo thin films prepared by magnetron sputtering," *Braz. J. Phys.*, vol. 36, no. 3B, pp. 982–985, 2006.

[8] T. Klinkert, "Comprehension and optimisation of the co-evaporation deposition of Cu (In, Ga) Se2 absorber layers for very high efficiency thin film solar cells," PhD Thesis, Université Pierre et Marie Curie-Paris VI, 2015.

[9] D. H. Shin, Y. M. Shin, J. H. Kim, B. T. Ahn, and K. H. Yoon, "Control of the Preferred Orientation of Cu(In,Ga)Se2 Thin Film by the Surface Modification of Mo Film," *J. Electrochem. Soc.*, vol. 159, no. 1, pp. B1–B5, 2012.

[10] E. J. Friedrich, R. Fernández-Ruiz, J. M. Merino, and M. León, "X-ray diffraction data and Rietveld refinement of CuGaxIn1-xSe2 (x=0.15 and 0.50)," *Powder Diffr.*, vol. 25, no. 03, pp. 253–257, Sep. 2010.

[11] B. GRZETA-PLENKOVIC, S. Popovic, B. Celustka, and B. Santic, "Crystal data for AgGaxIn1 _ xSe2 and CuGaxIn1-xSe2," *J Appl Cryst*, vol. 13, pp. 311–315, 1980.

[12] C. Insignares-Cuello, C. Broussillou, V. Bermúdez, E. Saucedo, A. Pérez-Rodríguez, and V. Izquierdo-Roca, "Raman scattering analysis of electrodeposited Cu(In,Ga)Se $_2$ solar cells: Impact of ordered vacancy compounds on cell efficiency," *Appl. Phys. Lett.*, vol. 105, no. 2, p. 021905, Jul. 2014.

[13] W. Witte, R. Kniese, and M. Powalla, "Raman investigations of Cu(In,Ga)Se2 thin films with various copper contents," *Thin Solid Films*, vol. 517, no. 2, pp. 867–869, Nov. 2008.

[14] K. Zhang *et al.*, "Fabricating highly efficient Cu(In,Ga)Se2 solar cells at low glass-substrate temperature by active gallium grading control," *Sol. Energy Mater. Sol. Cells*, vol. 120, pp. 253–258, Jan. 2014.

[15] H. Mönig *et al.*, "Gallium gradients in chalcopyrite thin films: Depth profile analyses of films grown at different temperatures," *J. Appl. Phys.*, vol. 110, no. 9, p. 093509, 2011.

[16] F. Kessler and D. Rudmann, "Technological aspects of flexible CIGS solar cells and modules," *Sol. Energy*, vol. 77, no. 6, pp. 685–695, Dec. 2004.

[17] H. Wang *et al.*, "Effect of substrate temperature on the structural and electrical properties of CIGS films based on the one-stage co-evaporation process," *Semicond. Sci. Technol.*, vol. 25, no. 5, p. 055007, May 2010.

[18] P. Jackson *et al.*, "High quality baseline for high efficiency, Cu(In1−x,Gax)Se2 solar cells," *Prog. Photovolt. Res. Appl.*, vol. 15, no. 6, pp. 507–519, Sep. 2007.

[19] H. Tanino, "Raman Spectra of CuGaxIn1-xSe2," *Jpn. J. Appl. Phys.*, vol. 32, pp. 436–438, 1993.

[20] C. Rincón *et al.*, "Raman spectra of the ordered vacancy compounds CuIn 3 Se 5 and CuGa 3 Se 5," *Appl. Phys. Lett.*, vol. 73, no. 4, pp. 441–443, 1998.

[21] C.-M. Xu *et al.*, "Composition dependence of the Raman A_1 mode and additional mode in tetragonal Cu–In–Se thin films," *Semicond. Sci. Technol.*, vol. 19, no. 10, pp. 1201–1206, Oct. 2004.

[22] J. Hedstrom *et al.*, "ZnO/CdS/Cu (In, Ga) Se/sub 2/thin film solar cells with improved performance," in *Photovoltaic Specialists Conference, 1993., Conference Record of the Twenty Third IEEE*, 1993, pp. 364–371.

[23] Y. Sun *et al.*, "Review on Alkali Element Doping in Cu(In,Ga)Se 2 Thin Films and Solar Cells," *Engineering*, vol. 3, no. 4, pp. 452–459, Aug. 2017.

[24] A. Urbaniak *et al.*, "Effects of Na incorporation on electrical properties of Cu(In,Ga)Se2-based photovoltaic devices on polyimide substrates," *Sol. Energy Mater. Sol. Cells*, vol. 128, pp. 52–56, Sep. 2014.

[25] Leeor. Kronik, David Cahen, and Hans Werner Schock, "Effects of Sodium on Polycrystalline Cu(In,Ga)Se2 and Its Solar Cell Performance," *Adv. Mater.*, vol. 10, no. 1, pp. 31–36, 1998.

[26] F. Pianezzi *et al.*, "Unveiling the effects of post-deposition treatment with different alkaline elements on the electronic properties of CIGS thin film solar cells," *Phys. Chem. Chem. Phys.*, vol. 16, no. 19, p. 8843, 2014.

[27] David W. Niles, Kannan Ramanathan, Falah Hasoon, and Rommel Noufi, "Na impurity chemistry in photovoltaic CIGS thin films: Investigation with x-ray photoelectron spectroscopy," *J. Vac. Sci. Technol. A*, vol. 15, no. 6, 1997.

[28] S.-H. Wei, S. B. Zhang, and A. Zunger, "Effects of Na on the electrical and structural properties of CuInSe2," *J. Appl. Phys.*, vol. 85, no. 10, pp. 7214–7218, May 1999.

[29] D. Rudmann, D. Brémaud, H. Zogg, and A. N. Tiwari, "Na incorporation into Cu(In,Ga)Se[sub 2] for high-efficiency flexible solar cells on polymer foils," *J. Appl. Phys.*, vol. 97, no. 8, p. 084903, 2005.

[30] D. Rudmann, "Effects of sodium on growth and properties of Cu(In,Ga)Se_2 thin films and solar cells," ETH Zurich, Switzerland, 2004.

[31] A. Chirilă *et al.*, "Potassium-induced surface modification of Cu(In,Ga)Se2 thin films for high-efficiency solar cells," *Nat. Mater.*, vol. 12, no. 12, pp. 1107–1111, Nov. 2013.

[32] D. Shin *et al.*, "Effects of the incorporation of alkali elements on Cu(In,Ga)Se 2 thin film solar cells," *Sol. Energy Mater. Sol. Cells*, vol. 157, pp. 695–702, Dec. 2016.

[33] I. Shogo, "Alkali incorporation control in Cu(In,Ga)Se2 thin films using silicate thin layers and applications in enhancing flexible solar cell efficiency," *Appl. Phys. Lett.*, vol. 93, no. 12, Sep. 2008.

[34] D. Rudmann *et al.*, "Efficiency enhancement of Cu(In,Ga)Se[sub 2] solar cells due to post-deposition Na incorporation," *Appl. Phys. Lett.*, vol. 84, no. 7, p. 1129, 2004.

[35] M. Saadat, M. Moradi, and M. Zahedifar, "CIGS absorber layer with double grading Ga profile for highly efficient solar cells," *Superlattices Microstruct.*, vol. 92, pp. 303–307, Apr. 2016.

[36] K. Decock, J. Lauwaert, and M. Burgelman, "Characterization of graded CIGS solar cells," *Energy Procedia*, vol. 2, no. 1, pp. 49–54, Aug. 2010.

[37] T. M. Friedlmeier *et al.*, "High-efficiency Cu(In,Ga)Se2 solar cells," *Thin Solid Films*, Aug. 2016.

[38] N. E. Gorji, U. Reggiani, and L. Sandrolini, "A simple model for the photocurrent density of a graded band gap CIGS thin film solar cell," *Sol. Energy*, vol. 86, no. 3, pp. 920–925, Mar. 2012.

[39] S. Schleussner, U. Zimmermann, T. Wätjen, K. Leifer, and M. Edoff, "Effect of gallium grading in Cu(In,Ga)Se2 solar-cell absorbers produced by multi-stage coevaporation," *Sol. Energy Mater. Sol. Cells*, vol. 95, no. 2, pp. 721–726, Feb. 2011.

[40] W. Witte *et al.*, "Gallium gradients in Cu(In,Ga)Se_2 thin-film solar cells: Gallium gradients in CIGS thin-film solar cells," *Prog. Photovolt. Res. Appl.*, vol. 23, no. 6, pp. 717–733, Jun. 2015.

[41] M. Stanley, M. Jubault, F. Donsanti, and N. Naghavi, "Flexible Cu (In, Ga) Se2 Based Solar Cells Using Mo Foils as Substrate," *Phys. Status Solidi C*, vol. 14, no. 10, 2017.

[42] K. Orgassa, U. Rau, Q. Nguyen, H. Werner Schock, and J. H. Werner, "Role of the CdS buffer layer as an active optical element in Cu (In, Ga) Se2 thin-film solar cells," *Prog. Photovolt. Res. Appl.*, vol. 10, no. 7, pp. 457–463, 2002.

[43] M. A. Contreras *et al.*, "Optimization of CBD CdS process in high-efficiency Cu(In,Ga)Se2-based solar cells," *Thin Solid Films*, pp. 204–211, 2002.

[44] O. Lundberg, M. Edoff, and L. Stolt, "The effect of Ga-grading in CIGS thin film solar cells," *Thin Solid Films*, vol. 480–481, pp. 520–525, Jun. 2005.

[45] T. Dullweber, U. Rau, M. A. Contreras, R. Noufi, and H.-W. Schock, “Photogeneration and carrier recombination in graded gap Cu (In, Ga) Se 2 solar cells,” *IEEE Trans. Electron Devices*, vol. 47, no. 12, pp. 2249–2254, 2000.

CHAPTER 4

When there is a huge solar energy spill, it is just called a "nice day."

- Anonymous, *2018*.

$Cu(In,Ga)Se_2$ SOLAR CELLS ON STAINLESS STEEL SUBSTRATES

This chapter discusses aspects related to the growth and fabrication of CIGS solar cells on stainless steel substrates. In the case of stainless-steels, Fe is the basic alloying element, representing at least 80% of their composition. It is reported that the presence of Fe in the CIGS leads to the formation of deep levels in the bandgap and generate electronic traps in the CIGS [1] [2]. On the other hand, it is reported that elements such as Ti and Cr are relatively neutral towards CIGS [3]. It is possible to limit the diffusion of impurities such as iron or Ni by several means. The main path to limiting the diffusion of impurities is to deposit a diffusion barrier between the substrate and the back contact which as discussed in section 4.2.1. Another way to reduce the diffusion of impurities in the CIGS is to reduce the deposition temperature of the CIGS. Indeed, the diffusion coefficient of impurities depends on the temperature according to the Arrhenius law. It has been shown that the reduction of the deposition temperature of CIGS down to 475 °C on stainless steel and without layer barrier leads to cells with higher efficiencies and lower Fe concentrations compared to the one made at 600 °C [4]. However, as observed in chapter 3, obtaining a high quality CIGS at low temperature requires a significant adaptation of the deposition process. First the properties of the stainless steel substrates used in this work will be discussed. Afterwards, a first study on the impact of the use of Cr barrier layer on the properties of the absorbers will be presented. The optimized 3-stage process for Mo substrates at a temperature of 480 °C (see sec. 3.4) will be used for the CIGS growth. For this study, four different types of stainless steel substrates without any barrier layers will be used. Finally in the last part of this chapter, the effect of other deposition methods such as CURO on the properties of the CIGS absorber on stainless steel will be discussed.

4.1 PROPERTIES OF STAINLESS STEEL

As already discussed in section 1.3.2, metals are suitable substrates in the fabrication of CIGS cells. Stainless steel is usually preferred compared to other metals because of its low cost and availability. Its major drawback however, remains the presence of detrimental Fe atoms (see section 1.3.4). The presence of metallic impurities can be managed by the

use of diffusion barrier layers. The thermal conductivity of stainless steel is ~14.5 $Wm^{-1}K^{-1}$ at 20 °C which is substantially lower than that of Mo foil substrate (142 $Wm^{-1}K^{-1}$). The resistivity of stainless steel is ~7.0×10^{-7} Ωm while its electrical conductivity is 1.45×10^{6} $\Omega^{-1}m^{-1}$ at 20 °C [5][6]. These properties are summarized in table 4.1 and are compared to Mo and SLG.

	Stainless Steel	**Mo**	**SLG**
Coefficient of thermal expansion CTE (10^{-6} K^{-1})	9.4 – 12.5	4.8 – 5.9	9
Fusion Temperature (°C)	1510	2,623	562
Thermal conductivity at 20 °C ($Wm^{-1}K^{-1}$)	14.5	142	0.937
Electrical conductivity ($\Omega^{-1}m^{-1}$)	1.43×10^{6}	17.9×10^{6}	1.3×10^{-13}
Resistivity (Ωm)	7.0×10^{-7}	5.5×10^{-8}	7.9×10^{12}

Table 4.1 Comparison of physical properties of Stainless Steel, Mo and SLG

The high temperature of fusion of stainless steel makes it viable for use in CIGS depositions involving high temperature. Furthermore, stainless steel has a coefficient of thermal expansion (CTE) of 9.4 – 12.5×10^{-6} K^{-1} which closely matches that of CIGS. This reduces the impact of stress between the CIGS absorber and the substrate. However, it should also be noted that in the CIGS architecture, the Mo back contact is sandwiched between the stainless steel substrate and the CIGS absorber layer. As observed in table 4.1, there exists a mismatch between the CTE of stainless steel and Mo and this could lead to delamination issues. The first set of experiments involving the impurity barrier layer were carried on generic stainless steel substrates supplied by MBE Kompnenten.

4.2 IMPURITY BARRIER LAYER

It is known that stainless steel substrates contains Fe which is detrimental to cell performance when the Fe atoms diffuse into the absorber [7] [8] [1]. The presence of Fe atoms causes a decrease in the open-circuit voltage (V_{oc}), short-circuit current density (J_{sc}) and fill factor. It is reported that this could likely be caused by deep level acceptor defects Fe_{In} and Fe_{Ga} which form a broad acceptor-type defect band and cause bulk recombination [8] [1]. A recent study further indicated that Iron-ion doping in $Cu(In,Ga)Se_2$ thin films substantially facilitated the formation of grain boundaries and

additional shunt paths, leading to high probability of electron-hole recombination and a dramatic decrease in the conversion efficiency of the solar devices [9]. It is however possible to limit the diffusion of impurities either by reducing the deposition temperature of the CIGS as tested in the previous paragraph or by depositing a diffusion barrier between the substrate and the back contact. Some examples of results obtained by research groups using various barrier layer methods are given in table 4.4.

Group	**Barrier layer**	**Processing Temperature (°C)**	**η_{ref} (%)**	**η (%)**	**Ref**
Chonbuk National University, Korea	Homomorphic Cr_2O_3	600	8.6	10.6	[10]
Yeungnam University, Korea	Mo	530	4.9	9.1	[11]
EMPA	Ni/Cr bi-layer	450 - 550	-	18.0	[12]
ZSW	Mo	600	4.4	11.4	[2]
ZSW	Enamel layers	600	0.0	17.6	[13]
EMPA	Low temperature	475 - 600	-	17.7	[4]
ZSW	Al_2O_3 and SiO_x	550	-	10.9	[14]
Nankai University	AlN	530	7.6	11.8	[15]
ETRI, Korea	SiO_x	-	7.4	12.4	[16]
ETRI, Korea	Cr	570	7.9	9.0	[3]

Table 4.4 Results obtained by different groups working on barrier layers for CIGS deposition on stainless steel. The reference efficiency refers to the cell with no barrier layer deposited.

Various materials have been studied for the barrier properties and effectiveness in blocking the diffusion of Fe atoms from the steel substrate into the CIGS absorber layer. These materials can be broadly grouped into insulating and non-insulating barriers. Insulating barriers are suitable for monolithic integration in CIGS modules. Examples include SiO_x and Al_2O_3 which are also sometimes referred to as dielectric barrier layers. Their insulation properties are tested by sputtering small amounts of Mo contacts on the barrier layers and measuring the resistance and breakdown voltages of the layers before and after CIGS deposition [14]. Herz *et al.* studied the insulation and barrier properties of SiO_x and Al_2O_3 and combi layers prepared by RF magnetron sputtering, sol-gel and/or

plasma CVD with thickness ranging between 1 – 6 μm. The substrates used were Cr-steel, Kovar and Titanium. They obtained a best cell efficiency of 10.9 % on Cr-steel with no NaF post treatment [14]. Li *et al.* also investigated the effect of using AlN film, deposited by DC magnetron sputtering, to block the diffusion of Fe impurities. A thickness of 1.0 μm was deposited on stainless steel foils followed by the CIGS deposition at 530 °C. The cell with the AlN barrier layer had an efficiency of 11.8 % compared to 7.6 % for the cell with no barrier [15]. Another study using a thick layer of SiO_x revealed that a thick layer of SiO_x improved the insulation and Fe atom blocking in the stack. An efficiency of 11.8 % and 12.4 % was achieved using 1.0 μm and 2.0 μm of SiO_x respectively. The cell with no barrier on the other hand achieved only 7.4 % in efficiency [16]. However the most common conductive barrier layer is chromium. The latter can be deposited by evaporation or sputtering. In this case, the contact barrier can be deposited in the same equipment as the Mo rear contact, which can reduce production costs.

Cr is non-insulating and hence is not suitable for monolithic cell integration. Cho *et al.* investigated the use of Cr as barrier layer [3]. In this study, Cr thicknesses ranging from 0 nm – 1000 nm were deposited by DC magnetron sputtering. The CIGS absorbers were deposited at a substrate temperature of 570 °C. They reported that the vertical grain size, crystallinity, and strain of CIGS films obtained by XRD measurements varied little with Cr thickness. XRF measurements also revealed that Cu, In, Ga, and Se compositions were nearly constant. Efficiency of the best cell was pegged at 9.0 % and 7.9 % for the cell with no barrier layer [3]. With sufficient thickness and optimization, even the Mo back contact can act as a diffusion barrier layer. Studies by Blosch *et al.* using Mo as a barrier layer and back contact at a low substrate temperature of 475 °C (in order to reduce diffusion of Fe which is strongly dependent on temperature) revealed that a 500 nm thick layer of Mo is sufficient to block Fe impurities provided the CIGS deposition temperature is low enough. When a 160 nm thick layer of Mo is used, a decrease in all the cell's electrical properties is observed when compared to their individual reference samples [17]. Another study was carried out to test the viability of Mo_2N and/or Mo thin films as barrier layers against Fe [8] [11]. Zortea *et al.* applied a barrier layer consisting of 2 μm of Ni and 0.1 μm of Cr both of which were deposited by a chemical bath process. The CIGS absorbers were fabricated at various temperatures ranging from 400 °C (low temperature) to 550°C (high temperature) on mild steel substrates with a mirror finish and roughness $R_a < 0.10$ μm. NaF PDT was applied on all the samples and for the champion cell, NaF and RbF PDT was

applied. The champion cell reached a certified efficiency of 18.0 % with an MgF_2 anti-reflective coating [12].

4.2.1 Chromium barrier layer test

Chromium is selected for initial test of its barrier properties. The selection of Cr is mainly due to its availability and ease of deposition. The test was carried out to observe the influence, if any, of the presence of Cr as a Fe blocking agent on the electrical properties of the CIGS solar cells on stainless steel substrates. 0, 500, 800 and 1000 nm of Cr were deposited on stainless steel substrates by evaporation from 99.99 % pure Cr pellets placed in a crucible in the evaporation chamber. Then, 800 nm of Mo back contact was sputtered by DC magnetron on the samples (sec 2.3.1). In order to study the diffusion of Fe through the Cr barrier layer, one half of each sample was annealed in a furnace at 520 °C for one hour and then cooled down to room temperature. This triggered the diffusion of Fe from the stainless steel substrates. GDOES measurements reveals the Fe profile in the annealed samples. On the other half of the samples, CIGS absorbers were deposited at the standard substrate temperature of 480 °C. This combines a low temperature process and a barrier layer to block Fe diffusion. The emerging absorbers were processed into solar cells as already described in chapter 2. The architecture of the cell is shown in figure 4.3.

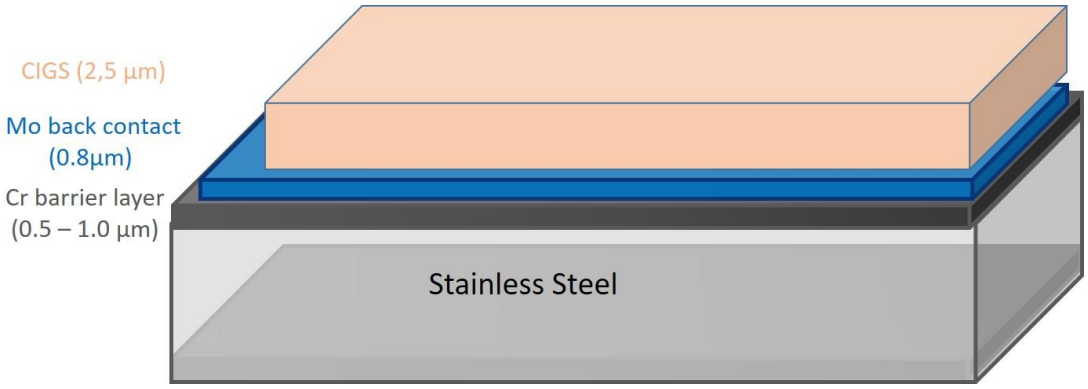


Figure 4.3. CIGS architecture showing the placement of the Cr barrier layer.

- Fe Impurity profile

GDOES measurements were done on the first half of the samples (annealed) in order to see the extent of diffusion of Fe impurities through the Cr barrier layer and the Mo back contact. Figure 4.4 presents the GDOES profiles of the samples after annealing. The shaded

areas represent the portion of the substrate that was etched by the plasma before the measurement was stopped. The Cr signal in this region does not drop to zero but levels out at ~20 % (atomic content). This is because the stainless steel substrates contain Cr which is an alloying material in the production of stainless steel. At the border of the shaded area, the Fe signal drops sharply. This is Cr barrier/SS interface and the sharp drop in the Fe signal indicates the extent of diffusion of Fe as well as the blocking effect of the Cr layer. The GDOES profile does not give the exact atom count of the Fe impurities but rather just gives a hint on the diffusion profile of the Fe atoms. The effective barrier region is identified as the region in the Cr layer where the Fe signal significantly drops to zero. The effective barrier region for the samples with 0.5 µm, 0.8 µm and 1.0 µm Cr barrier layer thickness are around 0.3 µm, 0.5 µm and 0.6 µm respectively. It is important to bear in mind again that this analysis is not quantitative.

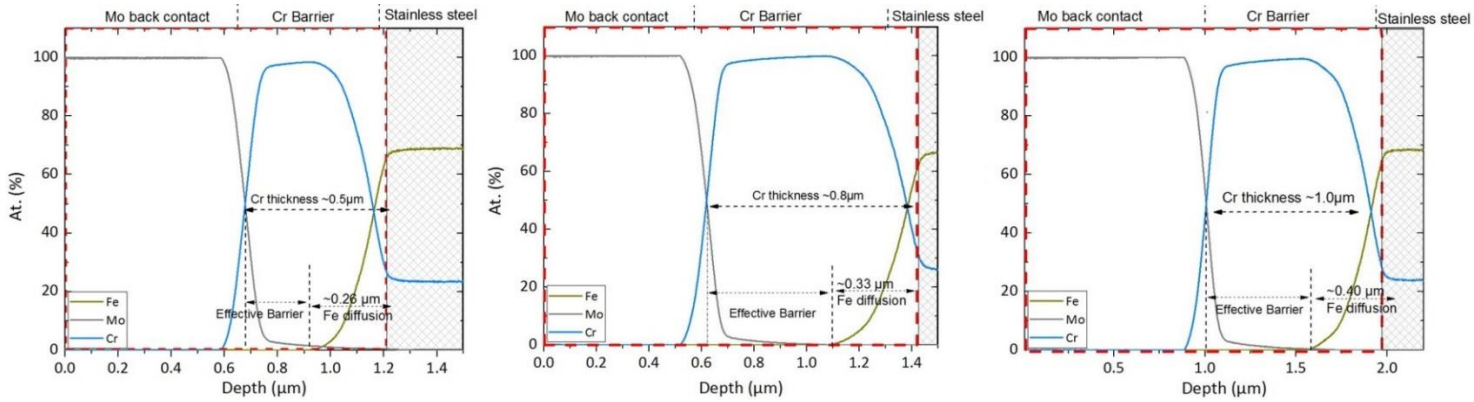


Figure 4.4. GDOES profile on SS/Cr/Mo layer showing the depth of diffusion of Fe and the effective Fe blocking capability of the 500 nm, 800 nm and 1000 nm thick Cr layers.

The cross-over of the Mo back contact and Cr barrier layer signals also indicate that some Cr diffused into the Mo back contact. This is not critical for the cell performance as it has been shown already that Cr is not detrimental to CIGS solar cell device performance [3]. In figure 4.5, the first few micrometers of the Mo/Cr/SS stack is shown with data adapted from the area under the red dashed box in figure 4.4. The yellow shaded area in figure 4.5 indicates the region of the Cr barrier layer.

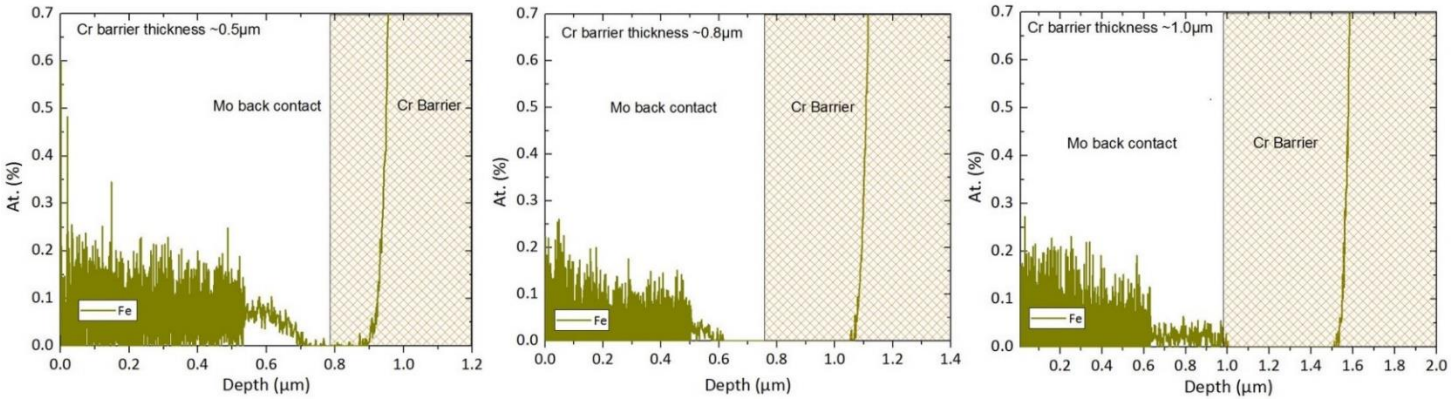


Figure 4.5. GDOES profile with a reduced y-axis scale showing Fe content in the first micron of the Mo/Cr/SS stack. The data is adapted from the area under the red dashed box in figure 4.4

The scale of the atomic content has been intentionally reduced in order to properly visualize the Fe profile in the Cr barrier and the Mo back contact. It is observed that the Fe signal drops in the shaded region in all three samples. The Fe profile in the Mo back contact (unshaded portion) on the other hand does not indicate major differences in the Fe content for the samples with 0.5 µm, 0.8 µm and 1.0 µm of Cr barrier. However, it can be seen that the atomic content of Fe in the sample with 0.5 µm Cr barrier reached up to ~0.5 – 0.6 % while the maximum obtained on the samples with 0.8 µm and 1.0 µm Cr barrier is ~0.25 – 0.28 %. This further indicates that a Cr barrier thickness of ~0.8 µm is sufficient enough to deter the diffusion of Fe impurities as will be confirmed from the electrical properties of the cells.

- CIGS absorber composition and morphology

The second half of the samples were reserved for the CIGS growth and cell fabrication. As indicated above, the CIGS deposition was carried out at a substrate temperature of 480 °C with the process parameters enumerated in table 4.5.

(1st stage)

Substrate Temperature, T_1	400 °C
In Flux	6.3 nm/min
Ga Flux	5.3 nm/min

(2nd stage)

Substrate Temperature, T_2	400 ↗ 480 °C
Cu Flux	8.0 nm/min

(3rd stage)

Substrate Temperature, T_3	480 °C
In Flux	8.3 nm/min
Ga Flux	3.0 nm/min

(NaF PDT)

Substrate Temperature, T	350 °C
NaF Flux	2 nm/min
Se Flux	57 - 61 nm/min
Duration	20 min
Annealing in Se atmosphere	10 min

Table 4.5 Summary of deposition parameters used on stainless steel substrates with different barrier layer thickness.

The process used is the standard 3-stage process (not optimized for stainless steel). This process was adopted on stainless steel as a first test involving stainless steel substrates because the optimized process described in chapter 3 had not yet been developed. The relatively low temperature combined with the presence of the Cr barrier layers further contributes to reducing the diffusion of detrimental Fe impurities. Following the deposition of CIGS absorbers on the samples, Energy Dispersive X-ray spectroscopy analysis (EDX) was done on the samples to estimate the amount of Fe detectable within 1 µm from the surface of the CIGS absorbers. A depth of 1 µm is specified here because the penetration depth of the e-beam probe used in the EDX analysis is ~1 µm.

Cr thickness (nm)	Fe detected (At. %)
0 (Ref)	2.51
500	2.16
800	1.53
1000	1.42

Table 4.5. EDX spectroscopy showing the amount of Fe detected in ~1 µm from the surface of the CIGS/Mo/Cr stack.

Table 4.5 shows the amount of Fe that was detected by the EDX measurement performed on the samples. The amount of Fe decreases systematically as the thickness of the Cr increased from 0 - 1000 nm which is logically expected. The EDX measurement however does not give the exact ppm count of the Fe atoms that diffused from the stainless steel substrate into the CIGS/Mo/Cr/SS stack.

The morphology of the absorbers, grown in the same experimental run, were observed by SEM as shown in figure 4.6.

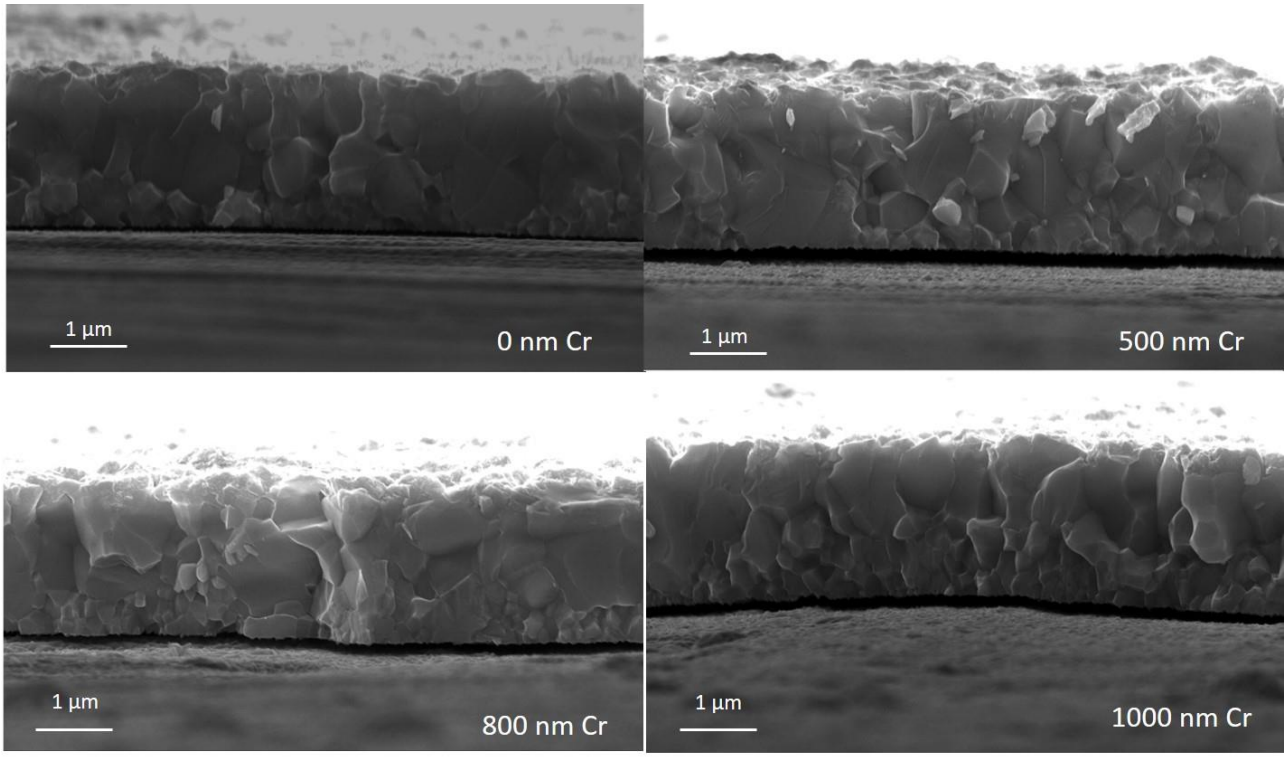


Figure 4.6. SEM cross-section images of the CIGS absorbers grown on stainless steel substrates with varying thickness of Cr barrier layer. Note that the Cr layers are not shown.

Regardless of the thickness of Cr barrier layer, all samples presented similar morphology and grain sizes. All samples, whatever the thickness of Cr, exhibited small grains near the back at the CIGS/Mo interface and significantly larger grains

extending from the mid-point to the surface of the absorbers. This shows clearly that, the presence (or not) of a Cr barrier layer has no effect on the CIGS absorber morphology. The occurrence of small grains near the Mo back contact points again the possibility of the increased Ga content in this region. EDX elemental composition measurements of the CIGS absorbers is shown in table 4.6 where a high GGI (0.44 – 0.46) is observed. In fact, it has been reported that an accumulation of Ga near the CIGS/Mo interface leads to small grain sizes and the material in this region is predominantly $CuGaSe_2$ [18] [19] [20]. As mentioned earlier, the CIGS/Mo/SS stack might present some adhesion issues due to a thermal expansion mismatch between the stainless steel. In the SEM images, it is observable that a small delamination of the CIGS absorbers occurs during the cutting of the samples. It appears that the delamination is more severe when there is a Cr barrier layer when compared to the reference sample. Indeed, the CIGS/Mo/Cr/SS stack is made up of four materials with different coefficients of thermal expansion, hence, we expect some mismatch which could manifest in form of delamination of the CIGS absorber.

Sample	Cr barrier (nm)	CGI	GGI
SS01	0	0.9	0.45
SS02	500	0.91	0.46
SS03	800	0.92	0.44
SS04	1000	0.89	0.46

Table 4.6. [Ga]/([Ga]+[In]) and [Cu]/([Ga]+[In]) values for the CIGS absorber with varying Cr barrier thickness

- Electrical properties of the finished cells

The current-voltage characteristics of the finished cells were measured under an illumination of 1 sun (1000 Wm^{-2}, AM1.5G).

Sample no	Cr thickness (nm)	Eff (%)	Voc (mV)	Jsc (mA/cm^{-2})	FF (%)
SS01	0	13.8	630	30.5	72.0
SS02	500	14.2	640	31.2	71.2
SS03	800	14.0	640	30.7	71.4
SS04	1000	12.9	620	29.6	70.6

Table 4.7. Summary of the maximum electrical parameter values obtained on the finished cells with a Cr barrier layer.

Contrary to what was expected, the difference between the cells with/without a barrier layer was not profound. Table 4.7 reports the maximum values obtained for the cell made on each absorber while figure 4.7 is a box chart summary showing the distribution of the cells' electrical parameters. There is a slight increase in Jsc for the cell with 500 nm Cr barrier compared to the reference. However, the Jsc decreased for the cells with 800 nm and 1000 nm Cr barrier respectively. The same trend is observed for the Voc and FF. The cells with 800 nm and 1000 nm presented a large dispersion of the electrical parameters indicating that there exists some inhomogeneity in these samples. The cell with 500 nm however is homogenous with little dispersion. The inhomogeneity of the results might be due to the thicker Cr barrier layers as this is observed only for the cells with 800 nm and 1000 nm thick Cr barrier. Finally, it is noteworthy that this initial test on the stainless steel substrates with a Cr barrier layer and a CIGS deposition temperature of 480 °C yielded a maximum efficiency of 14.2 % with a Cr thickness of 500 nm. This is the best efficiency achieved on stainless steel in this thesis. The high efficiencies obtained on the samples was mainly due to a high Voc and FF.

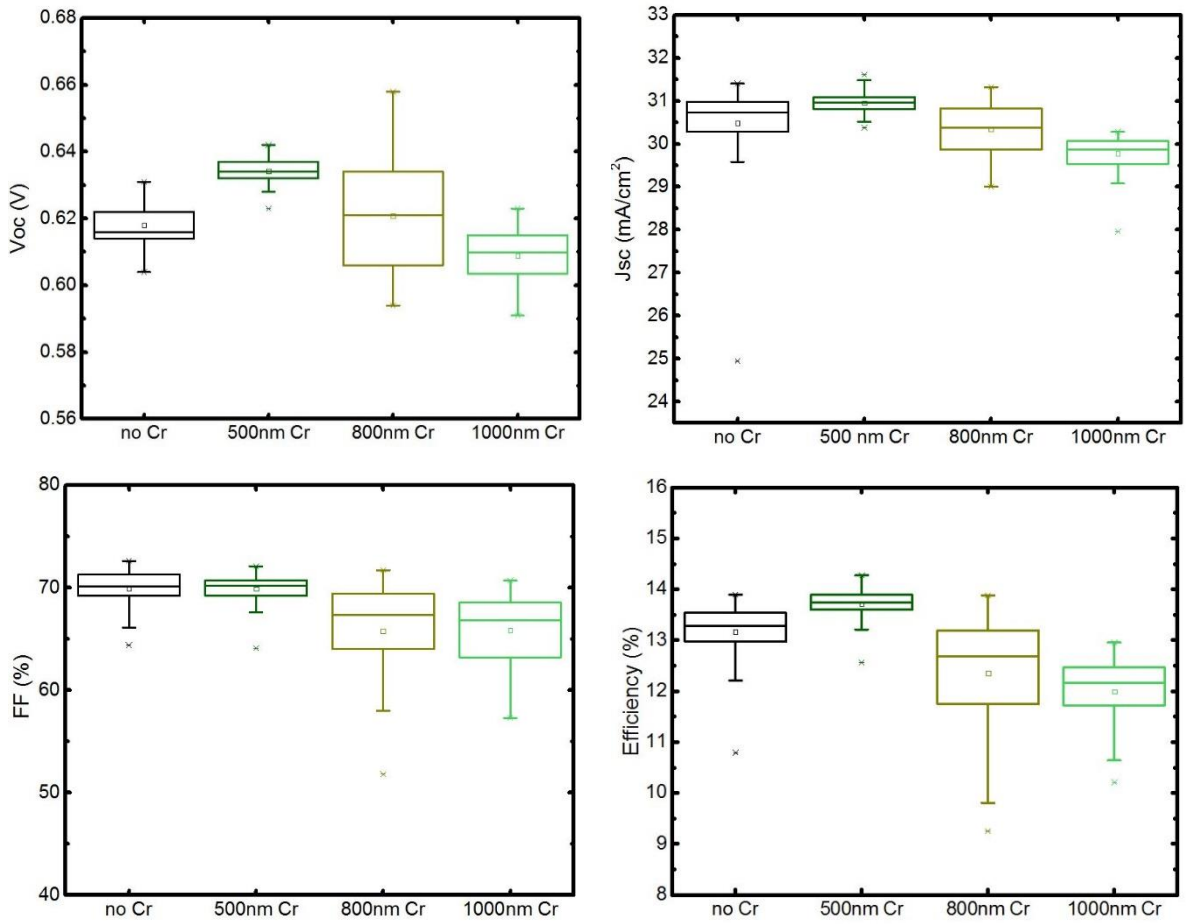


Figure 4.7. Box chart summary of the electrical properties of the cells with a Cr barrier layer. The reference has no Cr barrier layer.

The fact that the performances of the cells were similar except for the inhomogeneity of 800 nm and 1000 nm samples leads to a conclusion that; (i) the 800 nm thick Mo back contact played a role in increasing the total effective impurity barrier as this has already been confirmed that the back contact can impede the diffusion of Fe impurity [4] [17] and (ii) the deposition temperature of 480 °C which is the standard process temperature was not high enough to trigger the diffusion of Fe impurities detrimental enough to severely degrade cell performance [21]. The EQE response of the cells (figure 4.8a) are almost identical with no major differences that can be attributed to the presence of the Cr barrier layer. In fact, the difference in Jsc between the best cell (500 nm Cr) and the reference cell is 0.7 mA/cm^2. The best cell, achieved with a Cr barrier thickness of 500 nm is shown in figure 4.8(b)

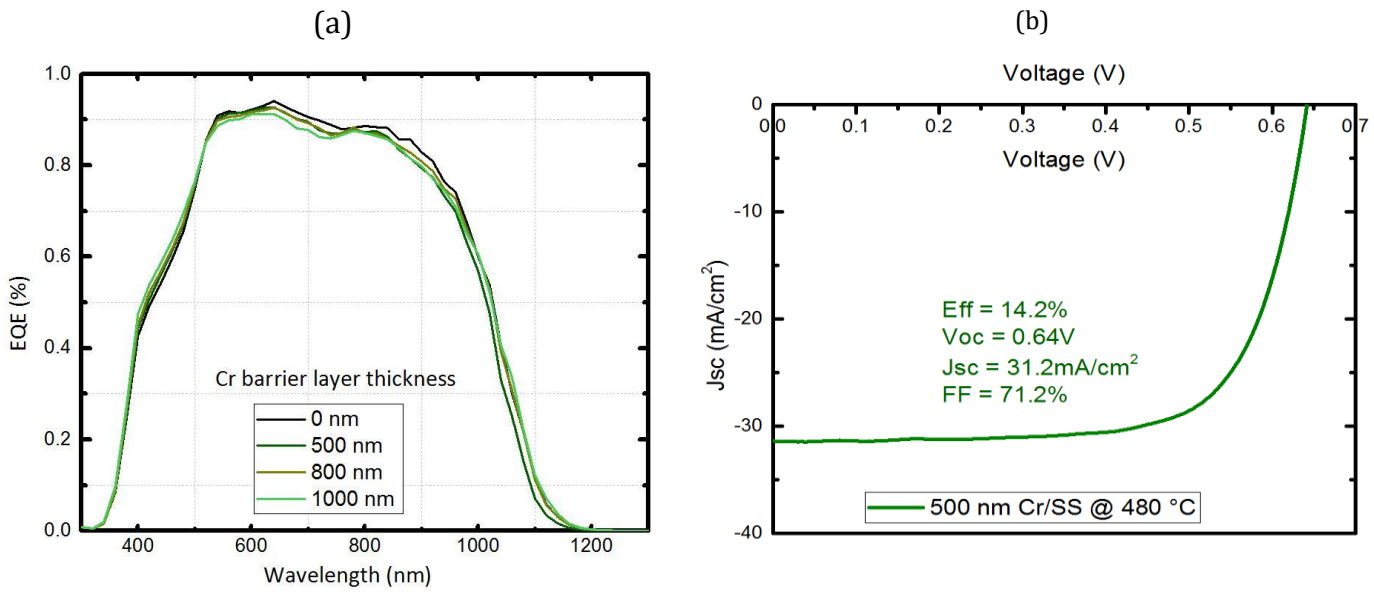


Figure 4.8. (a) EQE spectral response of the cells with varying thickness of Cr barrier layer and (b) I-V curve of the best cell with 500 nm of Cr barrier layer.

4.3 IMPACT OF SUBSTRATE TYPE ON CIGS ABSORBER GROWTH AT LOW TEMPERATURE

In section 4.1, we discussed the properties of the stainless steel substrates used in this work. While in previous chapter absorber with high Ga content were prepared, in this section the impact of four different types of stainless steel substrates without any barrier layers on the growth of the absorbers will be studied. In this part the optimized 3-stage process for Mo substrates at a temperature of 480 °C (see sec. 3.4) will be used for the CIGS growth. The stainless steel substrates used in this study were supplied by Aperam and consists of four types differing in their in terms of their roughness and elemental composition.

4.1.1 Elemental composition of the substrates

Stainless steel is mainly composed of Iron which is alloyed with other metals in varying proportions to match its desired application. We measured the respective elemental compositions of the four stainless steel types using EDX measurements. The results are presented in table 4.2. The table shows only the main constituents of steel type. Substrates type II and III have thicknesses around 0.2 mm while substrates type I and IV are slightly thickness (0.3 and 0.25 mm respectively). These thickness were provided by the manufacturer as part of the product specifications.

Stainless Steel	Thickness (mm)	Cr (%)	Ni (%)	Mo (%)	Si (%)	Fe (%)
Type I	0.3	16.4	-	-	0.70	82.9
Type II	0.2	20.6	-	1.1	0.68	76.8
Type III	0.2	17.2	-	-	0.64	82.1
Type IV	0.25	20.5	7.5	-	0.64	71.4

Table 4.2. Elemental composition of the stainless steel substrates

As observed in table 4.2, all four substrates are mainly composed of Fe (70-80%) and Cr (16-20%) with traces of Si (0.65-0.70 %). Substrate type IV contains also about 7.5% of Ni which is absent in the other substrates while type II contains trace amount of Mo (~1%).

4.1.1 Surface morphology

The SEM images of the surface morphology of the stainless steel substrates with a magnification of 10^4 are reported in Figure 4.1. As observed the, surface of the substrates are not completely smooth and some surface features can be seen across all steel types. These features arise from the fabrication and rolling process of the stainless steel substrates and have an effect on the general roughness of the substrates.

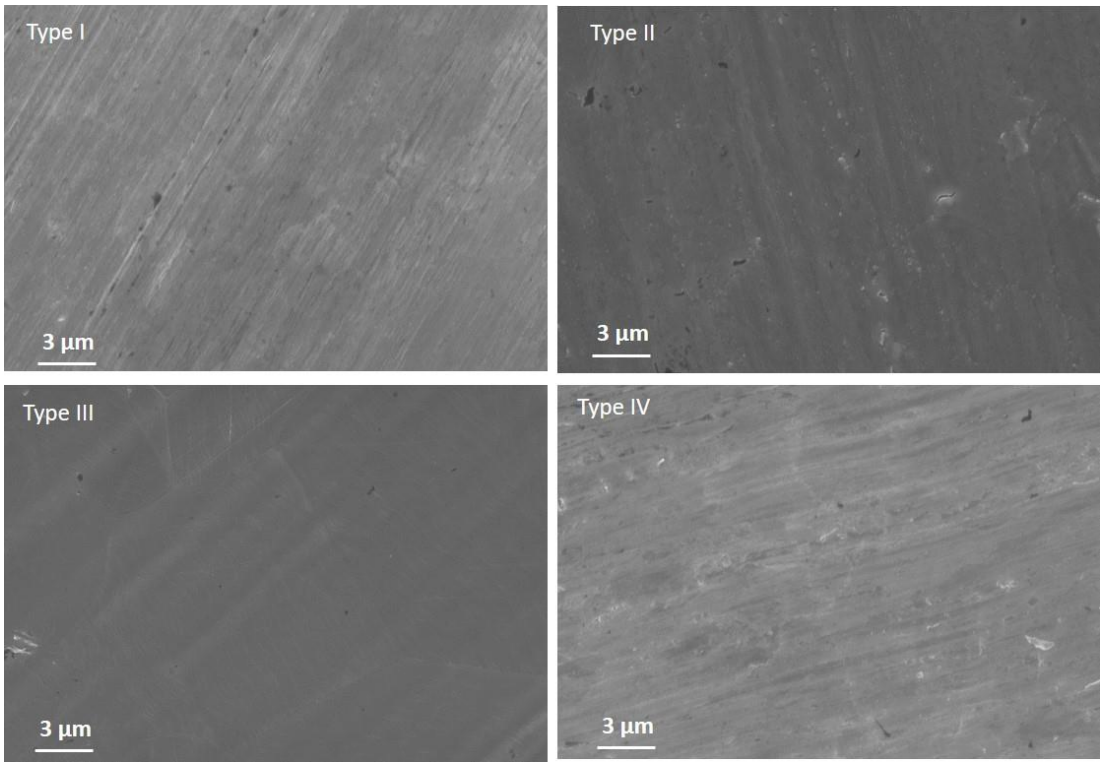


Fig. 4.1. SEM surface image of the four stainless steel substrates showing their surface features.

AFM is a more accurate and precise way of observing these features and measuring the roughness of the surfaces. In figure 4.2, the 2D and 3D AFM scans of the surfaces are shown. The measurements were done across a 20 × 20 µm surface area of the respective substrates. Table 4.3 lists the average roughness of the substrates. The AFM scans shows troughs and peaks with random distribution across the surface of the substrates. Type I and IV have the same average roughness of ~82 nm. Type II has the lowest surface roughness of 67 nm while type III emerged with the largest surface roughness.

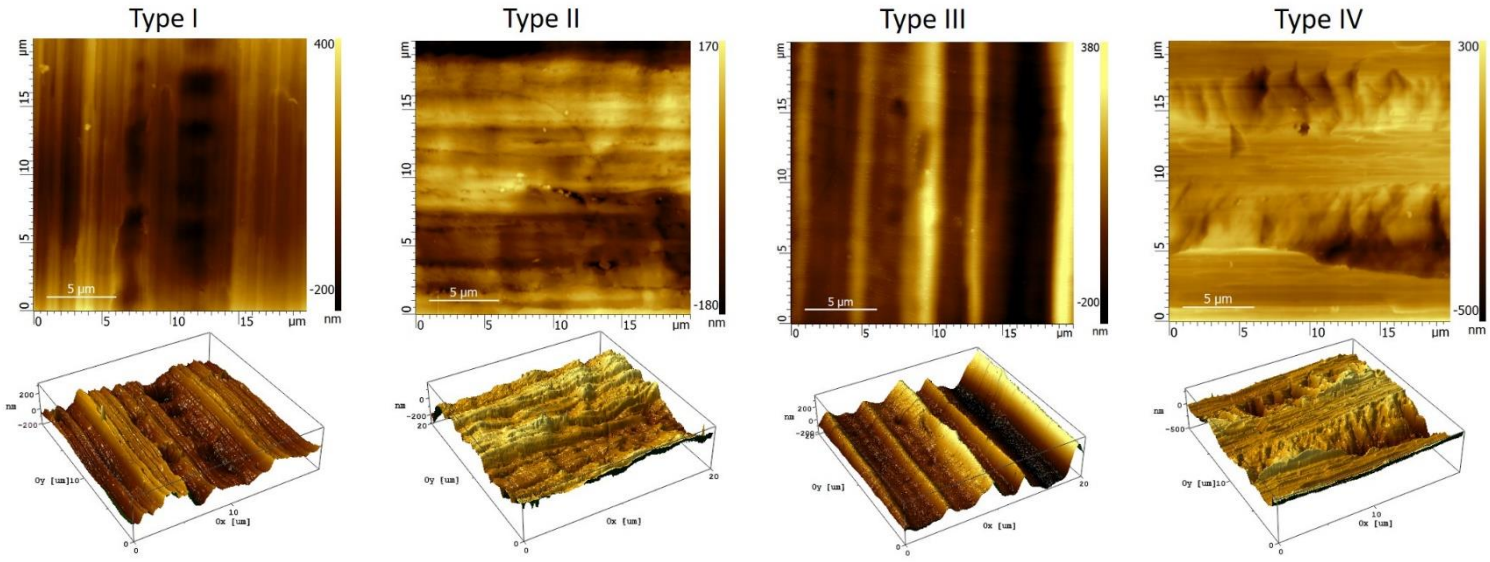


Fig. 4.2 AFM 2D and 3D scans of the stainless steel substrates supplied by APERAM

The roughness of the substrates are still considerably much higher than that of SLG which is only a few nm (~3 nm) or that of the Mo/SLG stack which is less than 10 nm depending on the sputtering conditions. These surface irregularities can have a negative impact on the performance of CIGS cells fabricated on these substrates (see section 1.3.4).

Stainless Steel	Thickness (mm)	R_a (nm)
Type I	0.3	82
Type II	0.2	67
Type III	0.2	93
Type IV	0.25	83

Table 4.3 Average surface roughness of the stainless steel substrates.

4.3.1 Absorber Deposition

The stainless steel substrates were cleaned in an ultrasonic bath for 20 min followed by a sputter deposition of 800 nm Mo back contact layer on the stainless steel substrates. Table 4.8 summarizes the process parameters for the absorber deposition and Na incorporation. The imposed substrate temperature in the first stage is 400 °C and is ramped up to 480 °C at the start of the second stage. After the formation of a slightly Cu-poor film at the end of the 3rd stage, the substrate temperature is ramped down to 350 °C

and post-treated with NaF according to the Na incorporation method discussed in sec 3.3. After Na post-treatment, the absorber is further annealed for 10 min and finally ramped down to room temperature. A reference sample on a Mo foil substrate was also made for comparison.

(1st stage)	
Substrate Temperature, T_1	400 °C
In Flux	6.3 nm/min
Ga Flux	2.7 nm/min
(2nd stage)	
Substrate Temperature, T_2	400 ↗ 480 °C
Cu Flux	8.0 nm/min
(3rd stage)	
Substrate Temperature, T_3	480 °C
In Flux	7.5 nm/min
Ga Flux	2.0 nm/min
(NaF PDT)	
Substrate Temperature, T	350 °C
NaF Flux	2nm/min
Se Flux	57 - 61 nm/min
Duration	20 min
Annealing in Se atmosphere	10 min

Table 4.8 Summary of deposition parameters used on stainless steel substrates.

The cells were completed by depositing the CdS buffer layer via chemical bath deposition and depositing the i-ZnO/ZnO:Al window layer by sputtering.

4.3.2 Absorber material characterization

The final composition of the absorbers were measured by XRF and SEM imagery was used to study the morphology of the absorber layers. The Ga depth profile was measured using GDOES to visualize the evolution of the Ga content in the films while electrical measurements were done to study the I-V characteristics of the cells made from these absorbers.

- Absorber composition and morphology

The final absorber composition of the films measured by XRF for the [Cu]/[Ga]+[In] (CGI) and [Ga]/[Ga]+[In] (GGI) ratios is shown in table 4.9.

	CGI	GGI
Steel Type I	0.83	0.28
Steel Type II	0.84	0.28
Steel Type III	0.83	0.28
Steel Type IV	0.85	0.28
Mo foil	0.81	0.24

Table 4.9. Elemental compositions of the CIGS absorber deposited on four types of stainless steel substrates.

The values for the GGI of the absorber layers are identical (GGI = 0.28) for all the samples. The CGI also can be regarded as constant ($0.83 \leq CGI \leq 0.85$). This is expected as the layers were fabricated in the same experimental run. On the other hand, the reference sample on Mo foil exhibited a lower GGI (0.24) and CGI (0.81). SEM cross-section of the individual samples reveals the grain sizes inherent in the samples (figure 4.8). All the CIGS thin films fabricated on the stainless steel substrates exhibit small grain sizes (~150 – 200 nm) originating at the back surface and extending through the bulk of the films to the surface. The grains increase in size near the front surface (300 – 350 nm) but these are still quite small grains when compared to the reference CIGS film on the Mo substrate (grain size ~600 nm). The grains on the Mo foil are very well crystallized to form large grains with less grain boundaries. The large grains extend from the back contact to the surface of the CIGS film. Large grain sizes in CIGS are usually ascribed to a higher substrate temperature which leads to the formation of single-phase films during recrystallization and hence larger grain size [22][23]. Since the imposed substrate temperature was the same for all the fabricated absorbers, a possible explanation for the observed difference in grain sizes might be the difference in the thermal conductivity of Mo and stainless steel. Mo has a high thermal conductivity (142 W/mK) which is one order of magnitude greater than that of stainless steel (14.5 W/mK) hence making it a much better conductor of heat than

stainless steel. This means that Mo will reach a set temperature much faster than stainless steel when both materials are heated at the same rate. Hence, in the second stage of the deposition process when the substrate temperature is ramped up, we predict that the CIGS film growth on Mo foil will reach the set temperature quickly which will favor recrystallization and formation of larger grain sizes.

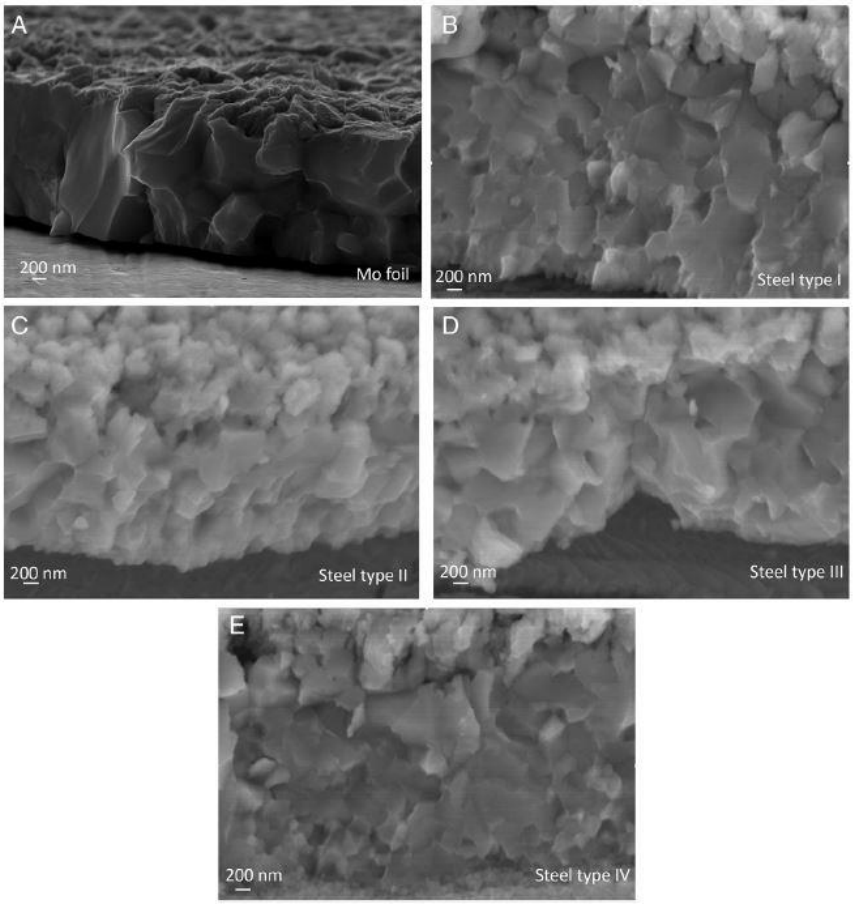


Figure 4.8. SEM cross section of CIGS absorbers deposited on (a) Mo foil (b) Stainless steel type I (c) Stainless steel type II (d) Stainless steel type III (e) Stainless steel type IV.

- ## Gallium grading and absorber crystal structure

The gallium gradient in the absorbers was measured by GDOES. Figure 4.9 compares the evolution of GGI profile through the bulk of the absorbers made on the different stainless steel substrates and on the Mo foil. Although the deposition of absorbers on different substrates were made with the same process parameters and in the same run, the Ga gradient in the GDOES measurement differs from one sample to the other. Stainless steel type I and II have identical profiles while on type III and IV, there is an accumulation of Ga near the back contact and front surface of the absorber.

In general, the notch of the CIGS films on stainless steel is lower than that on Mo. Surprisingly, on Mo foil with a GGI of 0.24 measured by XRF, we observe that the Ga grading towards the front and back and also the notch is higher than for stainless steel substrates. Normally we would expect the notch to be lower and to correspond to the value obtained from the XRF measurement. This should be further investigated. Steel type III and IV profiles at the back side are closer to the absorbers deposited on Mo substrates

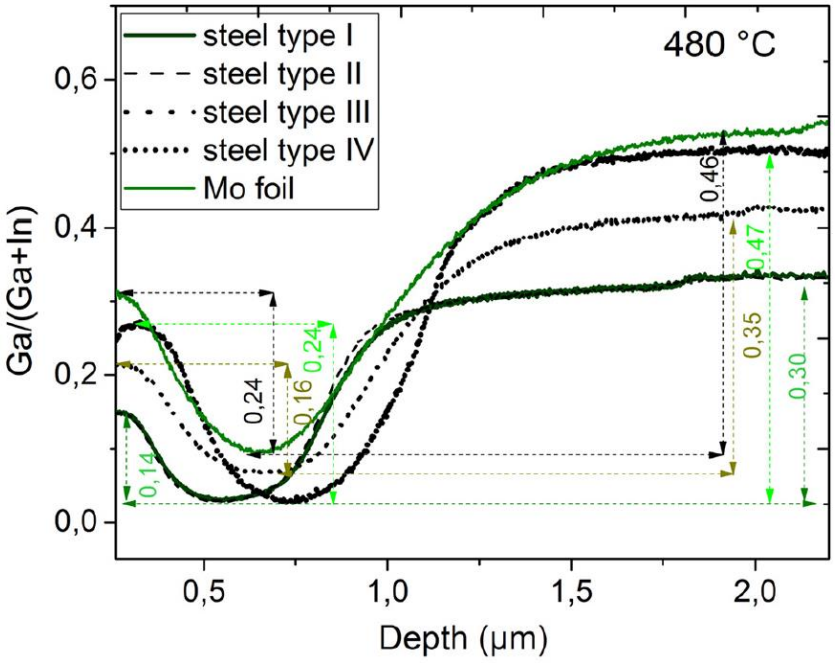


Figure 4.9. GDOES profile showing the evolution of the GGI of the films across the bulk of the absorber.

The Ga profiles of the absorbers on stainless steel type III and IV do not follow any trend with respect to substrate thickness or surface roughness regardless of having the same GGI value (0.28). This might suggest the presence of Ga-rich and Ga-poor CIGS phases in the absorbers. The XRD diffractogram of the samples in figure 4.10 gives some insight on this. Contrary to what is observed on Mo foil substrate where the preferred CIGS orientation perpendicular to the (112) lattice plane, the preferred CIGS orientation on the stainless steel substrates is perpendicular to the (220)/(204) lattice plane. The orientation of CIGS films prepared by coevaporation has been shown to depend on several parameters including substrate type, temperature and orientation of the Mo back contact [24][25][26].

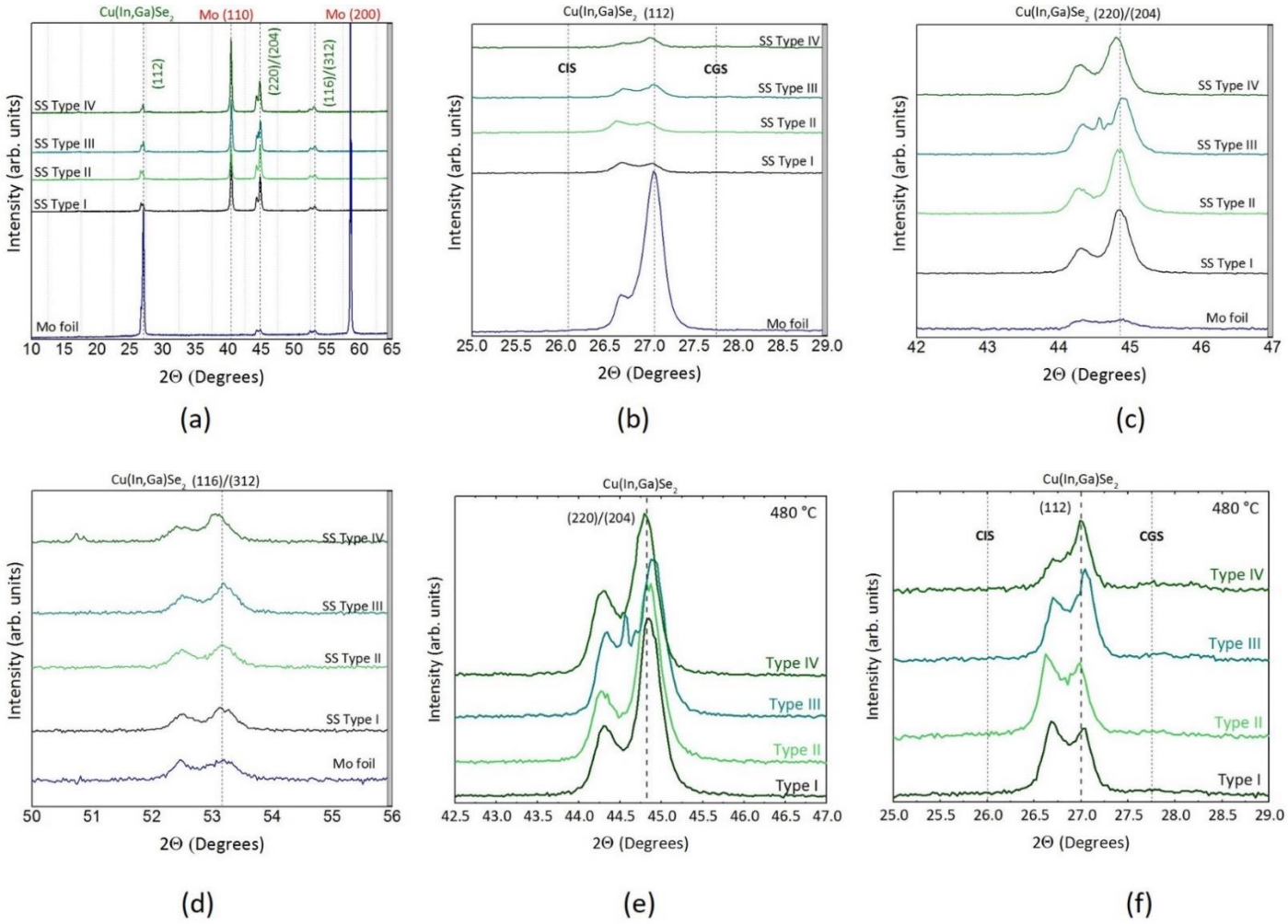


Figure 4.10. XRD diffractogram of CIGS absorbers deposited on (a) different stainless steel substrates. The CIGS absorber made on Mo foil has also been added for comparison, (b) XRD diffractogram showing the (112) intensities of the samples (c) XRD diffractogram showing the (220)/(204) peak (d) XRD diffractogram showing the (116)/(312) peak, (e) and (f) are the (220)/(204) and (112) peaks of only the absorbers on stainless steel.

The orientation of sputtered Mo is perpendicular to the (110) lattice plane which resulted in a preferred (220)/(204) orientation of the CIGS absorbers made on stainless steel. This confirms what was reported by Schlenker *et al.* that on (110)-oriented Mo, the orientation perpendicular to the (220)/(204) lattice plane is usually preferred in the CIGS absorbers [27]. However, the orientation of Mo foil is preferentially perpendicular to the (200) and (211) lattice planes although the (211) peak for the Mo foil is not shown. Figure 4.10(b) – (d) compares the (112), (220)/(204) and (116)/(312) CIGS peaks of the samples on stainless steel versus that on Mo foil which clearly shows the preferential orientation of the films to be perpendicular to the (112) lattice plane on Mo and perpendicular to the (220)/(204) lattice plane on stainless steel. In figures 4.10(e) and (f), only the absorbers on the stainless steel substrates are presented. The presence of two CIGS phases is

confirmed by the appearance of a double peak. In figure 4.10(e), a double peak is observed on the four substrate types with the exception of type III where 3 peaks are observed. This supplementary peak observed at 44.5° on the type III stainless steel is likely an artefact. The double peaks have been identified by comparing with the ICDD 00-035-1102 database for CIGS. The peaks correspond to different CIGS phases mainly the Ga-rich and Ga-poor phases. What is observed is a more intense peak for the Ga-rich phase ($Cu(In_{0.4}Ga_{0.6})Se_2$) occurring at 2θ = 44.9° and a smaller peak for the Ga-poor phase ($Cu(In_{0.7}Ga_{0.3})Se_2$) at 2θ = 44.4°. In figure 4.10(f), the phases identified are the $Cu(In_{0.7}Ga_{0.3})Se_2$ (Ga-poor) occurring at 26.6° and $Cu(In_{0.4}Ga_{0.6})Se_2$ (Ga-rich) occurring at 27.1°. The two dotted lines mark the peak positions for a pure CIS and pure CGS film. The position of the double (112) peak for the films on stainless steel type III and IV shifts to higher 2θ values which could mean that the Ga-rich phase is dominant. This is supported by the increase of Ga content towards the back and front contact of the absorbers as shown in figure 4.6. In stainless steel types I and II, the intensity of the peak at 2θ = 26.6° is higher than the one at 27.1° indicating a higher proportion of the $Cu(In_{0.7}Ga_{0.3})Se_2$ phase. Figure 4.11 compares the Raman spectra of the individual samples.

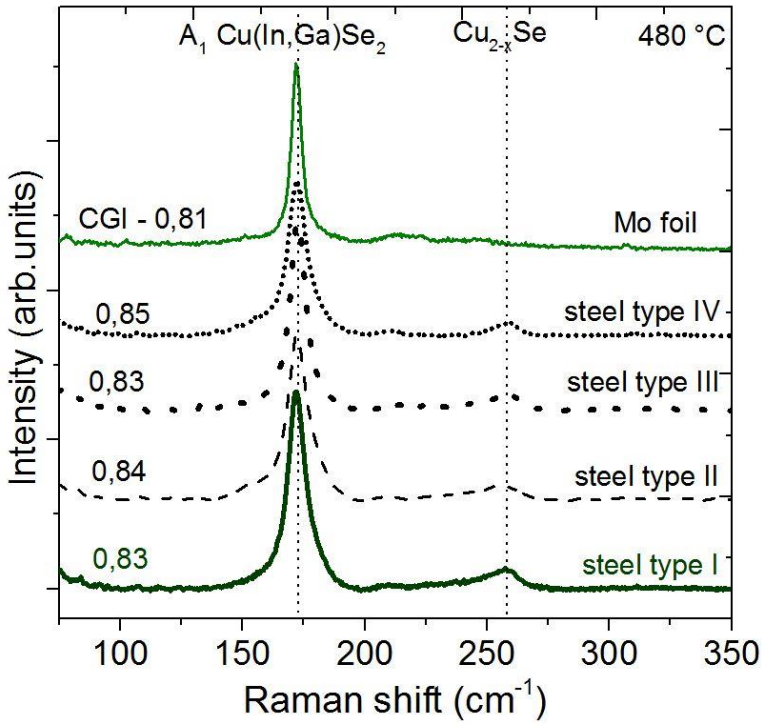


Figure 4.11. The Raman spectra of the CIGS absorbers deposited on stainless steel types I – Iv and on Mo foil

The A_1 mode for the CIGS films lies between a Raman shift of 172–178 cm^{-1} [28]. It is also observed that the CIGS absorbers on the steel substrate exhibit an additional mode

occurring at ~260 cm^{-1} which is usually assigned to the A_1 mode of Cu-Se binary compounds [29] [30] [31]. This is however not seen on the CIGS absorber deposited on Mo foil. Typically, Ordered Vacancy Compounds (OVC) phases should appear as a broad left shoulder at around 150 cm^{-1} for the Cu poor samples (CGI < 0.7) [28] [32]. However our samples had a CGI above 0,7 and although the samples on the steel substrates had a slightly higher CGI compared to that on Mo, the shoulder broadening due to OVC phases is not observed. These results lead to conclusion that the roughness of the individual stainless steel types did not have an impact on the growth of the CIGS absorbers and the performances of the solar cells.

4.3.3 Solar device properties

The performance of the cells was evaluated from their respective I-V characteristics measured under an illumination of AM 1.5G at 25 °C. Figure 4.12 shows the distribution of the electrical parameters of each of the solar cells as a function of the type of the substrate used. Their performances are summarized in Table 4.10.

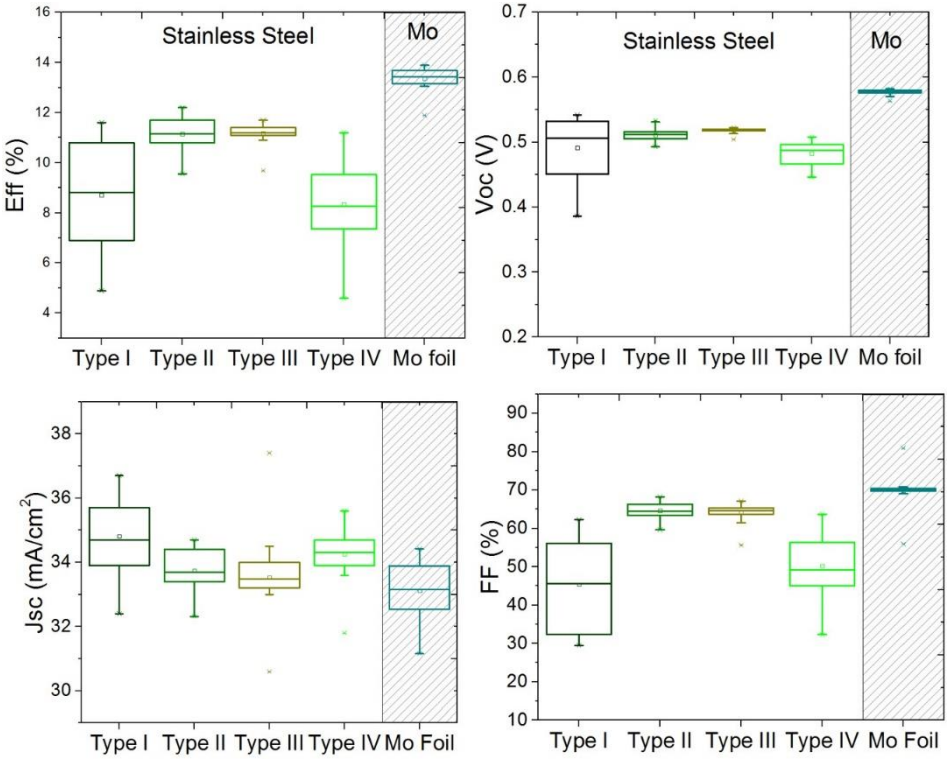


Figure 4.12. Box chart showing the distribution of the electrical parameters of the cells on various stainless steel type I – IV and on Mo foil.

The cells made on type II and III stainless steel had the least dispersion in their electrical properties especially fill factor and Voc. This points a higher degree of homogeneity compared to types I and IV. A maximum Voc of 530 mV was achieved on type I stainless

steel and this value dropped to 520 mV for types II and III and 510 mV for type IV. The Jsc of the cells on the stainless steel substrates was fairly constant between 34 mA/cm^2 – 35 mA/cm^2. The fill factor on the other hand was 68 % and 67 % for the cells on type II and III respectively which both had the least substrate thickness of 0.2 mm. As the thickness of the substrates increases up to 0.3 mm (type I), the fill factor decreases accordingly reaching 62 %. The maximum efficiency obtained was 12.2 % on type II stainless steel. However, all the cells on the stainless steel substrates did not perform better than the reference cell on Mo foil which exhibited superior properties and reached a maximum efficiency of 14.0 %. This efficiency resulted notably from a better Voc and fill factor compared to stainless steel.

	Eff (%)	Voc (mV)	Jsc (mA/cm^2)	FF (%)
Steel Type I	11.6	530	35.3	62
Steel Type II	12.2	520	34.5	68
Steel Type III	11.8	520	34.0	67
Steel Type IV	11.2	510	34.5	64
Mo foil	14.0	580	34.2	70.4

Table 4.10. Summary of best cell performances on stainless steel and Mo foil reference.

In summary, it is observed from figure 4.12 that the most homogeneous results are obtained on steel type II and III as well as on the Mo foil. This homogeneity observed in type II and III can neither be explained by the surface roughness of the substrates nor by the Ga gradient in the absorbers. There is no trend linking the homogeneity of results observed to the roughness of the substrates. Moreover the Ga gradients in both cells are different. At this stage, one can postulate that beyond the roughness of the substrate and the Ga gradient of the absorber, there must be some other phenomena impacting the solar cell performance. This could be due to the diffusion of some impurities (Fe) from the substrate to the absorber and not easily detectable by GDOES, XRF or EDX measurements [33] [34] [4]. it is noteworthy that a reference cell on soda lime glass (SLG) (not shown) made using the same process reached an efficiency of 15,7% with a Voc of 640 mV, Jsc of 34.2 mA/cm^2 and fill factor of 71.7 %. This further suggests that the poor performances of the cells on metallic substrates are either substrate dependent or due to poor Na

incorporation. Hence further analysis and optimization is required to improve the performance on the metals.

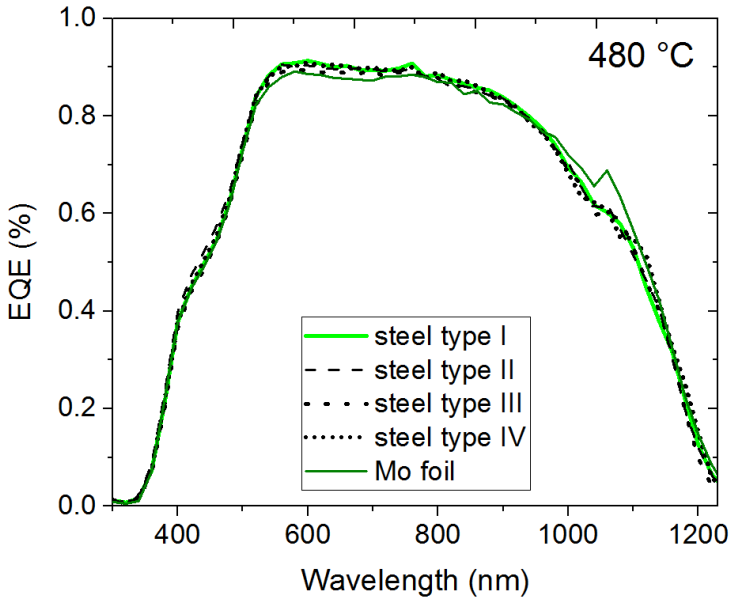


Figure 4.13 (a)The EQE spectral responses and (b) the I-V curve of the samples

The EQE responses in figure 4.13(a) are identical. This makes it difficult to correlate the EQE response curve to the data obtained from GDOES. Indeed, we expected to see a higher absorption of photons in the long wavelength region of the spectrum for the cells on the stainless steel substrates since they had a lower Ga notch. However, this correlates quite well with the measured Jsc of the samples.

4.3.4. Summary

CIGS cells have been made on a Mo substrate and 4 stainless steel substrates differing mainly in their elemental compositions with varying amounts of Fe and Cr as well as their polishing. The CIGS absorbers were deposited using a 3-stage deposition process optimized specifically for Mo substrates. As expected, the cell on the Mo foil reached better efficiencies up to 14.0 %. On the other hand, the best efficiencies among the stainless steel substrates was 12.2 % and was achieved on stainless steel type II. Analysis has shown no correlation between the cell performance, the substrate roughness and Ga gradient in the absorber. The SLG reference cell had an efficiency of 15,7% and by comparing the Voc of all the cells, it becomes clear that either the post-treatment of Na might be inadequate on the metallic substrates or some impurity diffusion occurred leading to significantly lower Voc. However, there remains much room for improving the cell performance on stainless steel. The steps to be taken to improve the electrical

properties of the cells include studies on process optimization, Ga gradient, impurity diffusion barrier incorporation and Na incorporation.

In the last part of the thesis, CIGS depositions have been made using another coevaporation system at the Institut des Matériaux Jean Rouxel, Nantes (IMN) and incorporating the CURO coevaporation process.

4.4 CURO DEPOSITION PROCESS

The last part of the thesis were carried out at Institut des Matériaux Jean Rouxel, Nantes (IMN). The experimental work on the stainless steel substrates was done using the **CURO** (Cu – Rich – Off) and the 3-stage processes. The 3-stage process has already been discussed in details (sec. 2.2.1). The CURO process is an acronym for "Copper-Rich-Off". As the name denotes, it is a 2-stage coevaporation process that starts with conditions that favors Cu-rich growth. This can lead to larger CIGS grain sizes.

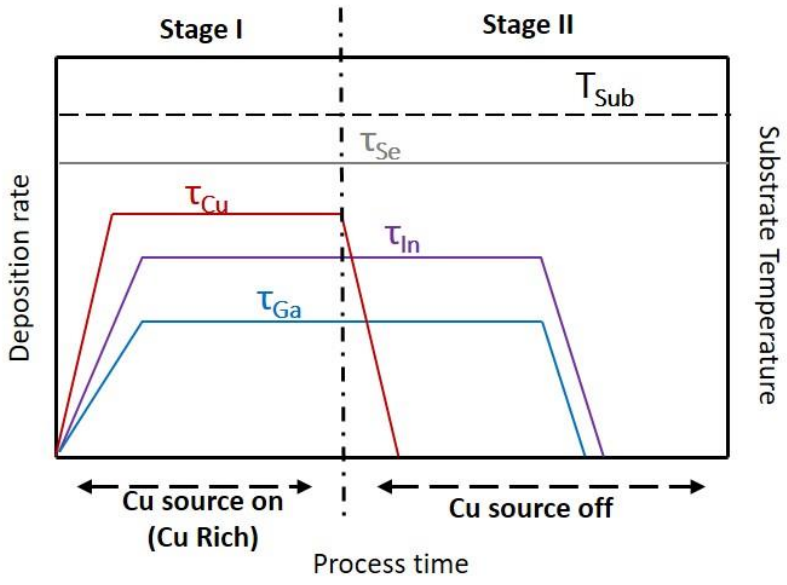


Figure 4.12 Graphical illustration of the CURO process. τ represents the fluxes of the individual elements

As seen in figure 4.12, the CURO process is achieved by supplying a high Cu flux in relation to the In and Ga fluxes. This ensures that a Cu-rich film is formed in the first stage when the sources are open and left for a pre-set duration. At the start of the second stage, the Cu flux is turned off while the In and Ga fluxes are left constant. This converts the Cu-rich film into a final Cu-poor absorber layer. Hence the process is called CURO as the growing film goes from Cu-rich to a final Cu-poor (after the Cu flux is turned off). The presence of excess Cu at the beginning of the process leads to the formation of Cu-Se phases between

the crystals of the chalcopyrite phase. This can result in a relatively rough morphology due to an intermixing with In and Ga in the second stage of the process [35] [36]. A high substrate temperature (500 – 600 °C) is used in this process and is kept constant. A Se overpressure is employed to ensure proper incorporation of Se in the growing film. The Se-to-metal ratio is ~5 in order to reach sufficient Se content. The In and Ga fluxes in the second stage start to consume the Cu-Se (Cu-rich) phase. This continues till the emissivity of the film starts to decrease until all the Cu-Se binaries have been consumed leaving a stoichiometric film. Since the fluxes of In and Ga are still left on for a short time after reaching stoichiometry, the final film is slightly Cu-poor.

4.5 FABRICATION OF CIGS ABSORBERS VIA THE CURO PROCESS

In this section, the CURO process is employed for the growth of CIGS films on the stainless steel substrates. No barrier layer is deposited on the stainless steel substrates. The goal is to investigate the effect of the deposition process on the quality of the CIGS absorbers grown on the steel substrates. The principles governing the different coevaporation processes used in this thesis have already been explained in sec. 4.4). Samples were fabricated on SiN coated SLG, stainless steel type II and Mo foil substrates using the same process parameters. The SLG substrates were coated with SiN to block the diffusion of Na and mimic the CIGS growth on Na-free substrates. All the samples were subsequently subjected to NaF post-treatment to incorporate Na in the films.

4.5.1 CIGS absorber baseline at IMN

The Cu(In,Ga)Se_2 absorber deposition procedure is based on the standard deposition process used on SLG substrates at IMN. The process has been applied directly to the stainless steel substrates with no modification. The setup in the coevaporation chamber for these depositions is similar to that described in figure 2.7 with three exceptions; (i) the substrate holder is stationary and does not rotate, (ii) the substrate heating mechanism is via a halogen lamp and (iii) there is no shutter for the Se source, hence the substrate is always exposed to Se flux.

The fluxes of the individual elements during the CIGS growth are controlled by varying the operating power (OP) of the elemental sources. The deposition process was carried out at a constant substrate temperature of 570 °C. The details of the process is shown in table 4.11.

CURO method (1st step)

Substrate Temperature	570 °C
In OP (T_{In})	21 % (932.8 °C)
Ga OP (T_{Ga})	22.5 % (1016.8 °C)
Cu OP (T_{Ga})	46 % (1260 °C)
Duration	60 min

(2nd step)

Substrate Temperature	570 °C
In OP (T_{In})	21 % (932.8 °C)
Ga OP (T_{Ga})	22.5 % (1016.8 °C)
Cu OP (T_{Cu})	0 %
Duration	12 min

Table 4.11. Deposition parameters for the CURO process at IMN where OP is the operating power of the sources.

At the end of the CIGS growth, the samples were cooled to 400 °C and NaF post-deposition treatment was carried out on the samples with a NaF flux of 2.0 nm/min for 3 min. The Se flux is kept constant throughout the deposition. After NaF treatment, the samples remain exposed to the Se flux while being cooled down. When the substrate temperature reaches ~250 °C, the Se flux is turned off. A first set of samples was made on SLG and stainless steel in order to establish a baseline. Thereafter, depositions were made on stainless steel type II, Mo foil and SLG substrates to study the absorber properties. In these experiments, the CIGS depositions on the stainless steel were made with no barrier layer. However, the Mo back contact (~800 nm) sputtered on the stainless steel substrates can act as a barrier to Fe diffusion.

4.5.2 Excess Se deposition due to process incompatibility

The first batch of samples (on SLG and stainless steel) were deposited with the aim of confirming the process compatibility on the stainless steel substrates and establishing a baseline for the depositions. The composition of the CIGS films were measured by EDX and are enumerated in table 4.12. It is observed that when a glass substrate is used, a

slightly Cu-poor film (CGI = 0.98, GGI = 0.25) is obtained which ideally meets the baseline requirements for the CIGS films to be slightly Cu-poor with a GGI between 0.20 – 0.30. However, the samples fabricated on the stainless steel substrates reveal a peculiar result exhibiting a very high Se content (98.7 %) in the films which were also very Cu and Ga rich. This result was obtained on only the samples fabricated on the stainless steel substrate.

	Process	Cu (at. %)	In (at. %)	Se (at. %)	Ga (at. %)	CGI	GGI
1832-02 (SLG)	CURO	25.22	19.38	48.05	6.33	0.98	0.25
1834-02 (SS)	CURO	0.78	0.13	98.71	0.37	1.54	0.73

Table 4.12. CIGS absorber composition showing differences in elemental composition of the CIGS films on SLG and stainless steel using the same deposition method and parameters

To understand this phenomenon, SEM cross section imagery was carried out on the samples. Figure 4.14a and b shows the cross section of the CIGS absorbers on SLG and stainless steel acquired by SEM.

(a) (b)

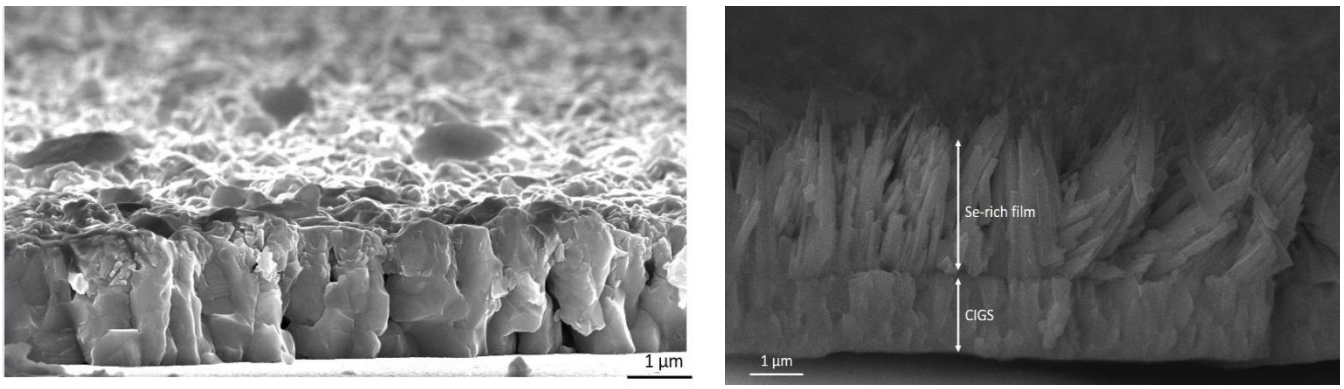


Figure. 4.14 SEM cross section of the CIGS absorber grown by the CURO process on (a) SiN coated SLG and (b) Stainless steel. The deposition process parameters are identical in both cases however, the stainless steel substrate is at a much lower temperature when the Se flux is turned off, hence leading to a deposition of the Se film seen in (b).

In figure 4.14a, the film is wholly CIGS and there is no excess Se accumulation on top of the CIGS absorber. On the contrary, in figure 4.14b, a few µm of Se film accumulated on the CIGS absorber layer creating two distinct layers; CIGS and a Se-rich film. This layer of Se-rich material is seen as spikes extending from the CIGS surface and having a well-defined interface with the CIGS layer below. This Se-rich layer is responsible for the high Se content (98.7 %) observed in the EDX measurements. This observation can be explained by reviewing the termination sequence of the standard depositions.

In standard depositions on SLG substrates, after NaF post treatment, the substrate temperature is ramped down to ~250 °C in a Se atmosphere before the Se is turned off. It should be noted however, that in the deposition system used here, there is no shutter for the Se source, hence turning off the Se flux (temperature ramp down to standby) does not immediately cut the Se supply. Instead, the Se flux falls gradually to zero as its source temperature drops. This means there will be a continuous deposition of Se on the surface of the absorber till the Se flux reaches zero. In the case of SLG, this does not pose any problem as the relatively high substrate temperature (250 °C) offsets the excess Se as most of it is re-evaporated. However in the case of stainless steel substrates which has a higher thermal conductivity, the substrate temperature falls faster than in SLG. Hence when the substrate set point temperature reaches 250 °C, the real substrate temperature in this *"cool down"* phase is already much lower than 250 °C. Therefore, any Se deposited on the surface is not re-evaporated from the absorber surface which will inevitably lead to a deposition of excess Se on the surface of the CIGS film. To avoid this unwanted excess Se deposition, the "cool down" phase was adjusted such that the Se flux was turned off while the stainless steel substrate temperature was around 300 °C. This ensures that the surface of the growing CIGS material is hot enough to re-evaporate any Se deposited during this phase. Figure 4.15 is an SEM image of the cross section of a sample grown with a Se cut off at a substrate temperature of 300 °C. There is no Se deposition observed as in the case just described above. The CGI and GGI are also within the expected range for device grade absorbers.

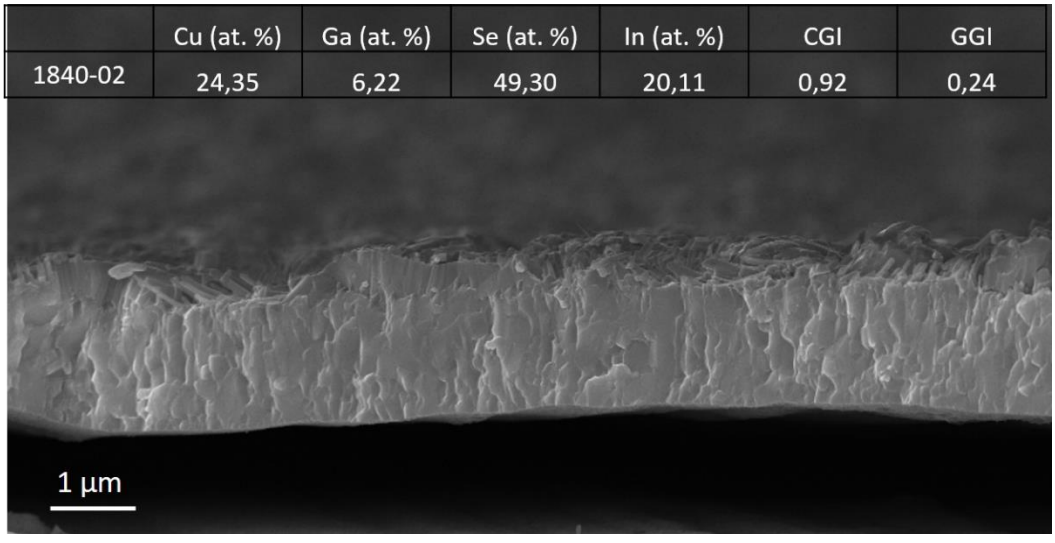


Figure 4.15. SEM cross section of a CIGS absorber grown by the CURO process on stainless steel. The substrate temperature for Se cut off has been increased to 300 °C.

In summary, the outcome of the CIGS absorber baseline experiment showed that the standard CURO process (typically applied on SLG) was incompatible with stainless steel. Hence, an adaptation of the process was necessary in order to obtain absorbers that were slightly Cu-poor and having no excess deposition of Se. In the next section, we will examine the properties of the CIGS absorbers deposited on stainless steel, Mo foil and SLG via the CURO process.

4.5.3 CIGS absorber properties

CIGS absorbers were grown on the 3 substrates (stainless steel type II, SiN coated SLG and Mo foil) using the CURO processes along with the parameters in table 4.13 and the modified cool down phase as described in sec. 4.5.1.

CURO (1st step)

Substrate Temperature	570 °C
In OP (T_{In})	23.5 % (983.3 °C)
Ga OP (T_{Ga})	27 % (1080.1 °C)
Cu OP (T_{Ga})	61 % (1367 °C)
Duration	25 min

(2nd step)

Substrate Temperature	570 °C
In OP (T_{In})	23.5 % (983.3 °C)
Ga OP (T_{Ga})	27 % (1080 °C)
Cu OP (T_{Cu})	0 %
Duration	13 - 22 min

Table 4.13. Deposition parameters for the CURO process at IMN where OP is the operating power of the sources.

- Absorber morphology and elemental composition

The elemental composition of the films were measured by XRF and presented in table 4.14. Since the process parameters are identical for all the depositions, we should expect a similar elemental composition in the CIGS absorbers. The absorbers grown on SiN coated SLG and stainless steel were identical in terms of their elemental composition with a CGI of 0.67 and GGI of 0.22.

	Cu (at. %)	In (at. %)	Se (at. %)	Ga (at. %)	CGI	GGI
1878 (SiN/SLG)	20.34	23.65	49.47	6.53	0.67	0.22
1880 (SS)	20.61	23.67	48.85	6.87	0.67	0.22
1881 (Mo)	22.17	14.77	55.73	7.32	1.00	0.33

Table 4.14. Elemental compositions of the CIGS films fabricated on various substrates by the CURO process

Although the same process was applied on all three samples, the absorber on the Mo foil (1881) has a CGI of 1.00 and GGI of 0.33 which is more Ga-rich than its counterparts. It is not fully understood why this variation occurs but the XRF data reveals an In content of 14.77 % which is much lower than what was obtained on SiN/SLG and stainless steel. This could suggest an inadequate supply of In during the deposition process. This hypothesis is inconclusive as there was no mass spectrometer present during the depositions in order to monitor the presence (or not) of the elemental species desired in each step of the deposition process. The cross section SEM images in figure 4.16 gives more information on the morphology and grain sizes of the samples.

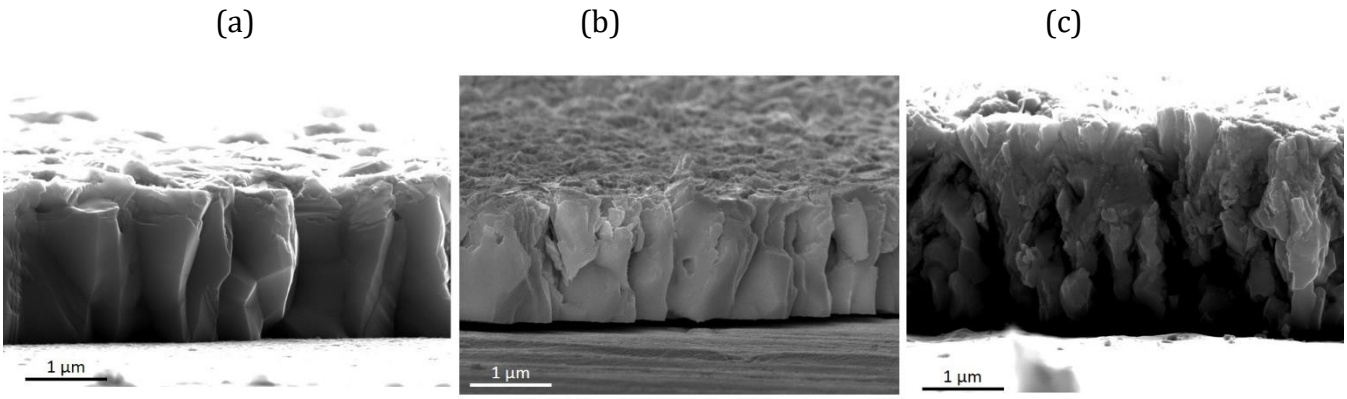


Figure 4.16. Cross-sectional SEM images of the CIGS thin films grown on (a) SiN coated SLG (b) Stainless Steel and (c) Mo foil.

The absorber deposited on SiN/SLG exhibited the largest grain size. The individual grains are columnar and span the entire thickness of the CIGS thin film. The absorber on the stainless steel substrate also exhibits large grains although not as well formed as those on SiN/SLG. A slight delamination of the CIGS absorber is also observed on the stainless steel substrate. On the contrary, the absorbers on the Mo foil substrate has very small grains. The small grains extends from the back contact to the surface of the absorber. Since all the samples were grown in Cu-rich conditions, large grain sizes are expected. However, the

appearance of small poorly formed grains on the Mo foil substrate might be correlated to the atomic compositions of each constituent element obtained from the XRF measurements especially the particularly low In composition on the Mo foil substrate.

- Absorber crystalline structure and Ga profile

In order to study the crystal orientation of the CIGS absorbers, XRD diffraction was performed on the samples. The results are shown in figure 4.17 and indicates the preferred orientation of the absorbers. The diffractogram depicts a preferred orientation perpendicular to the (112) lattice plane on the three substrates. The (220)/(204) and (116)/(312) peaks are also visible across the three substrates however with less intensity than the preferred (112) peak. The Mo (110) peak is detected only on the SLG and stainless steel substrate while the Mo (200) peak is visible on the Mo foil substrate. As already explained (sec. 3.1.1), the orientation of sputtered Mo is strongly perpendicular to the (110) lattice plane while the orientation of Mo foil is perpendicular to the (200) and (211) lattice planes. It is interesting to note that for CURO deposition process, unlike the results obtained in sec. 4.3, the preferential orientation of the CIGS absorbers is perpendicular to the (112) lattice plane regardless of the substrate used.

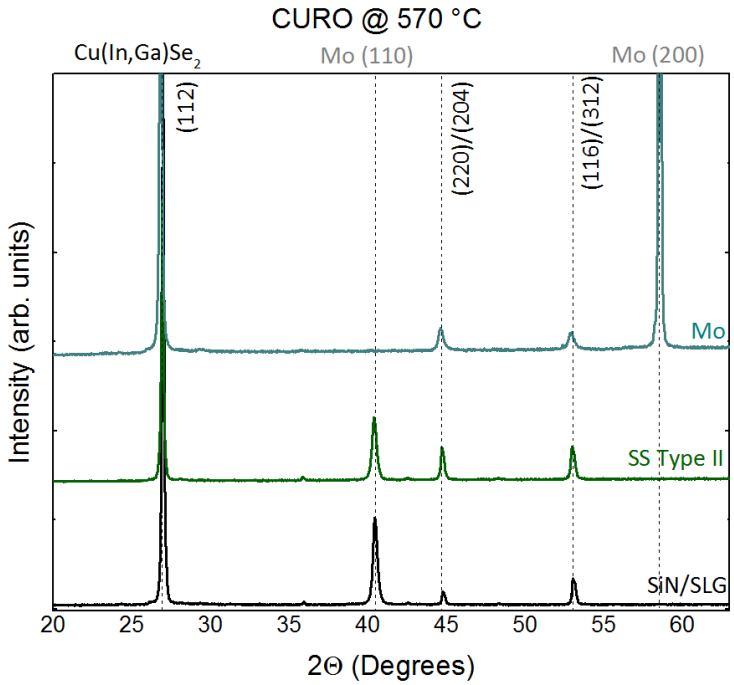


Figure 4.17. XRD diffractogram of the CIGS absorbers deposited by CURO process on SiN/SLG, Stainless steel and Mo foil.

The Ga composition across in the bulk of the CIGS absorbers as a function of the substrate used and measured by GDOES is shown in figure 4.18. The GGI on the three substrates

appears flat in the bulk of the absorber and then increases near the surface. The increase in the GGI composition near the surface is greatest for the absorber on SLG. The GGI of the absorbers grown on stainless steel and Mo are identical at a depth of ~0.7 µm from the surface to the back contact. The sharp increase in Ga content near the surface of the absorbers can indeed be explained by the design of the CURO deposition process.

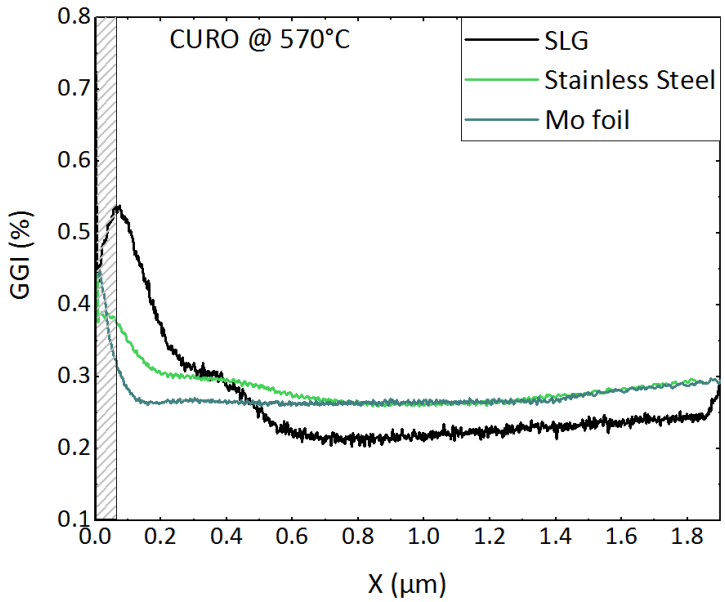


Figure 4.18. Ga profile in the CIGS absorbers grown on Si/SLG, stainless steel and Mo foil.

The GGI profile is relatively flat in the bulk because from the start of the process, Ga and In are evaporated alongside with Cu at a constant flux till a Cu-rich film is obtained.

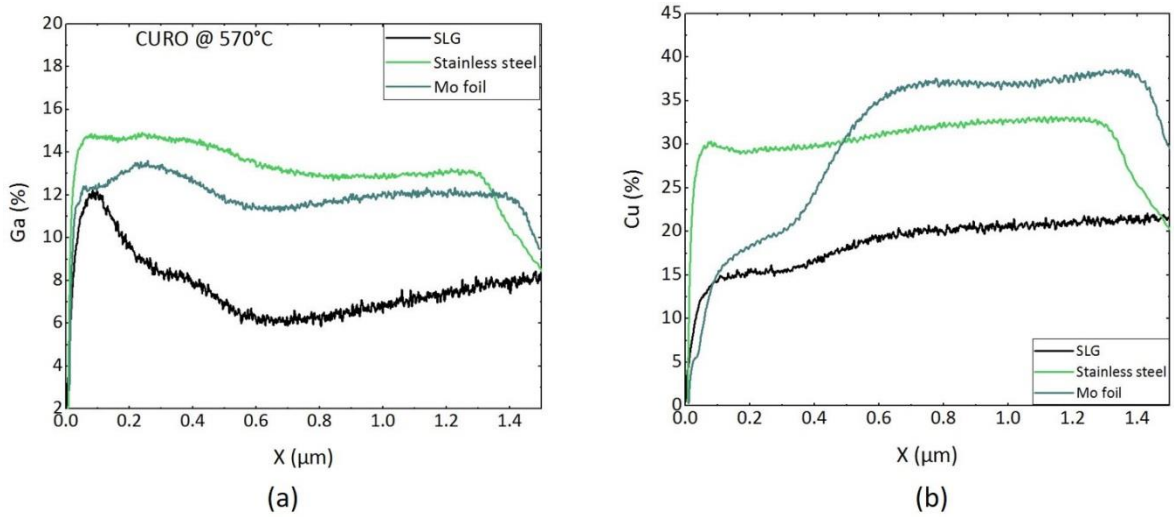


Figure 4.19 (a) Ga and (b) Cu profiles of the absorbers on different substrates measured by GDOES.

The sharp increase in the Ga content towards the front surface then occurs when the Cu flux is turned off, leaving only In and Ga fluxes which leads to a final slightly Cu-poor film. Hence, we can identify the sharp increase in Ga as the Cu-rich to Cu-poor transition in the CURO process. Figure 4.19a shows the Ga content in the absorbers. The increase towards the surface of the Ga content is observed here as in figure 4.18. The Ga compositions on the stainless steel and Mo foil however are considerably larger than on SLG. This contradicts the CIGS compositional results obtained from XRF where the GGI on SLG and stainless steel are identical (0.22). Furthermore, we can observe the occurrence of a Ga gradient, with a notch around 0.6 μm – 0.8 μm for the three samples. The Ga gradient is steeper on SLG than on the metallic substrates. This could be explained by the substrate temperatures, emissivity and conductivity (sec. 3.2.1 and 4.5.2). As explained, for the same imposed temperature, the real measured temperature on Mo foil and stainless steel is higher than that measured on SLG. The higher temperature of the metal substrates might have played a role in favoring a faster diffusion of Ga during the deposition process which hence manifests as a flatter gradient. The Cu profiles of the samples is shown in figure 4.19b and we can immediately observe that the Cu profile on the Mo foil is much higher than on SLG and stainless steel which is supported by the XRF measurements for the CGI of the samples. Although the samples on SLG and stainless steel had identical CGI and GGI values, the Cu composition of the sample on stainless steel is higher than on SLG and averages out at ∼30 % compared to ∼20 % on SLG. Moreover, the Cu content of the absorbers on SLG and Mo foil start to decrease at an absorber film depth of ∼0.6 – 0.7 μm. This coincides with the sharp increase in the Ga content (figure 4.18 and 4.19a) and the position where the increase in the Ga content occurs. By contrast, on the stainless steel substrates, the Cu drops very sharply at the surface of the absorber.

In the last part we tried to fabricate solar cells from the absorber, however, unfortunately no functioning cell was obtained as the cells were shunted. This occurred due to the mechanical scribing method which was neither adequate nor adapted to the metal substrates.

CONCLUSION

This chapter has so far discussed the results of various tests involving the deposition of CIGS absorbers on flexible stainless steel substrates. Firstly, the properties of stainless steel that makes it an attractive candidate for CIGS cell fabrication was presented. Stainless steel has a very high fusion temperature which makes it suitable for high temperature processes (>600 °C) sometimes encountered in CIGS fabrication. With a coefficient of thermal expansion (CTE) of 9.4 – 12.5 × 10^{-6} K^{-1}, stainless steel is quite suited for CIGS absorber growth since there is a close match between the thermal expansions of both materials.

The main challenge with stainless steel substrates is the presence of Fe which is the main alloying metal in steel. Fe atoms are very detrimental to CIGS solar cells hence it is imperative to devise a means of preventing such detrimental diffusion of Fe. Most commonly, an impurity barrier layer is deposited on the stainless steel substrates prior to the back contact deposition. Another way is to implement a low temperature CIGS deposition process since the diffusion of Fe is directly proportional to temperature. A concise literature review was presented which reviewed the common barrier materials that have been used on stainless steel substrates. Subsequently, we tested the effectiveness of a Cr barrier layer in blocking Fe diffusion in the absorbers. An annealing test revealed the extent of Cr diffusion in the back contact after heating up to 520 °C. In order to really reduce the impact of Fe, we combined the Cr barrier layer with a relatively low temperature process (480 °C) which has been used extensively in this thesis. The results showed a decreasing Fe content as the thickness of Cr increased as measured by EDX. The samples have similar performances except for the cell with a 1000 nm thick barrier layer. The best result was obtained with a 500 nm thick Cr layer, with CIGS absorbers presenting a GGI around 0.46 and CGI around 0.91 leading to an efficiency of 14.2 % with a Voc of 640 mV, Jsc of 31.2 mA/cm^{-2} and fill factor of 71.2 %.

CIGS absorbers and cells were then fabricated on the four stainless steel types in order to compare the performances of the substrates and to compare them with Mo foil. For this set of experiments, the best CIGS deposition conditions, optimized in chapter 3 for Mo foils, were used. The average roughness of the four substrates was around 81 nm which is much higher than Mo/SLG stack (10 nm). The thickness of the substrates ranged between 0.2 – 0.3 mm.

Contrary to what was observed on Mo foils, the preferential orientation of the CIGS absorbers on the four stainless steel substrates was perpendicular to the (220)/(204) lattice plane. The grain sizes were generally smaller than the grain sizes of the absorber on the Mo foil substrate. Furthermore, no correlation was established between the stainless steel substrate roughness and the performance of the cells. A measure of the cell properties revealed stainless steel type II as the best performing among the group with an efficiency of 12.2 %. For these cells the GGI was around 0.84 and the CGI around 0.28. The Voc and fill factor of all the cells on the steel substrates however remained quite low; 510mV < Voc < 530mV and FF < 68 % which is lower than the reference deposited on Mo foil substrate (580 mV) and much lower than the reference deposited on SLG substrate (Voc = 640 mV).

These results clearly pointed out that due to the thermal conductivity and the composition of the substrate (the presence or absence of Na or other impurities such as Fe), the same CIGS deposition process parameters doesn't lead to similar absorber composition and cell performances. Finally a comparison of these results to the first set of results using a Cr barrier layer shows clearly that for stainless steel, higher efficiency can be obtained by varying the composition of the absorber and by increasing the GGI up to 0.48 and the CGI up to 0.91. However, regardless of the optimizations done, the cell performances remains lower than the SLG references.

In the last part of the thesis, a different deposition process, the CURO process was used for the CIGS growth on stainless steel type II at 570 °C, and compared to samples using SiN coated SLG and Mo foil substrates. First, a baseline was established by adapting the process to suit stainless steel substrates after it was observed that an excess of Se was deposited on the films when the Se cut-off temperature was too low for the stainless steel and Mo substrates. SEM images revealed very large columnar grains on SLG and stainless steel and small rains on Mo foil. The absorbers on Mo foil had a particularly high Cu and Ga content when compared to SLG and stainless steel. It is suspected that this might be due to inadequate supply of Indium during the process. The XRD diffractogram revealed a preferential orientation perpendicular to the (112) lattice plane of the films regardless of the substrate type. These results are different from the results obtained in chapter 3 showing clearly that for a 3-stage process the Mo preferential orientation impact directly the preferential orientation of the absorbers. Unfortunately, we were unable to measure the performances of these cells due to heavy shunting caused by the scribing method.

REFERENCES

[1] T. Eisenbarth, R. Caballero, C. A. Kaufmann, A. Eicke, and T. Unold, "Influence of iron on defect concentrations and device performance for Cu(In,Ga)Se2 solar cells on stainless steel substrates: Influence of iron on Cu(In,Ga)Se2 solar cells," *Prog. Photovolt. Res. Appl.*, vol. 20, no. 5, pp. 568–574, Aug. 2012.

[2] R. Wuerz, A. Eicke, F. Kessler, and F. Pianezzi, "Influence of iron on the performance of CIGS thin-film solar cells," *Sol. Energy Mater. Sol. Cells*, vol. 130, pp. 107–117, Nov. 2014.

[3] D.-H. Cho *et al.*, "Photovoltaic performance of flexible Cu(In,Ga)Se2 thin-film solar cells with varying Cr impurity barrier thickness," *Curr. Appl. Phys.*, vol. 13, no. 9, pp. 2033–2037, Nov. 2013.

[4] F. Pianezzi *et al.*, "Electronic properties of Cu(In,Ga)Se $_2$ solar cells on stainless steel foils without diffusion barrier: Electronic properties of CIGS solar cells," *Prog. Photovolt. Res. Appl.*, vol. 20, no. 3, pp. 253–259, May 2012.

[5] Engineering Toolbox, "Thermal Conductivity of Metals." [Online]. Available: https://www.engineeringtoolbox.com/thermal-conductivity-metals-d_858.html.

[6] A. M. Helmenstine, "Table of Electrical Resistivity and Conductivity," 2018. [Online]. Available: https://www.thoughtco.com/table-of-electrical-resistivity-conductivity-608499.

[7] P. Blösch *et al.*, "Comparative Study of Different Back-Contact Designs for High-Efficiency CIGS Solar Cells on Stainless Steel Foils," *IEEE J. Photovolt.*, vol. 1, no. 2, pp. 194–199, Oct. 2011.

[8] L. Li, X. Zhang, Y. Huang, W. Yuan, and Y. Tang, "Investigation on the performance of Mo2N thin film as barrier layer against Fe in the flexible Cu(In,Ga)Se2 solar cells on stainless steel substrates," *J. Alloys Compd.*, vol. 698, pp. 194–199, Mar. 2017.

[9] G.-L. Chiu, T. Subburaj, S. Som, C.-Y. Ou, and C.-H. Lu, "Influence of doping iron ions into Cu (In, Ga) Se2 films in the morphology and photovoltaic properties of thin-film solar cells," *J. Ceram. Process. Res.*, vol. 18, no. 10, pp. 754–759, 2017.

[10] J.-K. Sim, S.-K. Lee, J.-S. Kim, K.-U. Jeong, H.-K. Ahn, and C.-R. Lee, "Efficiency enhancement of CIGS compound solar cell fabricated using homomorphic thin Cr 2 O 3 diffusion barrier formed on stainless steel substrate," *Appl. Surf. Sci.*, vol. 389, pp. 645–650, Dec. 2016.

[11] D.-I. Kim, K.-B. Kim, M. Kim, and C.-W. Jeon, "Effect of the Mo Structure on CIGS Solar Cells Fabricated on Stainless Steel Substrates," *Isr. J. Chem.*, vol. 55, no. 10, pp. 1064–1069, Oct. 2015.

[12] L. Zortea *et al.*, "Cu(In,Ga)Se2 solar cells on low cost mild steel substrates," *Sol. Energy*, vol. 175, pp. 25–30, Nov. 2018.

[13] R. Wuerz, A. Eicke, F. Kessler, S. Paetel, S. Efimenko, and C. Schlegel, "CIGS thin-film solar cells and modules on enamelled steel substrates," *Sol. Energy Mater. Sol. Cells*, vol. 100, pp. 132–137, May 2012.

[14] K. Herz *et al.*, "Dielectric barriers for flexible CIGS solar modules," *Thin Solid Films*, vol. 403, pp. 384–389, 2002.

[15] B. Li, J. Li, L. Wu, W. Liu, Y. Sun, and Y. Zhang, "Barrier effect of AlN film in flexible Cu(In,Ga)Se2 solar cells on stainless steel foil and solar cell," *J. Alloys Compd.*, vol. 627, pp. 1–6, Apr. 2015.

[16] Y. D. Chung *et al.*, "The thickness effect of SiOx layer in CIGS thin-film solar cells fabricated on stainless-steel substrate," in *2010 35th IEEE Photovoltaic Specialists Conference*, Honolulu, HI, USA, 2010, pp. 003401–003402.

[17] P. Blösch *et al.*, "Diffusion barrier properties of Mo back contacts for Cu(In,Ga)Se2 solar cells on stainless steel foils," *J. Appl. Phys.*, vol. 113, no. 5, p. 054506, 2013.

[18] M. S. Kim, R. B. V. Chalapathy, K. H. Yoon, and B. T. Ahn, "Grain Growth Enhancement and Ga Distribution of Cu(In[sub 0.7]Ga[sub 0.3])Se[sub 2] Film Using Cu[sub 2]Se Layer on Cu–In–Ga Metal Precursor," *J. Electrochem. Soc.*, vol. 157, no. 1, p. B154, 2010.

[19] M. M. Islam *et al.*, "Effect of Ga/Cu Ratio on Polycrystalline Thin Film Solar Cell," *Adv. Optoelectron.*, vol. 2011, pp. 1–6, 2011.

[20] M. Raghuwanshi, "Influence of Grain Boundary Chemistry on the properties of CIGS photovoltaic cells," PhD Thesis, University of Rouen, 2015.

[21] X. Liang *et al.*, "Substrate temperature optimization for Cu(In, Ga)Se 2 solar cells on flexible stainless steels," *Appl. Surf. Sci.*, vol. 368, pp. 464–469, Apr. 2016.

[22] H. Wang *et al.*, "Effect of substrate temperature on the structural and electrical properties of CIGS films based on the one-stage co-evaporation process," *Semicond. Sci. Technol.*, vol. 25, no. 5, p. 055007, May 2010.

[23] W. Thongkham, R. Sakdanuphab, C. Chityuttakan, and S. Chatraphorn, "Effect of diffusion barrier and substrate temperature on the physical properties of flexible Cu (In, Ga) Se2 thin film solar cells," *J Met. Mater. Miner.*, vol. 20, pp. 61–65, 2010.

[24] T. Klinkert, "Comprehension and optimisation of the co-evaporation deposition of Cu (In, Ga) Se2 absorber layers for very high efficiency thin film solar cells," PhD Thesis, Université Pierre et Marie Curie-Paris VI, 2015.

[25] D. H. Shin, Y. M. Shin, J. H. Kim, B. T. Ahn, and K. H. Yoon, "Control of the Preferred Orientation of Cu(In,Ga)Se2 Thin Film by the Surface Modification of Mo Film," *J. Electrochem. Soc.*, vol. 159, no. 1, pp. B1–B5, 2012.

[26] J.-H. Yoon, W.-M. Kim, J.-K. Park, Y.-J. Baik, T.-Y. Seong, and J. Jeong, "Control of the preferred orientations of Cu(In,Ga)Se $_2$ films and the photovoltaic conversion efficiency using a surface-functionalized Mo back contact: Control of the preferred orientation of CIGS films," *Prog. Photovolt. Res. Appl.*, vol. 22, no. 1, pp. 69–76, Jan. 2014.

[27] T. Schlenker, V. Laptev, H. W. Schock, and J. H. Werner, "Substrate influence on on Cu(In1-x,Gax)Se2 film texture," *Thin Solid Films*, vol. 480–481, pp. 29–32, 2005.

[28] W. Witte, R. Kniese, and M. Powalla, "Raman investigations of Cu(In,Ga)Se2 thin films with various copper contents," *Thin Solid Films*, vol. 517, no. 2, pp. 867–869, Nov. 2008.

[29] H. Tanino, "Raman Spectra of CuGaxIn1-xSe2," *Jpn. J. Appl. Phys.*, vol. 32, pp. 436–438, 1993.

[30] C. Rincón *et al.*, "Raman spectra of the ordered vacancy compounds CuIn 3 Se 5 and CuGa 3 Se 5," *Appl. Phys. Lett.*, vol. 73, no. 4, pp. 441–443, 1998.

[31] C. Insignares-Cuello, C. Broussillou, V. Bermúdez, E. Saucedo, A. Pérez-Rodríguez, and V. Izquierdo-Roca, "Raman scattering analysis of electrodeposited Cu(In,Ga)Se $_2$ solar cells: Impact of ordered vacancy compounds on cell efficiency," *Appl. Phys. Lett.*, vol. 105, no. 2, p. 021905, Jul. 2014.

[32] C.-M. Xu *et al.*, "Composition dependence of the Raman A $_1$ mode and additional mode in tetragonal Cu–In–Se thin films," *Semicond. Sci. Technol.*, vol. 19, no. 10, pp. 1201–1206, Oct. 2004.

[33] W. K. Batchelor *et al.*, “Substrate and back contact effects in CIGS devices on steel foil,” in *Photovoltaic Specialists Conference, 2002. Conference Record of the Twenty-Ninth IEEE*, 2002, pp. 716–719.

[34] F. Pianezzi *et al.*, “Influence of Ni and Cr impurities on the electronic properties of Cu(In,Ga)Se 2 thin film solar cells: Influence of Ni and Cr impurities in CIGS,” *Prog. Photovolt. Res. Appl.*, vol. 23, no. 7, pp. 892–900, Jul. 2015.

[35] J. Schulte, “Investigations of the reactive co-sputtering deposition of Cu (In, Ga)(S, Se) 2 absorber layers for thin film solar cells,” 2014.

[36] J. Kessler, C. Chityuttakan, J. Lu, J. Schöldström, and L. Stolt, “Cu (In, Ga) Se2 thin films grown with a Cu-poor/rich/poor sequence: growth model and structural considerations,” *Prog. Photovolt. Res. Appl.*, vol. 11, no. 5, pp. 319–331, 2003.

CHAPTER 5

Solar power is not about fashion, it is about survival.

-Sir Norman Foster, *Florence, 1993*.

GENERAL CONCLUSION AND PERSPECTIVES

CIGS solar cell technology has become trendy in recent years. One of its charms is its potential to be fabricated on flexible substrates that are lightweight, hence increasing its use cases and applications. This thesis has been all about the fabrication of CIGS thin film solar cells on flexible metallic substrates. The aim was to study, understand and optimize the growth and fabrication process of CIGS absorbers on Mo and stainless steel substrates in order to improve the yield of the solar cells with performances as close as possible to those on soda-lime glass substrates.

Although glass is a convenient substrate with many positive characteristics such as its smooth surface, sufficient temperature stability, ability to act as a source of alkali elements, and electrical insulation, it is rigid, fragile, and heavy. Solar cells on a flexible substrate such as a metal foil have several additional advantages: A metal foil can withstand the typical CIGS processing temperatures, or even enable higher temperatures. Notwithstanding, the major issues with these substrates are the substrate's surface roughness, presence of detrimental impurities and Na incorporation. To bypass these difficulties, the approach of this work consisted of comparing Mo foil substrate to stainless steel substrate. While glass substrates remains very smooth, the Mo foil and stainless steel used in this thesis was found to have an average roughness of 83 nm (RMS ≈ 103 nm).

Mo foil

An interesting feature in the use of Mo foil is the fact that it can act both as the substrate and back contact hence eliminating the need to sputter any additional Mo back contact as well as preventing the diffusion of any detrimental impurities such as Fe. Firstly, to facilitate the understanding of the CIGS growth mechanism, the substrate temperature in the coevaporation chamber was calibrated using an infrared camera. This temperature measurement revealed the absolute temperatures of the materials tested. It was observed that Mo has a lower emissivity than SLG/Mo and SLG/Mo/CIGS. Furthermore, for the same imposed temperature, Mo is at a much higher temperature compared to SLG/Mo and SLG/Mo/CIGS (sec. 3.2.1). The temperatures mentioned in this work refers to the imposed temperatures. A comparison of the properties of Mo foil and SLG showed that

glass is very smooth (R_a ~3 nm) while Mo is rougher (R_a ~83 nm). Furthermore, SLG has a great advantage of containing Na impurities that naturally diffuse into the CIGS absorber bulk during the deposition process. The incorporation of Na in the absorbers has been shown to be beneficial for CIGS solar cells.

The selection of the standard deposition temperature was done by evaluating the properties of the absorbers fabricated at 450 °C, 465 °C and 480 °C using the standard 3-stage process. A GGI of 0.38, 0.37 and 0.33 was obtained for the absorbers deposited at 450 °C, 465 °C and 480 °C respectively. The absorbers had a preferential orientation perpendicular to the (112) lattice plane regardless of the temperature of deposition. The best performance of 9.0 % was obtained on the sample fabricated at 480 °C. This was due to a significantly higher Voc (530 mV) when compared to the other samples (512 – 519 mV). This led to a selection of 480 °C as the default deposition temperature for subsequent experiments.

The optimization of depositions on Mo foil presented two major challenges. Firstly, due to the high conductivity of Mo, it becomes difficult to observed temperature changes during the formation of Cu_xSe binaries in the second stage. This is very crucial as it used in the end point detection. On Mo foil however, the temperature change during this phase of the process is about ~2.5 °C compared to ~21 °C on SLG substrates. To bypass this hurdle, the temperature scale on the process graph is adjusted in order to visualize the small change in T. Secondly, the absorbers fabricated has significantly low CGI values (0.75) while we desired CGI values between 0.88 – 0.95. To resolve this, the termination phase (typically 6 min) after the end of the 3rd stage was shortened progressively with no NaF PDT. This resulted in a corresponding increase in the CGI up to 0.92 when the termination phase was limited to 1 min while the GGI remained fairly constant. Adopting the 1 min termination time, the effect of NaF PDT was studied by trying various NaF deposition recipes. A reference cell (no NaF PDT) was also made for the sake of comparison. All the samples had a preferential orientation perpendicular to the (112) lattice plane which has been repeatedly observed for CIGS absorbers deposited on Mo foil. The addition of Na led to huge gains especially in the Voc and fill factor. The best cell had a Voc of 600 mV and a FF of 70.4 % compared to 0.51 mV and 65.2 % for the reference cell with no NaF PDT.

Further studies on the Ga gradient was carried out as part of the optimization efforts to improve the yield of the CIGS cells fabricated on the Mo substrates. In practice, this was

implemented by varying the Ga flux in the 3rd stage of the deposition process while keeping all other parameters in the 1st and 2nd stages constant. NaF PDT was carried out on the samples as described in sec 3.4. A reduction of the GGI occurred which was expected as the Ga fluxes were reduced in the 3rd stage. Indeed, the samples $C_{0.24}$ presented gains in Jsc (~2.3 mA/cm^2). The EQE response further revealed that the gain in Jsc was due to increased spectral absorption in the long wavelength region. This ultimately led to superior cell efficiencies of 14.0 % for the champion cell. We further observed that modifying the process parameters in the efforts to optimize the deposition process led to a modification of the nature of the CIGS absorbers which in turn led to a modification of the CdS buffer layer growth kinetics. This was validated by depositing the CdS buffer layer on a standard absorber and another absorber with the modified and optimized process. The results obtained mainly from the EQE response of the absorbers revealed that CdS buffer layer growth was faster on the modified CIGS absorbers. Finally, the impact of a sputtering an extra layer of Mo back contact on the Mo foil was studied. 100 nm and 800 nm of Mo was sputtered on the Mo foil substrates prior to CIGS deposition (sec 3.6). The absorbers were fabricated at 480 °C and 550 °C respectively. At 480 °C, the presence of a sputtered Mo layer was detrimental to the cell performances with the most profound effect being on the Jsc and efficiency which both dropped to about 48 % of the values of the reference cell. The results led to the conclusion that the sputtered back contact is only beneficial for cell properties at elevated temperatures in our case, 550 °C. At 550 °C, the efficiency, Voc and FF improves by ~10 % for the 800 nm thick sputtered Mo back contact.

Stainless Steel

Fe, the main alloying metal in stain steel is known to be detrimental to CIGS solar performance. We utilized four different stainless steel types which differed in their composition and thickness. The substrates had a minimum Cr composition of 16 %. To prevent the diffusion of Fe atoms into the absorber layers, a Cr barrier layer coupled with a low temperature process was implemented. GDOES measurements on an annealed Mo/Cr/SS stack revealed the extent of Fe diffusion through the Mo back contact. The results revealed that a minimal Cr thickness (500 nm) coupled with the low temperature process was sufficient to block the detrimental Fe atoms. An efficiency of 14.2 % was obtained which was the best obtained on stainless steel in this work. Next, in order to select the ideal stainless steel substrate among the four different types, we fabricated CIGS

absorbers and cells. The CGI and GGI of the absorbers on the steel substrates were nearly identical. The grains sizes were also similar and had no clearly defined large columnar grains. The crystalline structure studied by x-ray diffraction also revealed a preferred orientation perpendicular to the (220)/(204) lattice plane as opposed the absorber on Mo foil where the orientation is perpendicular to the (112) lattice plane. The best cell was obtained on stainless steel type II which was also the most homogenous in terms of the electrical parameter distribution. No correlation was deduced between the CIGS cell performances and the surface roughness and/or composition of the stainless steels. The experiments utilizing the CURO process yielded no functional cell due to heavy shunting arising from the scribing process. However, we noted that the standard process usually applied to SLG depositions needed to be adapted for depositions involving metallic substrates. This observation arises from the excess Se deposition at the end of the deposition process due to a low Se cut-off temperature.

To conclude we observe that the growth and composition of the absorbers are highly substrate dependent and the thermal conductivity of substrate directly impacts the deposition conditions, the composition and the performance of cells. Thus for each type of substrate, a deep optimization of deposition conditions is necessary.

For the further optimization of $Cu(In,Ga)Se_2$ based solar cells on flexible metallic substrates, the following routes are proposed:

- The poor Voc observed on the metallic substrates might be due to inadequate alkali incorporation and the Ga composition (GGI). In this thesis, we only treated the samples with NaF and the impact of GGI have not been deeply studied for each substrate type of substrat. However, a combination of an adequate GGI and heavier alkali metals (K, Rb, Cs) used in the post treatment can improve the cell performance [1].
- Low temperature process. Although we employed a deposition temperature of 480 °C. It is possible to further lower the deposition temperature which is especially important for stainless steel substrates. Lowering the temperature to levels where the diffusion of Fe is inhibited, coupled with optimizing the Mo back contact structure and thickness, the efficiency on stainless steel substrate can be improved. As seen in several studies, the Mo back contact depending on its design can be sufficient enough to block Fe diffusion on stainless steel substrates [2] [3].

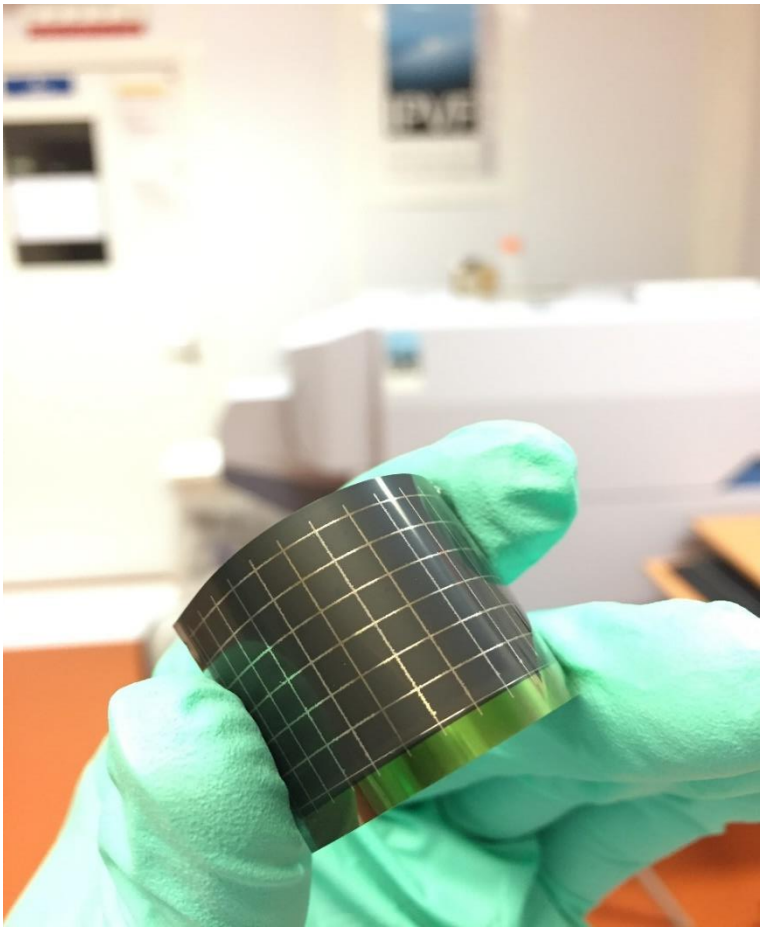


Figure 5.1. A flexible CIGS cell fabricated in this thesis on a 0.15 mm thick Mo foil substrate.

To conclude, in this thesis, CIGS cells have been successfully fabricated on Mo foil and stainless steel substrates. A maximum efficiency of 14.0 % was achieved on Mo foil and 14.2% which remains lower than performances of cells on soda-lime glass substrates. It is noteworthy that very few studies exist on the deposition of CIGS absorber on Mo substrate using the 3-Stage process. A typical flexible CIGS cell on Mo substrate and fabricated at 480 °C using the 3-stage process is shown in the figure 5.1.

REFERENCES

[1] P. Jackson, R. Wuerz, D. Hariskos, E. Lotter, W. Witte, and M. Powalla, “Effects of heavy alkali elements in Cu(In,Ga)Se $_2$ solar cells with efficiencies up to 22.6%,” *Phys. Status Solidi RRL - Rapid Res. Lett.*, vol. 10, no. 8, pp. 583–586, Aug. 2016.

[2] D.-I. Kim, K.-B. Kim, M. Kim, and C.-W. Jeon, “Effect of the Mo Structure on CIGS Solar Cells Fabricated on Stainless Steel Substrates,” *Isr. J. Chem.*, vol. 55, no. 10, pp. 1064–1069, Oct. 2015.

[3] F. Pianezzi *et al.*, “Electronic properties of Cu(In,Ga)Se $_2$ solar cells on stainless steel foils without diffusion barrier: Electronic properties of CIGS solar cells,” *Prog. Photovolt. Res. Appl.*, vol. 20, no. 3, pp. 253–259, May 2012.

APPENDIX

A. MATERIAL CHARACTERIZATION TECHNIQUES

A1. Scanning Electron Microscopy

Scanning Electron Microscope (SEM) is a characterization method used to observe the morphology of the CIGS films. Surface and/or cross section SEM images gives qualitative insight into grain size of the CIGS films. The SEM characterization used in this thesis was done on a *Zeiss Merlin VP compact* SEM machine. The electron acceleration voltage used was 15 kV with a working distance of 5 mm. Energy Dispersive X-ray Spectroscopy (EDS) measurements can also be carried out using the SEM machine to determine the elemental composition of the thin films.

A2. X-ray Diffraction

X-ray diffraction (XRD) measurements were carried out to study the crystallographic structure of the CIGS absorbers. This was done on a *PANalytical Empyrean* equipment with a Cu $K\alpha_1$ radiation in the θ - 2θ Bragg-Brentano geometry. The principle of XRD is based on the constructive interference of monochromatic X-rays and a crystalline sample. The X-rays are generated by a cathode ray tube, filtered to produce monochromatic radiation, collimated to concentrate, and directed towards the sample. The characteristic x-ray diffraction pattern generated in an XRD analysis provides a unique "fingerprint" which helps to identify the crystals present in a sample. In this thesis, XRD was used mainly to identify the various CIGS phases present in a sample as well as other species that might be present in the sample.

A3. Glow Discharge Optical Emission Spectroscopy

The samples in this work were characterized using a *HORIBA Scientific GD-Profiler 2*. Glow discharge optical emission spectroscopy (GD-OES) is a characterization method used to measure the depth profiles of constituent elements in a sample. This is achieved by detecting emissions from atoms decomposed by the Argon plasma. The collisions between the sample atoms and the argon atoms leads to excitation and subsequent emission of light at specific wavelengths. The material composition can hence be determined by the analysis of the emitted light.

A4. X-ray Fluorescence

Energy dispersive X-ray fluorescence (XRF) is a characterization method used for measuring the thickness of a sample as well as the qualitative and quantitative determination of the elemental composition of a material. The sample is usually excited with the primary X-ray radiation. When this occurs, electrons from the inner electron shells are knocked out of orbit. Electrons from outer electron shells fill the resultant voids hence emitting a fluorescence radiation that is characteristic in its energy distribution for a particular material. This fluorescence radiation is analyzed by a detector. It is a non-destructive process and the incident X-ray has no lasting impact on the sample material.

A5. Raman Spectroscopy

The Raman spectroscopy analysis were carried out with a *Horiba Jobin-Yvon LabRam* instrument with a 532 nm excitation laser. When monochromatic radiation falls upon a sample, it interacts with the sample. This interaction could be reflection, absorption or scattering in some manner. If the frequency (wavelength) of the scattered radiation is analyzed, not only is the incident radiation wavelength seen (Rayleigh scattering) but also, a small amount of radiation that is scattered at some different wavelength (Stokes and Anti-Stokes Raman scattering). It is the change in wavelength of the scattered photon which provides the chemical and structural information.

A6. Atomic Force Microscope

An atomic force microscope is a high resolution scanning probe microscope that has a resolution that can be measured in fractions of a nanometer. It uses a cantilever with a sharp but tiny probe that scans the surface of the specimen. When the tip of the probe travels near to a surface, the forces between the tip and sample deflect the cantilever according to Hooke's law. The AFM measurements in this work were done on a *Horiba Jobin-Yvon* OmegaScope AFM platform in a non-contact mode. The measured area was 20 × 20 μm. In the non-contact mode, the tip vibrates slightly above its resonance frequency and does not contact the surface of the sample. Recording the distance between the tip and sample at each point allows the software to construct a topographic image of the sample surface.

B. SOLAR DEVICE CHARACTERIZATION

B1. External Quantum Efficiency

The External Quantum Efficiency (EQE) is measured with an IQE200 Newport instrument. The range of the wavelength measured is 300 nm – 1300 nm. Usually, a silicon cell is used to calibrate the detector for wavelengths 300 nm ≤ **λ** ≤ 1050 nm while a Germanium cell is used for the range 1050 nm ≤ **λ** ≤ 1300 nm. EQE is defined as the ratio of the number of charge carriers collected by the solar cell to the number of photons of a given energy incident on the solar device from outside (incident photons) and is given by the following expression where N_e = number of e^- produced and N_υ = number of absorbed photons:

$$QE_\lambda = \frac{N_e}{N_\upsilon}$$

B2. Current – Voltage characteristics

After scribing of the cells, their current-voltage (I-V) characteristics were measured by a 4 points probe connected to an Agilent voltage source. Light or dark measurements can be performed on this setup. For the measurements under illumination, the parameters used is AM1.5 global spectrum, with an irradiation of 1000 W/m^2 on a Newport class AAA instrument). The measurement temperature of 25 °C was achieved by placing the samples on a temperature regulated surface.

C. TEST OF THE OPTIMIZED PROCESS (MO SUBSTRATES) ON SLG AND BOROSILICATE GLASS

As discussed in chapter 3, the deposition process was optimized for depositions on Mo foil substrate. The developed process was tested on sodalime glass and borosilicate glass at 450 °C. This temperature was selected in order to avoid bending the SLG substrate during deposition. The absorbers were deposited on Mo foil, SLG and Borosilicate glass in the same experimental run to avoid run-to-run variations. The XRD diffractogram, Ga gradient and I-V characteristics of the cells are presented.

	CGI	**GGI**
SLG	0.67	0.22
Mo foil	0.75	0.27
Borosilicate	0.78	0.25

Table C.1. XRF measurements showing the elemental composition of the absorbers on the different substrates

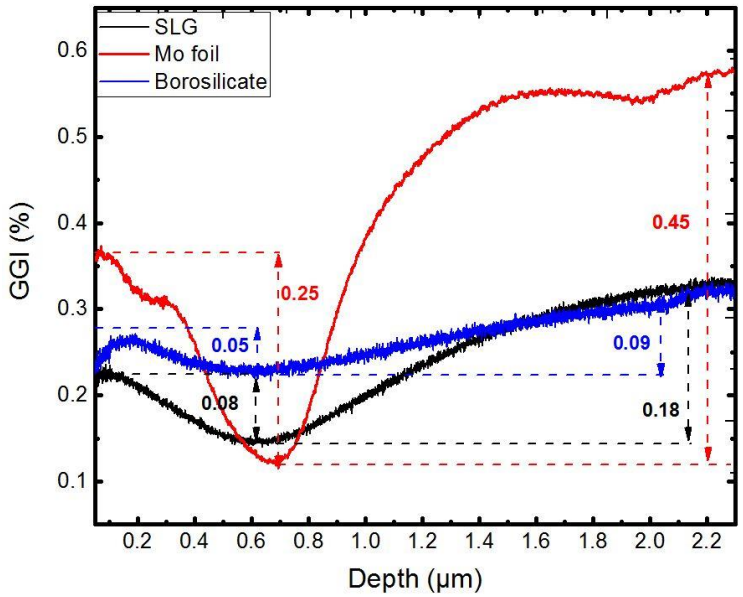


Figure C.1. Ga depth profile of the samples fabricated on different substrates, measured by GDOES

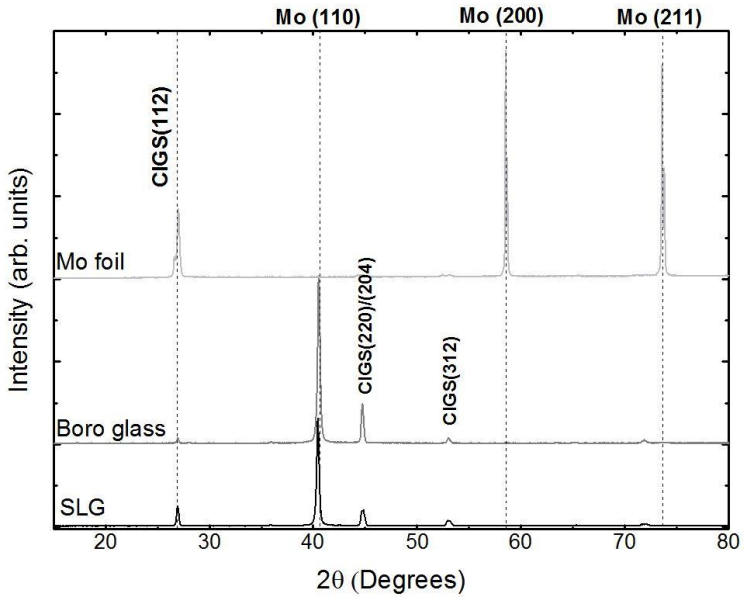


Figure C.2. XRD diffractogram of the samples. Notice the absence of the Mo(110) peak on the Mo foil substrate. The preferred CIGS orientation on Mo foil is perpendicular to the (112) lattice plane, while the preferred orientation is perpendicular to the (220)/(204) lattice plane on SLG and Borosilicate glass

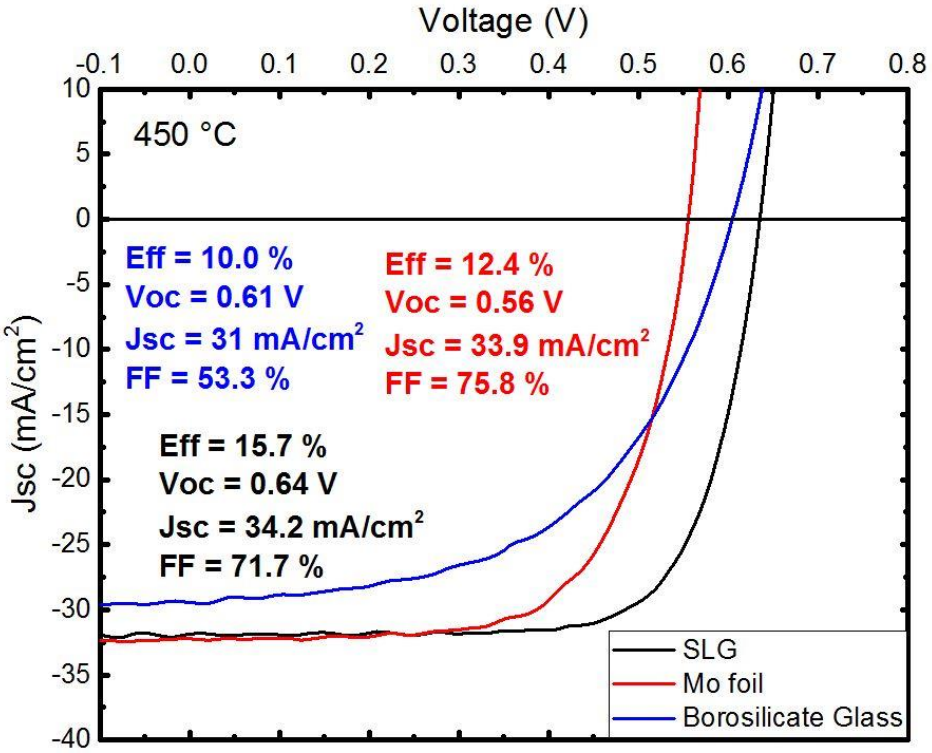


Figure C.3. I-V characteristics of the sample. The champion cell is obtained on SLG with 15.7 % efficiency. The superior performance on SLG can be linked but not limited to the superior Na incorporation and the nature of the substrate.

DEVELOPPEMENT DE CELLULES PHOTOVOLTAÏQUES A BASE DE CIGS DE HAUTE PERFORMANCE SUR SUBSTRATS METALLIQUES

Résumé en français étendu

Introduction

La demande mondiale d'énergie a fortement augmenté ces dernières années. L'année 2017 a vu la demande mondiale d'énergie augmenter de 2,1% contre 0,9% en 2016 et une moyenne de 0,9% sur les cinq dernières années. Cette augmentation de la demande et de la production d'énergie s'est accompagnée d'une augmentation correspondante des émissions de carbone, les combustibles fossiles représentant encore 81 % de la demande énergétique mondiale en 2017. Au cours de la même période, les émissions de CO2 ont augmenté de 1,4 %, atteignant un nouveau record historique de 32,5 gigatonnes (Gt). On s'attend à ce que la tendance mondiale des besoins énergétiques continue d'augmenter régulièrement, au moins pendant les deux prochaines décennies, plus des deux tiers de cette croissance provenant des pays en développement où la croissance économique et démographique est la plus forte. La figure 1 représente la croissance annuelle moyenne de la demande mondiale d'énergie.

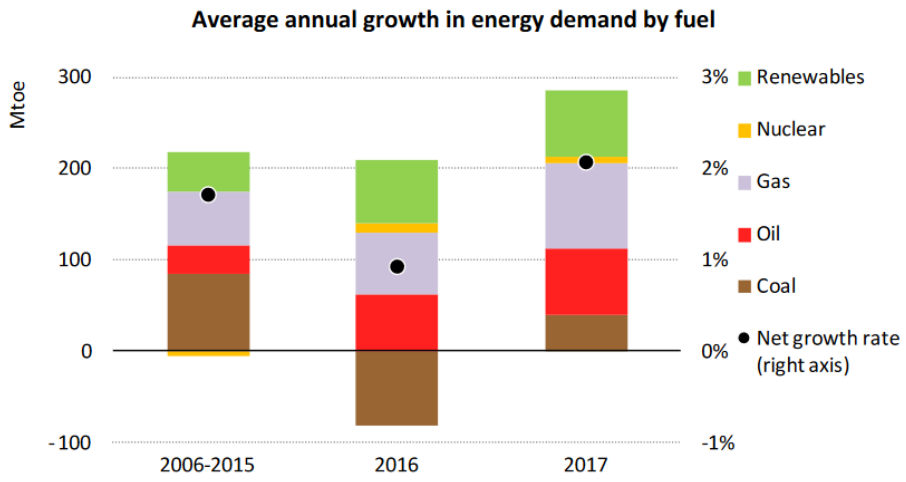


Figure 1. Graphique représentant la croissance annuelle moyenne de la demande mondiale d'énergie

Pour réduire les émissions de CO2, il est important de réduire la dépendance à l'égard des sources d'énergie fossiles et d'accroître le développement et l'adoption de technologies d'énergie renouvelable. Il est intéressant de noter que la demande d'énergie renouvelable a connu la plus forte croissance en 2017 (figure 2). Fin 2017, la production basée sur les énergies renouvelables a augmenté de 167 GW, soit une croissance de 8,3 %. Ces données reflètent la transition vers une exploitation propre et durable de l'énergie. Les énergies

renouvelables représentent à elles seules environ 25 % de la production mondiale d'électricité (section 1.1.2).

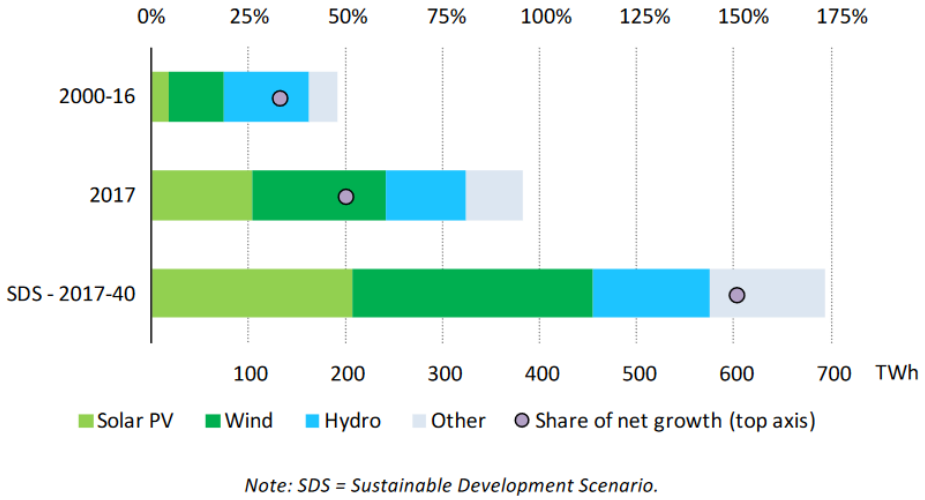


Figure 2. Croissance mondiale annuelle moyenne de la production d'électricité à partir d'énergies renouvelables par technologie

Une part importante des technologies d'énergie renouvelable est la production d'énergie photovoltaïque (PV) qui est composée de cellules/modules PV solaires. Le marché du photovoltaïque est aujourd'hui dominé par les technologies du silicium cristallin (c-Si). Cependant, l'écart est comblé par des cellules solaires Cu(In,Ga)Se_2 (CIGS) qui sont des cellules solaires à couche mince. Il a gagné en popularité au cours des dernières années puisque l'efficacité record sur ce type de cellule a récemment atteint jusqu'à 23,0 %. Cette thèse est donc centrée sur le développement de cellules CIGS de haute performance fabriquées sur des substrats métalliques flexibles.

Cellules solaires à base de $Cu(In,Ga)Se_2$

The structure of a typical CIGS solar cell is shown in figure 3. In its most basic form, a CIGS cell is made up of a layered stack comprising the bottom flexible substrate (stainless steel or Mo), a Mo (Mo) back contact, the CIGS absorber, a CdS buffer layer and a transparent conducting oxide (TCO).

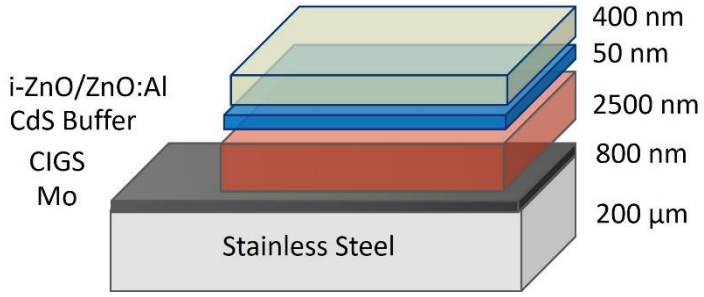


Figure 3. Architecture de cellule CIGS sur un substrat flexible en acier inoxydable

Chaque couche de la cellule CIGS représentée sur la figure 3 a une fonction unique ;

(i) Le $Cu(In,Ga)Se_2$ de type p : Cette couche absorbe la lumière incidente et génère des paires e-h.

ii) La couche CdS de type n : C'est la couche tampon qui est en contact direct avec la couche absorbante, forme la jonction p-n et aide à la séparation des charges.

iii) La bicouche ZnO/ZnO:Al : Il s'agit d'une électrode conductrice transparente (TCO) située en haut de la cellule. Il recueille les électrons générés.

(iv) Le contact arrière Mo : Celui-ci est déposé directement sur le substrat et sert de contact arrière qui recueille les trous.

Cette configuration s'appelle la configuration du substrat, ce qui signifie que la lumière entre dans la cellule par le haut. Le substrat agit comme un support donnant une certaine rigidité à la cellule et maintenant toutes les autres couches en place. Bien qu'il existe plusieurs méthodes de dépôt pour la fabrication des absorbeurs CIGS, le procédé de coévaporation en 3 étapes est utilisé dans ce travail pour la réalisation des absorbeurs CIGS. Cette méthode nécessite l'évaporation simultanée de Cu, In, Ga et Se dans une chambre à vide poussé (figure 4) à une température de traitement de 400 à 480 °C.

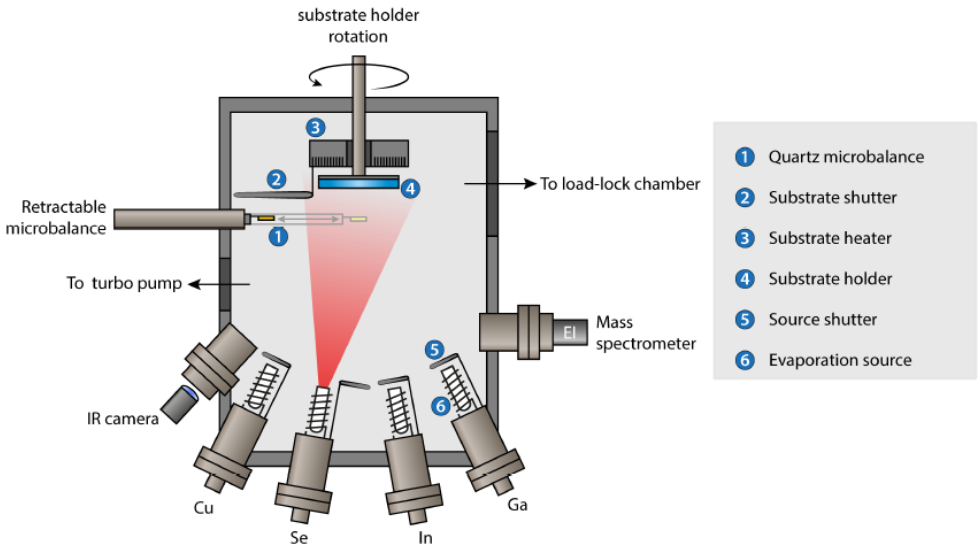


Figure 4. Dépôt CIGS par coévaporation des éléments constitutifs

Substrats métalliques flexibles

La technologie des cellules solaires CIGS est devenue à la mode ces dernières années. Cela s'explique notamment par le fait qu'il peut être fabriqué sur des substrats souples et légers, ce qui augmente le nombre de cas d'utilisation et d'applications. L'objectif de cette thèse est d'étudier, comprendre et optimiser le processus de croissance et de fabrication des absorbeurs CIGS sur des substrats en Molybdène et en acier inoxydable afin d'améliorer le rendement des cellules solaires. Bien que le verre soit un substrat pratique avec de nombreuses caractéristiques positives telles que sa surface lisse, sa stabilité de température suffisante, sa capacité à agir comme source d'éléments alcalins et son isolation électrique, il est rigide, fragile et lourd. Une cellule solaire sur un substrat flexible tel qu'une feuille métallique présente plusieurs avantages supplémentaires. Une feuille de métal peut résister aux températures de traitement typiques du CIGS, ou même permettre des températures plus élevées. Dans le cas d'un substrat flexible en feuille de Mo, la feuille de Mo peut jouer le rôle de contact arrière aussi bien que le substrat, réduisant ainsi le nombre d'étapes de fabrication nécessaires. L'inconvénient est que les métaux sont exempts de Na, d'où la nécessité d'ajouter du Na à l'extérieur des absorbeurs CIGS pendant le processus de fabrication de l'absorbeur. Le tableau 1 résume les résultats des recherches sur les cellules CIGS fabriquées sur différents types de substrats métalliques.

Substrat	Méthode de dépôt	Rendement (%)	Commentaires
Companies			
Acier inoxydable	Coevaporation	17.7	Global Solar Energy (Hanergy)
Acier inoxydable	Pulvérisation et sélénisation	17.3	Miasolé
Acier inoxydable	Pulvérisation et sélénisation	17.0	Midsummer
Acier inoxydable	Pulvérisation et sélénisation	14.0	Nuvosun (Dow)
Acier inoxydable	Électrodéposition et sélénisation	15.4	Solopower
Feuille d'aluminium	Non-vacuum printing	17.1	Nanosolar
Research Institutes			
Acier émaillé	Coevaporation	18.7	ZSW
Titane	In-line 3-stage coevaporation	17.9	Aoyama Gakuin University, Japan
Ti-coated Stainless Steel	Coevaporation	17.7	EMPA
Feuille de Mo	Coevaporation	14.6	AIST
Acier inoxydable	Coevaporation	17.4	NREL
Cu	-	<10	IST, Germany
Titane	-	12	ZSW

Table 1. Des gains de rendement à la pointe de la technologie publiés par différentes entreprises et instituts de recherche

• Les defis de la fabrication de cellules CIGS sur des substrats metalliques

Malgré les progrès de la recherche sur les cellules CIGS flexibles sur substrats métalliques, les efficacités de conversion réalisées jusqu'à présent sont considérablement inférieures à celles des cellules CIGS préparées sur substrats en verre rigide. Les limites d'efficacité ont été attribuées au manque de Na dans les substrats métalliques, à la présence d'impuretés métalliques nuisibles diffusées par la feuille métallique et à la rugosité du substrat, entre autres. Nous en discuterons brièvement.

Rugosité de substrat

Contrairement aux substrats en verre qui sont extrêmement lisses, les métaux ont des surfaces plus rugueuses en raison de leur nature, de leur fabrication et de leur procédé de laminage. La rugosité de ces substrats peut avoir un impact négatif sur les performances des cellules solaires pour plusieurs raisons. Cependant, on ne sait pas si l'effet provient

d'une différence de croissance du film - c'est-à-dire de cinétique - et donc de morphologie sur des substrats rugueux, ou si les caractéristiques de surface rugueuses fournissent des points de diffusion d'impuretés très nocives dans le CIGS ou même de shuntage du dispositif. Trois mécanismes ont été proposés dans lesquels la rugosité du substrat peut avoir un impact sur les performances du dispositif CIGS;

- *Shunts métallurgiques* : De grandes surfaces dépassant du contact arrière et/ou de la couche absorbante CIGS peuvent créer un chemin de dérivation pendant le fonctionnement de la cellule.
- *Impuretés* : A des températures de dépôt élevées, il y a une plus grande possibilité de diffusion des impuretés (Fe) du substrat métallique (acier inoxydable) dans l'absorbeur CIGS. Sur un support rugueux, cette diffusion d'impuretés est encore accentuée par une couverture inégale du support par le contact arrière en raison des caractéristiques en saillie du support. Ceci peut être évité en utilisant une couche barrière d'impureté appropriée.
- *Nucleation:* Les irrégularités de surface peuvent agir comme sites de nucléation pendant la croissance du CIGS, créant ainsi des défauts et des tailles de grains CIGS plus petites.

Incorporation du sodium

Les effets du Na sur les cellules CIGS sont principalement d'améliorer l'efficacité de la conversion en améliorant la tension en circuit ouvert et le facteur de remplissage. Le courant de court-circuit est cependant relativement peu affecté par la présence de Na. Dans les cellules CIGS traditionnelles fabriquées sur verre sodalime, le Na, naturellement présent dans le verre sodalime, se diffuse par le contact arrière Mo et dans l'absorbeur CIGS pendant l'étape de dépôt. Dans le cas des substrats métalliques cependant, le Na est absent et doit donc être incorporé par d'autres moyens afin de réaliser des cellules solaires à haut rendement.

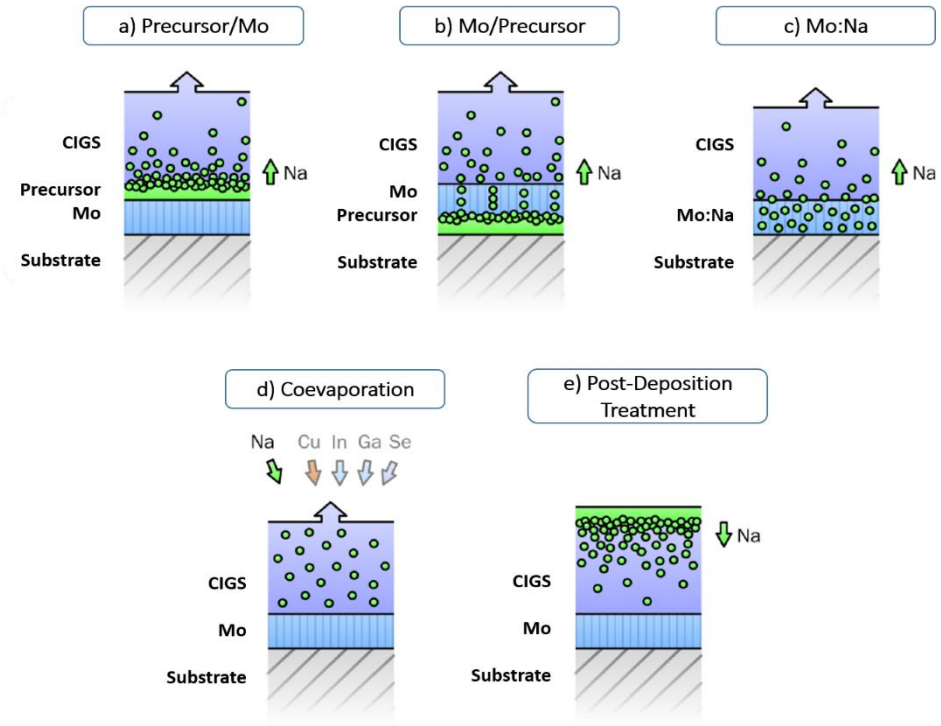


Figure 5. Méthodes d'incorporation de Na dans les absorbeurs CIGS sur substrats métalliques. a) Diffusion pendant la croissance CIGS à partir d'une couche précurseur déposée sur le contact arrière. b) Diffusion pendant la croissance CIGS à partir d'une couche précurseur déposée sous le contact arrière. c) Diffusion d'un contact arrière dopé au Na Mo:Na). d) Coévaporation éléments constitutifs CIGS pendant le dépôt. e) Traitement Post-Déposition d'une source Na.

La méthode préférée d'incorporation du Na utilisée dans cette thèse est le traitement post-dépôt de Na (PDT). Cependant, d'autres méthodes d'incorporation existent, comme le montre la figure 4.

Cellules solaires CIGS sur des feuilles de Mo

Grâce à ses propriétés, le Mo est largement adopté comme matériau de contact arrière approprié. Il s'agit notamment de sa stabilité à la température de traitement pour les absorbeurs CIGS, de sa résistance à l'alliage avec Cu et In ainsi que de sa faible résistance de contact à l'interface Mo/CIGS. Le tableau 2 est un résumé de ses propriétés.

Coefficient de dilatation thermique CTE (10^{-6} K^{-1})	4.8 – 5.9
Température de fusion (°C)	2,623
Conductivité thermique à 20 °C ($Wm^{-1}K^{-1}$)	142
Conductivité électrique at 20 °C ($\Omega^{-1}m^{-1}$)	$17{,}9 \cdot 10^{6}$
Résistivité (Ωm)	$5.5 \cdot 10^{-8}$
Structure cristalline	body-centered cubic

Table 2. Propriétés du substrat en feuille de molybdène

Les feuilles de Mo ont une épaisseur de ~150 µm et une rugosité de surface moyenne de 83 nm. L'orientation cristalline de la feuille de Mo est (200) et (211) tandis que celle d'un contact arrière Mo pulvérisé est (110). Cette différence d'orientation peut avoir un impact sur la croissance et l'orientation de l'absorbeur CIGS. Etant donné que nous utilisons une feuille de Mo comme substrat pour les dépôts CIGS, aucun contact arrière de Mo pulvérisé n'est déposé car le substrat joue également le rôle de contact arrière.

Pour réaliser les absorbeurs CIGS sur la feuille de Mo, nous avons tout d'abord commencé par sélectionner la température de dépôt appropriée en utilisant les paramètres du procédé de dépôt en 3 étapes décrits dans le tableau 3. Aucun sodium n'a été ajouté dans cette expérience. Les absorbeurs CIGS étaient pauvres en cuivre et avaient une valeur relativement constante [Cu]/([Ga]+[In]) (CGI) (0,74 ≤ CGI ≤ 0,75) alors que la GGI était dans les limites attendues (0,33 ≤ GGI ≤ 0,38). Nous en déduisons que quelle que soit la variation de $T_{2,3}$, les compositions élémentaires des absorbeurs étaient assez constantes puisque les flux étaient les mêmes.

(1ere étape)	
Temperature, T_1	400 °C
In Flux	6.3 nm/min
Ga Flux	5.3 nm/min
Duration	45 min

(2eme étape)

Substrate Temperature, T_2	400 ↗ 450 °C, 465 °C, 480 °C
Cu Flux	8.0 nm/min
Duration	41 – 46 min

(3eme étape)

Substrate Temperature, T_3	450 °C, 465 °C, 480 °C
In Flux	8.2 nm/min
Ga Flux	3.0 nm/min
Duration	23 – 29 min

Table 3 Paramètres de dépôt CIGS pour les couches d'absorbeurs avec des températures de 2ème et 3ème étages variables selon le procédé en 3 étapes.

Les mesures XRD ont révélé que l'orientation cristalline des films était de préférence (112) (figure 6a). L'orientation fortement préférée (112) du film CIGS pourrait suggérer que le précurseur $(In,Ga)_2Se_3$ formé au cours de la première étape du processus était orienté (006) car cela entraîne généralement une croissance des absorbeurs CIGS finaux dans le plan (112).

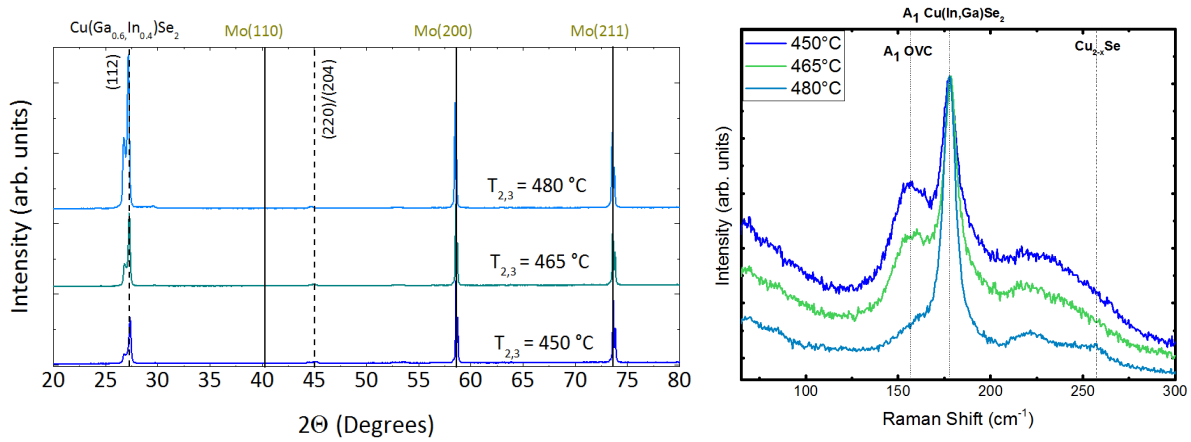


Figure 6a. Diffractogramme XRD des absorbeurs CIGS avec différentes températures de traitement (b) les spectres Raman des absorbeurs CIGS.

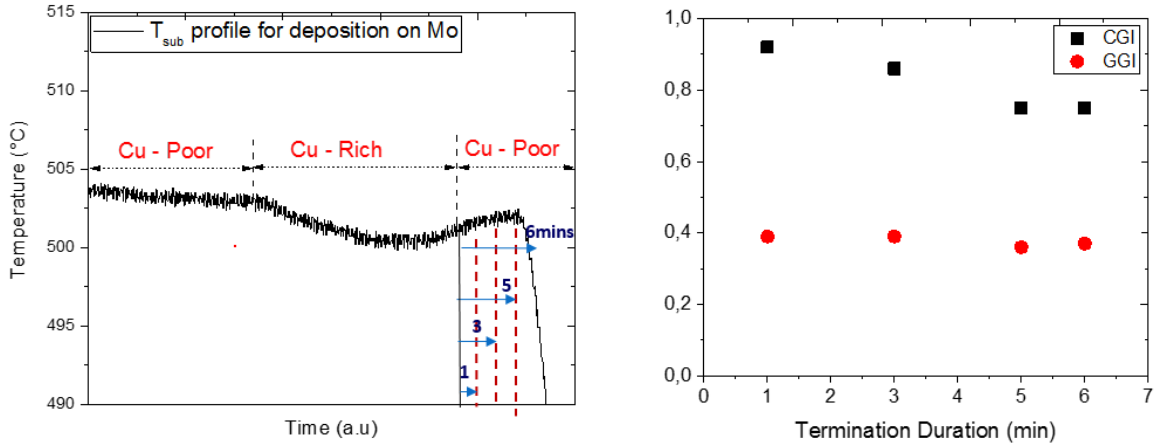
Les mesures de diffusion Raman nous permettent d'observer la présence de composés à vide ordonnés (OVC) tels que $Cu(In,Ga)_3Se_5$ ou $Cu_2(In,Ga)_4Se_7$ (figure 6b). Le pic principal des OEV A1 apparaît dans la région spectrale 150-160 cm^{-1}. L'apparition des OEV est prononcée lorsque la température de fabrication est de 450 °C. Les pics principaux des OEV Raman diminuent au fur et à mesure que la température augmente. A 480 °C, il n'y a pas de pic d'OVC autour de 150 cm^{-1}. Le tableau 4 montre les paramètres électriques des cellules fabriquées à différentes températures. Le faible Voc observé sur les échantillons

est dû à une absence d'incorporation de Na dans les absorbeurs. La température de dépôt de 480 °C, ayant atteint un rendement maximal de 9,0 % indépendamment de l'absence de traitement au Na, a été choisie comme température de fabrication par défaut.

	Voc (mV)	*Eff (%)*	*Jsc (mA/cm^{-2})*	*FF (%)*
450 °C	512	8.9	29.2	59.3
465 °C	519	8.1	27.3	57.7
480 °C	530	9.0	30.5	55.5

Table 4. Paramètres I-V des cellules CIGS traitées à différentes températures.

Ensuite, nous avons essayé de modifier le CGI des absorbeurs CIGS à 0,88 < CGI < 0,95. Bien qu'il n'y ait pas de consensus quant au ratio CGI idéal, on rapporte que les cellules CIGS à haut rendement ont un CGI dans cette plage. Ceci a été réalisé en réduisant systématiquement le temps de terminaison à la fin de la 3ème étape du processus de 6min à 1min. Il en est résulté une augmentation du CGI des couches absorbantes de 0,75 (6min) à 0,92 (1 min) comme le montrent les figures 7a et b. La variation du CGI n'a eu aucun effet sur la taille des grains comme le montrent les mesures SEM. La spectroscopie Raman a également révélé que le réglage du temps de terminaison n'a aucun effet sur la composition des absorbeurs. Aucun OEV ni binaire Cu n'ont été observés. L'efficacité des cellules a augmenté progressivement avec une augmentation du CGI et une diminution du temps de terminaison de la 3ème étape. Une efficacité maximale de 9,5 % a été atteinte pour la cellule terminée après 1 minute (CGI = 0,92). L'augmentation de l'efficience est principalement due à une augmentation de l'AF de 55,0 % (CGI = 0,75) à 65,1 % (CGI = 0,92) alors que les Jsc et Voc sont demeurés constants. Les résultats révèlent que nous sommes capables d'optimiser le CGI de nos films en ajustant la durée des 3 étapes. Nous avons amélioré le CGI de 0,75 à 0,92 sans ajout de Na.



(a) (b)

Figure 7. a) Profil de température de dépôt montrant la réduction des pas de temps de terminaison après la formation du plateau b) Évolution du CGI et du GGI pour chaque pas de temps de terminaison

- **Post-traitement NaF (PDT)**

Il est généralement admis que le dopage alcalin a pour effet de passiver les défauts aux limites des grains et des donneurs du CIGS sans affecter la cristallinité de l'absorbeur. Il a également été démontré que le Na augmente la concentration du trou dans l'absorbeur CIGS. Dans les substrats exempts de Na (pas de PDT), la concentration typique du trou dans le CIGS est d'environ 1014 cm^{-3}, cependant, en incorporant du Na par un procédé post-dépôt, la concentration du trou peut être accrue de 2 ordres de grandeur. L'effet bénéfique de Na est d'augmenter la tension à vide (VOC) et le facteur de remplissage (FF), ce qui augmente le rendement de l'appareil.

La TPD NaF a été réalisée à la fin du procédé en 3 étapes à une température inférieure du substrat de 350 °C et avec un flux NaF de 2,0 nm/min tandis que la durée du traitement variait systématiquement entre 0min (sans traitement), 10 min, 20 min et 30 min de l'exposition. Après le traitement au NaF, les échantillons ont été recuits dans une atmosphère de Se pendant 10 minutes.

Quelles que soient les conditions utilisées pour le dépôt de NaF et les traitements Se-post, aucun changement réel de l'IGG global des absorbeurs n'a été observé. Cependant, le CGI pour tous les échantillons avec incorporation de Na est légèrement inférieur à celui de la cellule de référence sans Na. Les profils XRD des échantillons ont révélé deux phases CIGS, identifiées par comparaison avec le fichier de définition CIGS 00-035-1102. Les phases

sont $CuGa_{0.3}In_{0.7}Se_2$ à 2θ=26.9° et $CuGa_{0.6}In_{0.4}Se_2$ à 2θ=27.3° qui apparaît comme un pic double (112). L'apparition de ces doubles pics est due à l'hétérogénéité de la granulométrie du Ga dans l'échantillon résultant du processus en 3 étapes. Les films avaient tous une orientation préférentielle (112). Le tableau 5 résume les propriétés de la cellule tandis que la figure 8a met en évidence la performance de la meilleure cellule par rapport à la référence. La figure 8b montre la réponse spectrale des deux cellules.

	Eff (%)	Voc (V)	Jsc (mA/cm2)	FF (%)
No Na (Ref)	10.3	0.51	31.1	65.2
Na10/Se10	13.1	0.59	31.5	70.5
Na20/Se10	13.5	0.6	31.8	70.4
Na30/Se10	12.9	0.6	28.1	68.8

Table 5. Résumé des propriétés électriques des échantillons ayant un traitement post-dépôt de NaF.

Les résultats montrent que l'incorporation de Na n'a pas d'impact sur le courant de court-circuit, mais qu'elle influence grandement la tension de circuit ouvert et le facteur de remplissage des cellules, ce qui conduit à de meilleures performances. La meilleure cellule a été obtenue avec un temps d'exposition NaF de 20 minutes suivi d'un recuit de 10 minutes dans l'atmosphère de Se.

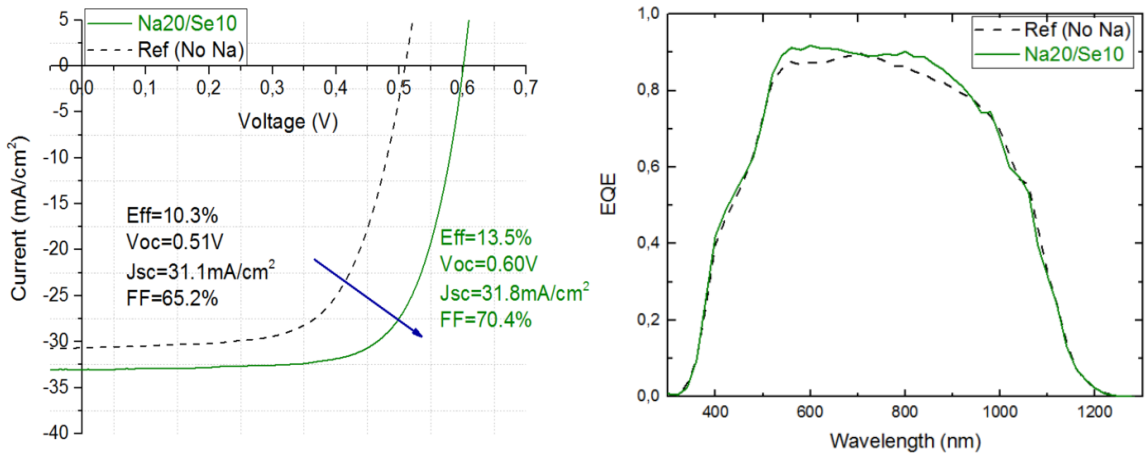


Figure 8. (a) Comparaison de la courbe I-V de la meilleure cellule avec incorporation de Na par rapport à Ref (pas de Na) (b) Courbe EQE pour les deux échantillons

• Gradient du Gallium dans les absorbeurs CIGS

Lorsque les absorbeurs CIGS sont fabriqués selon le procédé en 3 étapes, nous obtenons un gradient dans la composition de Ga à travers la masse de l'absorbeur. Ce gradient est

composé de compositions à Ga élevé près des surfaces avant et arrière de l'absorbeur et d'une composition à Ga faible au creux (encoche). L'encoche apparaît généralement près de la région de charge spatiale (SCR) selon le procédé de fabrication. L'écart de bande plus élevé près de la surface entraîne une augmentation du Voc en raison de l'élargissement de l'écart de bande dans la RCS et, puisque la partie dominante de la recombinaison se produit dans la région de charge spatiale, l'augmentation locale de l'écart de bande dans cette région peut réduire la recombinaison. Une faible teneur en Ga dans l'encoche entraîne invariablement une bande passante plus faible, ce qui a pour effet bénéfique d'augmenter la densité de photocourant grâce à une meilleure absorption des photons de faible énergie, tandis qu'à la surface arrière, la composition en Ga plus élevée de l'interface CIGS/Mo joue un rôle passif en créant un champ arrière qui repousse les porteurs minoritaires et réduit la recombinaison au contact arrière.

Les absorbeurs ont été déposés par le procédé en 3 étapes. Cependant, les flux de Ga ont été maintenus constants dans les premier et deuxième étages, tandis que dans le troisième étage, le flux de Ga a été réduit par étapes de 3,0, 2,5 et 2,0 nm/min. Ceci a eu un impact direct sur le GGI de l'absorbeur CIGS qui est passé de 0,34 (réf - 3,0nm/min) à 0,28 (2,5 nm/min) et 0,24 (2,0 nm/min). La tendance la plus intéressante est l'évolution du gradient de Ga qui a été mesuré par spectroscopie d'émission optique à décharge luminescente (GDOES).

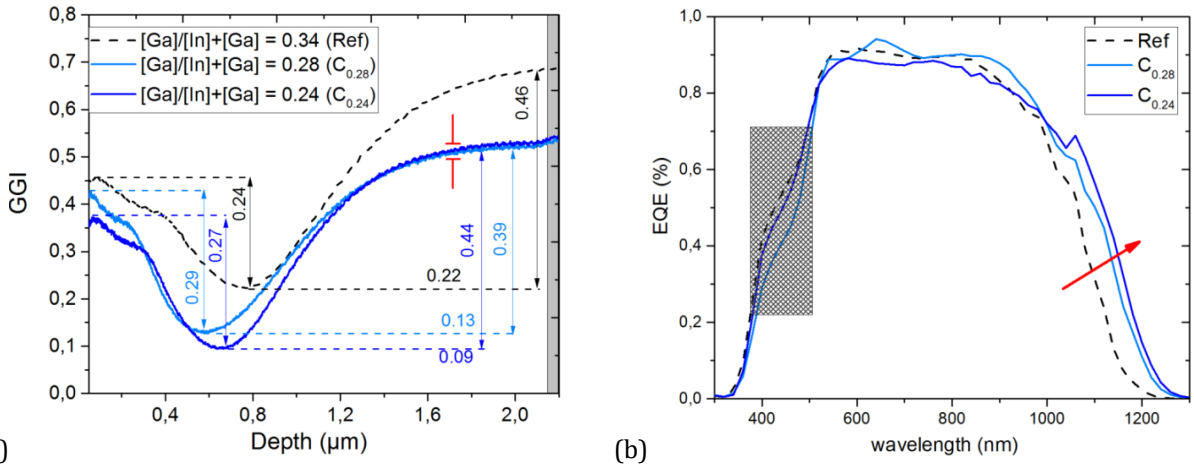


Figure 9. a) Profil GGI de la plus grande partie des absorbeurs mesurés par GDOES et b) Réponse EQE des cellules.

Les figures 9a et 9b montrent le profil GGI des absorbeurs et leurs réponses EQE respectives. Nous nous attendions à un profil Ga identique près de la surface arrière de l'absorbeur puisque les première et deuxième étapes des expériences étaient constantes.

Cependant, la cellule de référence a une GGI très supérieure aux cellules $C_{0.28}$ et $C_{0.24}$. Les échantillons modifiés ont également une entaille plus profonde que la référence, ce qui indique un écart de bande passante plus faible dans cette région. Dans les films $Cu(In,Ga)Se_2$, les gradients de composition conduisant à un gradient de bande interdite affectent également la pente de la partie longue longueur d'onde de la courbe EQE. Cette observation est évidente dans les mesures EQE des échantillons (figure 9b) alors que l'absorption augmente dans la région de longueur d'onde supérieure des photons incidents. On croit que cette différence de bande passante améliore l'absorption des photons à faible énergie. L'EQE de $C_{0,24}$ dépasse légèrement celui de $C_{0,28}$ et la différence peut être observée dans le Jsc mesuré des échantillons du tableau 6.

	GGI	Eff (%)	*V*oc (V)	*J*sc (mA/cm^{-2})	FF (%)
Ref	0.34	13.5	0.60	31.8	70.4
$C_{0.28}$	0.28	12.9	0.59	32.2	67.7
$C_{0.24}$	0.24	14.0	0.58	34.2	70.4

Table 6. Résumé des propriétés électriques des absorbeurs CIGS à gradient de Ga modifié

Nous avons obtenu un gain de courant de +2,3 mAcm^{-2} en comparant la meilleure cellule ($C_{0.24}$) avec la référence. On observe également une légère baisse du Voc, car l'GGI a diminué, mais nous avons pu atteindre une efficacité maximale de 14,0 % sur les substrats de Mo avec une modification du gradient de Ga.

• Impact d'un contact arriere de Mo par pulverisation cathodique

Étant donné que nous utilisons des substrats souples en feuille de Mo, nous n'avons pas besoin d'une couche supplémentaire de contact arrière en Mo pulvérisé. Cependant, le but de cette étude était d'identifier les effets bénéfiques, le cas échéant, de l'ajout d'une couche de contact arrière Mo comme dans la structure CIGS classique.

Avant le dépôt de l'absorbeur CIGS, 100 nm et 800 nm de contact arrière de Mo ont été pulvérisés sur les substrats de Mo. Un échantillon de référence (0 nm de Mo pulvérisé) a servi de référence. Les absorbeurs ont été déposés comme déjà décrit par le procédé de coévaporation en 3 étapes à 480 °C et 550 °C respectivement pour observer tout impact à ces températures.

Les mesures XRD des échantillons révèlent une tendance intéressante sur l'influence d'une couche pulvérisée de Mo. Pour une température de dépôt de 480 °C, une comparaison entre les pics CIGS (112) et (220)/(204) montre une faible influence de la couche de Mo pulvérisée sur l'orientation de croissance CIGS, le (112) reste l'orientation préférée. Lorsque la température de dépôt du CIGS est portée à 550 °C, on observe que l'orientation préférée du CIGS passe de (112) à (220)/(204) lorsque l'épaisseur de la couche pulvérisée de Mo augmente de 0 à 800 nm. En fait, il y a une augmentation progressive de l'intensité des pics (220)/(204) et une diminution du pic (112) de l'absorbeur CIGS à mesure que l'épaisseur du Mo pulvérisé augmente. En conclusion, à 480 °C, l'orientation préférée du CIGS est (112) quelle que soit l'épaisseur de la couche de Mo pulvérisée; cependant, à 550 °C, à mesure que l'épaisseur de cette couche de Mo pulvérisée augmente, l'orientation préférée du CIGS est (220)/(204).

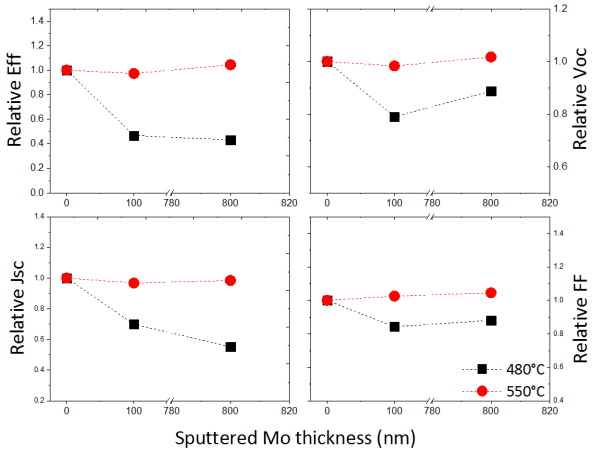


Figure 10. Performances relatives des cellules avec différentes épaisseurs de contact arrière en Mo pulvérisé.

La figure 10 compare le changement relatif des propriétés électriques des cellules aux deux températures de dépôt en fonction de l'épaisseur du contact arrière du Mo pulvérisé. A 480 °C, la présence d'une couche de Mo pulvérisée nuit aux performances de la cellule avec un effet plus profond sur le Jsc et l'efficacité qui tombent à environ 48 % des valeurs de la cellule de référence. En revanche, lorsque la température de dépôt est portée à 550 °C, l'efficacité, Voc et FF s'améliore d'environ 10 % pour le contact arrière du Mo pulvérisé de 800 nm d'épaisseur.

Cellules solaires CIGS sur des feuilles en acier inoxydable

L'acier inoxydable est un autre substrat métallique approprié et largement utilisé pour la fabrication des cellules CIGS. La température élevée de fusion de l'acier inoxydable le rend utilisable pour les dépôts CIGS à haute température. De plus, l'acier inoxydable a un coefficient de dilatation thermique (CTE) de 9,4 - 12,5 × 10^{-6} K^{-1} qui correspond étroitement à celui du CIGS. L'acier inoxydable est également bon marché et facilement disponible.

Bien que viable, l'acier inoxydable contient une quantité importante de Fe qui est le principal métal d'alliage. On sait que le Fe est nuisible à la performance des cellules CIGS car il entraîne la formation de niveaux profonds dans la bande passante et génère des pièges électroniques dans l'absorbeur CIGS. La diffusion des impuretés de Fe dans la cellule CIGS peut être limitée par l'application d'une couche barrière d'impuretés appropriée avant le dépôt CIGS. Des exemples de matériaux de couche barrière qui ont été testés incluent, sans s'y limiter, SiO_x, Al_2O_3, Cr, AlN et Mo. SiO_x et Al2O3 ont des propriétés isolantes et conviennent donc à l'intégration monolithique de modules CIGS. Une autre façon de limiter l'impact du Fe est de réduire la température de fabrication des absorbeurs car la diffusion du Fe est entravée à basse température.

- ### Étude des propriétés barrières du Chrome (Cr)

Les propriétés barrières du Cr ont été testées en incorporant du Cr (déposé par évaporation) sur les substrats en acier inoxydable et en évaluant les propriétés des cellules solaires CIGS fabriquées sur ces substrats. L'essai a été effectué en utilisant 0, 500, 800 et 1000 nm de la couche barrière de Cr. Les absorbeurs CIGS ont été cultivés selon le procédé en 3 étapes à 480 °C. La spectroscopie EDX a été utilisée pour mesurer la teneur en Fe trouvée dans les absorbeurs (tableau 7) qui a montré que la quantité de Fe détectée diminue systématiquement à mesure que l'épaisseur du Cr augmente. Ceci indique l'effet de blocage des couches de Cr.

épaisseur du Cr(nm)	Fe détecté (At. %)
0 (Ref)	2.51
500	2.16
800	1.53
1000	1.42

Table 7. Spectroscopie EDX montrant la quantité de Fe détectée dans la pile CIGS/Mo/Cr

Tous les échantillons, quelle que soit l'épaisseur de Cr, présentaient de petits grains près de l'arrière à l'interface CIGS/Mo et des grains significativement plus gros s'étendant du milieu vers la surface des absorbeurs, comme le confirme le MEB. Les caractéristiques IV des cellules ont révélé peu de différence entre les cellules dont l'épaisseur de la couche barrière de Cr varie. En fait, les propriétés sont très proches les unes des autres, ce qui nous amène à la conclusion que : (i) le contact arrière du Mo de 800 nm d'épaisseur a joué un rôle dans l'augmentation de la barrière d'impuretés efficace totale car il a déjà été confirmé que le contact arrière peut empêcher la diffusion des impuretés de Fe et (ii) la température de dépôt de 480 °C qui est la température standard du procédé n'était pas assez élevée pour provoquer la diffusion des impuretés de Fe suffisamment néfastes pour dégrader gravement les performances des cellules.

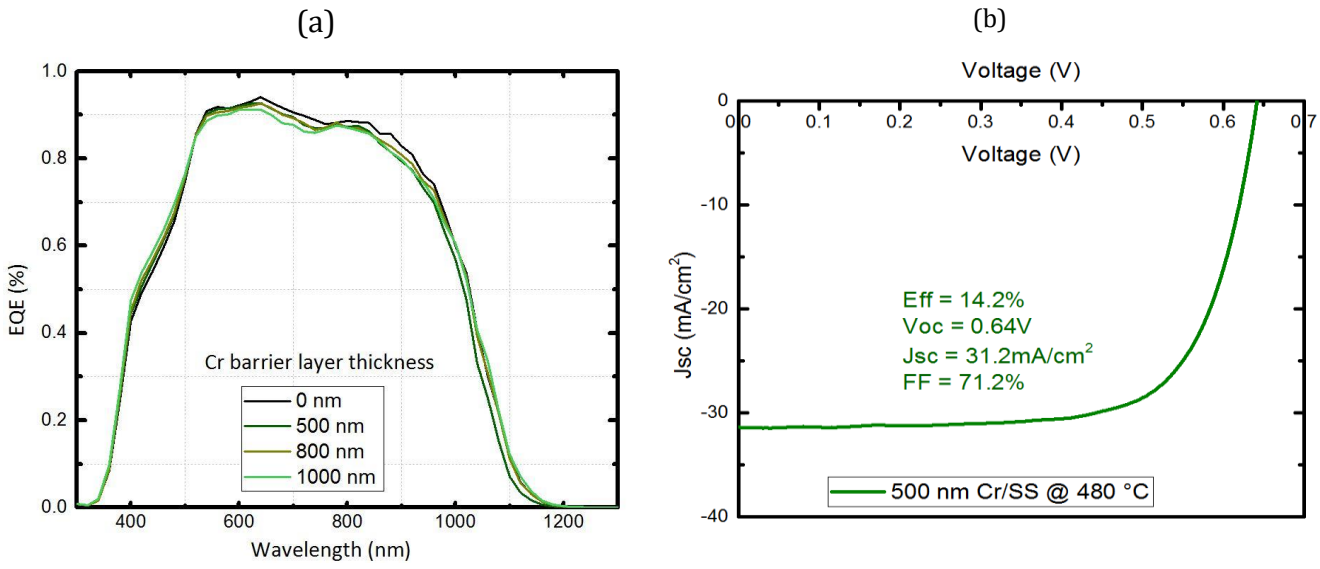


Figure 11. (a) Réponse spectrale EQE des cellules avec une épaisseur variable de la couche barrière de Cr et (b) courbe I-V de la meilleure cellule avec 500 nm de couche barrière de Cr.

La réponse EQE des cellules (figure 11a) est presque identique, sans différence majeure pouvant être attribuée à la présence de la couche barrière de Cr. En fait, la différence en Jsc entre la meilleure cellule (500 nm Cr) et la cellule de référence est de 0,7 mA/cm^2. La meilleure cellule, obtenue avec une épaisseur de barrière de Cr de 500 nm, est illustrée à la figure 11(b).

- ## Procede de depot CURO sur acier inoxydable

Cette partie du travail de thèse a été réalisée à l'IMN. CURO est l'acronyme de "Copper-Rich-Off". Comme son nom l'indique, il s'agit d'un processus de coévaporation en deux étapes qui débute dans des conditions favorisant une croissance riche en cuivre. Le procédé CURO est utilisé pour la croissance des films CIGS sur les substrats en acier inoxydable. Aucune couche barrière n'est déposée sur les substrats en acier inoxydable et le but est d'étudier l'effet du processus de dépôt sur la qualité des absorbeurs CIGS développés sur les substrats en acier. Le dépôt a été effectué à 570 °C sur le substrat en acier inoxydable et le SLG revêtu de SiN pour établir une base de référence et vérifier la compatibilité du procédé sur l'acier inoxydable.

Les mesures EDX (tableau 8) et SEM (figure 12) ont révélé que le procédé CURO standard appliqué sur SLG est incompatible avec l'acier inoxydable.

	Process	Cu (at. %)	In (at. %)	Se (at. %)	Ga (at. %)	CGI	GGI
1832-02 (SLG)	CURO	25.22	19.38	48.05	6.33	0.98	0.25
1834-02 (SS)	CURO	0.78	0.13	98.71	0.37	1.54	0.73

Table 8. Composition d'absorbeur CIGS montrant des différences dans la composition élémentaire des films CIGS sur SLG et acier inoxydable utilisant la même méthode et les mêmes paramètres de dépôt

On observe que lorsqu'on utilise un substrat de verre, on obtient un film légèrement pauvre en cuivre (CGI = 0,98, GGI = 0,25) qui répond idéalement aux exigences de base pour les films CIGS qui sont légèrement pauvres en cuivre avec un GGI entre 0,20 et 0,30. Cependant, les échantillons fabriqués sur les substrats en acier inoxydable révèlent un résultat particulier présentant une teneur en Se très élevée (98,7 %) dans les films qui étaient également très riches en Cu et Ga.

(a) (b)

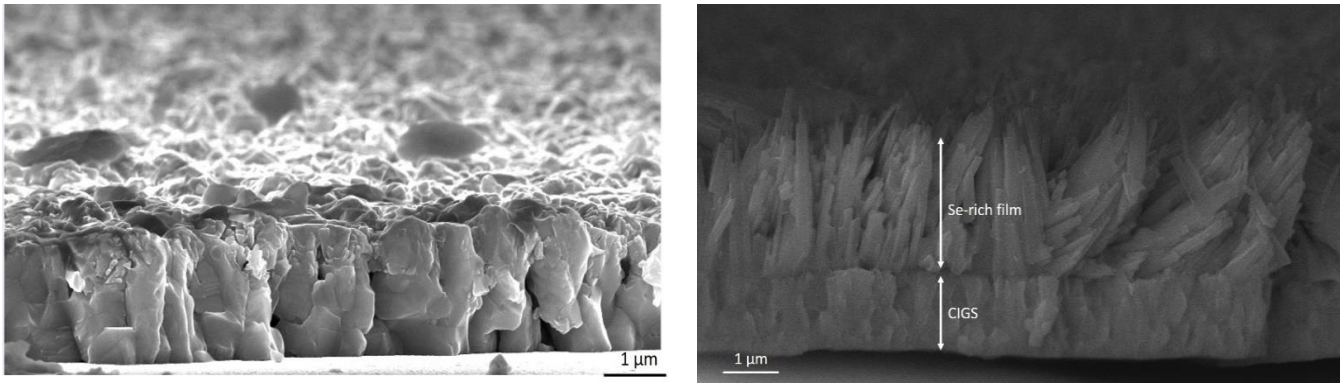


Figure 12. Section SEM de l'absorbeur CIGS obtenue par le procédé CURO sur (a) SLG revêtu de SiN et (b) acier inoxydable. Les paramètres du procédé de dépôt sont identiques dans les deux cas, cependant, le substrat en acier inoxydable est à une température beaucoup plus basse lorsque le flux de Se est désactivé, ce qui conduit à un dépôt du film de Se vu en (b).

L'incompatibilité du procédé résulte du dépôt d'un excès de Se dû à la basse température du substrat d'acier inoxydable (<250 °) pendant la phase de refroidissement. Le procédé a été modifié de telle sorte que la température du substrat en acier inoxydable soit de 300 °C pendant la phase de refroidissement. De cette façon, l'excès de Se déposé est réévaporé de la surface de l'absorbeur.

A la suite de ce procédé adapté, les absorbeurs CIGS ont été fabriqués selon le procédé CURO sur acier inoxydable, revêtement Mo et SiN SLG à 570 °C. La morphologie des absorbeurs est représentée sur la figure 13. L'absorbeur déposé sur SiN/SLG présentait la granulométrie la plus importante.

(a) (b) (c)

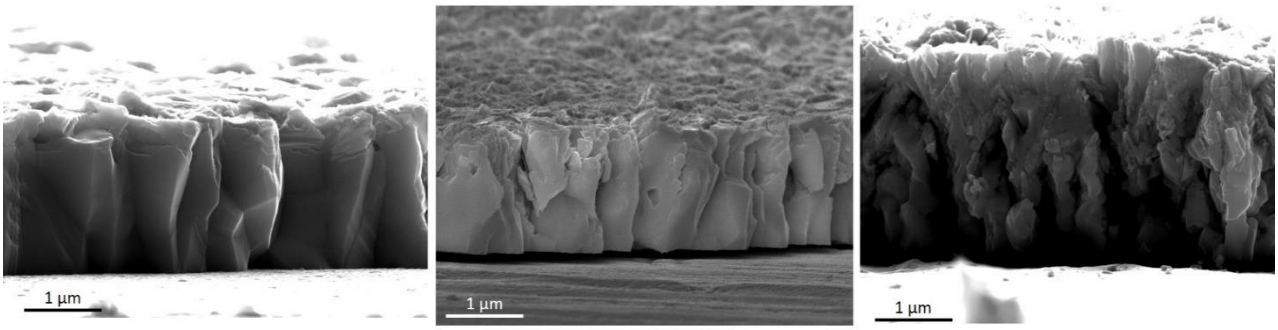


Figure 13. Images SEM en coupe transversale des couches minces CIGS cultivées sur (a) SLG revêtu de SiN, (b) acier inoxydable et (c) feuille de Mo.

Les grains individuels sont cylindriques et couvrent toute l'épaisseur de la couche mince du CIGS. L'absorbeur sur le substrat en acier inoxydable présente également de gros

grains, mais pas aussi bien formés que ceux du SiN/SLG. Au contraire, les absorbeurs sur le substrat en feuille de Mo ont de très petits grains. L'apparition de petits grains mal formés sur le substrat en feuille de Mo pourrait être corrélée aux compositions atomiques de chaque élément constitutif obtenues à partir des mesures XRF, notamment la composition In particulièrement faible sur le substrat en feuille de Mo (tableau 9).

	Cu (at. %)	In (at. %)	Se (at. %)	Ga (at. %)	CGI	GGI
1878 (SiN/SLG)	20.34	23.65	49.47	6.53	0.67	0.22
1880 (SS)	20.61	23.67	48.85	6.87	0.67	0.22
1881 (Mo)	22.17	14.77	55.73	7.32	1.00	0.33

Table 9. Compositions élémentaires des films CIGS fabriqués sur différents substrats par le procédé CURO

Les mesures XRD ont révélé une orientation fortement préférée (112) sur les trois substrats. Les efforts pour fabriquer un appareil fonctionnel à partir de ces absorbeurs se sont avérés vains. Ceci était dû à la méthode de rayage mécanique utilisée, qui a fortement détourné les cellules.

Conclusion

La comparaison entre 3 températures de dépôt a donné un rendement maximal de 9,0 % à 480 °C. En choisissant cette température comme température de dépôt standard, le CGI des absorbeurs a été optimisé en variant la durée de l'étape finale de terminaison dans la 3ème étape après que le plateau (CGI = 1) a été atteint. Ceci a conduit à une amélioration du CGI de 0,75 à 0,92 lorsque le temps était limité à 1 min après la formation du plateau sur la courbe du procédé. Le rendement enregistré a été de 9,5 %. Bien que le Voc et le Jsc soient restés relativement inchangés par cette modification, le FF s'est amélioré à mesure que le temps était réduit. L'incorporation de Na par PDT a été faite en utilisant le processus nouvellement développé. La meilleure cellule (13,5 %) a été obtenue lorsque la durée du flux de Na était de 20 min avec un post-recuit de soudure de 10 min. Le gradient de Ga a été accordé en jouant sur le flux de Ga dans le troisième étage de dépôt tout en maintenant les premier et deuxième étages constants. Par conséquent, la GGI initiale de la cellule de référence (0,34) a été réglée jusqu'à l'obtention d'un absorbeur avec une GGI = 0,24. L'augmentation correspondante de l'efficacité des cellules a donné un rendement de 14,0 %, ce qui est le maximum atteint sur les substrats en feuille de Mo. L'incorporation d'un contact arrière supplémentaire (Mo pulvérisé) a révélé une dégradation des performances de la cellule à une température de fabrication CIGS de 480 °C. Les performances de la cellule sont restées relativement inchangées avec une légère amélioration du rendement à 550 °C.

Sur des substrats en acier inoxydable, l'utilisation d'une couche barrière en Cr a permis d'obtenir le meilleur rendement de 14,2 % rencontré dans cette thèse sur l'acier inoxydable. Les résultats ont révélé peu de différence entre les cellules avec des couches variables de Cr. Les résultats étroitement appariés suggèrent qu'une épaisseur de Cr de 500 nm est déjà suffisante pour bloquer la diffusion du Fe. Cela s'explique en partie par (i) le contact arrière de 800 nm Mo qui possède également des propriétés de bloc et (ii) la basse température de fabrication de 480 °C qui ralentit dans une certaine mesure la diffusion du Fe. Dans la dernière partie, nous avons pu modifier le procédé standard CURO développé chez IMN et l'adapter aux substrats en acier inoxydable. Les absorbeurs CIGS à gros grains ont été obtenus sur de l'acier inoxydable et du SLG revêtu de SiN, mais de très petits grains ont été réalisés sur une feuille de Mo. En raison de la manœuvre des cellules, aucun dispositif de travail n'a été réalisé.

RÉSUMÉ

Dans cette thèse, les méthodes de fabrication et l'optimisation des absorbeurs CIGS déposés sur des feuilles flexibles en Molybdène et en acier inoxydable sont étudiées. La feuille de Mo agit à la fois comme substrat et comme contact arrière dans les cellules, réduisant ainsi les étapes de fabrication requises pour une cellule CIGS. D'autre part, l'acier inoxydable, bien qu'il nécessite une couche barrière contre les impuretés et un dépôt par contact arrière, reste économiquement plus intéressant. Les absorbeurs CIGS ont été réalisés par un procédé de coévaporation en 3 étapes. Ce travail étudie l'impact de différentes conditions de dépôt telles que la température, l'incorporation de Na et l'optimisation du gradient de Ga sur la performance de la cellule. Différentes techniques de caractérisation telles que les mesures XRD, GD-OES, IV et EQE ont été utilisées pour étudier les propriétés des cellules. Le procédé optimisé pour le dépôt CIGS sur feuilles de Mo a donné un rendement maximum de 14,0 %, ce qui est proche du rendement record mondial de 14,6 % atteint sur les substrats de Mo. Dans le cas de l'acier inoxydable, un inconvénient majeur est la présence d'impuretés Fe nuisibles qui créent des chemins de dérivation dans l'absorbeur. Pour réduire les effets néfastes de l'impureté de Fe, nous avons introduit une couche barrière tout en limitant la température de dépôt à 480 °C afin de réduire la diffusion efficace du Fe. Une efficacité maximale de 14,2 % a été obtenue avec une épaisseur de barrière Cr de 500 nm. Enfin, le procédé de dépôt CURO appliqué aux substrats d'acier pour étudier l'effet du procédé de dépôt sur la qualité de l'absorbeur.

MOTS CLES:

Substrats métalliques ; CIGS ; Rendement ; Cellule solaires

ABSTRACT

In this thesis, the fabrication methods and optimization of CIGS absorbers deposited on flexible Mo and stainless steel foils is studied. Mo foil acts as both the substrate and back contact in the cells hence reducing the manufacturing steps required for a CIGS cell. On the other hand, stainless steel despite requiring an impurity barrier layer and back contact deposition remains economically more interesting. The CIGS absorbers herein were realized by a 3-stage coevaporation process. This work studies the impact of different deposition conditions such as temperature, Na incorporation and optimization of the Ga gradient on the cell performance. Different characterization techniques such as XRD, GD-OES, IV, and EQE measurements were used to study the cell properties. The optimized process for CIGS deposition on Mo foils yielded a maximum efficiency of 14.0 % which is close to the world record efficiency of 14.6 % achieved on Mo substrates. In the case of stainless steel, a major drawback is the presence of detrimental Fe impurities that create shunt paths in the absorber. To reduce the detrimental effects of Fe impurity, we introduced a barrier layer while limiting the deposition temperature to 480 °C in order to reduce the effective diffusion of Fe. A maximum efficiency of 14.2 % was obtained with a Cr barrier thickness of 500 nm. Finally the CURO deposition process as applied to the steel substrates to investigate the effect of the deposition process on the absorber quality.

KEYWORDS:

Metallic Substrates; Efficiency; CIGS; solar cells